Howell, Jessie (2024) *Developing cytometry and inertial microfluidic tools to analyse and separate different cell cycle stages of Leishmania mexicana.* PhD thesis.

https://theses.gla.ac.uk/84653/

# Developing cytometry and inertial microfluidic tools to analyse and separate different cell cycle stages of *Leishmania mexicana*

Jessie Howell

Submitted in fulfilment of the requirements for the Degree of Doctor of Philosophy

James Watt School of Engineering

College of Science and Engineering

University of Glasgow

Supervisors: Dr Julien Reboud, Dr Melanie Jimenez and Dr Tansy Hammarton

Submission Date: 22/06/2024

# Abstract

The leishmaniases are a group of devastating diseases which affect around 350 million people, predominantly in developing countries. These diseases are caused by infection with the protozoan parasite *Leishmania*, yet despite its prevalence, much of the fundamental biology of these parasites is still unknown. One such area of research is the cell cycle, a process which is essential for the replication and survival of this parasite. This process has shown promise as a target for new therapeutic drugs, however, studying the cell cycle to identify such targets is made difficult by the high heterogeneity of cultures of these cells. Cultures contain cells in all stages of the cell cycle, making it difficult to understand and identify molecules controlling this process. While tools are available for synchronising cells at a single stage in the cell cycle, they are often sub-optimal, requiring lengthy processing times or introducing artefacts into the cells and affecting their molecular composition.

This thesis therefore explores inertial microfluidics as an alternative method for cell cycle synchronisation, relying purely on the morphological and mechanical characteristics of the cells to drive separation. Protocols using imaging flow cytometry were developed to provide high-throughput morphological information about the cells. As well as providing insight into the dynamics of the cell cycle, this enabled a deeper understanding of the behaviour of non-spherical cells within inertial microfluidic devices and subsequently an enrichment of desired cell populations. Finally, novel tools for the portable and high-speed imaging of particles within inertial microfluidic devices were demonstrated. As such, this work contributes both protocols and fundamental understanding to both the fields of *Leishmania* and inertial microfluidic research in the hope that these will prove beneficial to future work.

# Contents

# List of Figures

# List of Tables

## Acknowledgements

This report is submitted as fulfilment of the requirements for a Doctorate of Philosphy in Biomedical Engineering at the University of Glasgow. The work was carried out through the Division of Biomedical Engineering, at the College of Science and Engineering, University of Glasgow, Glasgow, UK. The Ph.D. programme started on the 06 January 2020 and was fully funded through an EPSRC Scholarship.

Firstly, I would like to acknowledge my supervisors Dr Melanie Jimenez and Dr Tansy Hammarton. You have both shown me what true leadership looks like, and through your examples, you have helped me to discover the researcher that I have become. I will be forever grateful.

To my friends and colleagues Andrew Farthing, Sulochana Omwenga, Alexandra Dobrea, Nicole Hall, Sophia Fochler, Andreia Went, Olubukola Owolodun... So many of you have contributed your time and efforts in supporting me and inspiring me, and constantly remaining me of why we do this. Thank you for keeping my spirits high and my sanity in check.

I would also like to acknowledge the Glasgow Imaging Facility, the Glasgow Flow Core Facility, and Amnis Corporation for their technical assistance.

To my parents for their endless love and encouragement, and for teaching me that through perseverance I can do anything.

And to my Alisdair. You have helped me to celebrate all of my wins, and consoled me through all of my loses. You’ve been my best cheerleader through it all. Thank you for always being in my corner.

## Declaration

I declare that, except where explicit reference is made to the contribution of others, that this dissertation is the result of my own work and has not been submitted for any other degree at the University of Glasgow or any other institution.

Printed name: Jessie Howell

Signature:

## List of Abbreviations

**CL** - Cutaneous leishmaniasis
**VL** - Visceral leishmaniasis
**MCL** - Mucocutaneous leishmaniasis
**PA** - Pentavalent antimonials
**FAZ** - Flagella attachement zone
**N** - Nucleus
**K** - Kinetoplast
**F** - Flagellum
**BB** - Basal body
**LPG** - Lipophosphoglycan
**PSG** - Promastigote secretory gel
**M** - Mitosis
**C** - Cyokinesis
**CRKs** - Cdc2-related kinases
**CDK** - Cyclin-dependent kinases
**RBCs** - Red blood cells
**FACS** - Fluorescence activated cell sorting
**MACS** - Magnetic actived cell sorting
**DEP** - Dielectrophoresis
**DLD** - Deterministic lateral displacement
**BF** - Brightfield
**MSC** - Microbiological safety cabinet
**IFC** - Imaging flow cytometry
**PFA** - Paraformaldehyde
**MeOH** - Methanol
**DCO** - Vybrant™ DyeCycle™ Orange
**DCR** - Vybrant™ DyeCycle™ Ruby
**DCV** - Vybrant™ DyeCycle™ Violet
**PI** - Propidium iodide
**SSC** - Side scatter

**AR** - Aspect ratio

**ARI** - Aspect ratio intensity

**1CF** - One circular focus

**2CF** - Two circular foci

**SN** - Short and narrow

**LN** - Long and narrow

**LW** - Long and wide

**SW** - Short and wide

**Re** - Reynolds number

**De** - Dean number

**ROC** - Receiver operating characteristic

**AUC** - Area under the curve

**TPR** - True positive rate

**FPR** - False positive rate

# Chapter 1

# Introduction

## 1.1 Project motivation

Throughout over 90 countries, the protozoan parasite *Leishmania* is transmitted by the bite of a female phlebotomine sand fly [1]. Infection with the parasite can develop into various diseases, with around 350 million people being at risk, around 1 million new cases and 30,000 deaths each year. These numbers are also expected to be underestimated due to misdiagnosis, asymptomatic infection and underreporting [2]. In humans, the three main clinical manifestations are cutaneous (CL), mucocutaneous (MCL), and visceral leishmaniasis (VL) although a wide spectrum of symptoms and presentations have been documented. CL is the most common form if the disease, presenting as lesions and ulceration of the skin. These can be self-healing or can take years, resulting in secondary infections, functional impairment and permanent scarring [3]. MCL occurs as a relapse, sometimes years after the initial cutaneous infections have apparently healed. Parasite migration to the nasal and oral cavities leads to facial disfigurement, vocal cord damage and destruction of the mucous membranes. Treatment is essential in MCL, with secondary infections incurring life threatening complications. VL is the most severe form of the disease, with a lack of treatment proving fatal in around 95% of cases [1]. This systemic infection is characterised by a swelling of the abdomen as a consequence of hepatomegaly and splenomegaly, with other symptoms including prolonged fever, weight loss and pancytopenia. In addition to the three main diseases described, asymptomatic infection is thought to represent the highest proportion of infections. While there is debate over whether asymptomatic infection can result in transmission, asymptomatic to symptomatic expression can occur due to various contributing factors and thus remains an important area of research [4]–[6]. On the other hand, zoonotic infections, particularly in domestic animals, are known to act as reservoirs and hinder eradication efforts [7], [8].

Despite its prevalence, leishmaniasis is classed as a neglected tropical disease, having significant health and social impact particularly in developing countries [9]. This is in part due to a lack of suitable treatment options or an approved human vaccine. Current methods of treating leishmaniasis, while effective, have various disadvantages: treatment options are often expensive and thus can be difficult for impoverish areas to obtain; all available drugs have a wide range of toxic side effects, which have resulted in fatalities in their own right; and an increase in drug resistance in some areas reduces their efficacy. There is thus an evident need for the development of new drugs to combat these devastating diseases. One area of research which shows particular promise for providing potential drug targets is the cell cycle – an essential process by which the cell replicates itself within its sandfly vector and mammalian host. However, the cell cycle of *Leishmania* is divergent from typical eukaryotes, with the proteins controlling this process being mostly unknown. Further research into the fundamental understanding of the *Leishmania's* cell cycle control is thus needed. These divergent processes also make studying the cell cycle challenging, as traditional methods of analysis are rendered ineffective. Therefore, this study aims to address the lack of tools available for the cell cycle analysis of *Leishmania*, as analysed using the species *L. mexicana*.

## 1.2 *Leishmania*

### Leishmania transmission

There are over 20 species of *Leishmania* parasites which cause disease in humans, transmitted by over 90 different species of sandfly [1]. These parasites are classified into either New World species (Viannia subgenus) or Old World species (Leishmania subgenus), with their geographical distribution being determined by their sand fly vector. 90% of all CL cases are found in Afghanistan, Algeria, Brazil, Iran, Peru, Saudi Arabia and Syria, while 90% of VL are found in Bangladesh, Brazil, India, Nepal and Sudan [10]. Furthermore, different species of the parasites are associated with different disease progressions. All species of *Leishmania* are able to cause CL while New World parasites (*L. (V.) braziliensis, L. (V.) panamensis,* and *L. (V.) guyanensis*) have a higher tendency to disseminate and cause MCL

[11]. On the other hand, only select species such as *L. donovani, L. infantum, L. tropicana* and *L. amazonensis* are able to cause VL [12], [13].

The polysymptomatic manifestations of the leishmaniasis are a result of the complex interplay between the host's immune response and the species of parasite. On the host's side, a strong cellular response is generally associated with better parasites control and low parasitaemia; however, over simulation can lead to MCL. On the other hand, a more humoral-based response is related to parasite dissemination and disease progression. *Leishmania* parasites are also able to modulate the hosts immune response by deactivating macrophages and preventing the production of proinflammatory mediators [14].

## Epidemiology

Historically, leishmaniasis has been thought of as a disease of developing countries. Overcrowding, poor housing and unhygienic conditions can provide a breeding ground for sandflies [15], [16]. In addition, low-income households have an increased likelihood of working and sleeping outdoors with no access to bed netting, increasing the risk of exposure to infected animals and sandflies. Malnutrition has also been shown to increase the risk of developing VL [17]. This problem is further exacerbated in the financial cost of acquiring treatment; while treatment may be free due to funding programs, costs can be incurred through travel to hospitals, unfunded stays overnight for treatment, time off work for such treatment or to care for ill individuals. In Nepal, it has been reported that that average cost of treatment for VL is greater than the annual household income [18]. Such costs have been reported to be paid for through the use of savings, the sale or rental or properties, the acquisition of high-interest loans or community aid, causing further financial and iatrogenic devastation to communities [19]. This in turn leads to poorer communities, exacerbating migration, urbanisation, displacement and conflict, increasing the risk of individuals contracting leishmaniasis [19]–[21].

In more recent times, leishmaniasis is emerging in developed countries; both autochthonously and imported by holiday makers, deployed military and immigration [22], [23]. In the U.S., an increase in the number and distribution of cases has been noted since the first recorded autochthonous case in Texas in 1903 [22]. Initially isolated to Texas, human cases have now been reported in Oklahoma, Arizona and North Dakota [24]–[26]. Non-imported zoonotic infections of horses and dogs have also been reported in Florida, Kansas and Ohio

[27], [28]. In 2015, *Leishmania* was classed as endemic in the US, while mandatory reporting still only applies to Texas [22]. However, the issue may be more widespread, with numbers being underrepresented due to lack of awareness, spontaneous healing of lesions and non-mandatory reporting. In Europe, all countries in the Mediterranean basin have been reported to be endemic for leishmaniasis, with the majority of cases being VL (69% compared to CL at 31%) [29], [30]. According to a recent review, *Leishmania* is re-emerging in various countries across Europe as well as migrating into previously unaffected areas [31]. Within many of these countries, domestic dogs act as a reservoir for *L. infantum*, with as many as 30% of dogs being seropositive.

Imported and/or non-endemic leishmaniasis is a growing concern for both for the affected individuals and for the introduction of leishmaniasis to previously unaffected areas [32]. This concern coincides with the increase in international travel which has been steadily growing to reach a peak of 1.46 billion people 2019 [33]. Imported cases of leishmaniasis from travel are generally highest from South America and the Middle East as a result of tourism and migration respectively [34], [35]. Tourism generally sees younger individuals contracting CL in areas such as Brazil and Costa Rica, while VL is more likely to be acquired from travelling in Europe. Younger travellers are more likely to contract CL during time spend outdoors or visiting forests where sandfly populations are high. In contrast, infants, children and the elderly are more likely to contract VL, hypothesised to be due to these individuals having weakened immune systems [35]. A lack of awareness contributes to the likelihood of contracting leishmaniasis as various precautions can be taken to reduce the chances of sandfly bite, such as using insect repellent, covering bare skin, and sleeping under bed nets [36]. For migration, a high number of cases are reported from the Middle East as a result of conflict among other things. CL has been endemic in Syria since before 1960 and up until the civil war in 2011 cases were reported to be 23,000 cases/year [37], [38]. This more than doubled in the early years after the onset of conflict, owing to an increase in impoverished conditions and the collapse in health services and vector control. Migration of over 4 million Syrian refugees additionally saw an increase in cases in neighbouring countries, causing local outbreaks within Syrian communities as well as introducing new species of *Leishmania* to areas [39], [40]. This is particularly true for Turkey, who accepted over 3 million refugees [40]. The increase in cases within Turkey are concerned to have direct implications for *Leishmania* transmission across Europe.

A contributing factor to the growing concern is climate change, with warmer temperatures increasing the suitability of areas for vector and reservoir habitation [41]. Sandflies are generally limited to areas which are above 15.6°C for at least 3 months of the year and will become dormant in winter at temperatures below 10°C. Research has also shown that sandfly activity favours warmer and drier conditions, with increased rates of proliferation and longer breeding seasons [42], [43]. In Europe, countries such as Germany are already seeing an increase in areas inhabited with sandflies, with recently studies suggesting new autochthonous transmission [41], [44]. Climate change modelling has shown that vectors will be able to reach areas as far north as England and Scandinavia [45], [46]. In the U.S., with increasing temperatures, different sand fly species are expected to be capable of migrating east and west, as well as far north as the Canadian border [22]. By 2080, it is predicted that the number of Americans at risk of infection will at least double [47]. In Morocco, climate change brings with it an increase in economic problems [48]. An increased frequency of drought and arid areas in the south has decreased access to water, affected food supplies and lead to uncontrolled migration, corresponding to higher cases of leishmaniasis and the migration into more northern areas [49].

## Diagnosis

There is very little standardisation of the diagnosis of leishmaniasis as all of the methods available have *pros* and *cons*. Typically, diagnosis is made through a combination of clinical, parasitological, molecular, and serological tests. Initial diagnosis is performed using the symptoms of the patient, as well as taking into consideration location (i.e. if in a region endemic for CL) and/or travel history. There are a plethora of clinical signs of leishmaniasis although most manifestations start with a small itchy papule developing between 2 weeks and 3 months after infection. After this point, the lesion can spontaneously heal or develop different characteristics [50]. Lesions are painless (unless infected), can ulcerate, vary in number (up to 300), with or without surrounding satellite lesions (multiple mini lesions in close proximity to the primary lesion) [5]. With developed lesions, the mucosal linings such as the nose and mouth should be examined to assess for MCL; initial symptoms include stuffiness and nasal inflammation but left untreated can develop into disfiguring lesions.

From clinical symptoms alone, CL and MCL can often be misdiagnosed and mistreated as bacterial infections, dermatitis, haemorrhoidal masses and even cancer due to the similarities in presentation [51]–[53]. This is more common in regions where leishmaniasis is not endemic. VL on the other hand has very different symptoms including a fever, swollen lymph nodes, swollen abdomen, weight loss, fatigue and discoloured patches of skin [54]. Diagnosis of VL relies purely on parasitological and molecular methods due to the non-specific nature of the symptoms. In developing countries, VL can often be misdiagnosed as malaria or enteric fever while in developed countries cancer is similarly suspected [52], [55].

With a suspected infection of CL or MCL, a biopsy sample is taken from a lesion. The confirmation of diagnosis requires the identification of whole parasites or/and parasite DNA from the samples, depending on the tests available [56]. Historically, detection of whole parasites (parasitological diagnosis) was viewed as the gold standard for diagnosis due to its high specificity, though the sensitivity depends on the species of *Leishmania*, where the biopsy was taken, the method it was acquired, and the skill of the medical professional [50], [55], [57]. Various methods are used to visualise the infecting parasites, including histopathology, microscopy of press-imprint-smears stained with Giemsa, or through cell culture [50], [58]. PCR now is the primary method of detection, identifying *Leishmania*-specific ribosomal or kinetoplast DNA. However, expensive equipment and the requirement of experienced staff limit its accessibility in developing countries. PCR has the added benefit of determining the specific species and strain of *Leishmania*, which has implications for disease development, treatment, and prognosis [59]. Commonly, the mini-exon gene is used for genotyping, with different strains having variations in both sequences and length [60].

The methods of diagnosis of VL are similar for that of CL and MCL, with some additional considerations. Diagnosis *via* direct visualisation is more invasive as the parasite proliferates within the internal organs. Tissue samples are usually collected from the spleen, bone marrow or lymph nodes, which each give varying degrees of sensitivity. Splenic samples have the highest sensitivity at up to 98.7%; however, sample collection is painful and can result in fatality from severe bleeding if complications arise [55]. Once the sample is collected, visualisation of the parasites is carried out *via* histopathology, microscopy or culture. PCR based diagnosis can be much less invasive than tissue samples as blood are often analysed; however, if blood samples are negative then splenic or bone marrow samples are used. There are various gene targets which have been suggested for PCR-based diagnosis of VL, with sensitivity generally being reported to be between 82.3-100%. As with above, PCR diagnosis is limited to facilities which have suitable equipment and trained personnel. As such, attempts are being made to develop serological test to diagnose VL from the presence of host antibodies against *Leishmania* parasites, or parasite antigens. Anti-*Leishmania* antibodies are present in the blood during infection, with a variety of tests currently available. However, using antibodies gives rise to two main issues: antibody tests can remain positive for months or even years after cure of the disease; and up to 32% of asymptomatic individuals can be positive for antibodies [61]. Furthermore, many of the antibody tests have drawbacks which limits their accessibility, particularly in developing countries such as requiring specialised equipment (e.g. enzyme linked immunosorbent assays), skilled personnel (e.g. immunoblotting), and are expensive (e.g. direct agglutination test). Another downside to all aforementioned tests (with the exception of the direct agglutination test) is the requirement for electricity or laboratory equipment, which delays the diagnosis of patients, particularly those in rural areas.

To combat this issue, immunochromatographic (ICT) strip tests have been designed as rapid diagnostic tests for diagnosing VL in the field. Using a recombinant K39 protein, these single use tests take only 15 minutes and a drop of blood from a finger stick. In addition, they are reported to be highly sensitive and specific making them widely accessible [62]. Unfortunately, these tests still occasionally test positive in healthy individuals and remain positive in patients cured of their VL for long periods of time. The sensitivity of different antibody tests has also been shown to be variable in different regions, thought to be due to different ethnic backgrounds and antibody responses [63]. Finally, antigen detection may prove to be a better method of diagnosis than antibody, with various tests showing high sensitivity as well as a reduction in the number of positive cases after patients were cured of VL [64]–[66].

### Treatment and prevention

Current methods of treating leishmaniasis primarily rely on pentavalent antimonials (PA), which has been the first line of treatment for CL, MCL and VL for over 70 years [67], [68]. While treatment with this family of drugs is effective at clearing the pathogens, there are various disadvantages, with the drug being expensive, having a wide range of toxic side effects and an emergence of drug resistance. For mild cases of CL with little chance of progression to MCL, often no treatment is given to avoid unnecessary exposure to the toxic compounds, which have been reported to induce cardiotoxicity and sudden death in a very low number of patients [68], [69]. In contrast, treatment for MCL and VL is essential, a lack of which can result in permanent disfigurement and death. In India, it has been documented that over 60% of patients do not respond to PA treatment due to microbial resistance [59]. Alternatives to PA are miltefosine, paromomycin, and liposomal amphotericin B, which, despite have varying degrees of efficiencies, treatment durations, and side effects are becoming more widespread [70]. Even with the more recent introduction of these drugs, resistance resulting in disease relapse is already beginning to emerge [71]. There are currently no drug treatment options which are both highly effective and toxin free, emphasising the need for new treatment methods [72]. Various drugs are currently undergoing development in clinical trials and are showing good potential as effective and safer anti-leishmanial compounds, but the regional variation in responses and the concern for resistance maintains a driving force for the continual development of new treatment options [73], [74].

While treatment is essential for the remedy of active cases of disease, prevention is always better than cure. For leishmaniasis, naturally acquired immunity is achieved after successfully fighting an infection, preventing the likelihood of secondary infections [75]. Thus far, despite a wide range of methods being tested (and four vaccines available for canine leishmaniasis), no vaccines are currently available for human use [76]. For many infections, the injection of killed, attenuated or inactivated pathogens (or their proteins), with or without immune system-stimulating agents (adjuvants) is sufficient to confer protection [77]. This is not the case for leishmaniasis, which have seen many prospective vaccines fail. The only artificial method to induce robust and long-lasting protection has been with leishmanization; the intentional inoculation of individuals with live parasites [78]. While this method still produces the formation of lesions, the pathology is reduced compared to naturally acquired infection and confers immunity for life. Leishmanization is licensed in some high-risk regions to prevent more serious manifestations of the disease; however, it is unsuitable for vaccination in lower-risk areas. One area of vaccine development using similar methodology is the use of genetically altered live-attenuated *Leishmania*. By knocking out genes which are important to the parasite's replication *in vivo*, immunity can be induced while limiting parasite load and disease severity [79]. Another vaccine candidate of particular interest is an adenoviral-vectored leishmaniasis vaccine which has been proven to be safe in humans and induce a potent cell mediated immune response [80], [81].

## Structure of a *Leishmania* cell

The parasite itself belongs to the diverse family of parasitic protozoa called Kinetoplastida, characterised by the presence of a DNA containing organelle called the kinetoplast (Fig. 1.1). Of these organisms, *Trypanosoma* and *Leishmania* are the only two families which cause disease in humans. While the members of this group undergo various morphological changes during the course of their life cycles and cell cycles, their ultrastructure remains highly conserved [82]. Unlike in typical eukaryotes which have multiple mitochondria throughout the cell, kinetoplastids have one very large mitochondrion and a single site of mitochondrial DNA, known as the kinetoplast. The kinetoplast DNA consists of a network of mini- and maxicircles of mitochondrial DNA which encode guide RNAs, the role of which are still unclear [83]–[85]. As with all eukaryotes, the genomic DNA is contained within the nucleus which, in *Leishmania*, is positioned posterior to the kinetoplast. One of the most visible differences between typical eukaryotic cells and trypanosomes is the presence of a flagellum, which contributes to cellular motility as well as playing a role in intracellular environment sensing [86], [87]. At the base of the cell, the flagellum exits the cell body at the flagella pocket; an invagination of the cell membrane acting as a site of endo/exocytosis within the parasite and serves as a key feature in development and pathogenicity [88]–[90]. The flagellum connects to the body's cytoskeleton at the flagella attachment zone (FAZ). In *Trypanosomes*, the FAZ has been demonstrated to contribute to cell division, affecting both the size of the cell and organelle organisation. However, for *Leishmania* this is not the case, with FAZ disruption instead affecting cell size but not replication [91], [92]. The basal body caps the end of the flagellum and is connected to the kinetoplast membrane *via* a collection of filaments [93], [94]. Finally the shape and length of the cell body is determined by microtubules which are modified throughout the life cycle and cell cycle contributing to the heterogeneity seen in morphology [89].

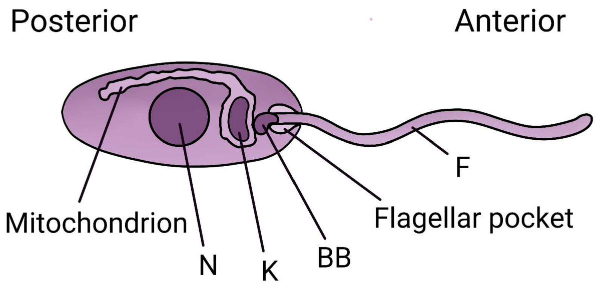

**Figure 1.1: Structure of a *Leishmania* promastigote**
Graphical representation of a *Leishmania* cell, denoting the single mitochondrion, nucleus (N), kinetoplast (K), basal body (BB), flagellar pocket and the flagellum (F). Image is not to scale.

### ***Leishmania mexicana's*** **life cycle**

To be able to survive in both mammals and sand flies, *Leishmania* has a complex life cycle with two distinct life cycle stages: the promastigote stage within sandflies and amastigote form in their mammalian hosts (Fig. 1.2). Within sand flies, there are 4 generally accepted stages, primarily defined by cell morphology due to a lack of molecular markers [89]. When a sandfly takes a blood meal, a peritrophic matrix forms from digestive secretions to encase the blood. The peritrophic matrix has been described to act as a physical and chemical barrier to protect the midgut endothelium from damage *via* physical particulates or pathogens ingested with the blood [95]. When amastigotes are ingested, the change in environment induces their differentiation into replicative procyclic promastigotes (Fig. 1.2A); the early promastigote stage [96], [97]. At this stage, if the sandfly is incompatible with the species of *Leishmania* then the parasites will be killed *via* the digestive secretions. In compatible species, after a couple of days the cells become longer and more motile, differentiating into nectomonad promastigotes [97], [98]. These cells are capable of escaping the peritrophic matrix and migrate to the sandfly's anterior midgut where they bind to the epithelium *via* their lipophosphoglycan (LPG) coat. Attachment to the midgut *via* these glycolipids establishes the infection; loss of which renders the cells susceptible to toxic compounds released during blood digestion, as well as excretion as faeces [99], [100]. These nectomonads are described as being non-replicative, thus evidence suggests the presence of a third promastigote form: leptomonads [97], [101], [102]. Further differentiation into short replicative leptomonad promastigotes enables the secretion of promastigote secretory gel (PSG); a major factor in *Leishmania* transmission [97], [103], [104]. PSG forms a plug in the sandfly's digestive tract and serves a variety of functions to increase transmission. Firstly, this PSG plug harbours a large proportion of leptomonads which subsequent differentiation into metacyclic promastigotes; the only mammalian infective stage of the parasite. The PSG is therefore the primary site for metacyclogenesis. Secondly, the plug modifies sandflies feeding behaviour by increasing feeding times and probing. Finally, the blockage has been hypothesised to induce regurgitation and the subsequent deposition of large numbers of metacyclic promastigotes into the dermis (Fig. 1.2B); however, this theory is still under debate [96]. In addition to being transmissible, this stage has also been shown to de-differentiate into a retroleptomonad [105]. Unlike metacyclic promastigotes, these cells are replicative and are thought to conserve untransmitted cells, subsequently increasing parasite load in the sand fly and higher levels of transmissible metacyclic promastigotes.

Once transmitted to a mammal, the hosts immune system responds to the invasion and migrates to the site of damage. Interestingly, while macrophages are the primary host for *Leishmania* replication, neutrophils have been demonstrated to be the first cell to be recruited and phagocytose the pathogens; a response which has been shown to benefit the survival of the parasites. Zandbergen *et al.* showed that *Leishmania* are able to survive within neutrophils for $\sim$ 48 hours before the neutrophils undergo apoptosis [106]. Recruited macrophages then ingest the infected, apoptotic neutrophils which modifies the macrophage to release anti-inflammatory cytokines, dampening the immune response. The macrophages are subsequently unable to produce IFN-γ, a crucial cytokine in the killing of *Leishmania* parasites [107]. Thus, the parasite within the engulfed neutrophil is able to infect the unsuspecting macrophage, for a “silent” infection (Fig. 1.2C). A metacyclic promastigote established within a parasitophorous vacuole will differentiate into a small, aflagellate, obligate intracellular amastigote within 72 hours [108] (Fig. 1.2D). Within this compartment, amastigotes scavenge nutrients from the macrophage facilitating their proliferation [109]. These can survive within macrophages for weeks, from which they erupt and are released into the blood and tissues to infect other cells (Fig. 1.2E), or are taken up by sandflies during a blood meal to repeat the cycle (Fig. 1.2F).

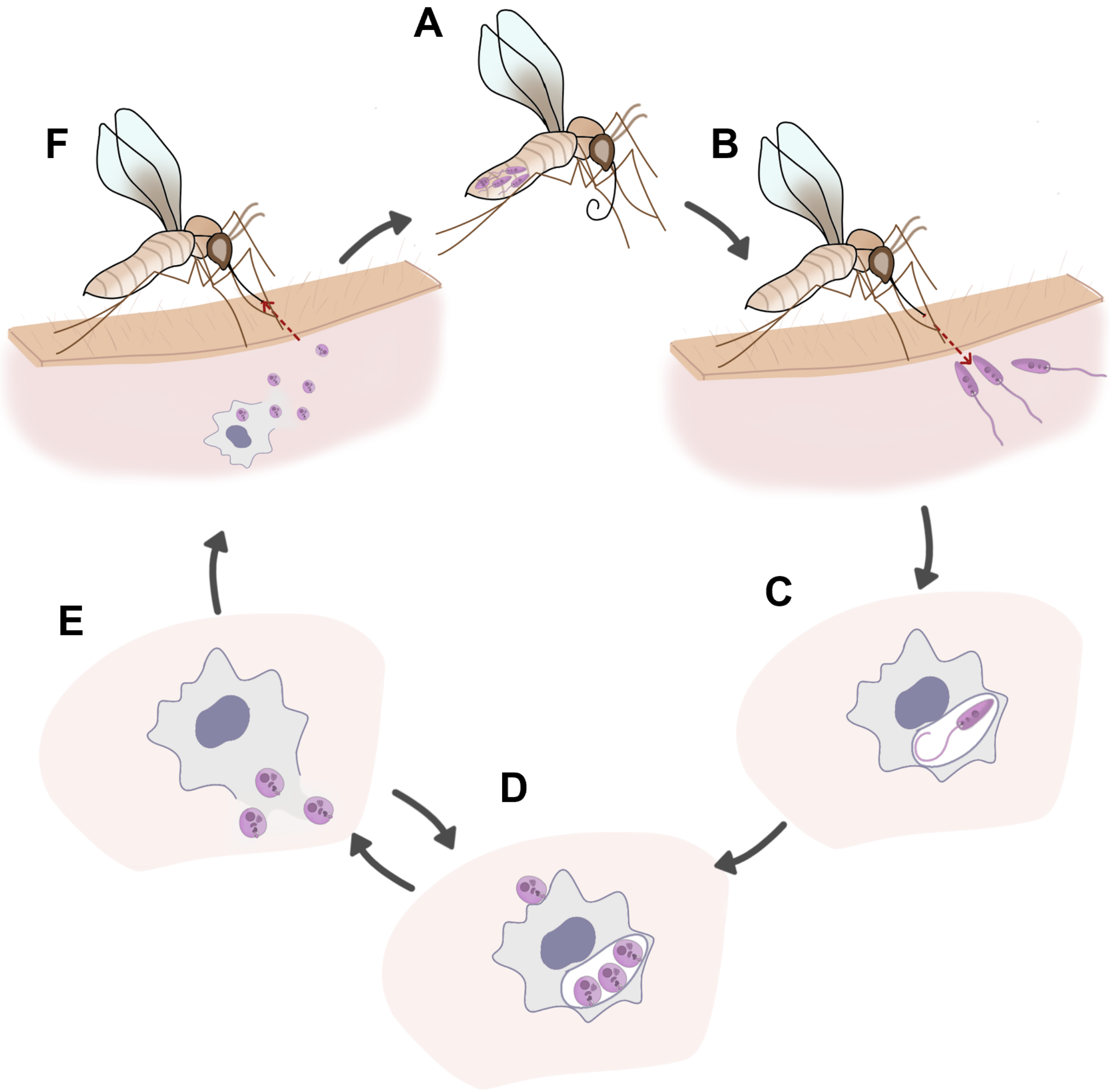

**Figure 1.2: Life cycle of *Leishmania (Leishmania) spp.***
Graphical representation of the dixenous life cycle of *Leishmania*. (A) *Leishmania* promastigotes live in the midgut of the female sandflies. Promastigotes differentiate into infective metacyclic promastigotes, which reside in the sandflies stomodeal valve (a valve between the sandfy's foregut and midgut). (B) When the infected sandfly takes a blood meal, these metacyclic promastigotes are injected into the skin of a mammal such as a human. (C) Within the skin, the metacyclic promastigotes are phagocytosed by immune cells, such as macrophages and neutrophils but are adapted to avoid degradation (D) Within the phagolysosome, the metacyclic promastigotes differentiate into amastigotes, which replicate within these parasitophorous vacuoles. (E) The amastigotes replicate until the host cell ruptures, releasing more amastigotes into the surrounding environment. These can either be re-engulfed by immune cells to undergo more replication (D) or get taken up by a sandfly during a blood meal (F). Within the sandfly, the amastigotes differentiate back into amastigotes to restart the life cycle. Image is not to scale.

## The cell cycle

In order for *Leishmania* to establish itself within both the sandfly and the mammalian host, it must be able to replicate itself. Replication is an essential process throughout the eukaryotic kingdom, resulting in the division of one cell into (for the most part) an exact copy of itself by a process called the cell cycle. In typical eukaryotes, the cell cycle consists of the phases gap 1 (G1), synthesis (S), gap 2 (G2), mitosis (M) and finally cytokinesis (C) (Fig. 1.3). During G1, cells assess their internal and external environments ensuing that conditions are met (i.e. sufficient nutrients and a lack of stress markers) [110]–[112]. This corresponds with cell growth and preparation for cell cycle progression. S phase sees the replication of DNA after which a second growth phase (G2) results in the synthesis of proteins required for mitosis. During these stages, detection of damaged DNA during checkpoints causes the cell cycle to be temporarily arrested to enable its repair by DNA repair machinery [113]–[115]. Mitosis is a highly dynamic stage, in which cells divide the replicated chromosomes between two nuclei, requiring processes such as the breakdown of the nuclear envelope, the condensing of DNA and the formation of a spindle [116]. Finally, cytokinesis results in the division of the cytoplasm to form two daughter cells. This is a highly conserved and tightly controlled process as improper division is costly, resulting in cell aberrations, loss of function and cell death [114]. Thus, for somatic cells which are not differentiating, the order and the timings of these changes is the same every time.

In typical eukaryotic cells, the cell cycle is controlled at a transcriptional level, with the synthesis of cell cycle related proteins occurring at specific points within the cycle [117], [118]. On a protein level, progression is controlled by protein kinases; enzymes that phosphorylate their substrate. Cyclin-dependent kinases (CDKs) are the major regulators of cell cycle progression, in conjunction with their corresponding cyclins [119]. In humans, the role and the timings of these CDKs, cyclins and associated proteins (e.g., CDK inhibitors, transcription factors and checkpoint kinases) in the cell cycle is well defined. For example, CDK4 and 6 associate with cyclin D inducing entry into the cell cycle, while the action of cyclin A and CDK2 causes progression through S phase (Fig. 1.3) [120]–[122]. The specific timings of these proteins and their corresponding transcription therefore acts as markers of cell cycle progression [118], [123].

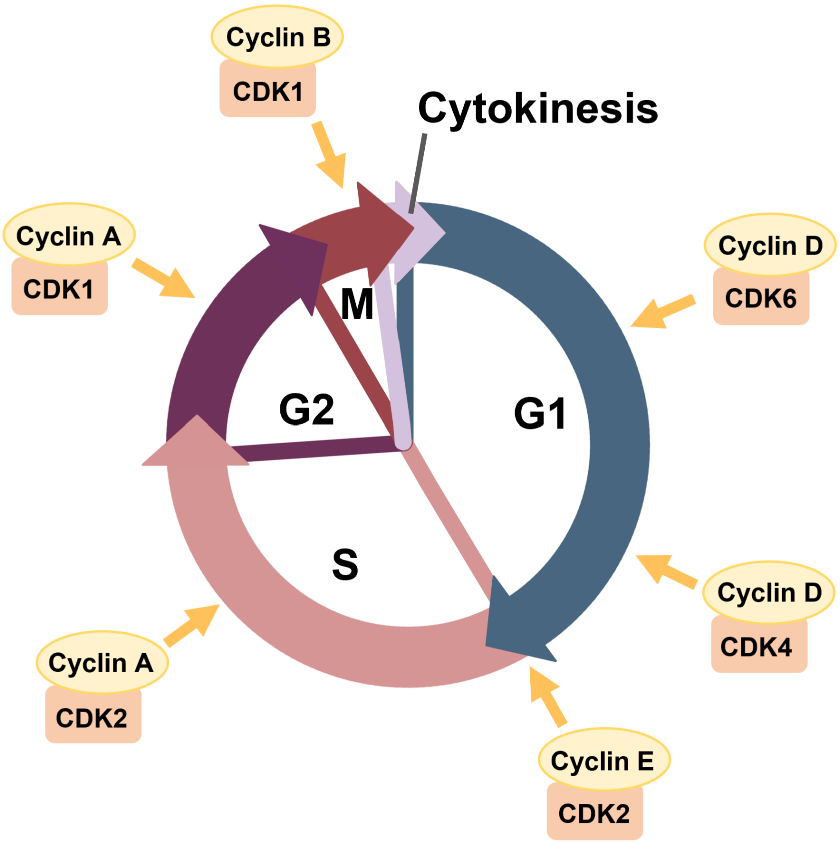

**Figure 1.3: Typical eukaryotic cell cycle.**
Schematic of the eukaryotic cell cycle, demonstrating progression through G1, S, G2, mitosis (M) and cytokinesis phases, and the corresponding cyclin and cyclin-dependent kinase (CDK) complexes regulating progression.

On the other hand, understanding of cell cycle progression in *Leishmania* is lacking, with most of our understanding coming from work in promastigotes. Early work by Chakraborty and Gupta in 1962 reported on the timings of the mitotic phases; however, it wasn't until 2011 that the full cell cycle was described [124]. By analysing the number of nuclei, kinetoplasts and flagella by microscopy; the quantity of DNA with flow cytometry; and the length of DNA synthesis with BrdU, the timings and morphological characteristics of G1, S and mitotic phases were resolved. The authors allude to the presence of a G2 stage; however, it was shown to be very short and thus described alongside the mitotic phase [125]. Wheeler *et al.* demonstrated that over the course of its 7.1 hr cell cycle, *L. mexicana* cells undergo precise and distinct size and shape changes (Fig. 1.4) [125]. Briefly, cells at the beginning of G1 are short and narrow. As they progress through G1, they increase in length, but not width. Cells maintain this elongated morphology throughout the course of S phase, where they simultaneously replicate both their nuclear and kinetoplast DNA, doubling the cell's DNA content [125], [126]. At the end of S phase, a second flagellum is seen to emerge from the cell body. Post-S phase, the authors speculated at a very short G2 phase, which is expected to see cells shrink in length and widen. Cells rapidly enter into mitosis where they appear short and wide. Unlike eukaryotic cells, the DNA doesn't condense and the nuclear envelope doesn't break down and over the course of an hour DNA segregation occurs. In *Leishmania*, the order of division of the nucleus and kinetoplast seems to vary between species, between reports, and even within a single species. In *L. mexicana*, traditionally it was thought that the nucleus divided before the kinetoplast, as is visualised by light microscopy and DNA staining [125]. More recent evidence using scanning electron microscopy suggests that, like in *L. major, L. tarentolae* and *T. brucei*, the kinetoplast divides first [126]–[128]. There are two possible explanations for the discrepancy in results for *L. mexicana*. Firstly, it is possible that the resolution of light microscopy is not high enough to be able to differentiate between two separated kinetoplasts when in close proximity. The second explanation is that, like *L. donovani*, a proportion of *L. mexicana* cells may divide their kinetoplast first, and due to the low numbers of cells analysed in this report (*n* = 56), a true representation of the population as a whole was not achieved. Therefore, to coincide with the work done later with DNA staining and light microscopy the kinetoplast is represented to divide after the nucleus. Work in *L. major* also demonstrated that the flagellar pocket begins to divide prior to mitosis and ends part way though. After the organelles have divided, a membrane extends through the centre of the cell, before a furrow forms at the anterior end of the cell, diving the cytoplasm between two daughter cells during cytokinesis. The two cells are joined only by their posterior ends (a doublet cell) before scission finally separates the two replicated cells.

In terms of cell cycle control, Trypanosomatids display a divergent method of protein regulation. Where typical eukaryotes use transcription to modulate the presence and quantity of cell cycle associated proteins, *Leishmania* instead rely on post-transcriptional modifications [129], [130]. This means that the majority of proteins are constitutively expressed, limiting the use of traditional transcriptomic studies. This therefore makes identifying cell cycle related proteins and assessing their function more of a challenge. One of the major works carried out in this regard was by Baker *et al.*, who attempted to use the clustered regularly interspaced short palindromic repeats (CRISPR) Cas9 system to knock out 208 protein kinases in the *Leishmania* genome and assessed their localisation through fluorescent fusion proteins [131]. Protein kinases are a diverse group of proteins which are characterised by a conserved catalytic domain. These proteins are of particular interest in anti-leishmanial drug

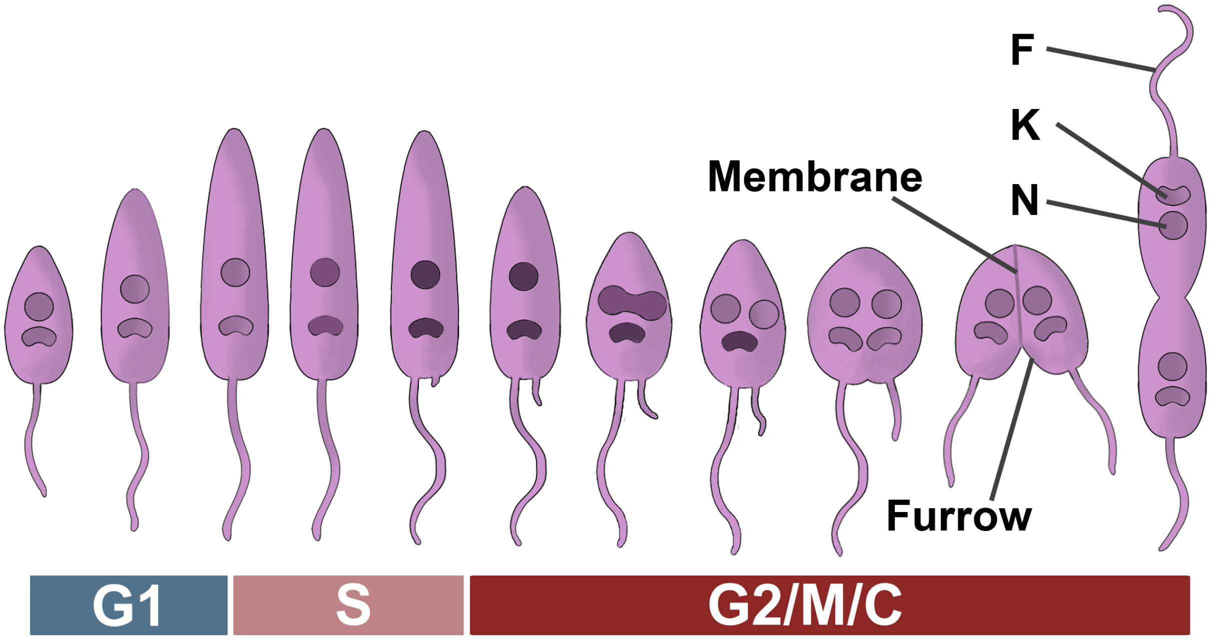

**Figure 1.4: Morphological changes throughout cell cycle progression in *L. mexicana.*** Throughout the course of *L. mexicana's* cell cycle, cells progress through G1, S phase (S), a very short G2 phase, mitosis (M) and cytokinesis (C). During this progress, cells double their DNA content within their nucleus (N) and kinetoplast (K) (represented by a darkening of their colouring), undergo changes to their length and width and double the numbers of organelles, including the N, K and flagellum (F). During cytokinesis, cells may have a membrane and/or a furrow.

development studies due to having key roles in cellular control and often being indispensable, with many having been shown to have roles in the cell cycle [132]. In the study by Baker, of the 11 CDK orthologues (named cdc2-related kinases, or CRKs), 6 were shown to be essential for cell survival, with their knockout failing to create a null mutant. These included CRK1, CRK3 and CRK12 which have previously been assessed in other work [131], [133]–[135]. Unlike CRK1, both CRK3 and CRK12 have been shown to regulate cell cycle progression [133], [136]. CRK3 is the most well studied CDK in *Leishmania* and is shown to be a functional orthologue of human CDK1, regulating the G2/M phase transition during the cell cycle [122], [133], [137]–[141]. It's knock down with the diCre system and its inhibition with flavopiridol resulted in cell cycle arrest at G2/M phase and caused cell death with higher doses [133], [139]. Similarly, chemical inhibition of CRK12, along with its corresponding cyclin CYC9, was achieved using a modified version a diaminothiazole compound which was originally identified to act against TbGSK3; a kinase with a plethora of functions in humans including intracellular signalling, apoptosis and cell division [10], [135]. In *L. donovani*, treatment of promastigotes with the modified drug resulted in the accumulation of cells in both G1 and

G2/M, with a decrease in S phase cells. In contrast, in *T. brucei* CRK12 has not been shown to affect the cell cycle, instead elucidating a role in endocytosis [136]. The additional three CRKs (CRK2, CRK9 and CRK11) have yet to be demonstrated to be cell cycle related. Five additional protein kinases were shown to be both essential and localise to the nucleus: AUK1, TLK, PKAC1, KKT2 and KKT3. AUK1 has previously been shown to affect cytokinesis in *Leishmania*, while in *T. brucei* AUK1 and TLK have been associated with mitosis [142], [143]. Similarly in *T. brucei*, PKAC1 affects basal body segregation [144]. Finally, KKT2 and KKT3 are kinetochore proteins, and are postulated to have roles in kinetochore function and assembly [145], [146]. Additional studies have demonstrated roles for AUK1, GSK and DYRK1 in cell cycle progression [142], [147].

### The cell cycle as target for drug treatment

In recent years, the cell cycle has emerged as a promising target for drug treatment due to its essential nature for disease progression, particularly for cancer therapeutics as well as neurological and parasite-driven diseases [148]–[151]. For cancer, cell cycle dysregulation is a requirement for its development, with breast cancer, gliomas, cervical carcinoma and sarcomas often showing mutations in CDK4/6 signalling pathway [150]. Initial drug development targeting this pathway proved efficient for halting breast cancer growth; however, their clinical action was shown to be non-specific with off target effects, gave low clinical response and had a lack of predictive biomarkers [121]. With non-specific targets, drugs can affect both the proliferating cancer cells as well as healthy cells, resulting in adverse effects [152]. Learning from these trials, subsequent development of compounds specifically targeting the CDK4/6 signalling pathway proved much more effective, with three such treatments being approved by the FDA as of 2018 [121], [153]. Since these successes, research into the role of other cell cycle signalling pathways, methods of synergising drug effects and treating side effects has led to the development of many novel drugs for various cancer types, with many currently in clinical trials [150], [154].

The cell cycle has also been indicated as a potential target for the treatment of leishmaniasis. Interestingly, CDK inhibitors developed for cancer treatment have similarly been trialled for use against *Leishmania*. The ability to repurpose drugs already approved for human use massively reduces the cost and times compared to new drug development. Flavopiridol was developed as a first-generation cancer treatment which is currently approved by the FDA for human use; however, it also inhibits *Leishmania's* CRK3 and induces cell death at high concentrations [133], [155]. Here, its use for *Leishmania* provides proof of concept that cell cycle inhibitors can act as therapeutic targets. Similarly, CRK12 inhibition with pyrazolopyrimidine compounds has shown good therapeutic potential, having minimal effects on human cells while have comparable anti-leishmanial properties similar to that of drugs currently used for treating leishmaniasis [135]. Another target which has been proposed for both cancer and *Leishmania* treatment is aurora kinase for which its inhibition with hesperadin in *Leishmania* has been postulated to have a role in cytokinesis and chromosomal segregation [142], [152]. Despite these targets showing a good potential for treatment, many questions still remain regarding their action, such as what the specific roles of these proteins are, the substrates of these kinases and how do these proteins regulate cell cycle progression. A lot of work is still needed to have a good understanding of the cell cycle to make informed decisions on developing drug targets.

### Current limitations of studying *Leishmania's* cell cycle

While the cell cycle provides promising targets for drug development, studying the cell cycle to both identify these targets and assess the effect of drugs is complicated by *Leishmania* diving asynchronously; cultures of cells have all stages of the cell cycle present simultaneously. One of the techniques commonly employed to circumnavigate this problem is through cell cycle synchronisation. Cell synchronisation is generally defined as a method of isolating a population of cells which are at the same stage in the cell cycle [156], [157]. After a single cell cycle stage has been isolated (from either parental cells or genetically modified cell lines), the resulting population can be subjected to molecular or cell cycle analysis [158], [159].

One of the most common methods employed in the literature for cell cycle synchronisation is through chemical treatment. By treating a culture with a cell cycle arresting drug, progression through the cell cycle is halted and the resulting population of cells accumulate at a single cell cycle stages. For *Leishmania*, flavopiridol and taxol are reported to block cell cycle progression at G2/M while hydroxyurea synchronises cells at the G1/S phase transition [139], [158], [160], [161]. Despite their widespread use, chemical treatment in this way provides a variety of challenges and caveats. Firstly, drug-based synchronisation is a lengthy procedure, with initial treatment times ranging from 8 – 24 hours and additional drug-release experiments to obtain other cell cycle stages requires sampling for hours afterwards [133], [145], [158]–[160], [162], [163]. Secondly, the lengthy treatment times have also been shown to induce artifacts such as DNA damage and cell stress responses, for example, which may bias proteomic experiments [164]. Thirdly, bulk treating cultures in this way is debated to result in biologically relevant populations of cells. While chemical arrest may block the progression of cells at a single cell cycle stage, it does not arrest all the other processes within the cells, i.e cell growth. Thus, synchronised cultures may maintain a high level of heterogeneity which is not indicative of the ”true” cell cycle [156]. Finally, efficiency of chemical-based synchronisation can vary depending on the drug used and the treatment times, with purities of between 21% and 95% being reported [133], [161].

Fluorescent activated cell sorting (FACS) is an alternate method of cell cycle synchronisation. Typically, this is carried out using a quantitative DNA stain to sort cells with different DNA contents (i.e. 2C, intermediate and 4C content of DNA) [165]. However, the resolution of FACS-based sorting is low as the fluorescence profiles generated from DNA staining only differentiate cells based on the quantity of DNA, providing no morphological or fluorescence localisation information. Therefore, late G1 cells cannot be distinguished from S phase cells, and mitotic cells stain similarly to cells in cytokinesis. Alternatively, size discrimination using the forward and side scatter is used to identify G1 cells; however, the yield is low, and other stages cannot be identified [166]. Furthermore, the sorting of rarer cell populations can also result in lengthy sorting times. Centrifugal counter-flow elutriation has been used to purify G1 phase *T. brucei* to > 95% based off cell size although this technique is yet to be reported with *Leishmania* [167].

While cell cycle synchronisation is fairly commonplace, there is much still debate over what classifies as a truly synchronised culture, what is only a population with a common feature (e.g. cells with 2C of DNA) and whether such populations can provide robust information into the molecular mechanisms of the cell cycle [156], [168]. Cooper (2003) argued that the following three criteria should be met in order for a population to be classed as synchronised: 1) that DNA content and/or pattern (e.g. the number of DNA containing organelles) is the same in all cells, 2) that the population progresses through the cell cycle in a synchronous manner and 3) the size distribution of the synchronised population should be narrower than the original asynchronous culture.

For *Leishmania*, generally criteria 1 and 2 are achieved using flow cytometery; through PI staining, the DNA is quantified to determine the proportions of cells in each of the different cell cycle stages. This is commonly carried out at various intervals after release from cell cycle arrest to track the synchrony through cell cycle progression. [133], [159], [169]. While synchrony generally is maintained for the duration of a single cell cycle, this can vary. Hassan *et al* (2001) showed that cells released from flavopiridol treatment only progressed in a semi-synchronous manner, while Simpson and Braly (1970) demonstrated that synchrony of hydroxyurea-treated *L. amazonensis* started to degrade after two cell cycles. The fairly rapid degradation of synchrony may be a result of incomplete cell cycle arrest, or the cells being arrested within a large temporal window. For example, *L. mexicana* cells were shown to spend almost 3 hours of a 7.1 hour cell cycle in G1. Therefore, cells arrested at the beginning of G1 *vs* the end of G1 will complete their cell cycle at very different times.

In addition to flow cytometery, criterion 1 has also been achieved using fluorescence microscopy to quantify the number of organelles. For example, da Silva *et al.* counted the number of kinetoplasts in *L. amazonensis* [159], while in *T. brucei*, the number of basal bodies were counted and the presence of mitotic/post-mitotic markers were assessed [167]. In contrast, criterion 3, as far as I am aware, had not yet been used to assess the quality of cell cycle synchronisation in *Leishmania*, presumably due to the labour-intensity nature of such analysis.

## 1.3 Microfluidic-based methods of cell separation

In recent years, microfluidics has emerged as a highly diverse area of research, relating to the study and application of small volumes of fluid within channels in the micrometer range. In diagnostic assays the use of low volumes of fluids is beneficial; for example, finger pricks can be used instead of invasive venous blood draws, and lower volume enables more difficult-to-collect samples to be used, such as tears and sweat. It also enables less reagents to be used per experiment, for example when using expensive antibodies. Of particular interest is its application in biological systems for the manipulation of cells. The small channels of microfluidic systems enable a heightened level of control and manipulation of individual cells such that cells can be ordered with even spacings in a line, isolated into a single well or trapped with reagents or other cell types within a single capsule. Furthermore, microfluidic based systems are often compact in size, lending to both portability and multiplexing, as well as maintaining cell viability and integrity [170]. One of the growing areas of microfluidics is its application for cell sorting. A plethora of techniques have been developed to take advantage of cells' physical properties, which are typically classified into label-based or label-free, and active or passive methods of sorting. While detailed reviews have been published elsewhere [171]–[173], an overview of these different techniques is given here (Fig. 1.5).

Label-based methods of sorting require the use of chemicals or molecules (such as fluorescent antibodies, dyes or fusion proteins) to identify cells of interest. The gold standard for label-based sorting is fluorescence activated cell sorting (FACS). FACS was developed in 1973, with current instruments being capable of analysing multiple fluorescent markers simultaneously to sort thousands of cells a second to a high level of purity, while typically maintaining cell viability [174]–[176]. It has been used to sort a wide range of cell types; however, its primary application is for the sorting of immune cells and cancer cells, taking advantage of the many biomarkers available for immunophenotyping [177]–[179]. One of the drawbacks of FACS; however, is its long processing times, particularly where high numbers of rare cell types are needed. Magnetic activated cell sorting (MACS) on the other hand similarly relies on the use of antibodies to identify cells of interest, although these antibodies are bound to magnetic beads. Thus, cells bound to these beads *via* the antibodies can be removed from the sample *via* magnetism. While only capable of targeting a single biomarker, it is high-throughput as sorts are performed in bulk rather than as single cells, and requires minimal equipment [176]. While FACS and MACS are both powerful tools for cell sorting, a fundamental limitation of these methods is the requirement for chemical or antibody labelling. The addition of dyes can affect normal cellular function, while the use of antibodies requires the presence of preidentified biomarkers to identify cells of interest, as well as increasing experimental costs.

Label-free approaches have therefore been developed to circumnavigate these caveats. These techniques rely purely on physical differences (such as differences in cell size, shape, deformability, density, refractive index, or polarizability), to identify cells of interest [172], [173], [180]. As a cell's properties are inherently linked to its function, environment and state, changes in one instance affecting the other [181]. This leads to cells with unique characteristics which can be exploited through active or passive methods of sorting.

Active sorting techniques apply an external force to physically move cell of interest towards a collection outlet. Such forces are generated by acoustic waves (e.g. acoustophoresis), an electrical field (e.g. dielectrophoresis; DEP), or light (optical techniques) [172], [182]–[187]. The strength of these forces can be finely tuned by the user and will act differentially based on particle size as well as particle density, polarizability, and refractive index respectively. While having precise control, active sorting often requires more complex set-ups with detectors, transducers, amplifiers and actuators. Furthermore, throughputs are often low due to the time needed for the forces to act on the cells, imposing limitations on their applications. In 2018, a new method of active cell sorting was described, using brightfield images (BF) of cells along with machine learning to automatically select cells of interest for acoustic based sorting [188]. Since then, various techniques using images, reconstructed images from electrical signals, and Raman spectroscopy have been described [189]–[192]. While this technique offers a high level of specificity and control, the required equipment is very expensive and flow rates are still very low in the range of μl.hour$^{-1}$.

In contrast passive methods rely on naturally occurring forces or processes for separation, such as hydrodynamic forces, cell motility and cell adhesion. While cell motility and adhesion are cell type specific (i.e. healthy sperm swim against the flow; neutrophils, but not red blood cells (RBCs), will adhere to a surface), the application of hydrodynamic forces has been used for a range of cell types as, most commonly, a size-based methods of separation [173], [193]. Deterministic lateral displacement (DLD) uses pillars to obstruct cells in flow, inducing migration across a channel in a size dependent manner. While DLD is high throughput, the inherent nature of using obstacles increases the risk of clogging the device, reducing its accessibility [194]. Expansion-contraction channels use repeating sections of narrow then wide channel dimensions to modify the fluid flow. This has been employed to trap large particles within the wide regions, or to focus larger cells towards the centre of the channel and smaller cells to the outer wall for particle separation [195]. The final label-free technique mentioned here is inertial microfluidics. Inertial microfluidics relies on the inertial forces generated in a fluid in a confined flow to induce separation. Depending on the geometry of the channel and the fluid flow rate, these forces can be manipulated to act differentially on particles of different sizes, shapes and deformabilities, resulting particles with different morphologies focusing to different positions along the channel’s width, for collection at channel outlets [196]. These devices typically work in the range of ml.min$^{-1}$ and are thus relatively high throughput. Interestingly, due to the highly customisable nature of these devices and their small footprint, they are compatible with multiplexing and parallelisation with flow rates up to 500 ml.min$^{-1}$ while maintaining purities of > 90% for various cell lines [170], [197]. In addition, inertial microfluidic focusing has been shown to have minimal effects on cell viability and gene expression [198].

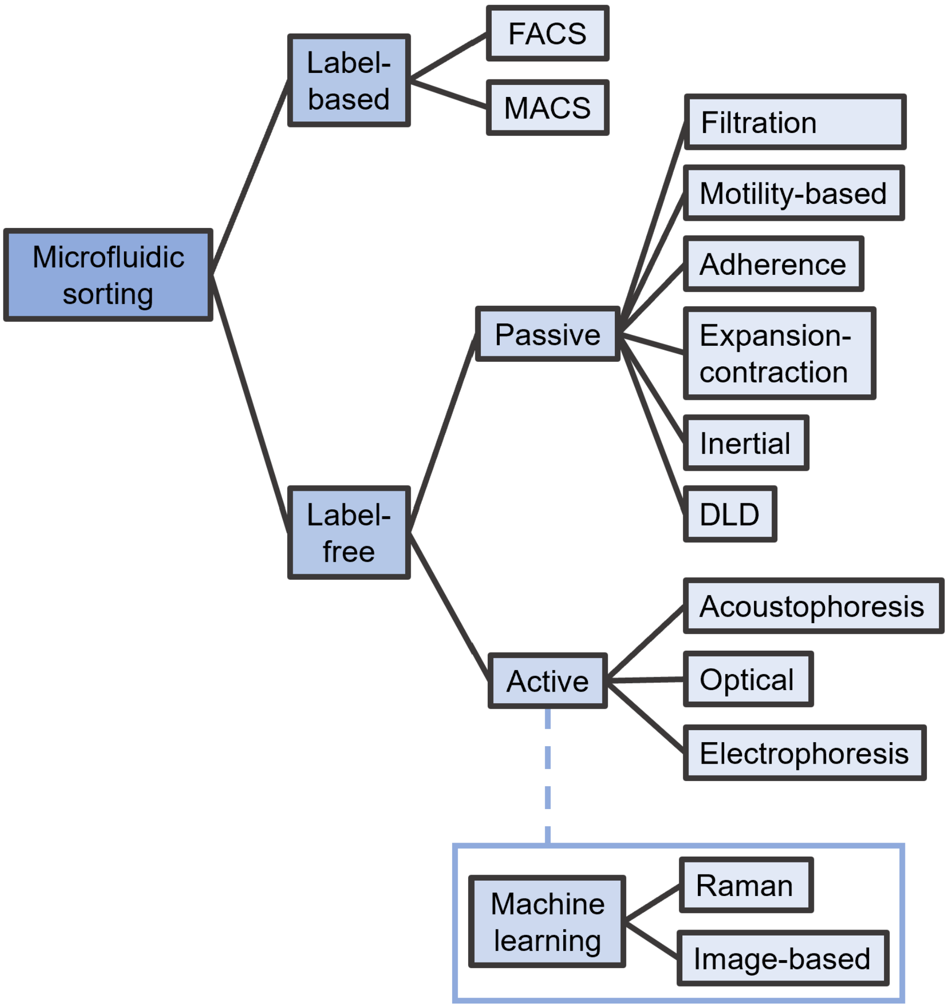

**Figure 1.5: Overview of microfluidic-based sorting techniques**
A plethora of microfluidic sorting techniques exist which can be divided into label-based (requiring the use of antibodies of dyes) or label-free (relying on inherent morphological and mechanical properties). These can be further classified into active or passive techniques which use the application of external forces vs inertial forces respectively to induce separation. An up-and-coming technique of label-free sorting employs the use of machine learning to identify differences in cell types based on predefined cell classifications. Such methods are not yet widely available.

### Requirements for the microfluidic-based separation of *L. mexicana's* cell cycle

In order to develop a morphology-based method of cell cycle synchronisation for *L. mexicana*, the following limitations were considered. Firstly, a label-based method of cell cycle separation was unsuitable as there are currently no molecular biomarkers to identify the different cell cycle stages of *L. mexicana*. Additionally, as has been discussed, FACS based sorting using a DNA dye is insufficient to isolate different cell cycle stages and is achieved using fixed cells stained with PI. Thus, a label-free method was required. Secondly, the sorting of live cells is advantageous as it provides more opportunities for cell cycle analysis post-synchronisation, such as: tracking fluorescence localisation throughout cell cycle progression; analysing the effects of potential cell cycle drugs; and analysing cell cycle aberrations due to knockouts. Furthermore, the use of live cells better preserves cell morphology which is important for identifying a cell's stage in the cell cycle [125]. The sorting of live cells must subsequently be high-throughput in order to reduce processing times. As live cells are still capable of progressing through the cell cycle, rapid sorting is required to maintain the purity of the sorted samples. In order use live cells for such downstream analysis, the sorted cells must remain uncontaminated. Additionally, microfluidic sorting often requires the uses of pressurised pumps for injecting the sample into the chip, increasing the risk of leaks and sample aerosolization. This is particularly true for high-throughput methods of separation, with increased flow rates, thus, subsequently increasing the risk of infection from this human infected pathogen. Therefore, sorting using a small and portable system was sought which would fit within a standard microbiological safety cabinet (MSC), such that active methods of sorting were avoided. Inertial microfluidics on the other hand has been used to sort a variety of difference cell types, achieving purities of over 90%. With those considerations in mind, inertial microfluidics was chosen to be developed as a method of cell cycle separation of *L. mexicana*.

## Inertial microfluidics

Initial focusing was first observed by Segré and Silberberg in the 1960s in a $\sim$ 1 cm circular tube; in this experiment, it was shown that $\sim$ 1 mm particles distributed evenly within the tube's cross-section at low fluid velocity while higher velocities led to particles aligning in an annular configuration [199]. It wasn't until 2007 that this observation was translated to a microfluidic channel. In this work, Di Carlo demonstrated that in a serpentine channel with a square cross section, particles, independent of their shape and density, focused precisely and reproducibly towards the centre of each of the four walls [200]. Using this theory, many channel designs have been developed to study its effect on particle behaviour. From these works, it is now generally accepted that particle focusing within a straight channel occurs as a result of the interactions between: a particle suspended in flow; the size of the channel; and the properties of the fluid [201]. By varying one or multiple of these parameters, particles can be manipulated in a reproducible way to align particles at particular positions within a channel. While particles focus in an annular formation within a round tube, quadrilateral channels are more common due to their easy of fabrication. In a square channel (aspect ratio (AR) = channel height

($h$)/channel width ($w$) = 1) there are four equilibrium positions; one at the centre face of each wall [202]. By changing the aspect ratio so that $h/w \neq 1$, the two focusing positions towards the shorter walls disappear, leaving the two focusing positions at the centreline of the longest channel wall (Fig. 1.6) [200], [203], [204]. While this is the most typical behaviour, alternate focusing patterns have been observed, with up to eight focusing positions being observed in both square and rectangular channels, and Bhagat *et al.* documenting particles spread across the width of the longest walls in rectangular channels [205], [206].

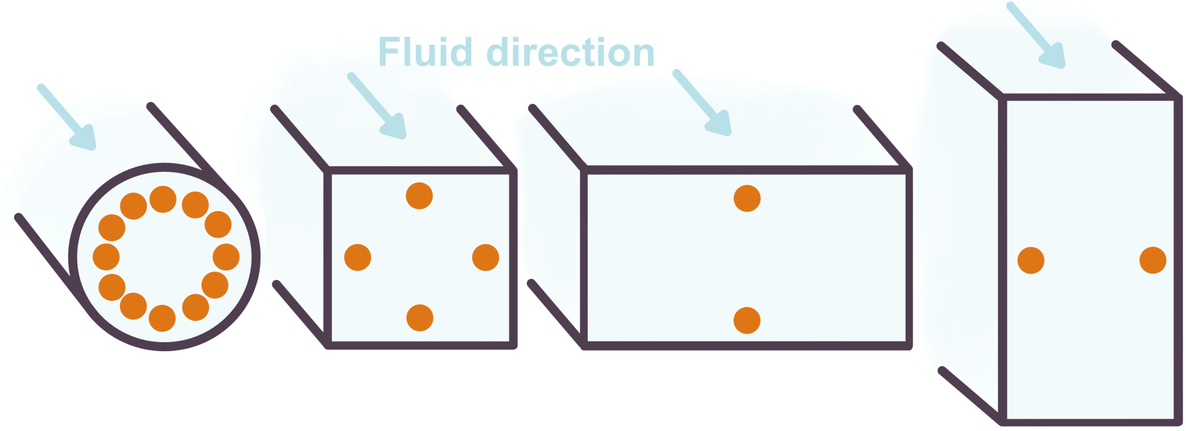

**Figure 1.6: Inertial focusing in different channel geometries**
Typical focusing positions of beads (orange) in straight channels with a circular (left), square (middle left), low aspect ratio (middle right) and high aspect ratio (right) cross section. The fluid direction is demonstrated with the light blue arrows.

These focusing behaviours arise due to the presence of hydrodynamic forces which act on particles suspended in the fluid. In order for focusing to occur, two conditions must be met. Firstly, there must be sufficient fluid inertia within the laminar flow regime [207]. This occurs when $\sim$ 1 < Reynolds number (Re) < $\sim$ 1000. The Reynolds number is a dimensionless number that describes the relationship between the fluid's inertial and viscosity,

$$Re \,=\, \frac{Inertial\, forces}{Viscous\, forces} \,=\, \frac{\rho U_m D_h}{\mu} \tag{1.1}$$

where $\rho$ = fluid density, $U_m$ = average fluid velocity, $\mu$ is the fluid viscosity and $D_h$ = hydraulic diameter

$$D_h \,=\, \frac{2hw}{(h\,+\,w)} \tag{1.2}$$

which, in a rectangular channel, relates the channel height ($h$) to its width ($w$). Where fluid inertial is too low (Stokes flow, or creeping flow) the forces acting on a particle are negligible and thus particles will follow the direction of the fluid [208]. Where the Reynolds number is too high, the turbulent regime is dominant and particle behaviour is unstable. Secondly, the particle must be of sufficient size within the channel: too small and the particle will remain distributed throughout the width of the channel instead of focusing to a single position. As a general rule, focusing will occur where $\lambda$ > 0.07, where $\lambda$ is the particle confinement ratio, calculated as:

$$\lambda \,=\, a/D_h \tag{1.3}$$

where $a$ = particle diameter. On fulfilment of these conditions, particle migration to a focusing position occurs in two stages. First, the shear-induced lift force and the wall-induced lift force act in opposition to guide particles to equilibrium positions towards the wall [209]. The shear-induced lift force ($F_S$ )arises due to the parabolic flow profile of the fluid and is directed towards the wall while the wall-induced lift force ($F_W$) repels particles away from the wall. The subsequent net lift force ($F_L$) is given as:

$$F_L \,=\, f_c \frac{\rho {U_m}^2 a^4}{D_h^2} \tag{1.4}$$

where $f_c$ = lift force coefficient [200], [205], [210]. The second stage of particle migration is caused by the rotation-induced lift force ($F_\Omega$) which acts more slowly to move particles towards the centreline of the channel (Fig. 1.7) [211]. While much work has been carried out in straight channels to understand the effect of fluid dynamics on particle focusing, their applications are predominantly limited to the focusing of particles in a line for particle detection, or for filtration to remove particles from the suspending liquid [212], [213]. In a straight channel without any modifications (i.e. such as expanding regions), it is difficult to achieve separation of differently sizes particles due to the high overlap in particle focusing position [201], [212]. However, as the channel dimensions, particle size, and fluid velocity are fundamentally linked to the strength of the forces within the channel, modifying one or all of these parameters has a marked effect on the focusing position of particles [200], [201], [214]–[220]. As such, a wide variety of experimental parameters have been assessed for their ability to improve particle separation.

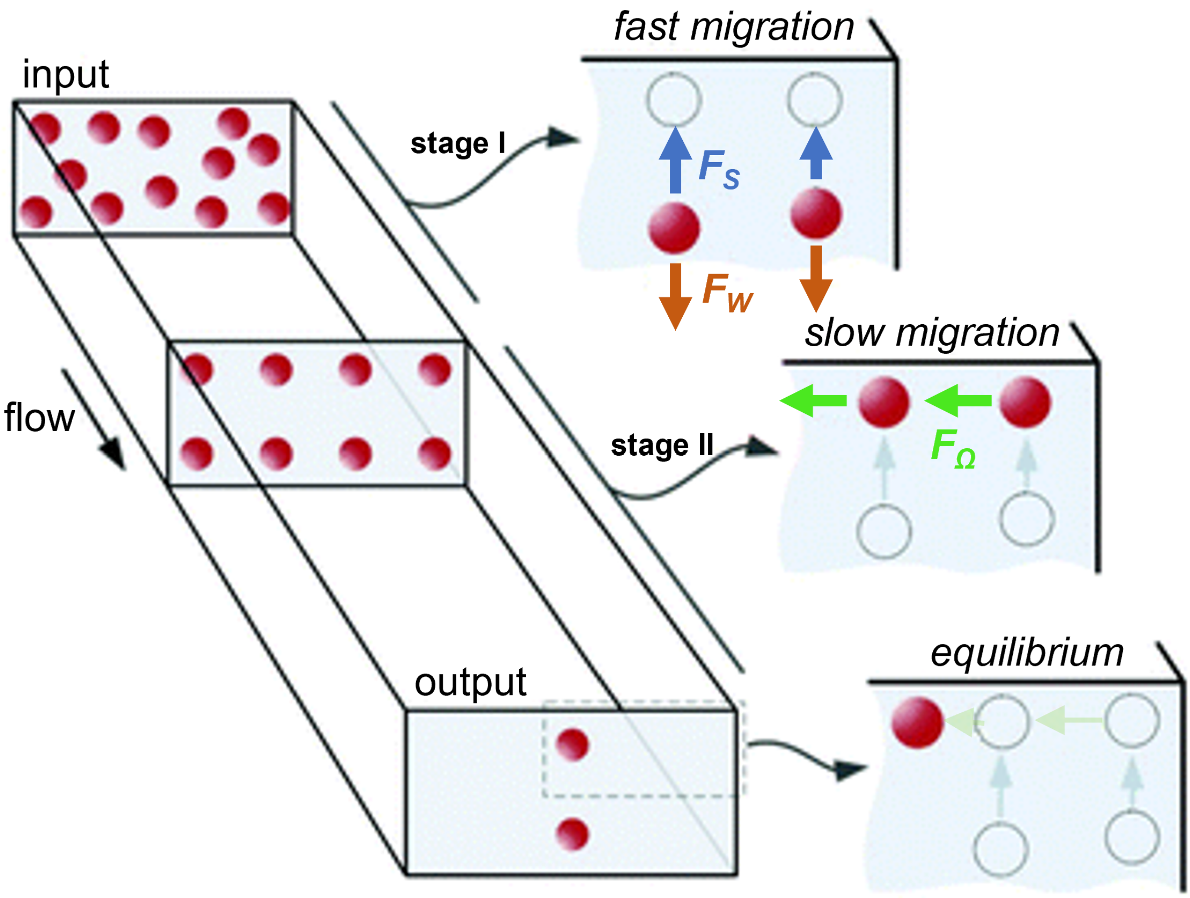

**Figure 1.7: Stages of inertial focusing in a straight channel**
Particle focusing within a low aspect ratio microfluidic channel occurs in two stages: in stage I, the shear-gradient ($F_S$) lift force and the wall-induced lift ($F_W$) force act on dispersed particles to rapidly migrate particles to their vertical equilibrium position within the flow. In stage II, the rotation-induced lift force ($F_\Omega$) results in a slow migration towards the centreline of the channel where particles remain in an stable equilibrium position. Reproduced from Zhou, J. and I. Papautsky "Fundamentals of inertial focusing in microchannels", Lab Chip, 2013. 13(6): p. 1121-32.[91], with permission from the Royal Society of Chemistry (license: 1492089-1).

One of the most well utilised design features for particle separation is the introduction of channel curvature, such as using serpentine and spiral channels [221]. This results in an asymmetric fluid flow due to centrifugal forces; the fluid is directed along the middle of the channel towards the outer wall, where it bifurcates to recirculate along the top and bottom of the channel, forming Dean vortices (Fig.1.8). These vortices result in particles experiencing a drag force ($F_D$),

$$F_D = 3\pi\mu U_{Dean}a \tag{1.5}$$

where $U_{Dean}$ is the average Dean velocity ($U_{Dean}$ = $1.8 \times 10^{-4}$ $\mathrm{De}^{1.63}$) and the Dean number

(De) is another nondimensional number which describes the force of the fluid recirculation [222]. This is given as:

$$De = Re\sqrt{\frac{D_h}{2R}} \tag{1.6}$$

where $R$ = radius of the curvature [221]. The $F_D$ generated by the secondary flow has three effects. Firstly, it reduces the focusing position of the same sized particles to a single lateral position while also increasing the speed of which particles reach their focusing position [200], [201], [223]. Finally, the $F_D$ acts concurrently with the $F_L$ to influence a particle's position within the channel. The strength of $F_L$ and $F_D$ are both dependent on particle size; however, as they scale differentially ($F_L \propto a^4$ and $F_D \propto a$) the equilibrium of these forces is different for particles of varying sizes. In a spiral channel, small particles with a $\lambda$ < 0.07 tend to follow the fluid direction and recirculate within the Dean vortices. For particles above this threshold, typically $F_L$ > $F_D$ resulting in focusing towards the inner wall [201]. Larger particles experience a greater $F_L$ and thus are found closer to the inner wall than smaller particles [201], [203], [224]. While $F_L$ scales faster with particle size, $F_D$ on the other hand scales faster with fluid velocity [223]. Therefore, by increasing the flow rate $F_D$ is capable of becoming the dominant force. In this scenario, smaller particles experience a higher $F_D$ and are the first particles to move away from the inner wall. Thus, through the modulation of channel geometry and flow rate, the focusing position of different sized particles can be finely tuned to achieve particle separation.

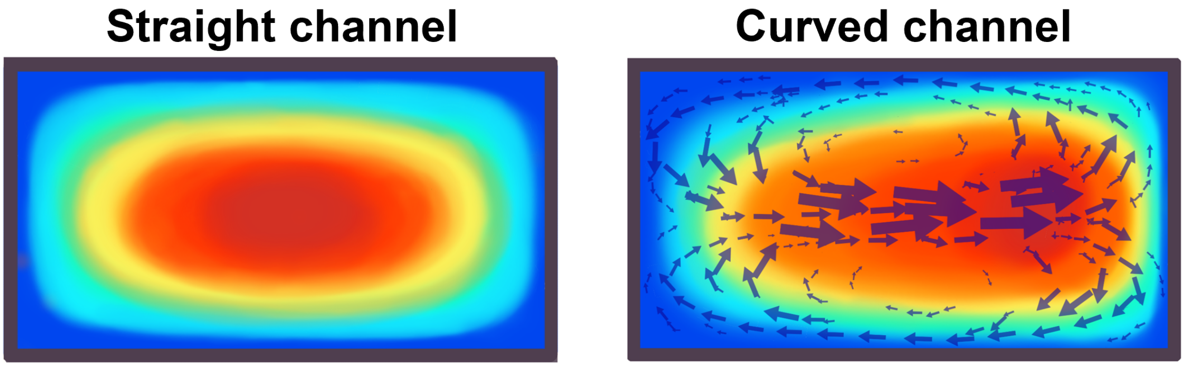

**Figure 1.8: Flow profile of a straight channel *vs* a curved channel**
A graphical representation of the velocity profile within a straight channel (left) vs that of a curved channel (right). The colours indicate the velocity within a channel, with red showing areas within the channel with the highest velocity, while dark blue areas demonstrate the areas with the lowest velocity. The purple arrows demonstrate the recirculation of fluid (Dean vortices) within the channel, with the size or the arrow representative of the strength of the $F_D$.

The nature of inertial microfluidics means that it is in theory, capable of sorting any cells with a sufficient difference in size. It has therefore been applied to many cell types and applications, including both parasite and cell cycle research. The most prominent application for inertial microfluidics in parasite research is for the detection and isolation of malaria infected RBCs to improve diagnosis *via* PCR. To this end, straight channels and expansion contraction arrays have been applied to remove large nucleated white blood cells or to take advantage of the increased deformability of RBCs [225], [226]. Straight channels and spiral channels have been used for the detection of *Giardia spp.*, and *Cryptosporidium parvum* from food and water [227]–[229]. Spiral channels have also been employed to diagnose *Giardia* infection from faecal samples [230].

Its application for cell cycle synchronisation has also been documented. In 2011, Lee *et al.* used a spiral channel for the synchronisation of four different mammalian cell types; the cancer cell lines HeLa cells and KKU-100, human mesenchymal stem cells and Chinese hamster ovarian cells [231]. In this work, the efficiency of synchronisation was assessed using PI-based DNA quantification. Each sorted population was analysed using flow cytometry to identify the proportion of cells in each of the cell cycle stages. In addition, the average diameter of the cells in each population was calculated from microscopy-based measurements to give an indication of cell size. The greatest enrichment was seen for hMSCs in G2/M from 27% to 50.6%, a near twofold increase. The highest purity was achieved for KKU-100 cells at 96.4%, a 1.3X increase from the control at 74.2%. In a similar experiment, Warkiani *et al.* used a spiral channel with a trapezoidal cross section, also for the cell cycle synchronisation of Chinese hamster ovarian cells [170]. Here, the authors used flow cytometry to quantify cell cycle enrichment, demonstrating that G2/M phase cells were enriched threefold and G1 cells increased from 60% to 80% [170]. Masaeli on the other hand used a straight channel to separate the different budding stages of yeast based on cell shape. Microscopy analysis was used to show that longer budding yeast were enriched from a purity of 6.6% to 31% while $\geq$ 90% of singlet cells were collected between two outlets [232].

## 1.4 Thesis aims and overview

As previously discussed, the tools currently available for synchronising *Leishmania's* cell cycle are inadequate, primarily relying on the addition of chemicals which disrupts cells' physiological state. This thesis therefore aims to develop new tools for the analysis of *L.*

*mexicana's* cell cycle through the following objectives:

1. Explore the use of imaging flow cytometry (IFC) as a method of high-throughput cell cycle analysis for *L. mexicana* to improve the understanding of how the parasites morphology relates to its stage in the cell cycle,
2. Use objective 1 to inform how the morphology of non-spherical cells affects inertial microfluidic focusing in order to design such a system for synchronising *L. mexicana's* cell cycle,
3. Develop portable sensing techniques for the high-speed detection of inert particles and live parasites within inertial microfluidic devices.

As such Chapter 2 provides details of the experimental procedures which were both developed and carried out throughout the course of this project. In pursuit of objective 1, Chapter 3 outlines the first application of imaging flow cytometry for cell cycle analysis of *L. mexicana*; an imaging technique for the high-throughput analysis of particles in both brightfield and fluorescence mode. Using this technology, a method was developed to achieve quantitative DNA staining in live cells using the DNA dye Vybrant™ DyeCycle™ Orange.

This protocol was used in Chapter 4 to analyse the relationship between the morphology of *L. mexicana* cells and their stage in the cell cycle. It was demonstrated that of the cell cycle stages, M/C phase cells had the most distinct morphology which could be used as a marker of their cell cycle stage. This enabled a high-throughput and automated method of cell cycle classification with a higher resolution than either microscopy or flow cytometry analysis alone. This analysis was taken a step further and by identifying the spindle using a fluorescent fusion protein, the timings of *L. mexicana's* cell cycle were defined, including the elusive G2 stage and a very early stage in the cell cycle which accounted for only 12 minutes of a 12.4 hour cell cycle.

In Chapter 5, inertial microfluidic spiral channels were explored for their potential as a method of cell cycle synchronisation. It was demonstrated that the elongated shape of *L. mexicana* caused an unusual focusing behaviour; all the cells, regardless of their shape, focused to the outer wall of the channel at intermediate Reynolds numbers (Re = 116.7). The flagellum was shown to have no effect on the equilibrium position of these cells while the particle confinement ratio was deemed to be an important factor for whether cells first focus to the inner wall, prior to migration to the outer wall at higher flow rates. Enrichment of morphologies associated with M/C were seen; however, the purity of the sample was lower than desired.

During this work, it was found that the techniques for analysing particle focusing were inadequate. While high-speed cameras provide high-resolution information on particle focusing, the bulky equipment associated with its setup prevented the analysis of live cells. In addition, the analysis of live cells post-sort was time consuming and introduced caveats into the process. Therefore, in Chapter 6 event-based cameras were tested as a low cost, low latency, portable method of high-speed particle tracking. Proof of principal experiments were carried out using a standard fluorescence microscope. The event-based camera demonstrated particle focusing positions comparable to that of a standard high-speed camera up to particle velocities of $\sim$ 4.9 $m.s^{-1}$ (Re = 250.0) for fluorescent particles and particles in brightfield up to 0.15 $m.s^{-1}$. Unfortunately, its application for the high-speed particle tracking of live *L. mexicana* was not achieved due to the low contrast of these cells.

Finally, Chapter 7 gives a general overview of the work carried out, outlining the main conclusions, caveats and proposals for future research.

# Chapter 2

# Materials and methods

## 2.1 *Leishmania* culturing

### 2.1.1 Culture

***General handling***

*Leishmania mexicana* (strain MNYC/BZ/62/M379) promastigotes containing the Cas9 T7 (C9T7) cassette were cultured according to [233]. Cultures were grown in M199 (Gibco) supplemented with 10% foetal bovine serum (FBS); 26.2 mM sodium bicarbonate; 0.005% haemin; and 40 mM 4-(2-hydroxyethyl)piperazine-1-ethanesulfonic acid (HEPES) pH 7.4. 32 $\mu g.ml^{-1}$ hygromycin B (Roche), 50 $\mu g.ml^{-1}$ nourseothricin sulphate (Jena Bioscience) and 10 $\mu g.ml^{-1}$ blasticidin S hydrochloride (InvivoGen) were added to cultures where needed (see Table 2.1 for details). Cultures of promastigotes were incubated at 27°C and experiments were performed on cells in their log phase of growth (cell densities between $1 \times 10^6$ $cells.ml^{-1}$ and $7 \times 10^6$ $cells.ml^{-1}$). Growth curves were performed on cell lines by seeding cells at $5 \times 10^5$ $cells.ml^{-1}$ and calculating the cell density at 24-hour intervals. Cell densities were calculated using a haemocytometer; 10 µl of cell culture was resuspended in between 10 – 200 µl of PBS/5% glycerol depending on visual inspection of the density of the culture. At least 100 cells were counted across the four corner quadrants of the haemocytometer and the cell density was calculated using Equation 2.1. The doubling time of a cell line was calculated using Equation 2.2,

$$Cell\ density = \frac{Number\ of\ cells\ counted}{Number\ of\ quadrants\ analysed} \times dilution\ factor \times 1 \times 10^4 \tag{2.1}$$

$$Doubling\ time\ =\ \frac{Duration\ \cdot\ ln(2)}{ln(\frac{Final\ concentration}{Initial\ concentration})} \tag{2.2}$$

**Table 2.1: Details of cell lines used**

| Cell line name | Genotype | Antibiotic resistance | Comments |
|---|---|---|---|
| *L. mexicana* parental | MNYC/BZ/62/M379 pTB007 | Hygromycin B<br>Nourseothricin sulphate | This cell line (Beneke et al, 2017) was gifted by the Gluenz lab. All other cell lines used here were generated from this cell line. |
| THT2A:mNG | MNYC/BZ/62/M379 pTB007<br>THT2A:mNG | Hygromycin B<br>Nourseothricin sulphate<br>Blasticidin S hydrochloride | Generated according to Beneke & Gluenz, 2019 using the plasmid pPLOTv1 blast-mNeonGreen-blast. |
| KINF:mNG | MNYC/BZ/62/M379 pTB007<br>KINF:mNG | Hygromycin B<br>Nourseothricin sulphate<br>Blasticidin S hydrochloride | Generated by Sulochana Omwenga according to Beneke & Gluenz, 2019, using the plasmid pPLOTv1 blast-mNeonGreen-blast. |
| mNG:ACS | MNYC/BZ/62/M379 pTB007<br>mNG:ASC | Hygromycin B<br>Nourseothricin sulphate<br>Blasticidin S hydrochloride | Generated according to Beneke & Gluenz, 2019 using the plasmid pPLOTv1 blast-mNeonGreen-blast. |
| MiniTurbo:ACS | MNYC/BZ/62/M379 pTB007<br>MiniTurbo:ASC | Hygromycin B<br>Nourseothricin sulphate<br>Blasticidin S hydrochloride | Generated according to Beneke & Gluenz, 2019 using the plasmid pPLOT-miniTurboID-blast-blast |

#### ***Generation and revival of stabilates***

Stabilates of each cell line used were generated and kept in liquid nitrogen for long term storage. Stabilates were generated by resuspending mid-log cell cultures in a solution of 70% FBS/30% glycerol to a 1:1 ratio. 1 ml of the resulting mixture was transferred into cryovial tubes, frozen for at least 12 hours at -80°C before being transferred to liquid nitrogen. To revive stabilates, cryovials were removed from liquid nitrogen and thawed in a gloved hand. Once thawed, the content of the vial was transferred to 9 ml M199 prepared as previously outlined, containing the appropriate antibiotics.

### 2.1.2 Generation of different cell populations

Promastigote form *L. mexicana* were differentiated into the amastigote form by resuspending late-log phase cells ($\sim$ 1 x $10^7$ cells.$ml^{-1}$) in Schneider's Drosophila insect medium (Invitrogen) supplemented with 20% FBS and adjusted to pH 5.5 [234]. Cultures were incubated at 32°C for at least 72 hours prior to the collection of amastigote-like cells. Differentiation was confirmed *via* microscopy-based inspection of morphological changes.

#### ***Treatment with flavopiridol and hydroxyurea***

Cell cycle synchronisation was carried out by Sulochana Omwenga through the addition of either 5 µM flavopiridol (Selleck Chemicals) or 5 mM hydroxyurea (Sigma) to mid-log phase cultures. The resulting cultures were incubated at 27°C for 10 hours prior to collection.

### *Deflagellation of* L. mexicana *cells*

Deflagellation of PFA-fixed or live cells was carried out by resuspending the cells in 5 ml of a solution containing 10 mM 1,4-piperazinediethanesulfonic acid (PIPES), 1 mM $CaCl_2$, 1 mM $MgCl_2$ and 0.32 M sucrose adjusted to pH 7.2, as outlined in [235]. Finally, 0.375 ml 0.075 M $CaCl_2$ was added before the sample was drawn into and expelled out of a 10 ml syringe 200 times. The syringe was fitted with a gel loading pipette, and the sample was kept on ice where possible. The resulting sample contained a mixture of isolated cell bodies, sheared flagella, intact cells (where shearing of the flagella did not occur), and cell fragments from ruptured cells. Either the mixture was used for the generation of flagellated beads (Section 2.3.1) or the cell bodies were fractioned out from the mixture by sucrose gradient centrifugation [235]. 3 ml of each of the sucrose solutions outlined in Table 2.2 were layered in a 15 ml falcon tube, with the 63% solution being the bottom fraction, the 53% solution being the middle fraction and the 33% solution being on top. The sheared cell sample was placed on top and the falcon tube was centrifuged at 800 *g* for 15 minutes at 4°C. The upper layers of the gradient were disposed of, while 10 ml 10 mM PIPES was added to the bottom 63% sucrose layer and centrifuged at 800 *g* for 10 minutes at 4°C. The sample was washed 1X in 1 ml PBS before being stored in 1 ml PBS at 4°C until needed.

**Table 2.2: Sucrose solutions**

| Layer | Sucrose solution (%) | 2 M sucrose (ml) | $ddH_2O$ (µl) | 0.166 M PIPES pH 7.2 (µl) |
|---|---|---|---|---|
| Top | 33 | 1.446 | 1374 | 180 |
| Middle | 53 | 2.323 | 497 | 180 |
| Bottom | 63 | 2.761 | 59 | 180 |

Three sucrose concentrations were prepared for sucrose gradient centrifugation using the defined volumes of 2 M sucrose, $ddH_2O$ and 1.66 M PIPES adjusted to pH7.2. Each concentration was layered in a falcon tube in the specified order.

***Generation of transfected cell lines***

Various cell lines (outlined in Table 2.1) were generated through clustered regularly interspaced short palindromic repeats (CRISPR)/Cas9 gene editing, as described in [236]. Firstly, PCR was carried out to amplify the donor DNA and single guide RNA (sgRNA) templates prior to transfection. This consisted of preparing dilutions of the appropopriate primers (Table 2.3; a 4 µM mixture was prepared for the sgRNA primer, and a mixture containing 5 µM each of the forward and reverse primers was prepared for donor DNA amplification. 10 µl and 8 µl of the respective primer dilutions were added to PCR tubes and frozen at -80°C for 30 minutes. After this time, 10 µl or 32 µl of the appropriate PCR master mix (see Table 2.4) was added to the frozen primer dilutions for the sgRNA template and donor DNA amplifications, respectively. The resulting mixtures were added to a pre-heated thermocycler and amplified using the settings outlined in Table 2.5. Once completed, amplification of the PCR products was confirmed by gel electrophoresis and the PCR products were stored at -20°C until needed. For gel electrophoresis, 1% (w/v) and 2% (w/v) gels were prepared by adding the required amount of agarose to 50 ml 0.5X of Tris-acetate-EDTA (TAE) buffer (0.5 mM EDTA, 20 mM Tris, 10 mM acetic acid). The mixture was heated in a microwave until vigorously bubbling and left to cool until warm to touch. 2.5 µl of SYBR® Safe (Invitrogen) was added and the solution was poured into a mould with a gel comb and left to set for 30 minutes. The 1% gel was used for analysing donor DNA PCR products, while the 2% gel being used for sgRNA PCR products. Gel tanks were filled with 0.5X TAE, to which the gels were added. 1 µl of each PCR product was added to 19 µl of loading dye (New England Biolabs), 10 µl of which was added a single of the gel. Additionally, a well was loaded with 10 µl of 1 Kb Plus DNA ladder (Invitrogen) and the 1% and 2% gels were run at 120 V for 45 minutes and 20 minutes, respectively.

**Table 2.3: Primer details for transfections**

| Name | Primer | Gene ID | Primer sequence (5`-3`) |
|---|---|---|---|
| PR495 | G00 sgRNA | - | AAAAGCACCGACTCGGTGCCACTTTTTCAAGTTGATAACGGACTAGCCTTATTTTAACTTGCTATTTCTAGCTCTAAAAC |
| PR567 | THT2A forward | LmxM.36.6280 | GCCGACGCTGTTTCTGCTGACCGCTATCCTGTATAATGCAGACCTGCTGC |
| PR570 | THT2A reverse | | CTGCACGTTCGCCTCCAACTTGTCGCTCATACTACCCGATCCTGATCCAG |
| PR569 | THT2A sgRNA | | GAAATTAATACGACTCACTATAGGGGGTTGGTTGCACGAAAGAAGTTTTAGAGCTAGAAATAGC |
| PR584 | KINF forward | LmxM.25.1950 | TCGTTCTCTCCGTCTCTCGGGGTGGCTGCCGTATAATGCAGACCTGCTGC |
| PR585 | KINF reverse | | TACCGCCACCTTGATGCTAGACGACGACATACTACCCGATCCTGATCCAG |
| PR586 | KINF sgRNA | | AAATTAATACGACTCACTATAGGCTCCTTGCACCAGCAAAGACGTTTTAGAGCTAGAAATAGC |
| PR635 | ACS forward | LmxM.25.0420 | GTGGCCAACAACCACCAGTATCACGGGCGCGGTTCTGGTAGTGGTTCCGG |
| PR636 | ACS reverse | | CGCACTATCAACCGCCTCGCTGCAACACCACCAATTTGAGAGACCTGTGC |
| PR637 | ACS sgRNA | | GAAATTAATACGACTCACTATAGGGCGCAGCGTTCGATGCTCTTGTTTTAGAGCTAGAAATAGC |

Description of the primers used for gene editing, designed using LeishGEdit [236].

**Table 2.4: Details of PCR master mix solutions**

| sgRNA master mix | | donor DNA master mix | |
|---|---|---|---|
| **Reagent** | **Volume (µl)** | **Reagent** | **Volume (µl)** |
| G00 primer (100 µM) | 0.4 | Approporiate plasmid template (30 ng/µl) | 0.5 |
| dNTP (10 mM) | 0.4 | dNTP (10 mM) | 0.8 |
| 10X Reaction buffer with 15 mM $MgCl_2$ | 2 | 10X Reaction buffer with 15 mM $MgCl_2$ | 4 |
| $ddH_20$ | 7 | $ddH_20$ | 22.1 |
| HiFi | 0.2 | HiFi | 0.4 |
| | | DMSO (100% v/v) | 1.2 |
| | | $MgCl_2$ solution (25 mM) | 3 |

The volumes given are for a single PCR reaction for the amplification of sgRNA and donor DNA. Volumes were scaled up as necessary. The reagents used were from the Expand™ High Fidelity PCR System (Roche). HiFi = high fidelity DNA polymerase, dNTP = deoxyribonucleotide triphosphate mixes, DMSO = dimethylsulfoxide.

**Table 2.5: Details of PCR reactions**

| PRC amplification of sgRNA template | | | | PRC amplification of donor DNA | | | |
|---|---|---|---|---|---|---|---|
| **Step** | **Temperature (°C)** | **Time** | **Comment** | **Step** | **Temperature (°C)** | **Time** | **Comment** |
| 1 | 98 | 30 s | Repeat steps 2-4 35X | 1 | 94 | 5 min | Repeat steps 2-4 40X |
| 2 | 98 | 10 s | | 2 | 94 | 30 s | |
| 3 | 60 | 30 s | | 3 | 65 | 30 s | |
| 4 | 72 | 15 s | | 4 | 72 | 2 min 15 s | |
| 5 | 72 | 10 min | | 5 | 72 | 7 min | |
| 6 | 4 | until removal | | 6 | 4 | until removal | |

The temperatures, timings and number of cycles through steps 2-4 are given for the amplification of sgRNA and donor DNA.

Transfections were carried out by pooling the amplified sgRNA and donor DNA PCR products, and the resulting mixtures were sterilised by heating at 95°C for 5 minutes. A transfection buffer was prepared by firstly making a solution of 200 mM $Na_2HPO_4$, 70 mM $NaH_2PO_4$, 15 mM KCL and 150 mM HEPES, which was adjusted to pH 7.4. 4.15 ml of this was then added to 1.25 ml 1.5 mM $CaCl_2$ and 4.6 ml $ddH_2O$ which was sterile filtered. This solution was the transfection buffer. 1 x $10^7$ cells per transfection were collected *via* centrifugation at 800 *g* for 10 minutes and washed 1X in 1 ml of transfection buffer. The cells were centrifuged again as above and resuspended in 200 µl of transfection buffer per transfection. In an electroporation cuvette, the sterilised PCR products were added along with the 200 µl of cells and electroporated using an Amaxa Nucleofector 2b using the X-001 program. The contents of the cuvette was transferred to 5 ml prewarmed M199, aliquoted into five 24 well plates and incubated at 27°C for between 8 and 12 hours. After this time, 1 ml M199 containing double concentrations of the appropriate drugs was added to each of the wells. Clonal populations were generated by diluting the cultures by 1:10, 1:50 and 1:100, and each dilution was added to at least 48 wells of a 96 well plate and incubated at 27°C. These plates were checked periodically for growth, and wells containing cells were cultured. Cell lines containing fluorescent fusion proteins were checked for fluorescence *via* microscopy or IFC (as outlined in Section 2.2.4).

## 2.2 Morphological and fluorescence analysis

### 2.2.1 Fixation

Where needed, fixation was carried out on cells prior to analysis by IFC, flow cytometry and inertial microfluidic sorting, either using paraformaldehyde (PFA) or methanol. Cell cultures were centrifuged at 1,000 *g* for 5 minutes and the supernatant was removed. For PFA fixation, cells were resuspended in phosphate buffered saline (PBS)/4% PFA to a density of $\sim$ 2 x $10^7$ cells.ml$^{-1}$. Cell suspensions were incubated for 15 minutes at 4°C unless otherwise stated, after which they were washed 3X times with PBS and resuspended in PBS until analysis. For methanol fixation, two methods were used. If cells were to be stained with propidium iodide (PI; Invitrogen), then the cells were washed 1X in PBS/5 mM ethylenediaminetetraacetic acid (EDTA), centrifuged at 1,000 *g* for 5 minutes and resuspended in 300 µl PBS/5 mM EDTA. 700 µl of ice cold 100% methanol was added to the suspension prior to incubation in the dark at 4°C for at least 12 hours. Samples were centrifuged at 1000 *g* for 10 minutes, washed once in PBS/5 mM EDTA and resuspended in 500 µl of PBS/5mM EDTA. If PI staining was not carried out, then cells were washed 1X in PBS and resuspended in 300 µl PBS to which 700 µl ice cold 100% methanol was added. Samples were incubated at 4°C in the dark for at least 12 hours until needed.

### 2.2.2 Immunofluorescence

Immunofluorescence analysis (IFA) was performed by Sulochana Omwenga to confirm mNG:KINF localisation to the spindle. 1 x $10^7$ *L. mexicana* promastigotes were washed 1X in PBS prior to fixing with 4% PFA. Here, the cells were incubated in 4% PFA at RT for 15 minutes (as opposed to the usual protocol with an incubation at 4°C). The cells were washed 1X in PBS and permeabilised using 4% bovine serum albumin (BSA)/0.075% Tween-20 for 10 minutes at RT. Once permeabilised, the cells were stained sequentially with four antibodies diluted 1:500 in 4% BSA/0.075% Tween-20. Each of the antibodies: mouse anti-mNeonGreen (IgG2c; Chromotek); rat anti-mouse IgG(H+L)- AlexaFluor488 (ThermoFisher); mouse anti-KMX-1 (IgG2b; Millipore Merck); and goat anti-mouse IgG2b(Fcγ)-AlexaFluor594 (ThermoFisher) were added to the cells, incubated for 2 hours at RT before being washed 2X with PBS. Cells were resuspended in PBS after the final wash and stored at 4°C until needed. The cells were additionally stained with DAPI (Fluoroshield™; Sigma) prior to microscopy analysis. The Fluoroshield™ was added directly to the sample, which was seeded onto poly-L-lysine-coated glass slides. Microscopy analysis was performed as outlined in Section 2.2.4.

### 2.2.3 Staining with fluorescent dyes

Various fluorescent dyes were used throughout this study for analysis by microscopy, flow cytometry, imaging flow cytometry or inertial microfluidics. Six different dyes were used to stain the DNA of live *L. mexicana* promastigotes: DAPI (4′,6-diamidino-2-phenylindole), Hoechst 33342 (Invitrogen), Vybrant™ DyeCycle™ Violet (DCV; Invitrogen), Vybrant™ DyeCycle™ Ruby (DCR; Invitrogen), Vybrant™ DyeCycle™ Orange (DCO; Invitrogen), and DRAQ5 (1,5-bis((2-(di-methylamino) ethyl)amino)-4, 8-dihydroxyanthracene-9,10-dione; BioLegend). These were all analysed by IFC, in addition to the Hoechst-stained cells being analysed by microscopy; cells were prepared using the same method for both IFC and microscopy analysis. Propidium iodide (PI) was used to stain the DNA of MeOH fixed *L. mexicana* cells which were analysed by flow cytometry and IFC. Staining of the cell body/membrane was achieved using MemGlow™ 640 (Cytoskeleton, Inc.) and MitoTracker™ Deep Red FM (Invitrogen). MemGlow™ stained-cells were analysed by IFC, while MitoTracker™-stained cells were analysed by microscopy, IFC and inertial microfluidic analysis.

For each DNA dye, 6 x $10^6$ live *L. mexicana* parasites were collected by centrifuging logarithmically growing cultures at 1000 *g* for 5 minutes. For staining with DAPI and Hoechst, the cells were resuspended in 60 µl PBS and either 5 µg.ml$^{-1}$ or 1 µg.ml$^{-1}$ of each respective dye was added. The cells were incubated at RT for 10 minutes prior to analysis. For the remaining DNA dyes, cells were resuspended in 1 ml of M199 medium to which the appropriate amount of dye was added. While at least three concentrations were trialled per dye, only the final concentration used for analysis is given here. DCV and DCR were added to the suspended cells at 40 µM and 12.5 µM, respectively, and incubated for 15 minutes at 27°C. DCO was added at 0.625 µM and incubated for 30 minutes at RT and DRAQ5™ (Invitrogen) was added at a concentration of 25 µM with an incubation of 15 minutes at RT. Cells stained with DCV, DCR or DRAQ5 were resuspended in 60 µl of PBS prior to analysis, while DCO-stained cells were centrifuged as above and the supernatant was aspirated to leave approximately 60 µl M199/DCO for resuspension. Live amastigote form *L. mexicana* were also stained as above with DCV or DCO.

For staining with PI, 10 µg.ml$^{-1}$ propidium iodide and 20 µg.ml$^{-1}$ RNAse A (Thermo Scientific) were added to methanol fixed cells (as previously outlined) prior to incubation at 37°C for 45 minutes in the dark. For flow cytometric analysis, the samples were transferred to a FACS tube. For IFC analysis, the PI-stained cells were centrifuged at 800 *g* for 10 minutes and the majority of the supernatant was aspirated to leave $\sim$ 60 µl which was used to resuspend the cells prior to analysis. All analysis was performed immediately after samples were prepared.

For staining with MemGlow™, 6 x $10^6$ live *L. mexicana* parasites were resuspended in 500 µl PBS, 2.5 µM MemGlow™ was added and the solution was incubated for 10 minutes in the dark at RT. Cells were washed 3X in PBS and resuspended in 60 µl PBS for IFC analysis. For staining with MitoTracker™, 6 µM dye was added to 1 x $10^7$ live *L. mexicana* promastigotes, resuspended in 1 ml PBS and incubated in the dark at 27°C for 15 minutes. Cells were washed 3X after incubation and resuspended in 60 µl PBS for live cell analysis *via* IFC. For microscopy or inertial microfluidic analysis, cells were fixed in 4% PFA as outlined above, before being washed 3X in PBS. After the final wash, the cells were resuspended in 1 ml PBS. 3 µl of this was added to a slide for microscopy analysis (see below), while the rest was resuspended in PBS to a concentration of $1x10^6$ cells.$ml^{-1}$.

## 2.2.4 Microscopy of *L. mexicana*

Microscopy images were taken of live unstained *L. mexicana*, fluorescently labelled cell lines or cells stained with Hoechst or MitoTracker™. 3 µl of the desired sample was seeded onto a glass slide, a cover slip applied, and imaged using an Axio Observer 3 using a Plan-Apochromat 63X/1.4 Oil Ph3 objective lens or a Plan-Neofluar 20X/0.5 objective. Images were taken using an Axiocam 305 mono camera and analysed using ZEN Blue software (Zeiss, version 3.3) or ImageJ/Fiji (version 2.9.0).

## 2.2.5 Imaging flow cytometry (IFC)

### *Acquisition*

All live, fixed, and/or stained samples (unless otherwise stated) were resuspended in 60 µl PBS prior to acquisition by IFC. The samples were loaded into an Amnis® ImageStream®X Mk II imaging flow cytometer (Cytek Biosciences) and analysed using INSPIRE™ acquisition software (version 2.0). The appropriate lasers and laser powers were selected as required for the fluorescent dyes/tags being analysed. The laser was set to the highest power capable, without the raw max pixel (the highest pixel intensity measured in each image) of the fluorescent dye/tag exceeding 2%. During acquisition, SpeedBeads® (Cytek) were automatically added to the sample *via* sheath fluid to calibrate the focus and speed of the imaging. At least 10,000 events were captured in brightfield (BF) and fluorescence modes at 60X magnification, with all events being recorded.

### *Analysis - masks*

Analysis of ImageStream data files was carried out in IDEAS™ software (version 6.2.187) as outlined in [237]. The first step of the analysis was to apply any appropriate masks. Masks are either user defined or automatically generated by the software to identify a region of interest (ROI) within each image from which all features (i.e. cell area, number of objects, fluorescence intensity) are calculated. Here, two user defined masks were generated. A cell body mask was developed to identify the cell body as a ROI and to exclude the flagellum. From this mask, any morphological measurements regarding the size or shape of *L. mexicana* cells were calculated. This comprised of the pre-defined BF mask in IDEAS™ to which an adaptive erosion coefficient of 71 was applied and subsequently filtered so that the mask had an area of > 50 pixels (equivalent to 5.56 $\mu m^2$). A mask was also developed for identification of the mNG:KINF fusion protein; this identified pixels from the mNG:KINF fluorescence images that had an intensity of > 100.

### *Analysis – standardised gating strategy*

Once the masks were generated, analysis strategies were applied to extract the populations of interest from the data. Three such strategies were developed for the work carried out in this thesis and outlined in [237]: a standardised gating strategy applied to all ImageStream files, a strategy for DCO-based cell cycle analysis, and an analysis template for mNG:KINF-based cell cycle analysis. The standardised gating strategy was used to identify a "processed" population from which morphological or further population analysis could be carried out. The aim of this strategy was to identify single, in-focus cells and gate out images containing doublets, debris and/or artefacts (e.g. images containing SpeedBeads®, out-of-focus cells, cells with incorrect masking, cell rosettes or images containing more than one cell). First, *Leishmania* cells were distinguished from SpeedBeads® and small debris (i.e. sheared flagella) by gating cells on the area of the cell body mask *vs* the intensity of side scatter (SSC). The area was calculated as the number of pixels in the cell body mask while intensity is calculated as the sum of the intensity of the pixels within the mask (here the default SSC mask) subtracted from the background. Singlet cells were identified next by gating cells on the area *vs* the aspect ratio of the cell body mask, with the aspect ratio being calculated by IDEAS™ by applying an ellipse of best fit around the mask and dividing the shortest dimensions (minor axis) by the longest dimension (major axis). Out-of-focus images were excluded from analysis by gating on cells with a gradient root mean square (RMS; a measure of pixel contrast) ≥ 55. Images containing a single mask (and thus a single cell) were selected using the spot count feature. Finally, images containing overlapping cells were excluded from analysis by gating on the cell body area *vs* cell body compactness. Compactness measures the degree of variation when measuring the radius of a cell at various points, considering all pixels and is intensity weighted. This resulted in the aforementioned "processed" population.

From this population, either morphological analysis was carried out directly or further gating was carried out to identify sub-populations of interest. This was achieved using either the DCO or mNG:KINF gating strategies to identify the different cell cycle stages of *L. mexicana*. For morphological analysis, parameters of interest were exported from IDEAS™ for each cell and imported into R (version 4.3.1). The following morphological parameters (as calculated from the cell body mask) were used throughout this work: area, aspect ratio, intensity of the BF image, circularity (measures how different a mask is from a circle), compactness (a measurement relating to the circularity while accounting for pixels intensity), height and width (the longest and shortest measurement of a bounding box around the mask, respectively), elongatedness (height/width), thickness_min and thickness_max (measure from the centreline of the cell to its narrowest and widest point, respectively), length, shape ratio (thickness_min/length), diameter (creates a circle from the area of the mask and measures the diameter) and the perimeter. Before plotting the resulting data points, data smoothing was carried out for length, thickness_max and thickness_min measurements. For these parameters, the resolution was relatively low, resulting in measurements calculated in increments of 0.33 µm for length and 0.66 µm for thickness_min and thickness_max. This was due to length being measured as the number of pixels along the midline of a mask multiplied by the pixel size (1 pixel = 0.33 µm) while the thickness_min and thickness_max (henceforth named width) features measured from the midline of the mask to the narrowest or widest point respectively, doubled and then multiplied by the pixel size. To smooth the data, a randomised value between -0.33 and 0.33 µm for each length measurement, or between -0.66 and 0.66 µm for each width and thickness_min measurement was added to each data point. For some data files, further morphological analysis was carried out to understand the distribution of cell sizes within a population. This consisted of classifying cells based on their dimension into either short (S; ≤ 10 µm in length) or long (L; > 10 µm in length) and narrow (N; < 4 µm wide) or wide (W; ≥ 4 µm wide). This resulted in the four following classifications: SN, SW, LN and LW. Data was plotted using R (version 4.3.1) in RStudio (version 2023.06.1 Build 524).

### *Analysis – DCO gating strategy*

For analysis of DCO stained cells, the standardised gating strategy outlined above was first applied to the data files to identify the "processed" population. From this population, further gating was carried out. Cells which had taken up the dye were identified by gating on the area of the cell body *vs* the intensity of DCO staining and images with in focus DCO staining were selected for by gating on a gradient RMS > 34. Analysis was carried out on the resulting

"DCO_processed" population to classify cells into the different cell cycle stages. Gates were manually drawn on the intensity of DCO staining to identify cells with 2C, intermediate content (Int.) or 4C of DNA. From these three populations, morphological analysis was first carried out to identify features associated with each of the cell cycle stages – the thirteen morphological parameters outlined above were calculated, data smoothing was applied, and the resulting measurements were plotted in R. From this analysis, the length and width measurements were identified as defining features of cell cycle stage and were subsequently used to subset the gated populations into different stages of the cell cycle (see Section 4.2.2 for details). Once the gating strategy and classification system was developed and validated in IDEAS™, analysis of the "DCO_processed" population was subsequently performed in R using the same gating thresholds after data smoothing had been carried out as previously described.

### *Analysis – mNG:KINF gating strategy*

For cell cycle analysis using the mNG:KINF cell line, as with the DCO stained cells, the standardised gating strategy was first applied to the acquired ImageStream files. Next, mNG negative (mNG-) cells were identified. This population was determined by acquiring ImageStream files of the parental C9T7 cells under the same illumination conditions as used for the mNG:KINF cells. The parental cells were then gated on the area of the cell body *vs* intensity of fluorescence to determine the standard level of autofluorescence in these *L. mexicana* parasites. This same gate was then applied to the mNG:KINF cells, thus identifying the mNG- population. Cells with a higher level of mNG expression were subsequently gated as mNG positive (mNG+) cells. Both of these populations were then categorised by their morphology into the four populations previously defined (SN, SW, LN and LW). Gates were drawn using the spot count feature on the mNG+ population to cells with either a single focus or two circular foci (2CF) of mNG:KINF fluorescence. The population with one focus was further divided based on a threshold on the aspect ratio intensity (ARI) of the focus such that cells with an ARI < 0.62 were named one circular focus (1CF) while cells with an ARI ≥ 0.62 were shown to have an elongated focus (predominantly corresponding to cells with a spindle). This resulted in 16 populations classified both on their morphology (SN, SW, LN and LW) and their mNG:KINF expression (mNG-, 1CF, elongated focus, and 2CF). Once gated, the cells within each of these populations were visually inspected, and various populations containing artefacts were removed from the analysis (see Section 4.2.5 for details). The remaining populations were classified into the different cell cycle stages, based on their morphology and mNG:KING localisation. The analysis was performed in excel in combination with visual inspection of the populations in IDEAS™. The proportions of cells in each population was used to calculate the timings of the cell cycle, using the equation shown in Equation 2.3, where $t$ is the duration of the cell cycle in hours and $y$ is the cumulative proportion of cells up to and including that stage in the cell cycle [125]). In order to calculate the time of progression $t$ was set to 12.4 hours (the population doubling time), while to calculate the units of progression through the cell cycle $t$ was set to 1.

$$x = t\frac{ln(1 - \frac{1}{2}y)}{-ln(2)} \tag{2.3}$$

### 2.2.6 Flow cytometry

Flow cytometry was performed with the assistance of the Glasgow Flow Core facility. MeOH-fixed and PI-stained cells (as outlined previously) were analysed in triplicate using a BD FACSCelesta™. 30,000 events were acquired per each of three replicates in the PE-CF594 channel. Cell cycle analysis was performed on the data as outlined below.

### 2.2.7 Cell cycle analysis

Automatic cell cycle analysis was performed in FCS Express™ (version 7.10.0007; DeNovo software by Dotmatics) in order to extract the percentages of cells in each of G1, S and G2/M/C phases. Triplicate samples stained with either PI or DCO were analysed by either flow cytometry or IFC. Debris removal was performed prior to cell cycle analysis. For IFC, this was performed in IDEAS™ by gating on the area of the cell body mask *vs* the intensity of the SSC. The resulting population was imported into FCS Express™. Flow cytometry data on the other hand was analysed directly in FCS Express™. Debris was removed *via* gating on the width *vs* the area of the fluorescence intensity. From the resulting populations the fluorescence intensity profiles were analysed using the multicycle feature which applied Rabinovitch & Bagwell debris subtraction [238], [239] and Dean/Jett/Fox cell cycle modelling [240]. The modelled data along with the calculated proportions of each of the cell cycle stages were extracted and plotted in R.

## 2.3 Generation of flagellated beads

### 2.3.1 Generation of flagellated beads

Mid-log MiniTurbo:ASC cells were incubated at 27°C in M199 (see Section 2.1.1) supplemented with either 10 µM biotin for at least 12 hours, or 600 µM of biotin for 10 minutes. After incubation, 4 x $10^8$ cells.ml$^{-1}$ were collected, washed twice in 10 ml PBS and were deflagellated as outlined above. The resulting mixture was centrifuged at 800 *g* for 15 minutes and resuspended in 3 ml PBS. 3 µl of magnetic streptavidin coated beads (ReSyn Biosciences) were added to 200 µl of the resulting sample and incubated at RT for 30 minutes with intermittent agitation. The resulting sample was added directly onto a glass slide and imaged *via* microscopy.

## 2.4 Spiral channel

### 2.4.1 Spiral channel

The spiral channel devices used throughout this work were manufactured by lithography in polymethyl methacrylate (PMMA, Epigem, UK) and consisted of a channel in an Archimedean spiral with 6 loops, an inlet and four outlets. Two different channel sizes were tested, the first with a rectangular cross section of 30 x 170 µm$^2$ (channel height x width) and a radius of 325 – 1950 µm (as measured from the centre to the inner wall of a loop) and the second design with a cross section of 60 x 360 µm$^2$ and a radius of 515 - 3805 µm (Table 2.6). A mid-pressure syringe pump (neMESYS 1000N, Cetoni, Germany) was used to inject samples into the inlet through 1/16" PTFE tubing with an internal diameter of 0.5 mm. For experiments requiring two pumps (i.e. fluid flow analysis), a second neMESYS M (Cetoni, Germany) pump was used. Both pumps were controlled using CETONI Elements (version 20210616) software to inject fluid into the channels at Reynolds numbers between 3.8 and 317.5, corresponding to pressures between 0.8 and 58.8 bar (Table 2.7). The pressure in each channel, for each flow rate was calculated using the Hagen-Poiseuille Equation, where the length of the spiral channel was 0.082 m. Live cells, PFA-fixed cells and polystyrene bead samples were prepared at a concentration of 5 x $10^5$ particles.ml$^{-1}$ in filtered PBS prior to injection into the microfluidic devices. Details of the bead sizes and shapes can be found in Table 2.8. Analysis of microfluidic sorting was carried out either by analysing the contents from the outlets post-sort or by imaging the channel during sorting.

For analysis post-sort, 60 ml live cells were sorted at both 0.7 and 1.5 ml.min$^{-1}$ (Re = 116.7 and 250, respectively). The density of cells in each of the outlets was determined (as outlined in Section 2.1.1 prior to microscopy imaging and IFC-based morphological analysis. The imaging of particles within the device was carried out using high-speed imaging, microscopy-based streak imaging, portable Dino-Lite-based streak imaging, confocal imaging and event-based imaging (as outlined below).

In an attempt to visualise the fluid flow within the channel, 1 – 26.5 µM fluorescein dye (fluorescein sodium salt, Sigma-Aldrich) was pumped into the outlet at the inner wall of the 30 x 170 µm$^2$ device while PBS was pumped into the middle outer outlet. The fluid was pumped at a range of flow rates between 0.2 and 1.5 ml.min$^{-1}$, with the fluorescein dye being pumped at ¼ rate of the PBS. Images were taken using standard microscopy as outlined in Section 2.4.2 at each turn of the channel and the images were analysed in MATLAB. Images were plotted as mesh plots with a contour plot underneath.

**Table 2.6: Radii measurements for each channel**

| **Loop No.** | **30 x 170 µm$^2$ channel radius (µm)** | **60 x 360 µm$^2$ channel radius (µm)** |
|---|---|---|
| I | 325 | 515 |
| II | 650 | 1173 |
| III | 975 | 1831 |
| IV | 1300 | 2489 |
| V | 1625 | 3147 |
| VI | 1950 | 3805 |

The radius for each rotation of the channel (loop) was measured from the centre of the channel inlet to the middle of the channel for each rotation.

**Table 2.7: Numerical description of the fluid flow within each channel**

| | Flow rate (ml.min$^{-1}$) | Velocity (m.s$^{-1}$) | Re | De | Pressure (bar) |
|---|---|---|---|---|---|
| 30 x 170 µm$^2$ | 0.2 | 0.7 | 33.3 | 3.8 | 7.8 |
| | 0.5 | 1.6 | 83.3 | 9.5 | 19.6 |
| | 0.7 | 2.3 | 116.7 | 13.3 | 27.4 |
| | 1 | 3.3 | 166.7 | 19.1 | 39.2 |
| | 1.5 | 4.9 | 250.0 | 28.6 | 58.8 |
| 60 x 360 µm$^2$ | 0.3 | 0.2 | 23.8 | 2.8 | 0.8 |
| | 1 | 0.8 | 79.4 | 9.2 | 2.5 |
| | 1.5 | 1.2 | 119.0 | 13.8 | 3.8 |
| | 2 | 1.5 | 158.7 | 18.5 | 5.1 |
| | 3.3 | 2.5 | 261.9 | 30.4 | 8.4 |
| | 4 | 3.1 | 317.5 | 36.9 | 10.2 |

From each flow rate, the velocity, Reynolds number (Re), Dean number (De) and pressure was calculated for each channel. The De was calculated using the radii for the sixth rotation of each channel.

**Table 2.8: Beads used for inertial microfluidic sorting.**

| Size | Shape | Fluorescence | Company |
|---|---|---|---|
| 2 µm | Spherical | Red | Magsphere Inc. |
| 4 µm | Spherical | None | Invitrogen |
| 5 µm | Spherical | Red | Magsphere Inc. |
| 5 µm | Spherical | Green | Magsphere Inc. |
| 6 µm | Spherical | None | Invitrogen |
| 8 µm | Spherical | None | Invitrogen |
| 10 µm | Spherical | Red | Magsphere Inc. |
| 10 µm | Spherical | None | Invitrogen |
| 2.6 x 3.2 µm$^2$ | Pear | None | Magsphere Inc. |
| 2.5 x 4.0 µm$^2$ | Pear | None | Magsphere Inc. |
| 3.8 x 5.1 µm$^2$ | Pear | None | Magsphere Inc. |
| 2.8 x 4.0 µm$^2$ | Peanut | None | Magsphere Inc. |
| 4.5 x 6.3 µm$^2$ | Peanut | None | Magsphere Inc. |
| 5.1 x 7.7 µm$^2$ | Peanut | None | Magsphere Inc. |

### 2.4.2 Imaging of inertial microfluidic sorting

***Streak imaging***

Two methods of streak imaging were performed: one method using a standard complementary metal-oxide-semiconductor (CMOS) camera (AxioCam 305 mono) and the other using a portable Dino-Lite (AnMo Electronics Corporation) microscope. Both imaging systems were used to capture long exposure images of fluorescent particles during microfluidic sorting. The CMOS camera was attached to an Axio Observer 3 and the channel was visualised using a Plan-Neofluar 20X/0.5 objective lens. Images were recorded using the software ZEN Blue (version 3.3) in triplicate using an exposure time of 4 s. The contrast of the images was adjusted in ZEN Blue prior to analysis (outlined below). On the other hand, in the software DinoCapture (version 2.0), 15 s videos were recorded using the Dino-Lite microscope at a magnification of $\sim$ 50X and a frame rate of 30 fps. For each 15 s video captured using the Dino-Lite, every frame was extracted in MATLAB and the average value of each pixel was calculated to produce a single representative image.

The images acquired from both the CMOS camera and the Dino-Lite were subsequently analysed in MATLAB to extract the corresponding intensities across the width of the channel. First, the sum of the three replicate images was calculated, thus resulting in a single image per flow rate. A ROI 50 pixels wide within the channel wall was extracted, averaged, and the resulting intensities were plotted as a violin plot.

### *High-speed imaging*

High-speed imaging of particle focusing within the microfluidic channels was performed using an AcCellerator cell analyser (Zellmechanik). This consisted of a high-speed camera, an AcCellerator L1 high powered LED, and an inverted microscope. Imaging of the channel width was performed at a ROI prior to where the channel expanded into the outlets, using a frame rate of 100 fps with a Plan-Neofluar 20X/0.5 or EC Plan-Neofluar 10X/0.30 M27 objective lens for the smaller or larger device, respectively. Data was acquired using Shape-In software (version 2.5.5.815) and the position of the particles within the channel was extracted using the software Shape-Out 2 (version 2.13.6) before being plotted in R.

### *Event-based imaging*

Two event-based cameras purchased from Prophesee (France) were used in this work, an EVK1 with a QVGA CD+EM sensor module, and a next generation EVK3 with a Gen3.1 VGA sensor. The EVK1 was fitted to an Axioskope and videos were recorded using Prophesee player software (version 1.4.1). Particles on a slide were imaged using a Plan-Neofluar 63x/1.25 Oil objective lens while the 60 x 360 $\mu m^2$ microfluidic channel was visualised using a Plan-Apochromat 10X/0.5 objective lens. In contrast, the EVK3 was attached to an Axio

Observer 3 and data was recorded using Metavision® studio (version 4.0.0). Particles both on a slide and within the 30 x 170 μm$^2$ channel were imaged using a Plan-Neofluar 20X/0.5 objective lens. For both sensors, particle sorting within the microfluidic devices was recorded for a variety of Reynolds numbers at the defined ROI. 15 s videos were recorded in triplicate in both BF and fluorescence mode. Due to the event-based cameras only capturing moving data, the position of the channel walls was not recorded. In order to know the location of the channel within an image, and thus the relative distance of each particle from the inner wall, a reference image of the channel was taken using a typical CMOS camera (AxioCam MRm or an AxioCam 305 mono). Data analysis was carried out in MATLAB to perform advanced particle tracking (carried out by Dr Yoann Altmann) or to extract the positive events within the channel (corresponding to moving particles). To extract the positive events, an appropriate frame rate and accumulation time was first selected for each video based on visual inspection of the recordings in Metavision® studio. MATLAB scripts to read, open and view the recorded data files using the selected frame rate and accumulation times were accessed from [241]. A MATLAB script was subsequently written to extract and plot the x coordinate of each positive event within the channel walls as a function of time. The three replicates for each flow rate were concatenated based on time (i.e. the events captured in each of the three 15 s videos were plotted sequentially over 45 s) in order to plot the events in a continuum.

#### ***Confocal imaging***

Confocal imaging was performed in an attempt to visualise the vertical position of focusing particles within the 30 x 170 μm$^2$ channel. 5 μm red fluorescent beads were pumped into the channel at 0.5, 1.0 and 1.5 ml.min$^{-1}$ (Re = 83.3, 166.7 and 250.0 respectively) according to Section 2.4.1. Particle focusing was imaged using a spinning disk confocal microscope, an EC Plan-Neofluar 10X/0.30 M27 objective and a PvCam camera. 15 z-stack images were taken in ZEN Blue over a depth of 50.54 μm (each image at 3.36 μm intervals) to ensure the entire 30 μm depth of the channel was captured, with both BF and fluorescence images being captured at each interval. The individual images were exported and further analysed in MATLAB. Firstly, the position of the channel walls was determined from a BF image. This enabled a ROI 50 pixels wide from being extracted from within the channel walls from the fluorescence images. The background was calculated as the average pixel intensity for each image and subtracted from each pixel. From the resulting images, the coronal plane (the cross section of the channel) was generated, consisting of a stack of 50 images. The average pixel intensity across these 50 stacks was taken, and the resulting image was plotted as an image with scaled colours.

# Chapter 3

# Quantitative cell cycle analysis of live *L. mexicana* parasites using imaging flow cytometry

## Highlights

- Imaging flow cytometry has been used for the first time to study the cell cycle of *L. mexicana*, demonstrating a high-throughput method of analysis of both the morphology and fluorescence signal in thousands of cells.
- A protocol was developed to achieve quantitative DNA staining in live *L. mexicana* promastigote cells without affecting cell morphology.
- Amastigote form *L. mexicana* were shown to stain differently to the promastigote form of the parasite

## Published work:

J. Howell, S. Omwenga, M. Jimenez, and T. C. Hammarton, **The use of imaging flow cytometry for rapid, high-throughput and automated analysis of the *Leishmania* mexicana promastigote cell cycle provides new insights into cell cycle events of short duration.** *bioRxiv*. (2023). 2023.07.24.550259. [237]

Data was partially presented at conferences:

1. J. Howell, M. Jimenez, T. C. Hammarton. **Imaging flow cytometric analysis of *Leishmania's* cell cycle.** (September 2022), *SPPIRIT*, Penicuik, UK.
2. J. Howell, M. Jimenez, T. C. Hammarton. **Imaging flow cytometric analysis of *Leishmania's* cell cycle.** (June 2022), *CYTO22*, Philadelphia, USA.

## 3.1 Introduction

Due to *Leishmania* parasites replicating asynchronously, it is important to be able to pinpoint a cell's stage in the cell cycle, for example, to be able to identify when a particular cell cycle-related protein is acting. As such, either microscopy or flow cytometry is employed for cell cycle analysis to identify morphological hallmarks and/or DNA contents associated with each stage in the cell cycle [89], [126], [142], [162], [242], [243].

Microscopy-based cell cycle analysis primarily relies on counting the numbers of nuclei and kinetoplasts, visualised using a DNA dye, within individual cells. While many dyes have been developed for the staining of DNA, in *Leishmania* DAPI and Hoechst staining are the primary dyes used for microscopy-based cell cycle analysis. DAPI staining is predominantly carried out in fixed cells and provides a stable fluorescence over time while cell fixation prevents cells from moving during imaging as well as "freezes" the cells at a particular moment in time. Hoechst on the other hand stains the DNA of live cells and is typically used in conjunction with transgenic fluorescent tags which might otherwise lose fluorescence during fixation [244]–[246]. While propidium iodide (PI), SYTO16, and DRAQ5 have been used during microscopy analysis of *Leishmania*, their use is uncommon [247], [248]. DNA dyes enable the visualisation of the DNA containing organelles within individual cells, and subsequently their classification into the cell cycle stages: with one nucleus and kinetoplast (1N1K) denoting cells in G1 and S phases; and both two nuclei and one kinetoplast (2N1K), and two nuclei and two kinetoplasts (2N2K) showing cells that have completed mitosis (Fig. 3.1). This analysis can further be supplemented with information on the size of the cell, the number of flagella (the second flagellum emerges at the end of S phase), progression through cytokinesis (formation of a membrane, furrow or cytoplasmic bridge) and the presence of markers such as spindle formation [126], [242].

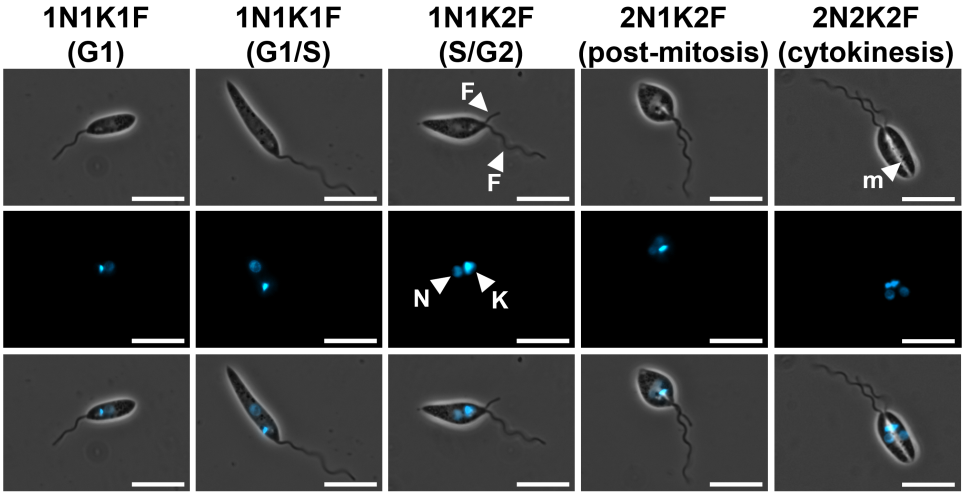

**Figure 3.1: Microscopy-based cell cycle analysis**
Examples of live *L. mexicana* cells stained with Hoechst and imaged at different stages of the cell cycle using microscopy. The top row shows the BF images, the middle row shows the corresponding fluorescence images while the bottom row shows a composite image of the two imaging modes. The number of nuclei (N), kinetoplasts (K) and flagella (F) in each cell are shown above each image, with examples of the different organelles being identified with white arrowheads (m; membrane). Scale bars; 10 µm.

While microscopy is a powerful tool, there are various limitations to its use for cell cycle analysis. For example, through such morphological assessment alone, late G1 and S phases cannot be differentiated as these cells have a similar morphology (both demonstrate elongated cell bodies with 1N1K1F) (Fig. 3.2), while the use of fixatives has been shown to introduce artefacts and alter cells' morphological and mechanical properties [249]–[251]. Microscopy-based analysis is time consuming, low throughput and labour intensive, often requiring lengthy processes for slide preparation, acquisition setting adjustments, imaging, and data processing. Image processing to extract relevant information (e.g. size measurements, spatial distribution of fluorescence, number of organelles) in sufficient quantities can often be the most time-consuming process in microscopy. For *Leishmania*, traditionally this must be done manually for each cell, resulting in low *n* numbers [127], [242], [252]–[254]. While their atypical morphology can provide a wealth of information, it can also lead to additional challenges with their flagella and often curved vermiform shape making automated cell body segmentation very difficult [255]. Despite tools having been specifically developed for kinetoplastid analysis, their applications are still limited to image cropping and contrast manipulation, fluorescence colocalization, and DNA spot counting, with morphometric analysis and fluorescent features only being automated in *Trypanosomes* and not *Leishmania* [256], [257].

DNA quantification, on the other hand, is traditionally achieved using flow cytometry; a high-throughput and sensitive tool for the detection and quantification of fluorescence in individual cells [258]. Unlike microscopy, flow cytometry only provides information on the strength of fluorescent signals, and while forward scatter measurements give an approximation of cell size, information regarding the spatial arrangement of organelles is not acquired. Instead, flow cytometry-based cell cycle analysis measures the strength of fluorescence of a quantitative DNA dye, which is thus proportional to the amount of DNA within a cell (assuming the DNA dye binds proportionally to both nuclear and mitochondrial DNA) [259]. Dividing cells start the cell cycle in G1 as diploid, having 2 sets of chromatids (2C) [120]. Throughout S phase, cells increase their DNA content through replication, resulting in 4 sets of chromatids (4C). The 4C DNA content is maintained throughout mitosis and cytokinesis until the two daughter cells fully segregate and complete the cell cycle. As such, the quantity of DNA (and thus the fluorescent signal) of a cell relates to its stage in the cell cycle.

As far as I am aware, PI is the only dye which has been used for DNA quantification for flow cytometry in *Leishmania*, despite DAPI being reportedly quantitative when analysed by microscopy [162], [242], [260]. However, Vybrant™ DyeCycle™ Violet (DCV) and Vybrant™ DyeCycle™ Orange (DCO) have been used in bloodstream form and procyclic form trypanosomes, respectively [261]. The intensity of PI fluorescence is analysed using a flow cytometer and plotted to give a DNA profile from which the proportions of cells with DNA contents of 2C, intermediate content (Int.), and 4C can be estimated (Fig. 3.2). A typical DNA profile shows a bimodal distribution with a peak for cells with 2C DNA content, a second smaller peak (at twice the intensity of the first) for cells with 4C DNA content, and with S phase cells falling between the two peaks having Int. DNA content. There are two ways in which the proportion at each stage of the cell cycle can be calculated: either through manual gating to identify the peaks by eye (Fig. 3.3A), or through the implementation of a cell cycle modelling algorithm (Fig. 3.3B). Manual gating is generally not recommended as it introduces bias and reduces reproducibility. Furthermore, the cell cycle is a continuous process with biological variation, resulting in an overlap in DNA quantity between cells in G1 and S phases, and S and G2/M/C phases. Manual gating therefore draws gates with sharp cut offs and does not take into consideration any amount of overlap. Computational modelling, on the other hand, is available through the programmes such as FCS Express™, ModFit LT™ and FlowJo ™. These use different algorithms to model the cell cycle stages based on the distributions of the data and are designed to take the overlap between the stages into consideration. While algorithms may provide unbiased and reproducible results internally, each software package uses different algorithms for calculating the proportion of cells in each of the cell cycle stages, giving varying proportions between methods [240], [262], [263]. Additionally, cell cycle models are unable to classify individual cells based on their cell cycle stage as these models only define the distributions of cells in the cell cycle within a population. Due to the lack of morphological measurements taken by flow cytometry, no more resolution in terms of cell cycle stage can be achieved (i.e. distinguishing M and cytokinesis phase cells, both with 4C DNA content) and thus, only the three populations outlined (G1, S and G2/M/C) are able to be approximated. While in mammalian cells, the different stages of the cell cycle can be identified *via* additional temporally specific biological markers (such as Cdt1 and CyclinB1 only being present during G1 and G2 respectively) [126], [163], [244], [264]–[267], no such cell cycle specific markers are available for *Leishmania* without knowing their localisation within the cell.

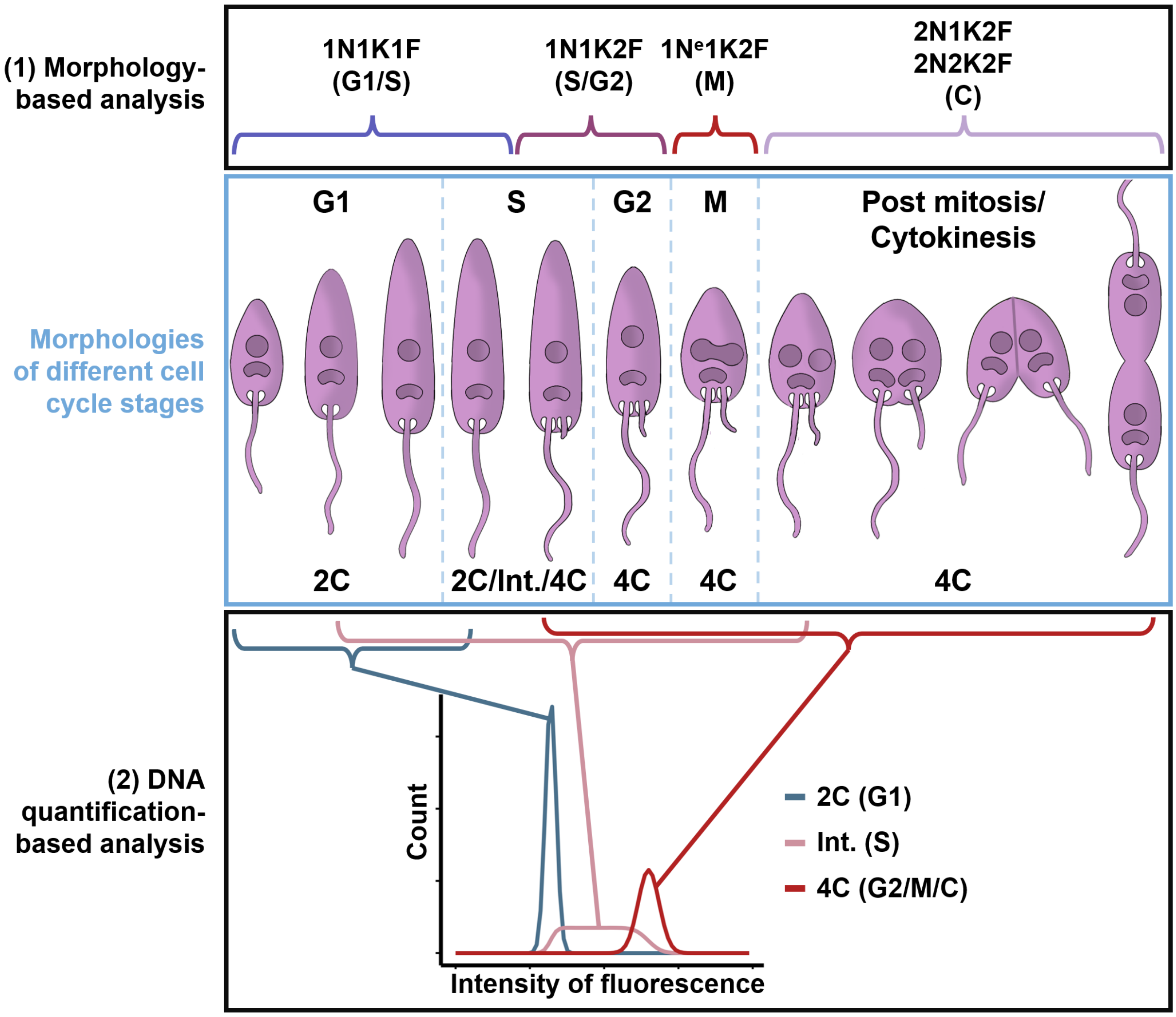

**Figure 3.2: Cell cycle analysis as carried out *via* microscopy and flow cytometry.** A comparison of morphology-based cell cycle analysis (1) *vs* DNA quantification-based cell cycle analysis (2). The blue box in the middle represents the “true” cell cycle classification, with the corresponding morphologies for each cell cycle stage falling within the dashed lines. The cell cycle stage and corresponding DNA content is given above and below the images, respectively. The contents of the black box in (1) demonstrates how microscopy analysis is used to classify cells based on the numbers of nuclei (N) kinetoplasts (K) and flagella (F), and/or the presence of an elongated (e) nucleus, a membrane or a furrow. The black box labelled (2) shows how cells are classified using DNA-quantification. From a DNA fluorescence profile, the cell cycle stages can be identified by applying a cell cycle modelling algorithm to identify the peaks of data corresponding to cells with 2C, Int. and 4C DNA content, which are associated with cells in G1, S and G2/M/C phases respectively. Overlap in seen between the different classifications, with early S and G1 phases and late S and G2/M/C phases having the same quantity of DNA.

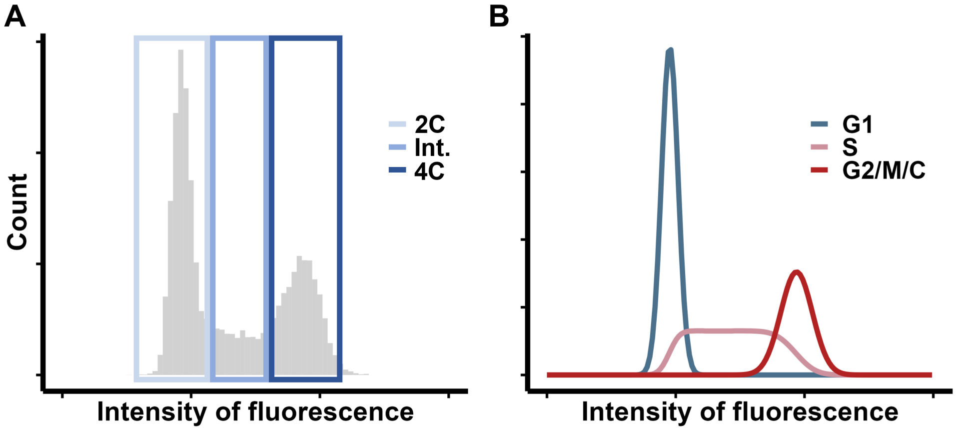

**Figure 3.3: Analysis of DNA fluorescence profiles can be manual or modelled**
Illustration of different methods of quantifying the cell cycle stages from flow cytometry data. (A) Manual gating uses gates drawn on the peaks of the data to identify populations with 2C, Int., and 4C content of DNA. (B) Modelling of the cell cycle stages was carried out using the multicycle feature in FCS Express™.

As outlined in Section 1.4, the aim of this thesis was to use inertial microfluidics, a morphology-based method of separation, to isolate the different stages of *L. mexicana's* cell cycle. In order to achieve this, it was necessary to better understand how a cell's morphology relates to its cell cycle stage for a large number of cells, especially in flow. As discussed, microscopy provides a high level of morphological information; however, the throughput for morphological and cell cycle analysis is extremely low, particularly for the analysis of multiple conditions. On the other hand, cytometry does not provide morphological information. Furthermore, both methods of cell cycle analysis primarily rely on the use of fixed cells which has implications for cell morphology and mechanical properties and subsequently for how they behave within microfluidic devices. Therefore, the aim of this Chapter was to explore whether imaging flow cytometry (IFC) enabled morphological and cell cycle analysis of live cells at in high-throughput inform microfluidic design.

Combining the morphological analysis capabilities of microscopy with the high-throughput in-flow nature of flow cytometry, IFC analysis (carried out here using an ImageStream®X Mk II, Cytek) uses a charge-coupled device (CCD) camera to capture images of individual cells in flow in both brightfield (BF) and fluorescence mode. From these images, a wide range of morphological and fluorescence information can be obtained, providing both spatial and quantitative information for each cell. One of the major benefits of ImageStream® analysis is the ability to identify regions of particular interest in both BF and fluorescence images, using masks. Masks are preset or user defined and are automatically applied to the images and adapted to fit every single object analysed. From these masks, a plethora of size, shape, texture, location and signal strength features can be analysed. IFC has been shown to be an effective tool for a wide range of applications such as cell morphological assessment, fluorescence localisation, and for assessing population dynamics [15-17]. In terms of cell cycle analysis, IFC has been applied to study: the effect of chemotherapeutic agents and gene knockouts on cell cycle progression; automated cell cycle classification and quantification; and assessment of asymmetrical nuclear division [268]–[272]. Its application has also been documented in *Leishmania* research, particularly for the study of host-pathogen interactions but also for the identification of amastigotes in blood and differentiation analysis [273]–[279]. To the best of my knowledge, it had yet to be used to study the cell cycle in *Leishmania*. This Chapter describes the methods developed for high-throughput cell cycle analysis of live *L. mexicana*, enabling both morphological and quantitative DNA analysis. The work described here is also outlined in Howell *et al.*, (2023) [237].

## 3.2 Results and discussion

### 3.2.1 IFC as a method of morphological and fluorescence quantification analysis for *L. mexicana*

Due to the novelty in application of IFC for cell cycle analysis in *Leishmania*, IFC was verified in its ability to perform DNA quantification and morphological measurements. First, DNA quantification was compared between the ImageStream® and a conventional flow cytometer (BD FACSCanto™ II). Methanol (MeOH)-fixed cells were prepared with PI as outlined in Sections 2.2.1 and 2.2.3. Each of three replicates was divided into two for analysis by IFC and conventional flow cytometry, with the help of the Glasgow Flow Core facility. The data were acquired according to Sections 2.2.5 and 2.2.6. The data from both cytometers were initially analysed in IDEAS® (the ImageStream's data analysis software) in order to remove debris – this was performed by only gating on the width *vs* the area of fluorescence for the flow cytometry data, and the area *vs* intensity of the side scatter (SSC) for IFC data (Fig. 3.4A and B, respectively). As the aim here was to compare the ability of both machines to quantify fluorescence, minimal gating was carried out in order to preserve the populations being analysed and not introduce any artefacts into the analysis as a result of differences in gating. Once the debris was removed, the intensity of fluorescence, as analysed by both cytometers, was extracted from IDEAS® and the cell cycle profiles from each cytometer were compared in FCS Express™ to give unbiased cell cycle analysis. Here, the multicycle function was used to calculate the proportions of cells in each of the stages of the cell cycle. The multicycle function applied the Dean/Jett/Fox method of cell cycle modelling and Rabinovitch and Bagwell's method for debris subtraction to give the fitted models plotted in figures 3.4C and D [238]–[240], with the calculated proportions being plotted in figure 3.4E [238], [239], [262]. While the flow cytometer gave slightly lower percentages of cells in G1 (42.7% *vs* 43.8% ), and higher numbers of G2/M/C (24.9% *vs* 26.3%) and S phases (32.4% *vs* 29.9%), the differences were shown to be non-significant (p-values of 0.38, 0.21 and 0.38 for G1, S and G2/M/C phases, respectively, as calculated by a t-test). Overall, both methods of fluorescence quantification were shown to be highly comparable in both the fluorescence profiles produced and the distribution of cell cycle stages, confirming IFC as a suitable method of fluorescence quantification analysis in *L. mexicana*.

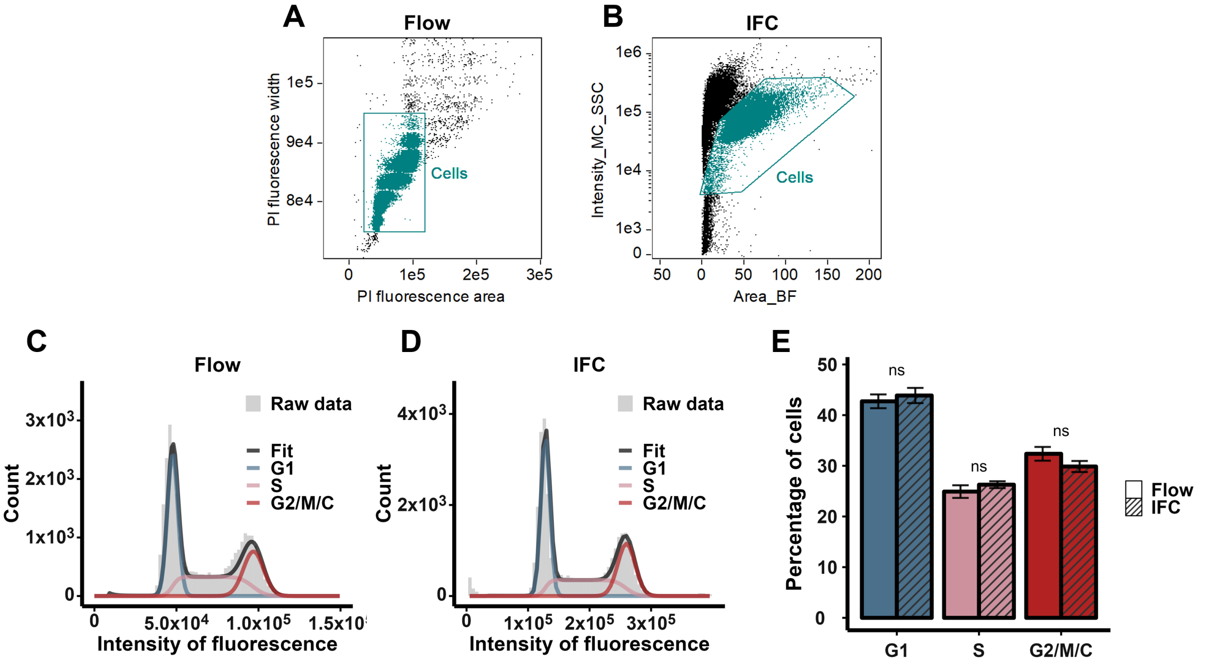

**Figure 3.4: IFC quantified DNA comparably to flow cytometry.**
MeOH-fixed and PI-stained *L. mexicana* were analysed *via* flow cytometry (Flow) and IFC according to Sections 2.2.6 and 2.2.5. The subsequent data files were analysed in IDEAS® to remove debris (black data points in the scatter plots). (A) For the flow cytometry data, this was performed by gating on the area *vs* width of the PI fluorescence. (B) For the IFC data, the cells were identified by gating on the area of the BF images *vs* the intensity of the SSC. The resulting "cell" populations (teal) were extracted from IDEAS® and imported into FCS Express™ ($n >$ 28,314 per replicate). (C-D) Cell cycle modelling was performed using the multicycle feature which applied a line of best fit (dark grey) to the raw data (light grey) and calculated the distribution of cells in G1 (blue), S (pink) and G2/M/C phases (red). A single replicate of three is displayed. (E) The percentage of cells in each cell cycle stage was extracted from the modelled fit. The error bars show the standard deviations of the three replicates. The statistical significance was calculated using a t-test, comparing the means of each cell cycle stage between both methods of analysis. ns = non-significant.

With DNA quantification by IFC giving comparable results to traditional methods of analysis, attention was turned to extracting relevant morphological information from IFC data. During data acquisition, any object that passes the camera (if sufficiently large or bright in BF or fluorescence mode), will be recorded as an event. Thus, the raw data acquired contained cell debris (i.e. sheared flagella, cell fragments, cell aggregates and cell rosettes) as well as SpeedBeads® (beads added to the sample during acquisition to calibrate the machine's flow speed and focus). Additionally, while a flow cell is used within IFCs to order cells in single file for detection, it is not 100% precise and thus images containing two cells (overlapping or separated) does occur. In order to eliminate these undesired events to reduce bias within the data, a robust pipeline was developed for *L. mexicana* morphological analysis. This pipeline consisted of four stages: 1) Identifying the cell body using a mask. 2) Applying a "standardised" gating strategy to identify individual, in-focus cells. 3) Performing any additional gating and masking to identify populations and features of interest. 4) Extracting the relevant information for further data analysis and plotting (Fig. 3.5A).

In IDEAS®, the first stage of this pipeline applied a user-defined mask to identify the cell body and exclude the flagellum (Fig. 3.5B and C). Details of the cell body mask can be found in Section 2.2.5. In the second step of the pipeline, features calculated from the cell body mask (i.e. area, spot count, compactness) were used to generate a "standardised" hierarchical gating strategy (Fig. 3.5D-H). This gating strategy was applied to all subsequent IFC carried out throughout this thesis, unless stated otherwise. The gates were drawn and validated by visually inspecting cells both within and outside the gate to ensure correct placement, and where needed, were adjusted accordingly. A detailed description of the gating strategy and the features used can be found in Section 2.2.5, but briefly, debris, cell rosettes, cell clumps and speed beads were gated out by plotting the area of the cell body mask *vs* intensity of the SSC (Fig. 3.5D). From the subsequent population, the area *vs* aspect ratio identified images where the size and shape were outwith the normal range for a single cell (Fig. 3.5E). In-focus cells were selected as images having a gradient root mean squared (gradient RMS) values ≥ 55 (Fig. 3.5F). Images with a single mask were identified using the spot count feature to exclude images containing multiple objects (Fig. 3.5G). Finally, images with overlapping cells were excluded using the compactness feature; objects with low compactness displayed an uneven outline which was unusual for a single cell (Fig. 3.5H).

The result of the outlined gating strategy was a "processed" population containing high-quality images of individual cells. Typically, this gating strategy removed between 30-50% of events initially collected during acquisition, depending on the quality of both the sample and the imaging. The vast majority of these were lost during gating for in-focus cells – due to the elongated nature of *L. mexicana*, any rotation of the cell within the flow caused the cell to pass through multiple focal planes and appear out of focus. While this loss is large, it was deemed necessary in order to acquire robust morphological measurements. From the "processed" population, the third step of analysis could be carried out as necessary to classify cells into sub-populations of interest, i.e. cells only in mitosis. Additional gating strategies are outlined elsewhere for such analysis. The final stage of the pipeline was to extract feature values of interest, such as area, length and width measurements for plotting graphs using the programming language R. This served various purposes: to smooth the data where image resolution affected the cell measurements, to directly compare the characteristics of different populations or conditions, and to enable statistical tests to be performed. Smoothing of the data was carried out for certain measurements (such as length and width), where large “steps” were present in the data (Fig. 3.5I). These steps occurred as a result of the low image resolution, with a pixel measuring 0.33 x 0.33 $\mu m^2$ when using the ImageStream’s 60X objective. As the length feature measures the number of pixels along the midpoint of a mask’s longest axis, and the width (measured using a featured called thickness_max) calculates the number of pixels from the midpoint of a mask to its widest point and then doubles it, these parameters are thus measured in increments of 0.33 µm and 0.66 µm, respectively. Details on how the data smoothing was performed can be found in Section 2.2.5. The generation of this pipeline enabled morphological features of *L. mexicana* to be extracted from ImageStream® data in a consistent and reliable manner.

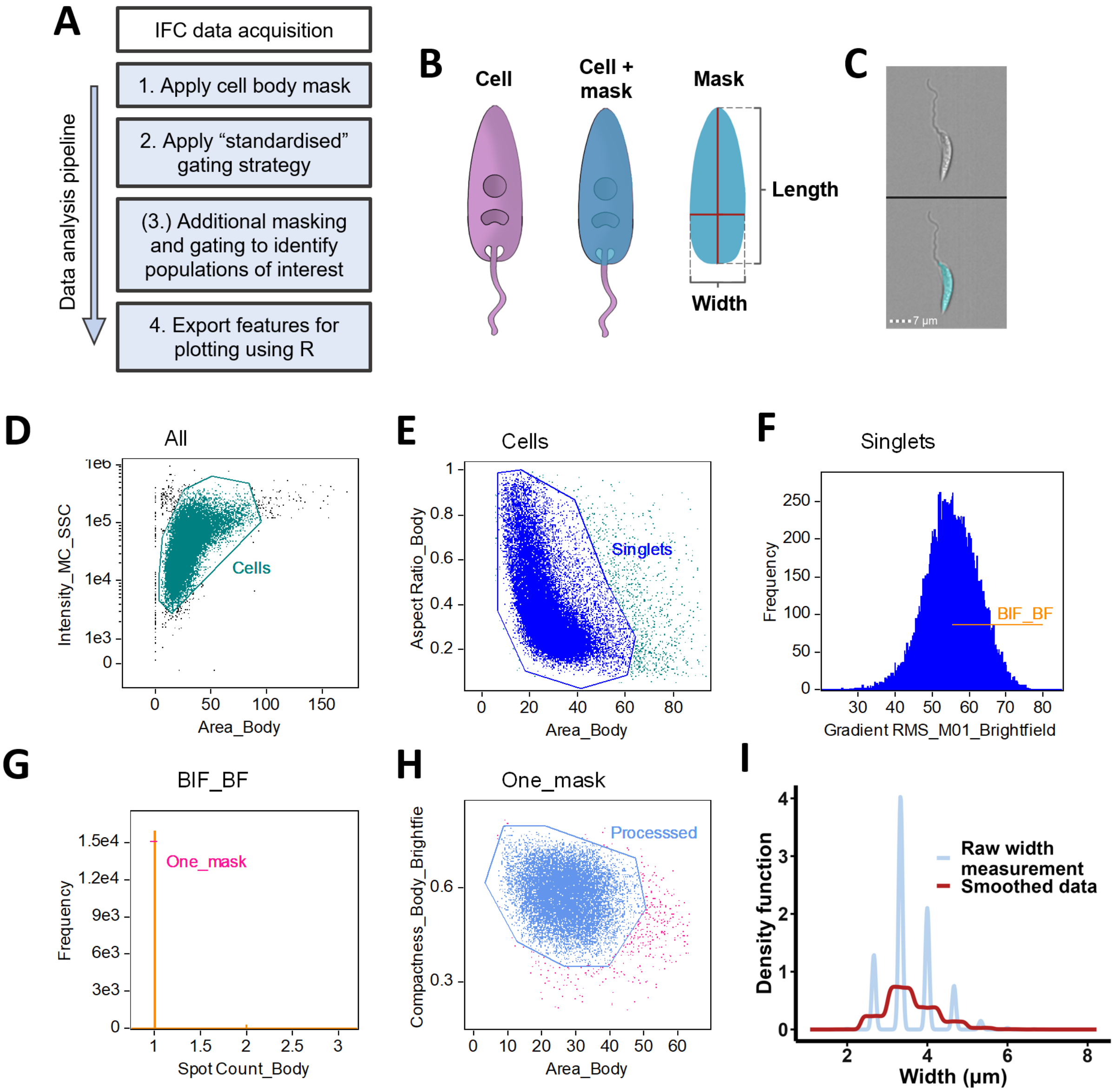

**Figure 3.5: ImageStream® data analysis pipeline.**
(A) Diagram representing the pipeline developed for analysing ImageStream® data. After data acquisition, the four steps in the blue boxed could be applied to the data, with step three being an optional step. (B) A graphical representation of a *L. mexicana* parasite (left), overlaid with a user defined cell body mask (middle). From the mask, morphological features such as the length and width were calculated (right), where length is the number of pixels down the midpoint of the mask, and the width (using the thickness max feature) measures from the midline of the mask to its widest point and doubles it. (C) Example of an IFC image of a live *L. mexicana* parasite (top) with an overlaid cell body mask (bottom). Scale bar: 7 µm. (D-H) The "standardised" gating strategy applied to all (unless otherwise stated) IFC data files. Each data point represents an event which was recorded by the ImageStream®, with each event consisting of images in both BF and fluorescence mode of a detected object in flow. (D) The area of the cell body mask was plotted against the intensity of the SSC for all events acquired, from which a population named "cells" was gated. (E) From the "cells" population (teal), the area of the cell body mask was plotted against the aspect ratio of the cell body mask. Gated cells were named "singlets" (dark blue). (F) The "singlets" population was plotted as a histogram using the gradient root mean squared

(RMS) feature. A gate was drawn to select cells with a gradient RMS value $\geq$ 55 (orange), identifying the best in focus images from the BF channel (BIF_BF). (G) From these in-focus images, images with a single mask (pink) were identified using the spot count feature. (H) Of these cells, the area of the cell body mask was plotted against the compactness of the cell body mask to exclude images containing overlapping cells, resulting in a population named "processed" cells (light blue). (I) Example of the raw width measurements of *L. mexicana* cells (as analysed by IFC) compared to the same data with smoothing applied.

With the analysis pipeline in place, the ImageStream® was subsequently tested for its ability to measure the morphology of *L. mexicana* promastigotes. As outlined earlier in this chapter, both DNA quantification and cell morphology are used for cell cycle analysis. Traditionally, these techniques are carried out on MeOH- or paraformaldehyde (PFA)-fixed cells to preserve their state at a single point in time as well as to prevent them from moving. The morphology of live and fixed cells was therefore analysed *via* IFC for two purposes: firstly, to validate that IFC was capable of analysing the unusual shape of *L. mexicana*, as well as to compare the differences in morphology between fixed and live cells. *L. mexicana* promastigotes were prepared, fixed, acquired on the ImageStream® and the data analysed as outlined in Sections 2.2.1 and 2.2.5, respectively. Example images for each of the different treatments are shown in figure 3.6A. Live cells were calculated to be on average 11.0 μm in length, with 95% of cells having a length of between 4.9 μm and 17.6 μm. Similarly, the average width was shown to be 3.6 μm, with 95% of cells being between 2.4 μm and 5.0 μm wide. This is comparable to the measurements obtained by Wheeler *et al.* (2011) using microscopy, where 980 fixed cells were measured to be between $\sim$ 5 μm to $\sim$ 15 μm in length and $\sim$ 2 μm and $\sim$ 6 μm in width [125]. While the ImageStream® measured cells as slightly longer and narrower than as in the literature, variation is expected due to different processing of samples, potential differences in cell cultures between research groups, and biological variation. In the samples fixed with PFA, cells were on average 9.8% shorter and 7.3% wider than their live counterparts (Fig. 3.6B and C). MeOH-fixed cells, on the other hand, appeared shorter and wider (40.0% and 6.7%, respectively). This resulted in 93.3% of MeOH fixed cells having a length of ≤ 10 μm compared to only 39.3% of live cells. As both methods of fixation altering morphology, live cells were therefore the preferred option for testing.

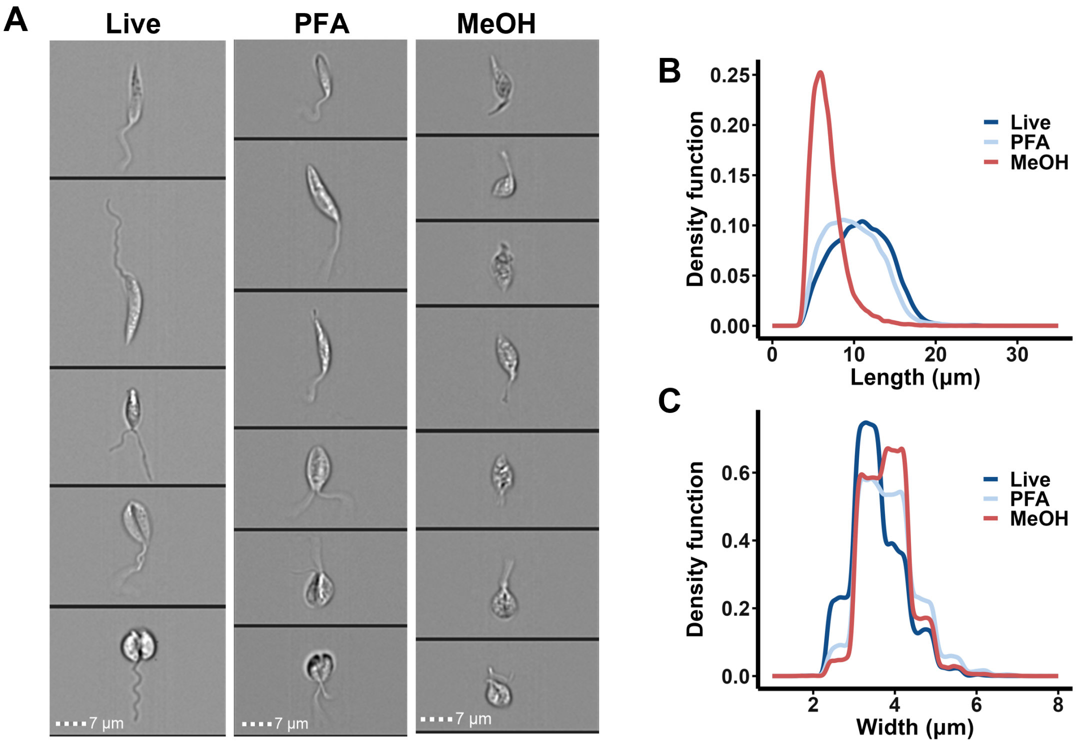

**Figure 3.6: ImageStream® analysis of *L. mexicana* promastigote morphology.** (A) Example IFC images of live, PFA- and MeOH-fixed *L. mexicana* promastigotes. Scale bars: 7 µm. Density plots of the length (B) and width (C) of live, PFA- and MeOH-fixed cells as measured by IFC. A single replicate of three is shown (*n* > 26,499 for each condition).

### 3.2.2 Typical DNA dyes are non-quantitative in live *L. mexicana* promastigotes

While using live cells maintained cell morphology at physiological levels, this required a DNA dye which is quantitative in live cells and could stain both the nucleus and kinetoplast. As mentioned earlier in this chapter, PI is the only dye which has been used for DNA quantitation for cytometric analysis in *L. mexicana*; however, as PI requires permeabilisation (which is achieved during fixation with MeOH and not PFA), it is thus unsuitable for this application. Therefore, various DNA dyes were tested (using at least three different concentrations) in their ability to provide both spatial and quantitative DNA information while maintaining cell morphology. Live *L. mexicana* promastigotes were stained with Hoechst, DAPI, Vybrant™ DyeCycle™ Ruby (DCR), DCV and DRAQ5, analysed by IFC and the subsequent DNA profiles compared to that of to a typical DNA profile obtained from MeOH-fixed cells stained with PI (Fig. 3.7). All dyes tested in live cells gave variable results, both in terms of their DNA profile and their fluorescence localisation within the cells. Firstly, none of the DNA dyes tested here proved to be quantitative, failing to produce a DNA profile with two distinct peaks. Instead, all dyes displayed a positively skewed distribution; an asymmetric distribution where there is a higher range of data points to the right of the distribution's peak, compared to the left side. The tested DNA dyes also showed variability in their fluorescence localisation within the stained cells, as seen in the example IFC images for each dye. Interestingly, despite Hoechst being most commonly used in live cells for microscopy analysis, for IFC analysis, DAPI and DCV provided the clearest staining of both nuclei and kinetoplasts, with Hoechst and DCR showing non-specific staining of the cytoplasm. Non-specific staining has been has previously been reported for DCR but not for Hoechst [280]. Finally, in accordance with the literature, DRAQ5 only stained nuclear DNA (Fig. 3.7F) [281].

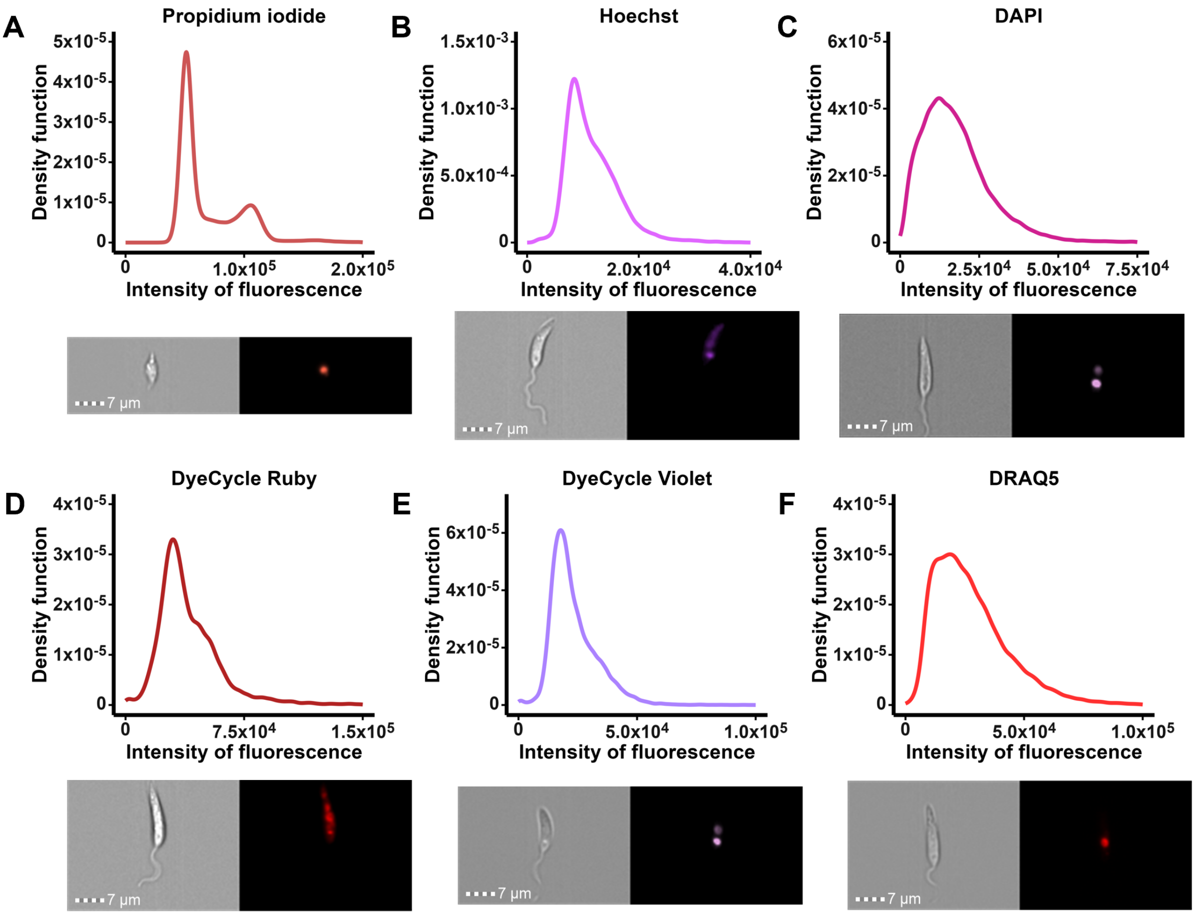

**Figure 3.7: Traditional DNA dyes for staining live cells are non-quantitative in *L. mexicana*.**
Various fluorescent DNA dyes were tested for their ability to quantitatively stain the nucleus and kinetoplast of live *L. mexicana* promastigotes. (A) A control showing a typical DNA profile obtained from a quantitative DNA dye, achieved using MeOH-fixed cells stained with PI. An IFC image corresponding to the fluorescence localisation of the reported dye is given below the DNA profile, with the BF image on the left and the fluorescence image on the right. (B-F) Equivalent DNA profiles obtained from staining live *L. mexicana* with Hoechst, DAPI, DCR, DCV and DRAQ5, respectively, with corresponding IFC images shown below each profile. A single representative replicate of three is given and $\sim$ 30,000 events were acquired for each replicate for each dye. Scale bars: 7 µm.

### 3.2.3 DCO as a robust cell cycle dye in live *L. mexicana* promastigotes

Finally, Vybrant™ DyeCycle™ Orange (DCO) was tested for its suitability as a quantitative DNA dye for live *L. mexicana*. Two initial tests were performed at a concentration of 10 µM dye and incubated at either 27°C for 30 minutes or at room temperature (RT) for 60 minutes (conditions 1 and 7 in Table 3.1), as pre the manufacturers recommendation. For both conditions, analysis with IFC showed aberrant cell morphologies (Fig. 3.8A) suggesting that the concentration of the dye was too high and potentially having cytotoxic effects. For both incubation conditions, serial dilutions were performed in addition to reducing the incubation times by half; an overview of the conditions tested is shown in Table 3.1. A variety of artefacts were observed for many of the conditions, either affecting cell morphology or showing suboptimal staining of DNA (Fig. 3.8). For example, these included suboptimal staining of the kinetoplast (Fig. 3.8B), the formation of a vacuole within the cell body (Fig. 3.8C), and fluorescence localising to outside of the nucleus and kinetoplast, even within the flagellum (Fig. 3.8D). From these results, it was observed that at a concentration of 0.63 µM, DCO was capable of providing a typical DNA profile (condition 6 and 12 in Table 3.1) (Fig. 3.8E). In contrast, a concentration of 1.25 µM DCO did not show two distinct peaks and resulted in a positively skewed distribution similar to that seen for the other DNA dyes tested (Fig. 3.8F). Concentrations of >1.25 µM were too bright for analysis by IFC and resulted in the fluorescence saturating pixels of the ImageStream's camera in > 2% of cells when using the lowest laser power of 1 mW. As outlined in Section 2.2.5, an arbitrary cut off of 2% was set as a threshold for acceptable levels of pixel saturation. As well as dye concentration, incubation times were also seen to play a role in DCO staining (Table 3.1) – incubating the cells with DCO at 27°C for 10 minutes resulted in only the nucleus and not the kinetoplast being visible in a large proportion of cells. In contrast, an incubation of 30 minutes at RT resulted in sufficient staining of both the nucleus and kinetoplast. Thus, a concentration of 0.63 µM with an incubation time of 30 minutes at RT was selected for further testing.

**Table 3.1: Conditions of DCO staining tested during protocol optimisation**

| | Concentration of DCO (μM) | Incubation temp. | Incubation time (mins) | Typical cell morphology | Acceptable DNA staining |
|---|---|---|---|---|---|
| 1 | 10.00 | 27°C | 30 | - | - |
| 2 | 10.00 | 27°C | 10 | - | - |
| 3 | 5.00 | 27°C | 10 | ✓ | - |
| 4 | 2.50 | 27°C | 10 | ✓ | - |
| 5 | 1.25 | 27°C | 10 | ✓ | - |
| 6 | 0.63 | 27°C | 10 | ✓ | - |
| 7 | 10.00 | RT | 60 | - | - |
| 8 | 10.00 | RT | 30 | - | - |
| 9 | 5.00 | RT | 30 | ✓ | - |
| 10 | 2.50 | RT | 30 | ✓ | - |
| 11 | 1.25 | RT | 30 | ✓ | - |
| **12** | **0.63** | **RT** | **30** | ✓ | ✓ |

To optimise the staining protocol of DCO, the concentration of DCO, and the incubation temperature and time were modified from the manufacturers recommended protocols (rows 1 and 7), and the morphology and DNA staining of the resulting cells was noted. Procedure resulting in aberrant cell morphologies (i.e. ruptured cells or cells seen with an enlarged vacuole) or suboptimal DNA staining (i.e. faint kinetoplast staining, staining outside the the nucleus and kinetoplast, or a DNA profile lacking two distinct peaks) were marked with "-". In contrast, protocols maintaining a typical morphology or showing both clear nucleus and kinetoplast staining and a typical DNA profile were marked with a "✓". The row highlighted in bold and green indicates the protocol selected for further analysis. A single replicate was carried out for each condition.

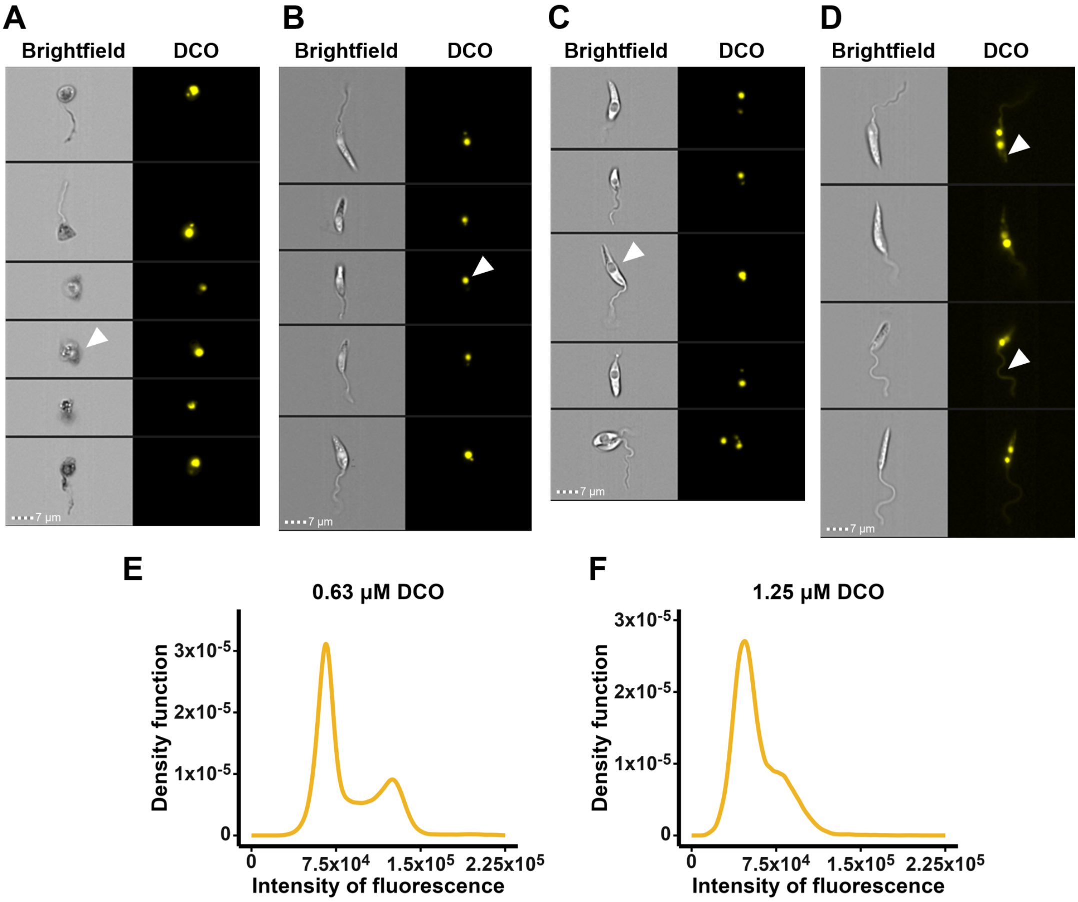

**Figure 3.8: DCO causes artefacts when suboptimal staining protocols are used.** Different DCO staining protocols (as analysed by IFC) affected cell morphologies or showed variation in DCO localisation. Example BF and DCO fluorescence images show cells where: cell morphology was affected with cells seeming to expel a dark matter (A), the kinetoplast stains faintly (B), cells form a vacuole (C) or DCO staining is non-specific, staining outside of he nucleus and kinetoplast (D). White arrowheads highlight the issue in each image. Scale bars: 7 µm. Quantification of the fluorescence from cells stained with either 0.63 µM (E) or 1.25 µM (F) of DCO resulted in typical and abnormal DNA profiles, respectively. ∼ 30,000 events were recorded per replicate. A singe replicate was performed for each condition.

Once the experimental conditions were established for DCO staining, it was tested whether staining live cells with DCO enabled the quantitation of DNA in a manner comparable to that of PI. *L. mexicana* promastigotes were stained with either DCO or PI and analysed using IFC according to Sections 2.2.3 and 2.2.5, respectively. Once acquired, the data were analysed using FCS Express™ (as outlined in Section 2.2.7), with the raw data plotted as a histogram and the modelled fit and cell cycle stages overlaid (Fig. 3.9A and B). From the modelled distributions, the percentages of cells in G1, S and G2/M/C phases were calculated (Fig. 3.9C). On initial inspection, the fluorescence profiles between DCO and PI looked slightly different with DCO having wider peaks for G1 and G2/M/C phases and with seemingly a higher overlap between the three cell cycle stages, as compared with PI (Fig. 3.9A and B).

However, when quantified with FCS Express™, the different staining methods were shown to be highly comparable, with a maximum difference of 1.8% between PI and DCO stained samples. A t-test confirmed that the differences between the cell cycle stage proportions, as measured by DCO and PI, were non-significant (p-values of 0.94, 0.63 and 0.57 for G1, S and G2/M/C phases, respectively), showing for the first time that DCO stains DNA quantitatively in live *L. mexicana* promastigotes.

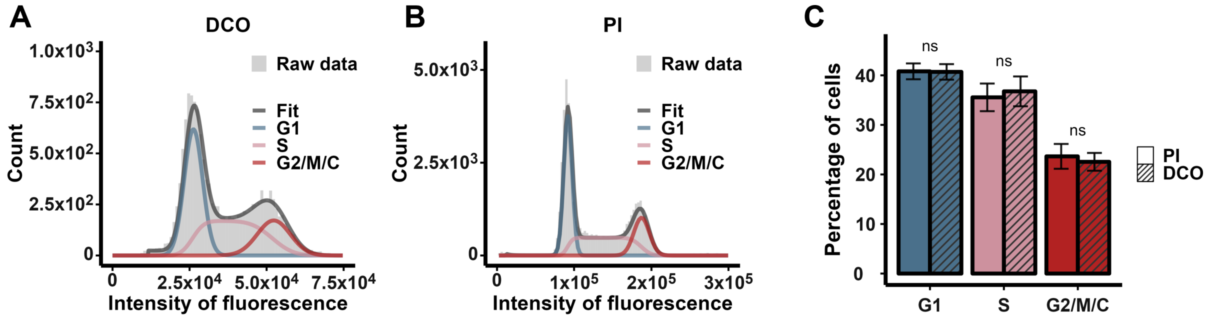

**Figure 3.9: DCO staining provides similar cell cycle quantitation as PI staining.** *L. mexicana* promastigotes were either stained live with Vybrant™ DyeCycle™ Orange (DCO) (A) or fixed with MeOH and stained with PI (B) according to Sections 2.2.3 and 2.2.1. The samples were analysed by IFC, for which the intensity of fluorescence was extracted from IDEAS® and imported into FCS Express™. Cell cycle modelling was applied to measured DNA profiles (light grey) to extract the distributions of G1 (blue), S (pink) and G2/M/C (red) phases ($n \geq$ 13,920 per condition, per replicate). (C) The percentage of cells in G1, S and G2/M/C phases calculated from the fitted model for three replicates per DNA stain. The error bars show the standard deviation between the three replicates with a t-test being performed for each cell cycle stage, comparing the means between the different stains. ns = $p > 0.05$.

Thus far it has been shown that DCO staining is quantitative in live cells and can be analysed using IFC and FCS Express™ to perform cell cycle analysis and extract the proportions of cells in G1, S and G2/M/C phases. As mentioned previously, the novelty of IFC is that it simultaneously provides spatial and morphological information alongside fluorescence quantitation, and therefore can combine typical microscopy-based cell cycle analysis of counting the numbers of DNA-containing organelles with high-throughput cytometry-based DNA quantification. In order to confirm that DCO was a suitable DNA dye for organelle-based cell cycle analysis, the localisation of DCO fluorescence (using the optimised staining protocol) was analysed (Fig. 3.10). Both the nucleus and kinetoplast were clearly stained with the dye exhibiting a preference for mitochondrial DNA since the kinetoplast stained more brightly than the nucleus. By counting the numbers of nuclei, kinetoplasts and flagella per cell, cells were classified into the different stages of the cell cycle. All arrangements of nuclei, kinetoplasts and flagella, which were previously identified by Wheeler *et al.* (2011) using microscopy [125], were identified here *via* IFC-based analysis of DCO staining. This consisted of cells with 1N1K1F, corresponding to cells in either G1 or S phases, 1N1K2F cells in either S or G2 phases and 2N1K2F and 2N2K2F cells which were in mitosis or cytokinesis. Thus, DCO staining was shown to stain the nucleus and kinetoplast clearly, enabling classification of cells into the different stages of the cell cycle based on their number of organelles.

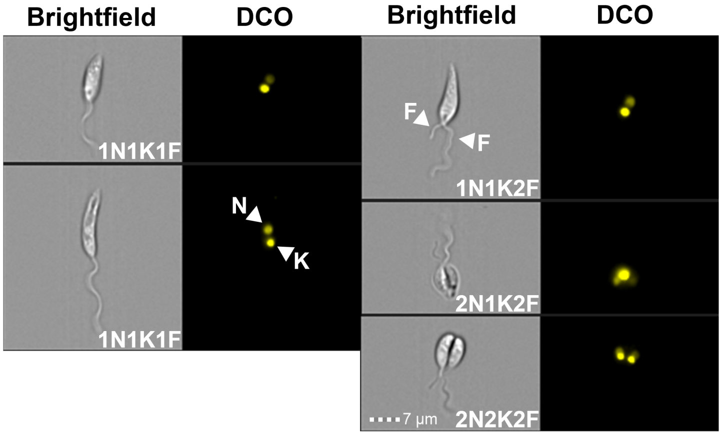

**Figure 3.10: DCO staining enabled the classification of cells into their cell cycle stages.** *L. mexicana* stained with DCO were were analysed by IFC. From the corresponding BF and fluorescence images, cells were manually classified based on their numbers of nuclei (N), kinetoplasts (K), and flagella (F). White arrowheads identify examples of a nucleus, a kinetoplast and two flagella. Scale bar: 7 µm.

### 3.2.4 Stability of DCO is time dependent

As previously described, maintaining the morphology of *L. mexicana* is essential for cell cycle analysis and for guiding microfluidic chip design. It has also been demonstrated that DNA dyes can have a wide range of effects, affecting both cell morphology (Fig. 3.7 and 3.8), cell proliferation [282] and viability [283], [284]. Therefore, the reproducibility of the staining and morphology of DCO-stained cells was assessed. Live *L. mexicana* were stained with DCO in triplicate, with each replicate being analysed repeatedly every $\sim$ 7 minutes over the course of 46 minutes (Fig. 3.11). The ImageStream® uses a very small quantity of sample during data acquisition, which is discarded post-analysis. Thus, there is no possibility of measuring the same cells twice, reducing the likelihood of artefacts arising from this analysis. It was seen that over time the intensity profile of DCO changes (Fig. 3.11A); the G2/M/C peak decreases in fluorescence intensity while the G1 peak remains consistent. This specific decrease in fluorescence in late cell cycle stages was unusual; photobleaching or dye degradation are the main causes of a decrease in fluorescence intensity; however, this typically occurs at the same rate in all cells. After $\sim$ 21 minutes, it was seen that multicycle modelling was no longer capable of distinguishing the G2/M/C peak from the S peak. Care was therefore taken to analyse the cells within 20 minutes of completing their incubation with DCO. Within this time, there were minimal impacts on the cell cycle profile (as determined by cell cycle modelling using FCS Express™) in addition to staining with DCO having negligible effects on cell morphology, with length and width measurements remaining comparable to unstained cells (Fig. 3.11B). Similarly, morphology was maintained between replicates (Fig. 3.11C). Finally, culturing cells in cell medium after incubation with DCO showed that the staining protocol had no effect on cell viability (Fig 3.11D), validating DCO as a robust DNA dye for live cell cycle analysis in *L. mexicana*.

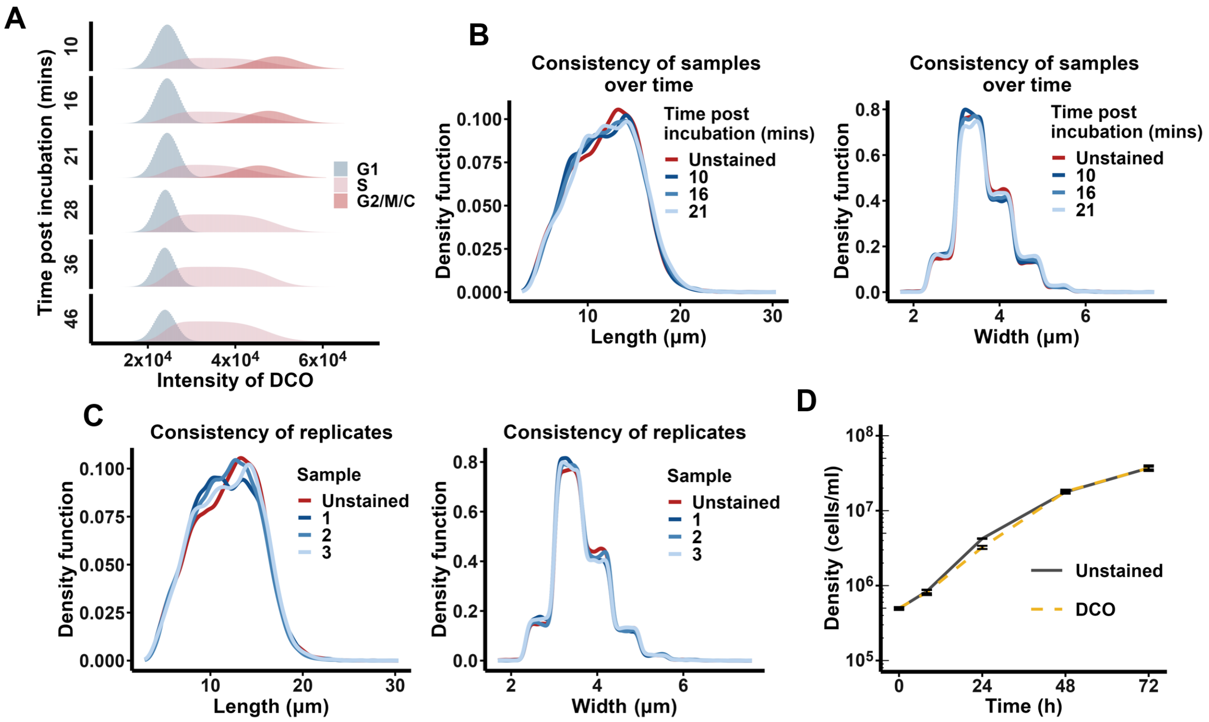

**Figure 3.11: DCO staining was stable and robust for 20 minutes post-incubation.** (A) Three replicates of live *L. mexicana* C9T7 promastigotes were stained with DCO using the optimised protocol and repeatedly analysed by IFC 10, 16, 21 28 36 and 46 minutes after incubation. The fluorescence profiles were extracted, analysed with FCS Express'™ multicycle feature, and the resulting distributions of the cell cycle stages were plotted. ∼ 30,000 events were collected per replicate. (B) The length and the width features of the DCO-stained cells were analysed at the time points up to 21 minutes post-incubation. An unstained sample was washed, centrifuged, resuspended in PBS and analysed by IFC immediately as a control. A single replicate of three is shown for each condition. (C) The length and width of DCO-stained cells at the first time point (10 minutes post-incubation) for the three replicates were compared to the unstained control. (D) Comparison of cell viability between cells stained with DCO then washed *vs* unstained and washed *L. mexicana* C9T7 promastigotes. Following washing, cells were resuspended in M199 medium at a density of 5 x $10^5$ cells.ml$^{-1}$ and cell densities were calculated after 8 hours and subsequently 24-hour intervals. Error bars show the standard deviation between three replicates.

### 3.2.5 Axenic amastigotes show different staining properties

The developed cell cycle staining protocol was also tested in its ability to stain axenic amastigotes, as cell cycle analysis has not previously been performed on this life cycle stage due to a variety of factors such as their small size making organelles difficult to identify, and lack of cell cycle specific morphological features (i.e. minimal changes to cell size and no visible flagella). Therefore, it was tested whether DCO staining and IFC analysis would provide insight into the morphological changes of amastigotes throughout the cell cycle. Unfortunately, incubation with DCO using the same protocol as optimised for promastigote cells did not seem to provide quantitative staining in amastigotes. Instead, a single peak of fluorescence was seen in the DNA profile (Fig. 3.12A) and examination of the fluorescence only showed staining of one DNA containing organelle. It was hypothesised that like in *T. brucei*, the mammalian form of the parasite would instead stain with DCV [261]. For the conditions tested neither DCO nor DCV provided quantitative staining in *L. mexicana* amastigotes (Fig. 3.12B). Further optimisation of the protocols for DNA staining may be required to achieved cell cycle analysis in these cells; however, this work was outside the scope of this study and was therefore discontinued.

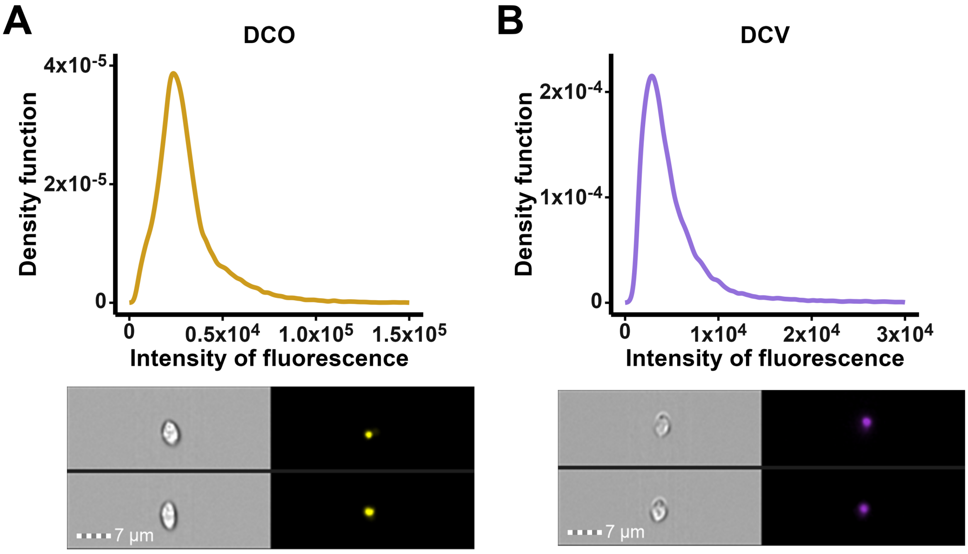

**Figure 3.12: DCO was unsuitable for cell cycle analysis in axenic amastigotes.** DNA profiles of *L. mexicana* axenic amastigotes stained with DCO (A) or DCV (B), with corresponding IFC images (left: BF images; right: fluorescence images) for each dye ($n \geq 27{,}664$ per replicate). Scale bars: 7 µm.

## 3.3 Discussion and conclusions

Cell cycle analysis is an important area of analysis in *Leishmania*, in order to understand the fundamentals of the parasite's biology, determine the function of individual proteins, and for potential targets for drug development studies. However, the tools currently available for assessing *Leishmania's* cell cycle are insufficient for providing an overview of the population as a whole. Often, morphological aberrations from cell cycle-related studies are identified; however, frequently, either no quantification is carried out or only a low number of cells are examined [252], [253], [285], [286]. Alternatively, flow cytometry is carried out to quantify changes in the proportions of large numbers of cells at each stage in the cell cycle; however, the lack of morphological information makes it difficult to, for example, identify the specific point of cell cycle arrest [286]–[288]. In this Chapter, the first use of IFC to overcome these limitations in *L. mexicana* is reported, offering a tool to provide both high-throughput morphological and cell cycle information.

This technology was demonstrated to be particularly well suited for kinetoplastid research; cells are analysed in suspension, which is analogous to their physiological state in culture as opposed to being seeded onto a slide, and IFC is capable of analysing $\sim$ 1000 cells/s. The lack of motion blur within the images enables live analysis of these highly motile cells without the addition of chemicals or fixatives, and the application of masks for ROI identification and morphological measurements decreases analysis times from hours to < 10 minutes (where gating strategies have been previously defined). Furthermore, the batch analysis of data files with the same gating strategy enabled multiple samples and conditions to be analysed in parallel, increasing throughput while reducing processing times and user bias (e.g. instances where a cell's organelle classification is uncertain can be subject to operator inconsistencies).

Here, a protocol was developed in order to achieve cell cycle analysis in live *L. mexicana*. The first step in developing this protocol was to find a DNA dye which maintained cell morphology, clearly stained the nucleus and kinetoplast and provided quantitative staining. Five dyes were selected for testing which have previously been reported to quantify DNA in mammalian cells [289]–[293]; however, as was shown here, were not quantitative for *L. mexicana*. The lack of dyes which stain DNA quantitatively in *Leishmania* has been hinted at in that only PI has been used for this purpose, and only in fixed cells, but this not been explicitly documented. I have demonstrated that in live *L. mexicana*, the suitability of DNA dyes for cell cycle analysis are highly variable, both in terms of fluorescence localisation, specificity of binding and ability to quantify DNA. Of the dyes tested here, only DCO was shown to be quantitative in live promastigote cells providing highly comparable results to DNA quantification with PI and clearly staining the nucleus and kinetoplast. For the first time, it has been demonstrated that both morphological and quantitative cell cycle information could be extracted from live cells in a high-throughput manner.

One of the considerations of the outlined protocol is that DCO was shown to be quantitative for only 20 minutes post-incubation, and after this time, the fluorescence intensity of the G2/M/C peak was shown to decrease. As the G1 peak did not decrease in fluorescence, this suggests that the change in the G2/M/C DNA intensity was not due to photobleaching of the dye, as this would affect all cells. Instead, this suggested that the change in fluorescence intensity was due to the cells themselves altering the levels of the dye within the cell (i.e. exporting the dye) or the intensity of the fluorescence (i.e. degrading or quenching the fluorescence or a reduced level of binding DNA). One possible explanation for this is that the dye was actively transported out of the cells, which occurred faster in cells in later cell cycle stages. In mammalian lymphoblast cells it has been reported that both Hoechst and DCV were extruded from the through ATP binding cassette (ABC) transporter proteins [294]. While the authors were unable to obtain a direct measurement, it was speculated that DCV was extruded out of cells faster than Hoechst, and in a dose dependent manner. Interestingly, this same class of transporter proteins are found in *Leishmania* and have been similarly shown to transport antileishmanial drugs out of the cells leading to drug resistance [295]–[297]. Life cycle dependent expression of these proteins has also been shown in *Leishmania*, with cell cycle dependent expression not yet having been analysed [298]. It is therefore possible that these ABC proteins are similarly responsible for the transport of DCO out of the cells. If this hypothesis is correct, then the variability in activity and expression of these transporters may also be an explanation for different DNA profiles seen for both different dyes and different life cycle stages.

While the optimised DCO-staining protocol was suitable for staining live *L. mexicana* promastigotes, the same was not the case for live *L. mexicana* axenic amastigotes. As was demonstrated in this work, slight differences in the conditions of DCO staining resulted in very different fluorescence presentations in the promastigote cells. It is highly possibly that, similarly to *T. brucei* [261], differences in cell composition between different life cycle stages affects the binding of dyes to DNA. For example, differences in the surface glycoconjugates may affect permeabilisation of the dye across the cell membrane [299]. In order to achieve cell cycle analysis of live amastigotes, the testing of various DNA dyes and optimisation of a staining protocol, as carried out here for promastigotes, is likely needed.

# Chapter 4

# Morphological analysis of the cell cycle of *Leishmania*

## Highlights

- IFC-based cell cycle analysis is improved through classifying cells using both their DNA content and morphology.
- Tagging the spindle associated protein KINF with a fluorescent marker enabled automatic identification of cells undergoing mitosis.
- Using the developed methods for high-throughput cell cycle analysis, the G2 phase of *L. mexicana's* cell cycle was quantified for the first time and deduced to last 38 minutes in a 12.4 hour cell cycle.

## 4.1 Introduction

Morphological analysis is a key tool in kinetoplastid research due to these cells' high heterogeneity and their poor compatibility with traditional methods of analysis (such as single cell sequencing and flow cytometric analysis of biomarkers). As *Leishmania* regulates its molecular processes though post-translational modifications of proteins (as opposed to gene transcription), most proteins are present at all cell or life cycle stages [300]. As such, morphological assessment of these parasites remains a primary indicator of cell health, differentiation status, protein function and cell cycle stage [125], [131], [235], [253], [301].

Analysing cell health through morphology is commonly used for assessing the toxicity of potential drug treatments, with cytotoxic drugs causing aberrations in cell shape [302], [303]. Such work is often supplemented with the use of fluorescent dyes to show DNA damage, and alterations in cell ultrastructure and membrane potential [304]–[307]. Along with the promastigote's location within the sandfly, morphological analysis is the gold standard for classifying cells based on their life cycle stage due to a lack of distinct and widely accepted biomarkers [97], [101], [102], [275], [301], [308]–[310].

The recent improvements and widespread accessibility of CRISPR in *Leishmania* has enabled the functional analysis of individual proteins [236]. The knockout of genes often result in phenotype changes which alludes to the function of the encoding protein. On the other hand, the fusion of proteins with fluorescent tags provides information on their localisation and/or translocation within a cell [131], [145], [233], [235], [311], [312]. A prime example of this is the work done by Baker *et al.* who carried out a functional screen of protein kinases, systematically tagging and knocking out 204 genes from *L. mexicana's* genome [131]. For each cell line successfully generated, the authors demonstrated fluorescence localisation to one (or more) of 11 locations, such as the nucleus, the mitochondria, or the cytoplasm. A few proteins were also described to have cell cycle dependent localisations such as PKAC1 which localised to the nucleus early in the cell cycle, and the cytoplasm and flagellum in the later stages. Finally, as discussed in Section 1.2, the shape of *Leishmania* is intrinsically linked to its stage in the cell cycle with cells experiencing changes to their length and width throughout this process.

Despite the wide range of applications requiring morphological analysis, there is a paucity in tools available for morphological characterisation, relying predominantly on microscopy. While it is indisputable that microscopy can provide information in a stunning amount of depth and resolution, its labour intensive and low throughput nature limits the number of cells that can be analysed and the types of studies which can be carried out. For example, the morphology of cells with induced gene knockouts commonly results in morphological changes [235], [313], [314], yet for high content studies such as that done by Baker *et al.*, minimal information was provided on the effect of the knockouts on the size or shape of the resulting cell lines, presumably due to the lengthy times associated with carrying out manual measurements. Another example where morphological assessment is often lacking is cell cycle analysis, which sees cells progress through many morphological changes at varying rates, resulting in large proportions of cells in G1 and S phases which obscure rarer populations such as G2. Therefore, building on the work which was carried out in Chapter 3, the aim here was to combine the developed DNA-quantification protocols with IFC-based morphological analysis to improve cell cycle analysis.

While IFC has previously been used to analyse the morphology of many cell types, the vast majority of work has been carried out on spherical cells, such as for analysing the prevalence of fluorescent spots, the automatic classification of sub-populations of cells and for the identification/characterisation of unreported cell types. Analysis of fluorescent spots has been used in cytotoxicity assays for the identification of micronuclei [315]–[317], visualisation of chromosomal defects with fluorescence in situ hybridization (FISH) assays [318]–[320], and particle internalisation assays such as analysing the infection of phagocytes [321], [322]. On the other hand, identification of sub-populations of cells often uses a combination of stains and morphological features as physical biomarkers. McGrath *et al.* discussed the use of IFC for identifying the maturation stage of haematopoietic cells based on the intensity of both BF and fluorescence images and dye localisation [323]. Johnson describes previously unidentified populations of platelets in cryopreserved samples [324], while various studies have used the high-throughput nature of IFC to identify rare populations of cells such as circulating endothelial cells or very small embryonic-like stem cells [325]–[327].

In contrast, the application IFC to analyse cell shape is less well documented. A study using stallion sperm showed that there was a relationship between reactive oxygen species production, and the prevalence of morphological defects. While this study analysed identified populations of cells by their morphology, the analysis was carried out manually with only 900 cells being analysed in total for 5 different stallions [328]. The morphology of the apicomplexan parasite *Eimeria tenella* was analysed under different incubation temperatures, having an increased aspect ratio at higher temperatures [329]. Aspect ratio has also been shown to be an identifier of pseudopod formation [330]. Classification of algae and phytoplankton has been attempted based on their morphologies to various degrees of success; however, such studies have proved to be difficult due to the high number of species and the heterogeneity associated with these organisms [331]–[333]. In such scenarios, machine learning and/or AI has been employed to assist with the automatic classification of cells based on their corresponding images. However, this often leads to issues, such as requiring training the model on known cell types, or having low levels of certainty during classification [334]. The differentiation of *Leishmania donovanii* has been tracked over time, analysing cells based on their symmetry *vs* their aspect ratio for classification into “round”, “oval” and “elongated”. Finally, the most relevant to this thesis is the work done in yeast. Here, the authors use cell morphology and DNA staining (using SYTOX) to identify different cells in G1, S and G2/M. They further demonstrate that by knocking out or overexpressing *nap1* the proportions of cells in G2/M were altered, along with the proportions of budding yeast [269].

In this chapter, the morphology of live *L. mexicana* with different DNA content was assessed using IFC to understand the relationship between the parasite’s shape and its stage in the cell cycle. It was demonstrated that by combining morphological analysis and DNA content that a higher level of resolution can be achieved than either by flow cytometry or microscopy alone, in a high-throughput manner. This understanding of morphology was then applied to cells expression a fluorescent tag on the spindle-associated kinase KINF, which enabled, for the first time, the quantification of the elusive G2 phase of the cell cycle in *L. mexicana* cells.

## 4.2 Results and discussion

### 4.2.1 There is high overlap in morphological parameters between populations classified using DNA content alone

Once a suitable protocol had been developed for the quantitative staining of DNA (Section 3.2.3), it was used to identify each individual cells’ stage in the cell cycle. As previously mentioned (Section 3.1), there are traditionally two ways in which this is achieved: by counting the number of nuclei and kinetoplasts; and through DNA quantification to identify 2C, Int. and 4C populations. As the ImageStream® uses both images and DNA quantification, it has the potential to classify cells using both methods, providing a higher level of resolution than either method in isolation. Initially, an attempt was made to mask nuclei and kinetoplasts to automate the counting of these organelles. While masks could be made to separately identify nuclei and kinetoplasts (Fig. 4.1A), they were not robust enough to provide accurate quantification on the number of organelles (Fig. 4.1B). The primary complications were the heterogeneity in presentation of the DCO fluorescence (differences in the brightness of nuclei due to e.g. differences in focus) and cell orientation; during ImageSteam analysis cells occasionally rotated and aligned in such a manner that their nuclei and kinetoplast overlapped. The resulting variation in the images resulted in inconsistent masking, for example, a mask was developed to identify just the kinetoplast; however, in a proportion of cells it identified both the nucleus and the kinetoplast (Fig. 4.1A and B).

While accurate quantification of the dots was difficult, the application of masks on the DNA was still able to provide insight into the dynamics of the cell cycle. It has previously been shown that the distance between the nucleus and the kinetoplast is linked to a cells stage in the cell cycle, with a higher distance being seen for longer cells [125]. The "delta centroid XY" feature calculates the centre position of two separate masks. Thus, here, the delta centroid XY feature was used to calculate the distance between the nucleus and the kinetoplast mask (Fig. 4.1C). In a situation where there are two nuclei in one cell, the average location between the two nuclei is taken. In agreement with the literature, a positive correlation was seen between the length of cells and the distance between their nucleus and kinetoplast; however, instead of analysing only 980 cells [125], here, 13,920 cells were analysed.

As masking on DNA proved to be unsuitable for automated cell cycle classification, instead, manual gates were drawn on the DCO intensity profiles to identify 2C, Int. and 4C peaks (Fig. 4.2A). The percentage of cells in each of these gates was plotted in figure 4.2B. However, gating on the DNA fluorescence intensity alone is known to be inadequate for cell cycle classification in that it does not account for the overlap seen between the stages [335]. Thus, it was hypothesised that cell morphology, instead of nucleus and kinetoplast analysis, may provide a means to further improve classification from the knowledge that the length and the width of cells change in a predictable manner during the course of the cell cycle. To take advantage of the ImageStream's capabilities, thirteen different morphological parameters were

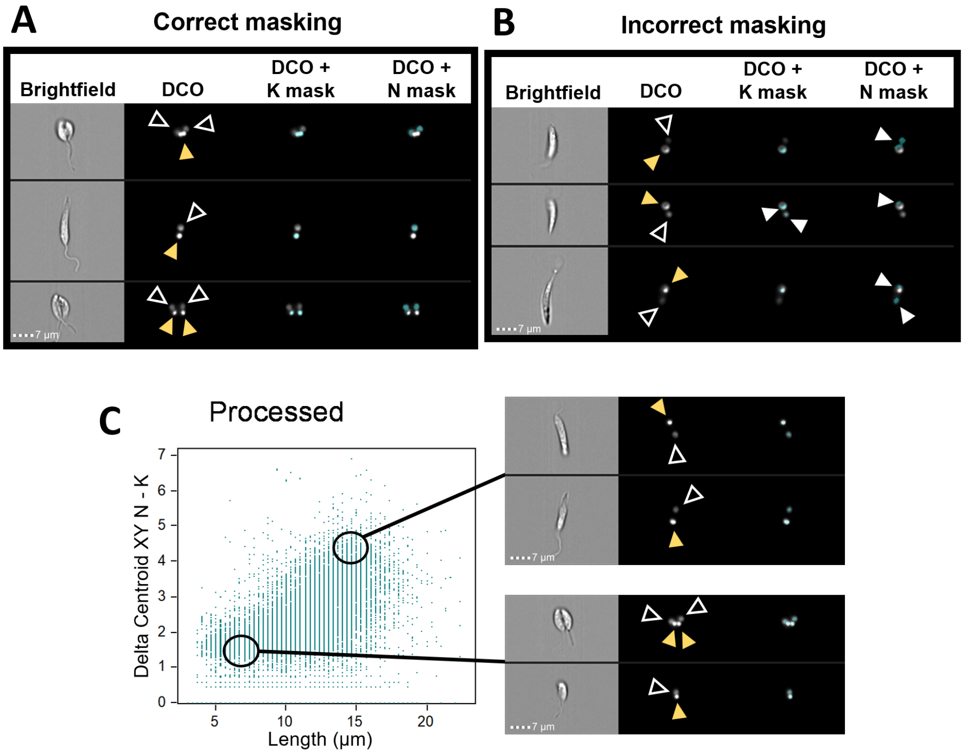

**Figure 4.1: Masks were unable to robustly distinguish the nuclei and kinetoplasts.** DCO-stained mid-log *L. mexicana* C9T7 cells were acquired by IFC and analysed in IDEAS™. Brightfield images are shown with their corresponding DCO fluorescence. Two masks are displayed, developed to identify either nuclei (N; black arrowheads with white outlines) or kinetoplasts (K; yellow arrowheads). Example images are shown where the mask accurately (A) or incorrectly (B) identifies the organelles of interest. The first row in (B) have a N mask which includes the kinetoplast. The second row shows a cell where both the N and K is identified as K, as well as the N and the K being identified by the K mask. The mask in the final row identifies both the N and K as N. White arrowheads indicate incorrect masking. (C) Using the delta centroid XY feature, the centre point of both the N and the K mask was identified (the centre point between two masks was calculated if the cell had e.g. two N) and the distance between the two centre points was measured. This was plotted as a function of cell length. Example images of cells with different organelle distances are shown on the right, and the region of the dot plot where they are located is marked with black circles.

calculated for each gated population. Details of how the parameters were calculated can be found in Section 2.2.5. Receiver operating characteristic (ROC) curves (Fig. 4.2C-E) were used to assess how well a particular parameter was able to distinguish an individual cell cycle stage – the further away the parameter from the central dotted line, the higher the correlation between that parameter and the defined cell cycle stage. Note that area and diameter measurements are so similar in their calculation that their curves overlap completely, appearing as only the diameter line. The ability of a parameter to identify a cell cycle stage was then quantified by calculating the area under the curve (AUC). From the ROC curves and the AUC values, it can be seen that all parameters varied in their ability to distinguish different cell cycle stages (Fig. 4.2C-F). For cells with 2C DNA content, area and diameter seem to be the best identifying features (AUC values of 0.23); for Int. DNA content cells area, diameter, height, and length all have AUC values of 0.68; while the width has the highest potential for distinguishing 4C DNA content cells from the other cell cycle stages, with an AUC of 0.74. However, the AUC values with the highest deviation from 0.5 were 0.23, 0.68 and 0.74 for 2C, Int. and 4C DNA content cells, respectively, indicating still a relatively high overlap in morphologies between all cell cycle stages.

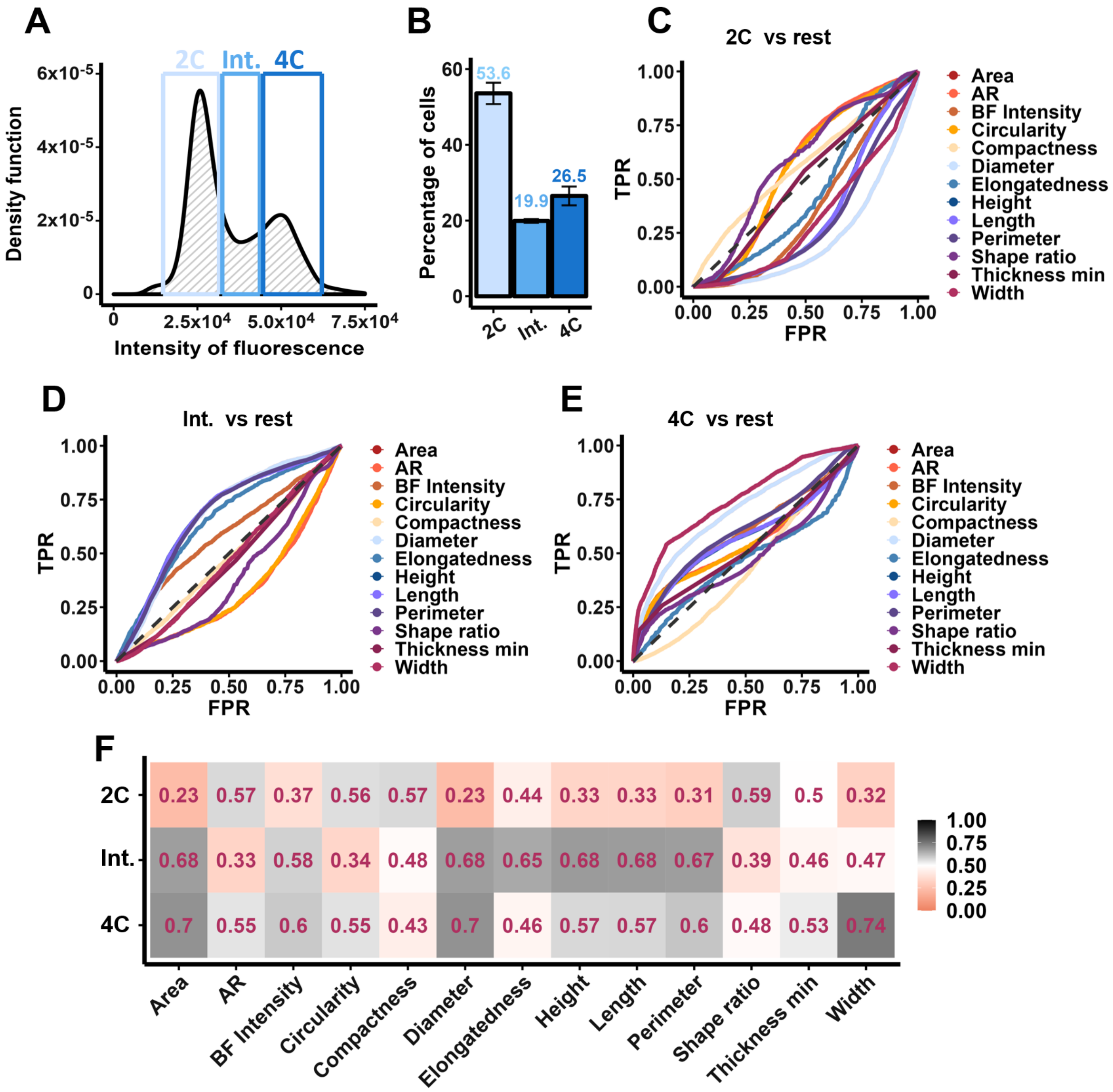

| | Area | AR | BF Intensity | Circularity | Compactness | Diameter | Elongatedness | Height | Length | Perimeter | Shape ratio | Thickness min | Width |
|---|---|---|---|---|---|---|---|---|---|---|---|---|---|
| 2C | 0.23 | 0.57 | 0.37 | 0.56 | 0.57 | 0.23 | 0.44 | 0.33 | 0.33 | 0.31 | 0.59 | 0.5 | 0.32 |
| Int. | 0.68 | 0.33 | 0.58 | 0.34 | 0.48 | 0.68 | 0.65 | 0.68 | 0.68 | 0.67 | 0.39 | 0.46 | 0.47 |
| 4C | 0.7 | 0.55 | 0.6 | 0.55 | 0.43 | 0.7 | 0.46 | 0.57 | 0.57 | 0.6 | 0.48 | 0.53 | 0.74 |

**Figure 4.2: When using manual gating alone, the cell cycle stages are morphologically similar.**

(A) Manual gating was carried out on the DNA profile acquired by IFC analysis of DCO-stained mid-log *L. mexicana* C9T7 cells. Gating identified the 2C, Int. and 4C peaks from the DNA profile, with (B) showing the percentage of cells in each gate. The error bars show the standard error across three replicates. (C-E) Receiver operating characteristic (ROC) curves of 13 morphological parameters were plotted for 2C-, Int.- and 4C-gated populations. For each parameter, the true positive rate (TPR) was defined as the probability that a cell, at a particular measurement, would be in the defined population (i.e. the 2C gated population). The false positive rate (FPR) was thus the probability that a cell, at a particular measurement, would in a different population (i.e. the rest). The dashed grey lines indicate a curve where there is no distinction in morphology between the defined cell cycle stage and the other cell cycle stages. (F) A heatmap of the area under the curve (AUC) values as calculated from the ROC curves for each cell cycle stage, for each morphological parameter. A value close to 0.5 (white) demonstrates parameters with a high overlap in the measured distributions between the defined cell cycle stage and the rest. In contrast, a value closer to 1 (black) or 0 (peach) identify parameters with a high deviation in distribution between the defined cell cycle stage and the rest, where the defined cell cycle stage measures higher or lower than the rest of the cells, respectively ($n$ = 13,920)

### 4.2.2 Cell cycle analysis is improved when including morphological measurements

When looking at the distribution of the individual morphological parameters, it was noted that elongatedness, length and perimeter showed a bimodal distribution for the 4C-gated population (Fig. 4.3A-C). Interestingly, for all three plotted parameters, the second peak of this distribution overlaps with the peak of the Int.-gated cells. As length has previously been shown to be related to cell cycle stage [125], this parameter was selected for further analysis. Visual inspection of cells within peak 2 (Fig. 4.3D) showed that longer 4C-gated cells had a morphology associated with that of S phase (elongated cells with 1N1K1F), consistent with cells in the Int. gate. In contrast, the majority ($\sim$ 80%) of the shorter 4C DNA content cells (peak 1, Fig. 4.3D) were in mitosis (2N1K1F) and cytokinesis (2N2K2F). From these data and visual inspection of the cells, a threshold of 10 µm was defined to separate the 4C-gated population into short ($\leq$ 10 µm) M/C cells and long (> 10 µm) S phase cells. At this stage, it was difficult to determine which population(s) contained G2 cells, as in *L. mexicana* this stage had yet to be precisely defined with its presence still mainly being inferred from studies in other organisms [125], [133], [162], [336], [337]. The classification of G2 is discussed later in Section 4.2.6. The resulting M/C population accounted for 9.6% of the population, in line with results previously obtained *via* microscopy [125]. The same 10 µm threshold was also applied to the Int. population (Fig. 4.3E). As S phase cells are known to be the longest cells, and in view of overlap between cells in the Int. gates and both the 2C and 4C gates, it was postulated that the short Int. gated cells in reality corresponded to cells in G1 and M/C cells. As previously described (Section 4.2.2), a higher width measurement is indicative of M/C cells and thus gating on the width was used to differentiate the narrow (< 4 µm) G1 cells from the wide ($\geq$ 4 µm) M/C, which was confirmed by visual inspection of cells (Fig. 4.3F).

While no means could be used to differentiate S phase cells from similarly long G1 cells in the 2C gate, length and width measurements proved to be highly useful parameters for resolving the overlap between cell cycle stages caused by manual gating. This was particularly beneficial for differentiating M/C cells from S phase cells within the 4C gate.

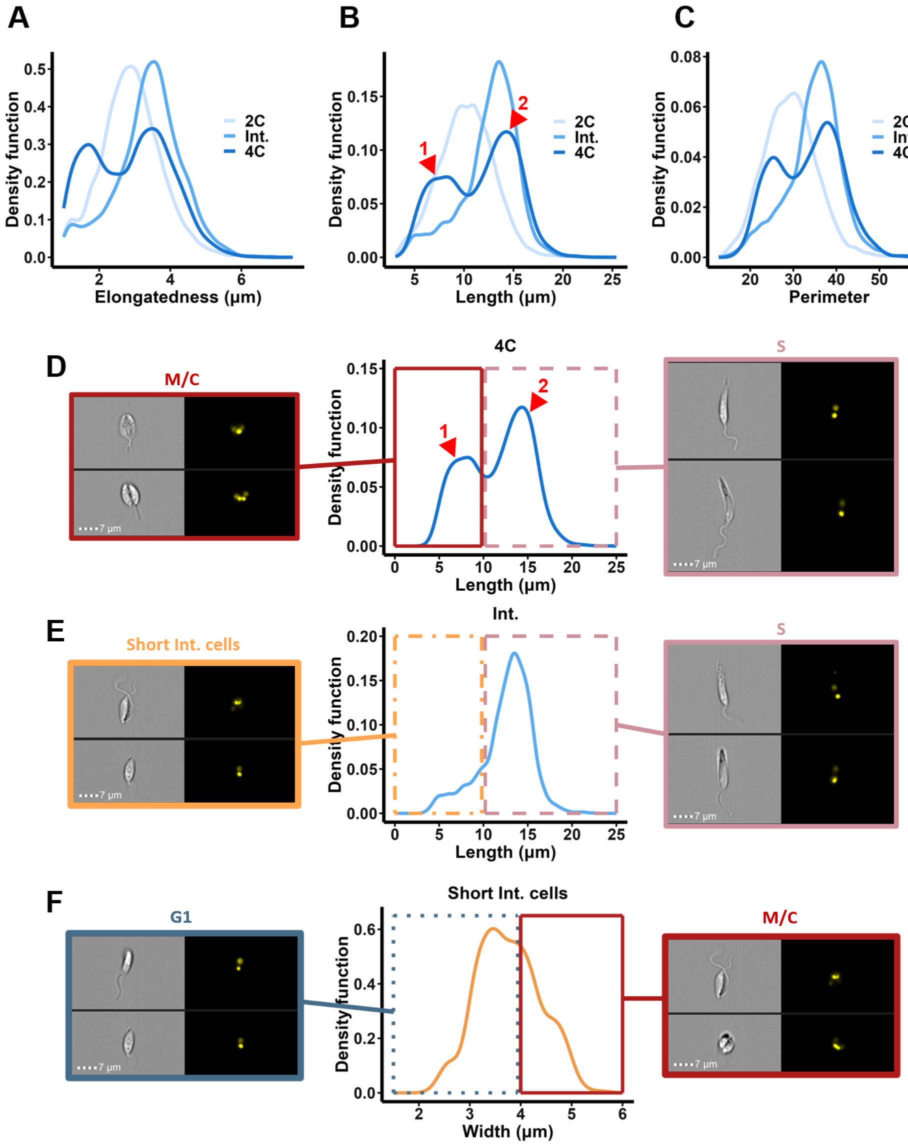

**Figure 4.3: Morphology increases the resolution of cell cycle analysis.** Elongatedness (A), length (B) and perimeter (C) measurements were calculated for the 2C-, Int.- and 4C-gated populations. The red arrowheads indicate the two peaks within the 4C population that were identified for further analysis. (D-E) The 4C and Int. populations were gated on their length – short ($\leq$ 10 µm in length) 4C cells were classified as M/C cells (solid red line gate), and both the long (> 10 µm in length) 4C cells and long Int. cells were classified as S phase (pink dashed line gate). (F) The remaining short Int. population (orange dotted and dashed line gate) was further divided based on their width, with narrow (< 4 µm) cells being classified as G1 (dotted blue line gate) and the wide ($\geq$ 4 µm) cells as M/C (textitn = 13,920) .

### 4.2.3 Morphology is an indicator of cell cycle stage

The outlined gating strategy was hence used to classify cells into G1 (53.6%), S/G2 (36.8%) and G2/M/C (9.6%) phases (Fig. 4.4A and B). There is still inherent overlap between the cell cycle stages; however, compared with the distributions seen when cell cycle modelling is applied (Fig. 3.6A), the method of analysis outlined here achieved individual cell cycle classification in a biologically relevant manner. By taking into consideration the morphology of cells for cell cycle classification, a truer representation of the biological variation was achieved, emphasising that intensity alone is indeed insufficient for the classification of individual cells.

From the resulting populations, the thirteen morphological parameters previously reported (Fig. 4.2) were reassessed for their ability to act as an indicator of cell cycle stage, and thus as the basis for inertial microfluidic sorting. From the ROC curves in figure 4.4C-E, it can be seen that various morphological parameters are further away from the centreline, indicating a high correlation between that parameter and the defined cell cycle stage. While the G1 population did not see much change (the highest deviation in AUC from 0.5 remained the area and diameter measurements at 0.23), due to the low numbers of cells reclassified from the Int. population into the G1 gate, S and M/C cells increased in their maximum AUC from 0.68 to 0.91 area/diameter and 0.74 to 0.95 respectively (Fig. 4.4F). M/C cells are of particular interest in this study; this is a highly dynamic stage of the cell cycle where cells separate their replicated organelles, alluding to highly specific temporal and spatial control mechanisms which are yet to be defined. For these cells, aspect ratio, circularity, elongatedness and width (AUC values of 0.94, 0.95, 0.07 and 0.9, respectively) all gave AUC values with a difference of $\geq$ 0.4 from 0.5, suggesting distinct morphological parameters potentially exploitable for inertial microfluidic-based sorting (Fig. 4.4G-I). In addition to having an AUC $geq$ 0.9, the width and aspect ratio measurements show good separation of of M/C phase cells (compared to G1 and S phase cells) when looking at the morphological distributions (Fig. 4.4H and I). Thus, width and aspect ratio were selected for further analysis, as outlined in Section 4.2.7.

Here, a robust method of cell cycle analysis is provided, giving biologically relevant cell cycle classification in a high-throughput and automated manner, in line with traditional methods of analysis. Additionally, this was taken a step further and improved analysis for the later stages in the cell cycle by defining G2 in *L. mexicana*.

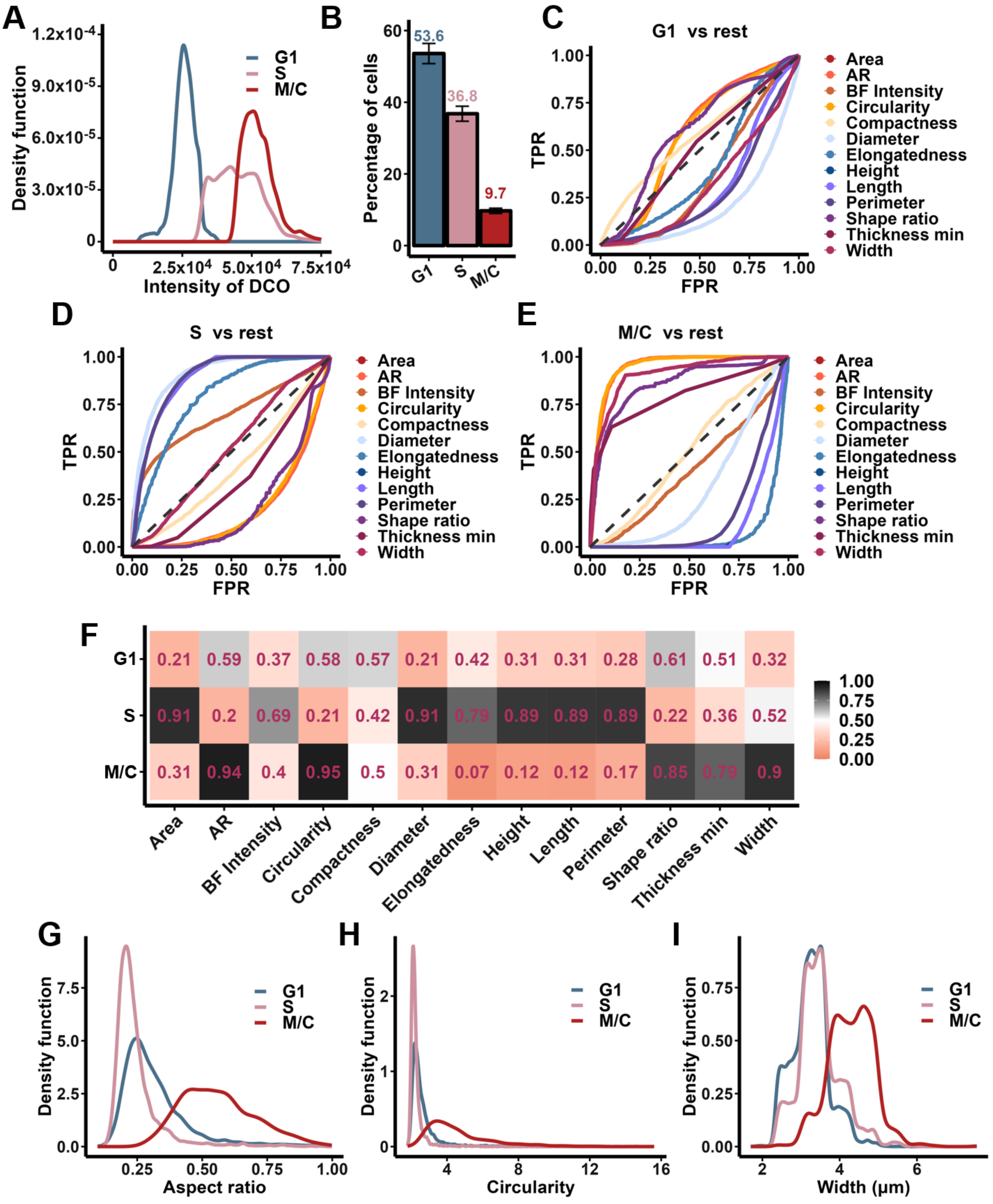

|  | Area | AR | BF Intensity | Circularity | Compactness | Diameter | Elongatedness | Height | Length | Perimeter | Shape ratio | Thickness min | Width |
|---|---|---|---|---|---|---|---|---|---|---|---|---|---|
| G1 | 0.21 | 0.59 | 0.37 | 0.58 | 0.57 | 0.21 | 0.42 | 0.31 | 0.31 | 0.28 | 0.61 | 0.51 | 0.32 |
| S | 0.91 | 0.2 | 0.69 | 0.21 | 0.42 | 0.91 | 0.79 | 0.89 | 0.89 | 0.89 | 0.22 | 0.36 | 0.52 |
| M/C | 0.31 | 0.94 | 0.4 | 0.95 | 0.5 | 0.31 | 0.07 | 0.12 | 0.12 | 0.17 | 0.85 | 0.79 | 0.9 |

**Figure 4.4: Morphology as an indicator of cell cycle stage.**
(A) DCO intensity profile showing cell cycle stage classification based on gating for both DCO intensity, cell length and cell width. (B) The percentages of cells in each of the cell cycle stages when classified based on DCO, and cell length and width. The error bars show the standard error across three replicates. (C-E) Receiver operating characteristic (ROC) curves of 13 morphological parameters for the populations identified in the 2C, Int. and 4C gates. For each parameter, the true positive rate (TPR) was defined as the probability that a cell, at a particular measurement, would be at the defined cell cycle stage. The false positive rate (FPR) was thus the probability that a cell, at a particular measurement, would be classified as a different cell

cycle stage (i.e. the rest). The dashed grey line indicates the ROC curve where no correlation between cell cycle stage and morphology is seen. (F) A heat map of the area under the curve (AUC) values as calculated from the ROC curves for each cell cycle stage. A value close to 0.5 (white) shows a high overlap in the measured distributions between the defined cell cycle stage and the rest, while a value closer to 1 (black) or 0 (peach) identify parameters where the defined cell cycle stage measures higher or lower than the rest of the cells, respectively. The aspect ratio (G), circularity (H) and width (I) of the classified G1, S/G2 and G2/M/C populations were plotted as density plots ($n$ = 13,920).

### 4.2.4 mNG:KINF-based cell cycle analysis in *L. mexicana*

As previously mentioned, G2 is an elusive stage in the cell cycle of *Leishmania spp.*, owing to its rapid nature and paucity of defining features. However, its position between S and M phases serves as a tool for identification, as achieved by da Silva in *L. amazonensis* [337]. In this work, da Silva used BrdU, EdU and DAPI staining to identify cells both at the end of DNA replication and at the end of mitosis. By subtracting the known timings of mitosis (0.59 hours), the duration of G2 was deduced (0.09 units of the cell cycle). In contrast, here the emergence of a second flagellum was used to mark the end of S phase and the formation of a spindle as the beginning of mitosis [125], [126], [337]. This resulted in three criterion which had to be fulfilled for G2 identification: have one nucleus; the presence of a second flagellum; and no spindle. Therefore, in order to identify cells in G2, the spindle first had to be identified. This was achieved by CRISPR-based tagging of KINF, a known spindle-associated marker in *L. mexicana* [244], [338]. The fluorescent marker mNeonGreen (mNG) was inserted upstream of the KINF gene to provide stable fluorescence expression in live cells (Fig. 4.5). The generation of the mNG:KINF cell line and its corresponding growth curves were performed by Sulochana Omwenga, details of which can be found in Section 2.1.2. From the growth curves of the parental C9T7 and mNG:KINF cell lines (Fig. 4.5B), it can be seen that both populations have a fairly comparable growth profile; the densities increase to around 2 x $10^7$ cells.ml$^{-1}$ over the first 48 hours and where they plateau for the next 48 hours. However, it is also seen that in the first 24 hours, the mNG:KINF cells grow faster than the C9T7 cells (with doubling times of 7.1 h and 11.5 h, respectively, as calculated using Equation 2.2). At this stages, the mNG:KINF cells having a highly comparable doubling time to what has been reported in the literature [125]. While this was the case, the time period between 24 and 48 hours was selected for calculating the doubling time as this is where the parental line grows the fastest, resulting in doubling times of 8.5 h and 12.4 h for the parental C9T7 and mNG:KINF cells, respectively. In order to confirm that the differences in growth rates did not affect cell cycle progression, the proportions of cells in each of the different cell cycle stages was compared between the parental C9T7 and mNG:KINF cell lines using DCO staining. More information regarding the staining of the mNG:KINF cells with DCO is given in Section 4.2.6. If the mNG:KINF tag affected cell cycle progression, then this would be reflected in the relative proportions of cells in each of the cell cycle stages. For example, if the synthesis of DNA was affected, then this may prevent cells from progressing to G2/M/C phases and would thus result in an increase in the proportion of cells in S phase, and a decrease of cells in G2/M/C. From figure 4.5C it can be seen that while there is a fairly high amount of variations between replicates (potentially due to slight differences in the quantity of DCO added to each sample), the proportions of cells in each of the peaks are comparable between the parental C9T7 cells and the mNG:KINF line, suggesting that the mNG:KINF tag has minimal effects on cell cycle progression.

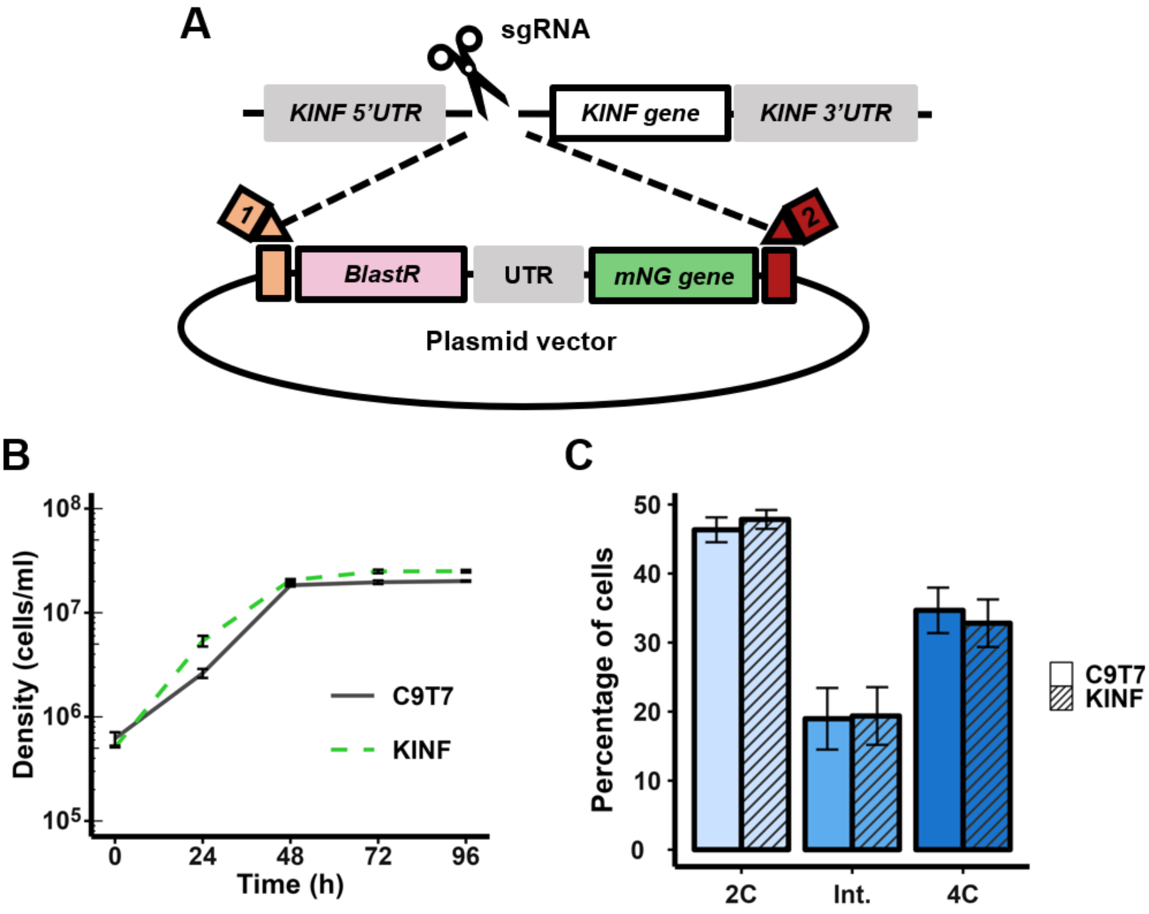

**Figure 4.5: Generation and growth of the mNG:KINF cell line.**
(A) Diagram representing the insertion of the mNG gene into the genome of the *L. mexicana* C9T7 cell line. The DNA sequence between the forward (1) and reverse (2) primers (details of which can be found in Section 2.1.1) was amplified during the PCR reaction of the donor DNA. This contained a gene for conferring blasticidin resistance (BlastR), an untranslated region (UTR) and a gene for encoding the mNG fusion protein. During transfection, the amplified single guide RNA (sgRNA) directed the Cas9 complex to create a double stranded break into the genome of *L. mexicana* C9T7 cells upstream (5') of the KINF gene. Cells that successfully integrated into the donor DNA at the location of the double stranded DNA break were subsequently blasticidin resistant, and expressed mNG:KINF. Image adapted from Beneke *et al.* (2017). (B) The growth of a single clone of the subsequent *L. mexicana* C9T7:mNG:KINF cell line (green dashed line) was compared to that of the parental C9T7 cell line (black solid line). Three flasks were prepared for each cell line and their corresponding densities were calculated every 24 hours and plotted as a growth curve. The error bars show the standard error for three replicates. (C) Both the parental C9T7 cells and the mNG:KINF cells were stained with DCO, analysed by IFC, and the DNA profiles manually gated to identify the percentages of cells in the 2C, Int. and 4C peaks. The error bars show the standard error for three replicates ($n \geq 8{,}624$).

In order to use mNG:KINF as a proxy for the spindle, Omwenga first confirmed by immunofluorescence analysis (IFA) that mNG:KINF co-localised with the spindle (Fig. 4.6). Similarly to the work done by Ambit *et al.*, the β-tubulin antibody KMX was used as a positive control to stain the spindle during mitosis, while an anti-mNG antibody was used for mNG:KINF identification. The parental C9T7 cell line was used as a control for background staining (Fig. 4.6A); staining with KMX and anti-mNG antibodies resulted in diffuse staining throughout the cytoplasm/cytoskeleton. As KMX stains β-tubulin (which is found soluble in the cytoplasm and comprises the cytoskeleton as well as the spindle), staining can be seen in all images. Similarly to the literature [244], mNG:KINF expression was seen in cells in cell cycle stages outwith just mitosis, with a single spot of fluorescence localisation being seen in early G1, late S and G2 phases (Fig, 4.6B, E and F, respectively). This focus of mNG:KINF expression in the nucleus was seemingly lost in cells later in G1 and/or S phases. The initial formation of the spindle can be seen in figure 4.6G, as identified *via* KMX staining in a cell with 1N1K2F. In cells further through mitosis with 2K, the spindle had an elongated shape, spanning the dividing nucleus (Fig. 4.6H). In all cells with elongated KMX staining, an elongated focus of mNG:KINF was also seen. During cytokinesis in cells with a 2N2K configuration (Fig. 4.6I), KMX staining of the spindle was no longer visible and instead an invaginating furrow can be seen cleaving the cell in two. In contrast, the mNG:KINF fluorescence was still clearly visible in these cells undergoing cytokinesis, localising to both daughter nuclei (Fig. 4.6I).

From these data, it was confirmed that mNG:KINF localised to, and thus acted as a proxy for, spindle identification. Additionally, four different presentations of mNG:KINF expression were deduced: no mNG:KINF fluorescence (mNG-), one single circular focus (1CF), an elongated focus corresponding to the spindle and two circular foci (2CF). The identification of the spindle in this way this acts as a marker for mitosis, with mNG:KINF foci localising to the nucleus at various points in the cell cycle.

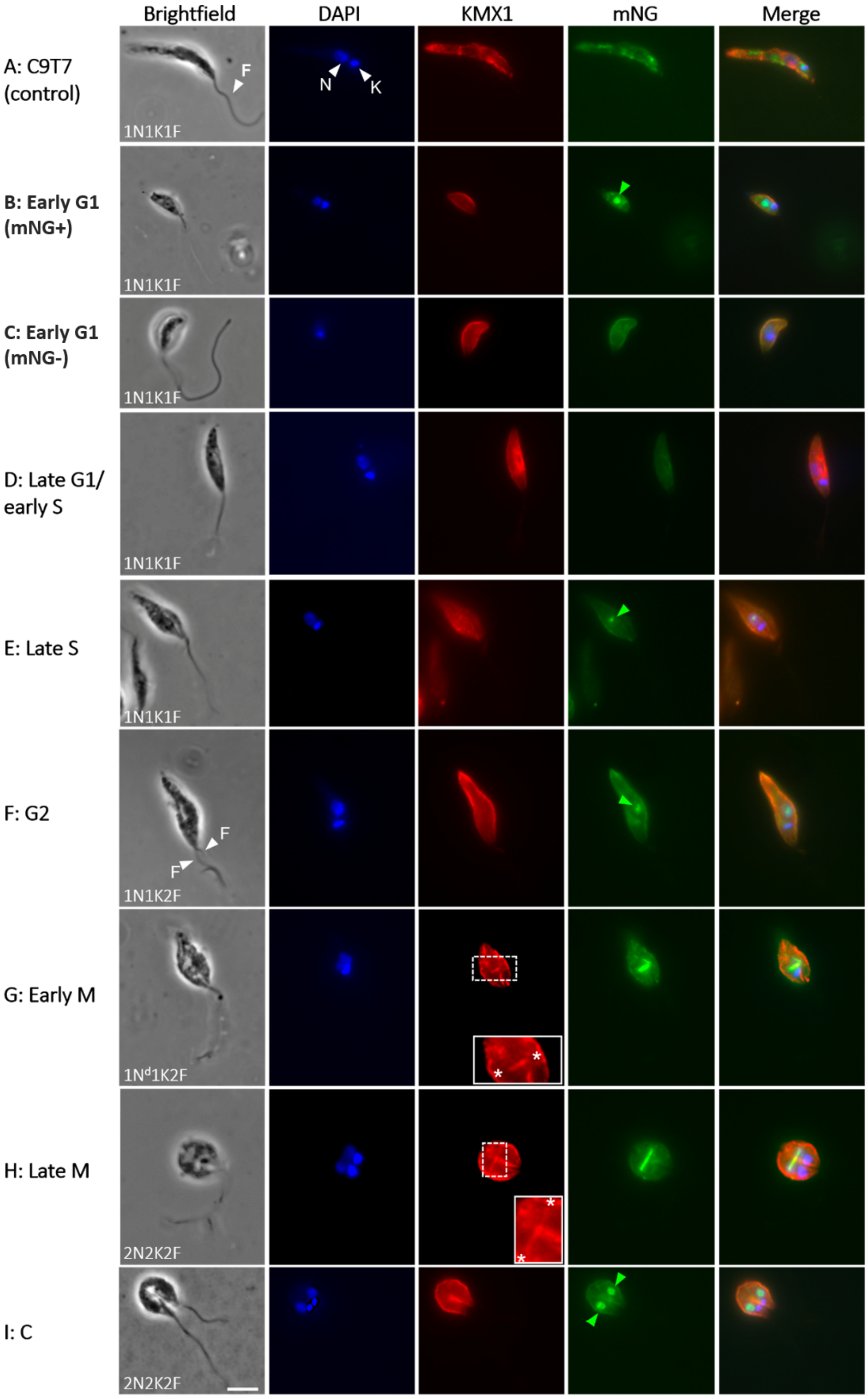

**Figure 4.6: mNG:KINF co-localises with the spindle .**
IFA of MeOH-fixed *L. mexicana* promastigote C9T7 cells (A) and C9T7 mNG:KINF cells (B-I) Panels from left to right: brightfield images; DNA stained with DAPI; β-tubulin stained with KMX; mNG:KINF stained with anti-mNG and a composite fluorescence image. The mNG:KINF cells were classified into their cell cycle stage as defined by their number of nuclei (N), kinetoplasts (K) flagella (F) (identified with white arrowheads) and mNG:KINF presentation (mNG:KINF positive; mNG+, no mNG:KINF fluorescence; mNG-, and the presence of a spindle). Spindles, as identified *via* KMX staining (dashed white boxes), have been enlarged in G and H (solid white box), with the ends of the spindle being marked with *. The green arrowheads show the localisation of mNG:KINF. Scale bar: 5 µm.

Generally, fluorescent proteins with a cell-cycle dependent expression are time consuming to analyse. With microscopy, hundreds if not thousands of cells have to be scored based on their fluorescence to identify the cells of interest. In flow cytometry analysing heterogenous fluorescence is unachievable as there is no spatial information to distinguish the different types of presentation. In contrast, this same cell cycle-dependent presentation can be taken advantage of using IFC; automatic classification of cell types based on fluorescence localisation reduces the need for additional markers of cell cycle stage. Thus, using mNG:KINF and morphological information, automatic classification of cells into early G1, late G1/S, late S, mitosis and cytokinesis was achieved, which subsequently enabled the manual identification and quantification of G2 cells.

Live mNG:KINF promastigotes were analysed with IFC (Fig. 4.7A). From the images the contrast with IFA is apparent, with cells having clear nuclear localisation without background fluorescence and cell morphology remaining intact. Manual inspection of the mNG:KINF fluorescent images confirmed the presence of all four previously identified cell cycle-dependent expressions. A mask was subsequently developed to identify the mNG:KINF fluorescence, capable of distinguishing all four localisation patterns (see Section 2.2.5 for details). This mask was much more robust than masking on DNA staining due to the homogeneity of fluorescence in a single image, as opposed to differentiating the nucleus and kinetoplast based on intensity of fluorescence. Prior to cell classification being carried out, analysis of cell morphology of the C9T7 mNG:KINF cell line revealed that the tagging of KINF had not affected morphology, as compared to the parental control, suggesting that the previously identified morphological thresholds (thresholds of 10 μm on length and 4 μm on width) indicative of cell cycle stage were still applicable (Fig. 4.7B).

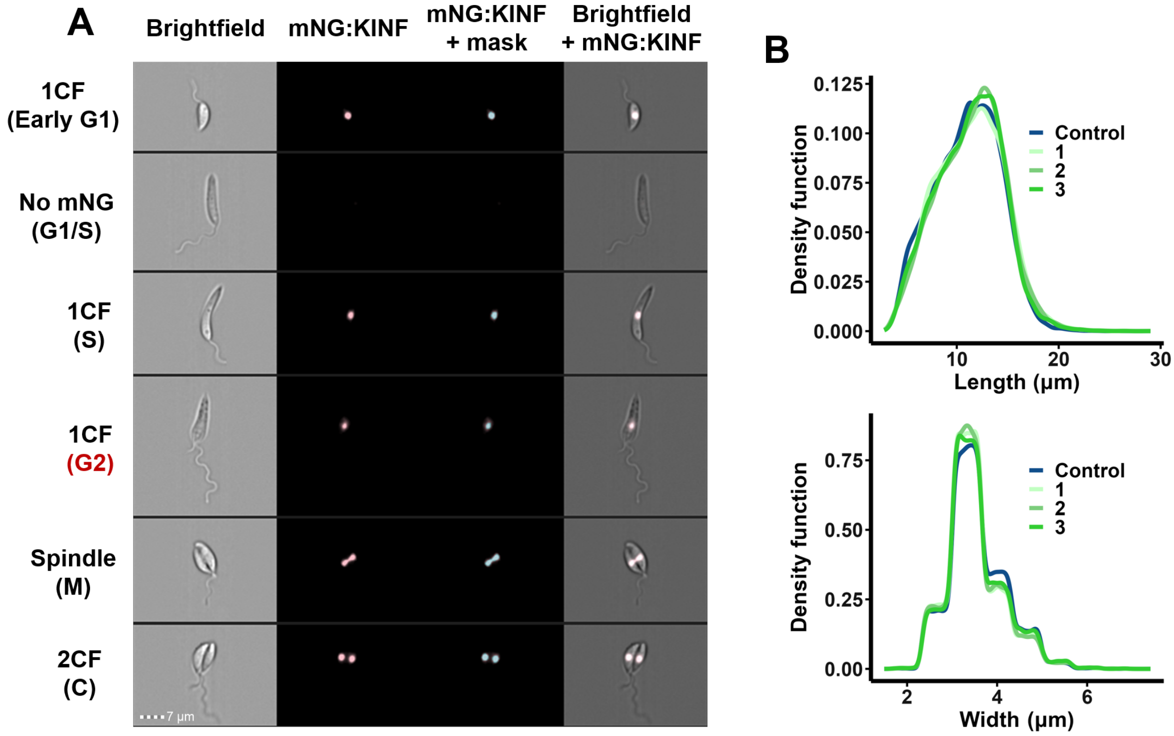

**Figure 4.7: ImageStream® based validation of mNG:KINF presentation.** (A) Example ImageStream® images of the C9T7 mNG:KINF cell line, showing the four different presentations of fluorescence: no mNG:KINF fluorescence (mNG-), one circular focus (1CF), an elongated focus (spindle), and two circular foci (2CF). The panels from left to right show the BF image, mNG:KINF expression, mNG:KINF expression with the applied mNG:KINF mask and composite images overlaying the BF and mNG:KINF images. (B) Length and width measurements of mid-log cultures of *L. mexicana* C9T7:mNG:KINF cells were taken in triplicate (1-3), and compared to the dimensions of a control population of the parental *L. mexicana* C9T7 cells (*n* $\leq$14,245). The length and width measurements were analysed by IFC, and the data was smoothed and plotted in R (see Section 2.2.5 for details). Scale bar: 7 µm.

### 4.2.5 Cell cycle classification using mNG:KINF and morphology

Using the mNG:KINF fluorescence mask, a gating strategy was developed to automatically classify the C9T7 mNG:KINF cells into the predefined expression patters of no mNG:KINF, 1CF, spindle, and 2CF. A schematic outlining the classification system is shown in figure 4.8A – initial preprocessing of the data was carried out as described in Section 2.2.5. From the "processed" population, a threshold on fluorescence intensity was set using parental C9T7 to identify mNG:KINF positive cells *vs* cells with no mNG:KINF fluorescence. From the mNG:KINF expressing cells, the spot count function was applied to identify cells with two mNG:KINF masks (the 2CF population) or one mask (one focus). Cells with one focus were further gated on their aspect ratio intensity (ARI). This measures the difference in intensity between the mask's major and minor axis, with elongated signals having a lower ARI; after visual inspection, cells with an ARI < 0.62 were classed as having a spindle. Values above this were considered as having 1CF. The distribution of these four populations can be seen in figure 4.8B. Each of these populations were further classified by morphology using the thresholds previously identified in Section 4.2.2. Each cell was assigned one of four morphological categories – short and narrow (SN), short and wide (SW), long and narrow (LN), and long and wide (LW), with short being $\leq$ 10 µm, long as > 10 µm, narrow being < 4 µm and wide being $\geq$ 4 µm. Each population was visually inspected and with mNG:KINF tagging acting as a proxy for nuclear staining and spindle formation and was assigned a cell cycle stage (Fig. 4.8C). All populations were classified into a single cell cycle stage with the exception of the four populations: no mNG:KINF SW, 2CF SN, 2CF LN and 2CF LW. The largest of these was no mNG:KINF SW at 5.9% of the total population, consisting of a mixture of cells in early G1, mitosis, post-mitotic cells, debris and aberrant/dead cells. The 2CF SN and 2CF LN populations possessed a small extra-nuclear dot of mNG:KINF fluorescence in the region of the kinetoplast while 2CF LW images predominantly contained two cells which were masked incorrectly. These four populations were subsequently removed from analysis.

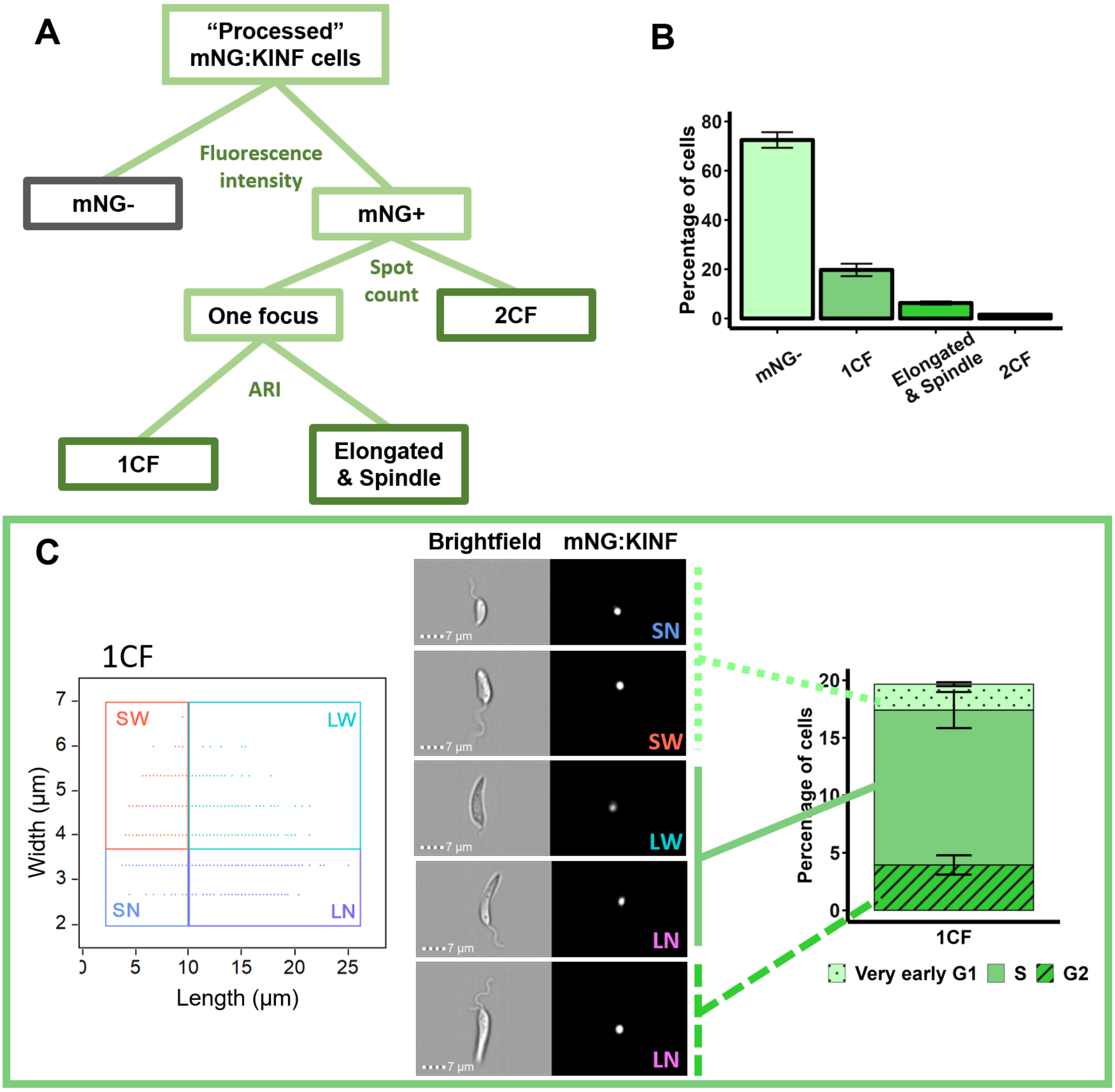

**Figure 4.8: ImageStream® based classification of mNG:KINF presentation.**
(A) Flow diagram of cell classification based on the four patterns of mNG:KINF expression, as analysed by IFC. The standardised and KINF gating strategies outlined in Section 2.2.5 were applied to the data files. From the mNG:KINF "processed" population, cells were classified based on their mNG:KINF expression. The populations were first gated based on their intensity of mNG:KINF fluorescence into having no mNG:KINF (mNG-) or expressing mNG:KINF (mNG+). The number of fluorescent spots of the mNG population was analysed using the spot count feature, identifying cells with one focus of mNG:KINF fluorescence or two (2CF). Finally, the aspect ratio intensity (ARI) of the fluorescence focus was analysed in cells with one focus, with cells with an ARI $\geq$ 0.62 being classified as having one circular focus (1CF), and cells with an ARI < 0.62 being noted as having an elongated focus or a spindle. Dark outlined boxes (grey and green) represent the four classifications of the mNG:KINF cells. (B) The percentage of cells in each of the four resulting populations was calculated ($n \geq$ 14,245 per replicate). Error bars show the standard error across three replicates. (C) The four populations of cells classified based on their mNG:KINF expression were each gated based on their length and width into short (S; $\leq$ 10 µm in length) or long (L; > 10 µm in length) and narrow (N; < 4 µm in width) or wide (W; $\geq$ 4 µm in width).

Left: an example of this classification is given using cells with 1CF. The four populations were identified in IDEAs. Middle: corresponding brightfield and mNG:KINF fluorescence images are given for each morphological category. From the resulting populations, cells were classified into the different cell cycle stages based on their mNG:KINF fluorescence and their morphology. G2 cells were manually identified as outlined in Section 2.2.5 as having two flagella and 1CF of mNG:KINF fluorescence. Right: the percentage of cells classified into each cell cycle stage are given for 1CF cells ($n \geq 2,492$ per replicate). Error bars show the standard error across three replicates.

### 4.2.6 Defining G2 in *L. mexicana*

Once all the *L. mexicana* C9T7:mNG:KINF cells had been classified, an attempt was made to identify the G2 population, consisting of cells with 1CF expression (i.e. no spindle) and the presence of a second flagellum. Firstly, the 1CF SW population was analysed; due to a lack of a spindle and only 1CF of fluorescence, these cells had not yet progressed to mitosis or cytokinesis. As previously shown in figure 4.3, a SW morphology was indicative of cells later in the cell cycle with a 4C DNA content, thus it was hypothesised that the 1CF SW cells were in G2. On visual inspection of this population, the majority (average of 79.9%) of the 1CF SW population had two flagella, confirming that they were indeed G2 cells. In addition, a small proportion of 1CF SW cells were either in early G1 (average of 11.7%; SW but one flagellum) or cytokinesis (average of 8.4%; displaying 2CF but which had been misclassified due to incorrect masking) (Fig. 4.9A). These early G1 and 2CF cells were manually identified within the 1CF SW population and reclassified accordingly, with the remaining 1CF SW cells with two flagella being classified as G2. G2 cells were also manually identified from the 1CF SN, LN and LW populations as having 1CF and two flagella, indicating that G2 cells accounted for 3.9% of the total population. As expected, G2 cells spanned a range of morphologies (Fig. 4.9B) but were predominantly (74.5%) short and wide, suggesting that G2 cells would be included in a sorted population with a threshold of $\geq 4$ µm. Furthermore, these results indicated that the G2 cells were associated with both the S and M/C populations during DCO-based cell cycle analysis.

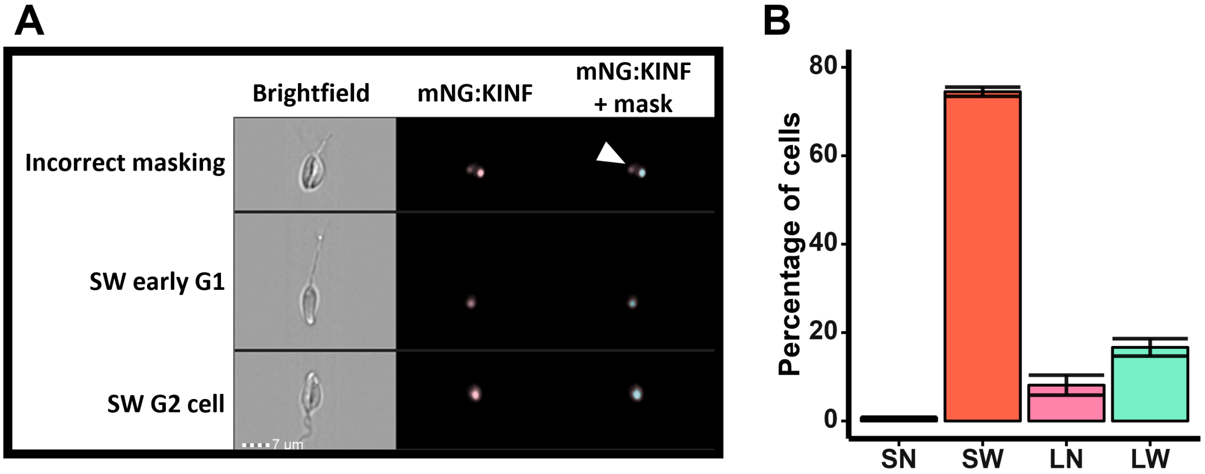

**Figure 4.9: Identification of G2 cells.**
A) Example IFC images of cells within the short and wide (SW) population with one circular focus (1CF) of mNG:KINF fluorescence. While the majority of these cells demonstrated 1CF and had two flagella (classed as G2 cells), this population also contained a subset of SW cells with incorrect masking of the mNG:KINF fluorescence, with only one focus being masked, as well as a population of SW 1CF cells with one flagella (early G1). The white arrowhead indicates the mNG:KINF focus which has failed to be identified by the mask. Scale bar: 7 µm. (B) The percentage of G2 cells classified as short (S; $\leq$ 10 µm in length) or long (L; > 10 µm in length) and narrow (N; < 4 µm in width) or wide (W; $\geq$ 4 µm in width) was plotted, with the error bars showing the standard error across three replicates ($n \geq 455$).

The resulting cell cycle classification gave detailed information about the later stages of the cell cycle; however, this method of classification resulted in poor segregation of cells in G1 and S phases; both of these cell types presented as > 10 µm in length, have no mNG:KINF fluorescence and one flagellum, with no visibly distinguishing characteristics. Here, this population accounted for $\sim$ 55% of cells. Therefore the DCO-based method of cell cycle analysis outlined earlier in this chapter was applied to the mNG:KINF cell line to better determine the proportions of cells in G1 and S phases. As the ImageStream® is capable of analysing both orange and green fluorescent tags, an attempt was made to simultaneously analyse the DCO staining and the mNG:KINF fluorescence. However, both fluorescent markers required excitation with the 488 nm laser with incompatible laser powers. The mNG:KINF fusion protein required a high laser power at 120 mW while DCO only required 3 mW. An attempt was made to tag KINF with mCherry which would instead use the 561 nm laser, thereby avoiding this issue; however, the mCherry tag displayed low fluorescence emission and thus was poorly detected by the ImageStream. Therefore, using the 488 nm laser at 3 mW, DCO staining was analysed in the mNG:KINF cell line in isolation. Omwenga prepared and analysed the samples on the ImageStream, while I carried out all of the data analysis. Firstly, the mNG:KINF cells were shown to have a similarly low level of fluorescence to unstained parental C9T7 cells, with a raw max pixel close to 0 (Fig. 4.10A and B). DCO staining of the mNG:KINF cells on the other hand averaged a raw max pixel value of $\sim$ 1,000 (Fig. 4.10C). Thus, the illumination of mNG:KINF cells with a laser power of 3 mW had minimal effects on the intensity of DCO fluorescence. The DCO-stained mNG:KINF cells were subsequently classified based on their DNA staining and morphology into populations of G1, S/G2 and G2/M/C (as outlined in figure 4.3), comprising 49.3, 39.8 and 10.9% of cells, respectively (Fig. 4.10D). Subsequently, by knowing the total percentage of mNG:KINF cells in G1 from the DCO-based cell cycle analysis (49.3%) and subtracting the number of known G1 cells from mNG:KINF tagging (1.8% of 1CF SN very early G1 cells and 18.1% SN no mNG early G1), 29.4% of the long no mNG:KINF cells were calculated to be in G1, while 25.6% were in S phase.

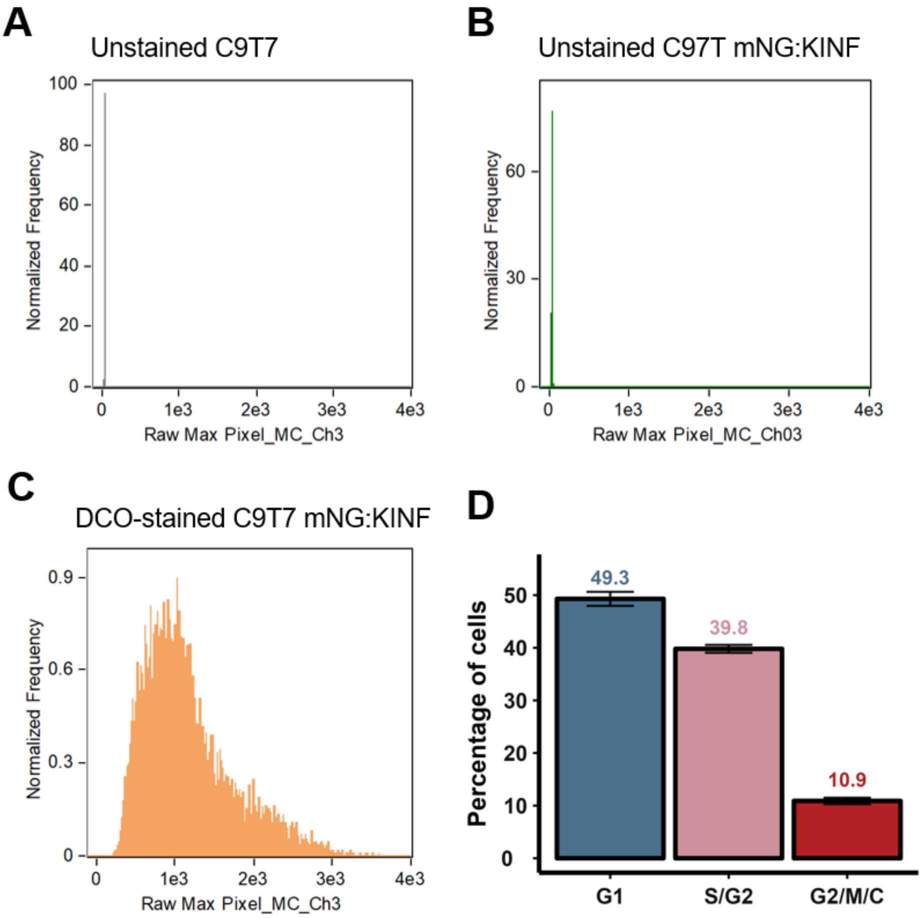

**Figure 4.10: DCO-based analysis of the mNG:KINF cell line.**
The fluorescence intensity of unstained control parental C9T7 cells (A) and the mNG:KINF cell line (B) was analysed using IFC with a 488 nm laser at a power of 3 mW as measured in channel 3. The raw max pixel was plotted; this measures the fluorescence intensity of the pixel with the highest value in each image. The fluorescence intensity of DCO-stained mNG:KINF cells were analysed for their fluorescence intensity by IFC using a 488 nm laser at 3 mW (C) and the percentage of cells in each of the cell cycle stages was determined based on gating on both their DCO intensity and their morphology (D). The error bars give the standard error of three replicates ($n \geq$ 9,261).

From the resulting proportions of the cell cycle stages, as defined by mNG:KINF tagging and morphology, the timings of each stage were calculated using the equation outlined by Wheeler *et al*. [125] (Equation 2.3) and are presented in Table 4.1. From a 12 hour and 24 minute doubling time, G1 takes $\sim$ 5 hours (0.40 u) and S takes $\sim$ 5 hours and 30 minutes (0.45 u). Within that time, mNG:KINF expression is seen to be lost at around 10 minutes into the cell cycle and re-expressed after 10 h and 25 mins. G2 lasts $\sim$ 40 minutes (0.05 u), mitosis an hour (0.08 u) and cytokinesis only $\sim$ 20 minutes (0.03 u). The calculated units of the cell cycle are consistent with the results obtained by Wheeler *et al*., who calculated G1 as between 0.37 and 0.4 u, S as between 0.4 and 0.6 u and post-S as between 0.14 and 0.18 u. The timings of the cell cycle as defined here are also in the same region as that of *L. amazonensis*, as defined by da Silva, with their G2 calculation being 0.09 u [337]. Overall, our results give good correlation with the literature, validating our outlined methods and the defined timings of G2. Thus, an updated view of *L. mexicana's* cell cycle can be found in figure 4.11.

**Table 4.1: Defined cell cycle timings as determined by mNG:KINF tagging.**

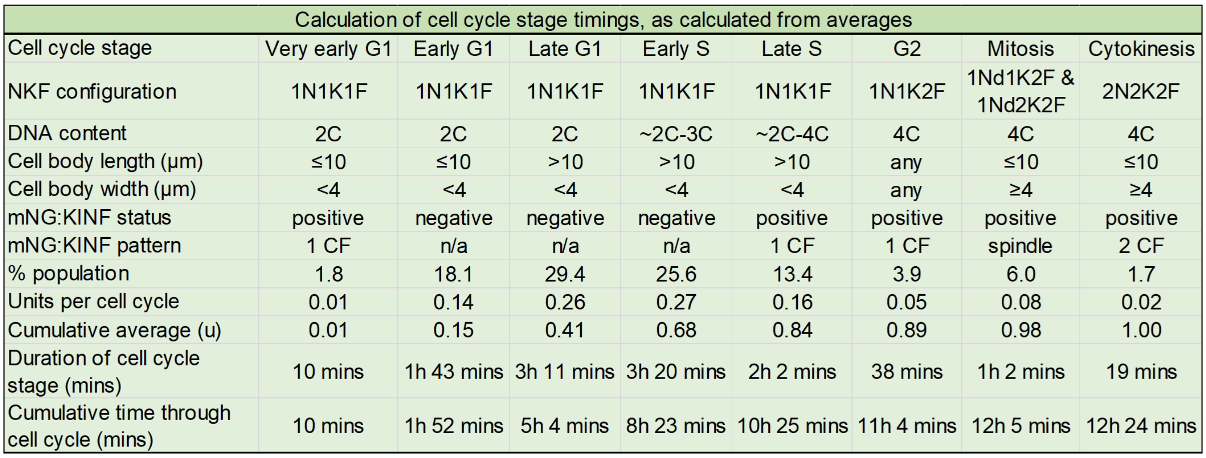

| Calculation of cell cycle stage timings, as calculated from averages | | | | | | | | |
|---|---|---|---|---|---|---|---|---|
| Cell cycle stage | Very early G1 | Early G1 | Late G1 | Early S | Late S | G2 | Mitosis | Cytokinesis |
| NKF configuration | 1N1K1F | 1N1K1F | 1N1K1F | 1N1K1F | 1N1K1F | 1N1K2F | 1Nd1K2F & 1Nd2K2F | 2N2K2F |
| DNA content | 2C | 2C | 2C | ~2C-3C | ~2C-4C | 4C | 4C | 4C |
| Cell body length (µm) | ≤10 | ≤10 | >10 | >10 | >10 | any | ≤10 | ≤10 |
| Cell body width (µm) | <4 | <4 | <4 | <4 | <4 | any | ≥4 | ≥4 |
| mNG:KINF status | positive | negative | negative | negative | positive | positive | positive | positive |
| mNG:KINF pattern | 1 CF | n/a | n/a | n/a | 1 CF | 1 CF | spindle | 2 CF |
| % population | 1.8 | 18.1 | 29.4 | 25.6 | 13.4 | 3.9 | 6.0 | 1.7 |
| Units per cell cycle | 0.01 | 0.14 | 0.26 | 0.27 | 0.16 | 0.05 | 0.08 | 0.02 |
| Cumulative average (u) | 0.01 | 0.15 | 0.41 | 0.68 | 0.84 | 0.89 | 0.98 | 1.00 |
| Duration of cell cycle stage (mins) | 10 mins | 1h 43 mins | 3h 11 mins | 3h 20 mins | 2h 2 mins | 38 mins | 1h 2 mins | 19 mins |
| Cumulative time through cell cycle (mins) | 10 mins | 1h 52 mins | 5h 4 mins | 8h 23 mins | 10h 25 mins | 11h 4 mins | 12h 5 mins | 12h 24 mins |

A summary of the classification and duration of *L. mexicana's* mNG:KINF cell cycle progression. Cells' DNA configuration, DNA content, cell body morphology (length and width) and mNG:KINF expression (mNG:KINF state and mNG:KINF pattern) were used to classify cells into the different stages of the cell cycle. The percentage of cells in each of the cell cycle stages was calculated from the number of cells falling within each category. The duration of the cell cycle was calculated in time (minutes and hours) and in units (u). These were calculated from the percentage population using the equation outlined by Wheeler *et al*. (2011), using a doubling time of 1 u and 12.4 hours, respectively. The cumulative time and units through cell cycle describes the time it takes to reach the end of the defined stage of the cell cycle in hours and units, respectively.

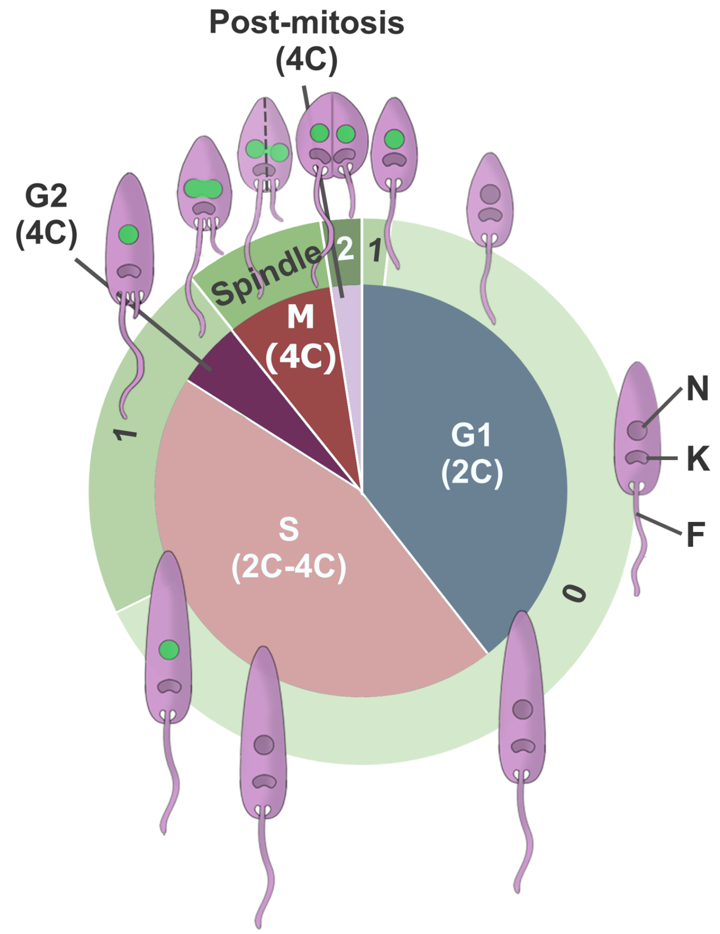

**Figure 4.11: Progression of *L. mexicana* mNG:KINF cells through the cell cycle.**
A schematic representing the cell cycle of *L. mexicana* mNG:KINF cells, demonstrating the morphology, DNA content (2C, 2C-4C and 4C) and mNG:KINF expression at different stages. Changes to the length and width of cells, the number of nuclei (N), kinetoplasts (K) and flagella (F) and the presence or absence of mNG:KINF expression in nuclei is shown. The inner circle shows the progression of cells through G1 (blue), S (pink), G2 (purple), mitosis (red) and post-mitotic (lilac) phases. The outer circle (green) shows the expression of mNG:KINF in relation to a cells stage in the cycle, with “0”, “1” and “2” showing cells with no mNG:KINF, one circular focus and two circular foci of fluorescence, and “spindle” showing cells with an elongated focus of mNG:KINF. The segments of the circles are to scale, indicating the timings of progression through the different stages of cell replication.

### 4.2.7 Best case scenario for sorting *L. mexicana*

With the cell cycle now well defined in terms of the timings of progression and the morphology relating to a cells stage, this understanding was used to guide the design of inertial microfluidic systems for cell sorting. As previously described in Section 1.2, there are a lack of robust methods of separating the cell cycle stages of *L. mexicana*, particularly procedures which do not introduce artefacts into the cells. Inertial microfluidics therefore serves as a passive method of sorting based on particle size, shape, and deformability. Sorting based on size can frequently reach purities of > 90% and can achieve separation of particles with differences in the nm range [339]–[342]. Inertial sorting of cell types where morphologies are closely related, particularly for the study of continuous processes like the cell cycle, circadian rhythm, and ageing are few [170], [231], [343], [344]. This is especially true for non-spherical cell types.

Here, the aim was to apply inertial microfluidics to the sorting of *L. mexicana’s* cell cycle stages. As has been demonstrated, *L. mexicana* promastigotes undergo a range of morphological changes, with earlier cell cycle stages appearing as prolate-like (elongated ellipsoids) with different aspect ratios, cells becoming more rounded in later cell cycle stages, having a single or two flagella, and having varying DNA content. While various morphological parameters have been modelled using beads, few studies have addressed the role of cell morphology and the interplay between these parameters for inertial microfluidic cell separation. Therefore, while simultaneous sorting of all stages of the cell cycle was the end goal, due to the lack of information on the contribution that these parameters have during inertial focusing, attention was first set to sorting mitotic and cytokinetic cells – these are the most heterogeneous and understudied population, as well as showing the most distinct morphology for sorting based on cell shape (Fig. 4.4). In Table 4.2, the morphological features most associated with M/C cells are outlined.

Based on these parameters, the theoretical sorting efficiencies (i.e. if sorting based on the morphological threshold defined was achieved with 100% efficiency) were calculated from thresholds guided by the data in figure 4.4 relating to M/C phase-associated morphologies (Table 4.3). A sorting threshold of $\geq$ 4 μm (i.e. an experiment designed to focus cells with a width of $\geq$ 4 μm) was calculated to give the highest yield of M/C cells, with 90.5% being collected at 100% sorting efficiency. However, this threshold on width also gave the lowest purity (48.4%) of M/C cells, including a large amount of short and wide early G1 cells. A sorting threshold of an aspect ratio of $\geq$ 0.4 gave a slightly higher purity at 53.9%; however, this compromised the yield, seeing a decrease to 87.1%. A more severe threshold on AR continued these trends. In all sorting scenarios based on a single morphological parameter alone, a low purity and/or enrichment would be achieved. This was unexpected, as from figure 4.4, M/C cells were shown to have a distinct morphology, particularly for width and aspect ratio measurements. The discrepancy in results is likely due to the low proportions of M/C cells (9.7%) within the sample, compared to G1 (53.6%) and S (36.8%) phases. Thus, while a low proportion of G1 and S phase cells may have a morphology similar to M/C cells, this may still represent a significant number of cells.

Therefore in Chapter 5 the role of a variety of morphological parameters were assessed for their contribution to cell sorting, in order to improve the understanding of factors contributing to inertial focusing with the aim of improving sorting efficiencies.

**Table 4.2: Morphological components differentiating M/C cells.**

| | Differentiating M/C morphology | | |
|---|---|---|---|
| | G1 | S | M/C |
| Aspect ratio | Low | Low | High |
| Length | Short - Long | Long | Short |
| Width | Narrow | Narrow | Wide |
| Shape | Prolate-like | Prolate-like | Spherical-like |
| No. flagella | One | One | Two |
| DNA content | 2C | 2-4C | 4C |

Summary of the average morphological features related to G1, S and M/C phases of cells. A low and high aspect ratio correspond to an aspect ratio of < 0.5 or $\geq$ 0.5 respectively while short and narrow correspond to lengths of $\leq$ 10 μm and > 10 μm, respectively. Wide and narrow morphologies correspond to an average width of < 4 μm and $\geq$ 4 μm respectively. The general shape, number of flagella and DNA content associated with each cell cycle stage is also given.

**Table 4.3: Hypothetical sorting efficiencies of M/C cells.**

| | Hypothetical sorting efficiencies of M/C | | |
|---|---|---|---|
| | Purity (%) | Enrichment | Yield |
| Width ≥ 4 μm | 48.4 | 4.3 | 90.5 |
| Aspect ratio ≥ 0.4 | 53.9 | 4.8 | 87.1 |
| Aspect ratio ≥ 0.5 | 65.2 | 5.8 | 61.1 |

## 4.3 Discussion and conclusion

The cell cycle remains a key area of *Leishmania* research, in improving the fundamental understanding of the parasite's biology, as well as for its potential as a target for novel drugs. Throughout *Leishmania's* cell cycle, while the cells are highly heterogeneous, the changes which are seen are highly predictable. Thus, as drugs targeting cell cycle regulatory proteins often cause morphological changes, and/or changes to the proportions of cells at each of the cell cycle stages, morphological analysis remains an important aspect of many drug and functional studies [139], [142]. Despite this, these studies are often limited in the type of morphological information which they extract due to lengthy analysis times, with studies often carrying out manual counts on the numbers of nuclei and kinetoplasts, and visually inspecting obvious changes to cell size and shape and all in low numbers of cells. In studies which take a more in-depth view of morphological changes, < 1,500 cells were analysed in total [60]. In the work carried out in this thesis, a wealth of information was acquired both in terms of cell cycle analysis and morphological measurements using IFC, requiring minimal preparation of cells.

Firstly, it was tested whether IFC could be used to analyse the numbers of nuclei and kinetoplasts per cell. Automatic spot detection has been used successfully in a wide range of cells, dramatically reducing the time taken for manual imaging and processing. Unfortunately, this was unfeasible for counting nuclei and kinetoplasts as the variation in fluorescence presentation between images caused issues in mask development. This was primarily the case where the signals overlapped and were only identified as one spot, thus leading to an underestimation of the number of nuclei or kinetoplasts per cell. While quantifying true numbers of spots was ineffective, information could still be gleaned from spot analysis which was demonstrated by the observed correlation between cell length and the distance between the spots, corresponding with work that has been reported in the literature; however, the throughput which was achieved using IFC was massively increased compared to microscopy [125].

While spot count analysis failed for DNA staining, instead, a detailed view of the cell cycle was provided by combining both morphological measurements with markers of the cell cycle. By using morphology and DNA staining, quantification of the different cell cycle stages was improved to a level that was comparable with manual microscopy measurements. With DNA content alone, cell cycle distributions of 53.6, 19.9 and 26.5% were measured for the 2C-, Int.-

and 4C-gated populations, respectively; however, by including morphological measurements, these were improved to 53.6, 36.8 and 9.7%, which closely corresponded with data generated by Wheeler *et al*. with microscopy measurements [125]. Importantly, the throughput of the analysis was significantly increased using IFC, in addition to being able to analyse live cells, which preserved the cells' morphologies. The use of live cells also enabled the analysis of fluorescent fusion proteins, which can get denatured during fixation, particularly during longer processing times. Here, the analysis of the fusion protein mNG:KINF was used to identify the spindle and provided a higher resolution of the cell cycle. By identifying cells with a single, circular focus of mNG:KINF and two flagella, elusive G2 cells were quantified and the timings of this stage were defined (38 minutes in a 12.4 hour cell cycle). The G2 population was shown to exhibit a range of lengths and widths, in line with what was expected. Additionally, using IFC and the method of analysis outlined, rare cell cycle stages were capable of being analysed such that a population of newly divided cells and a population of post-mitotic cells were identified, accounting for 2.2% and 1.7% of the total population, respectively. Such resolution which would be difficult to acquire with current microscopy and analysis techniques.

From these data, exploratory backtracking was also used to understand how different morphological parameters changed throughout the course of the cell cycle (Fig. 4.4). From such analysis, the M/C population came back as being the most morphologically distinct cell cycle stage, with AR, circularity, elongatedness and width parameters having the highest correlation with M/C morphologies from the thirteen parameters tested. These data have helped to improve the understanding of the role morphology plays in the cell cycle with the aim of guiding the development of morphology-based sorting.

# Chapter 5

# Inertial microfluidic focusing of *L. mexicana* in curved channels

## Highlights

- If an elongated morphology is conserved, then a cell's flagellation status does not affect inertial microfluidic focusing in curved channels.
- *L. mexicana* displayed highly different focusing behaviours to model rigid beads, providing evidence for the contribution of shape to sorting.
- A highly conserved focusing position at the outer wall was shown for *L. mexicana* cells, regardless of changes in cell size at high flow rates.
- Enrichment is achieved for short and wide cells at the inner wall, and long and narrow cells at the outer wall.

## Published work:

J. Howell, N. Hall, S. Omwenga, T. Hammarton and M. Jimenez **Impact of flagellated and elongated morphological phenotypes on the focusing behaviours of biological cells in inertial microfluidic devices.** *bioRxiv*. (2024). 2024.05.16.594321. [345]

Data was partially presented at the conference:

1. J. Howell, N. Hall, S. Omwenga, T. Hammarton and M. Jimenez. **The use of imaging flow cytometry to inform label-free, high-throughput, microfluidic-based separation of non-spherical cells.** (May 2024), *CYTO24*, Edinburgh, Scotland.

## 5.1 Introduction

Inertial microfluidics is an attractive method for the sorting of particles, offering a high-throughput, label-free and passive method of separation. While it is commonly described for sorting based on particle size, shape and deformability, size is the most widely utilised factor for driving inertial microfluidic separation [208], [210], [346]. The role of particle size has been well documented for rigid spherical particles in curved channels. As outlined in Section 1.3, for particles of different sizes above a particle confinement ratio (λ) of 0.07, beads will align at varying distances away from the inner wall [201]. Smaller particles tend to align towards the inner wall at lower Reynolds numbers, before migrating towards the channel centreline with increasing flow rates or channel curvature. As particle size increases, a higher Reynolds number is required to achieve similar focusing at the inner wall; however, once focused, larger particles are more resistant to additional changes in fluid velocity and maintain a more stable focusing position [201], [347]. Generally, the focusing positions of spherical cells show a good correlation to those of similarly sized rigid beads, and thus beads are often used for modelling particle behaviour prior to the sorting of cells [200], [231]. Most commonly, this has been shown for cancer cell isolation, taking advantage of the larger size of these rare cells for sorting [340], [348]–[354].

Deformability has also been shown to be an effective tool for sorting particles, where the presence of a deformability-induced lift force causes the migration of deformable particles away from more rigid particles [198], [355], [356]. While the reason for this migration is still not well characterised, this theory has been successfully applied to the separation of deformable cancer cells from blood, diagnosis of malaria through identification of infected red blood cells (RBCs) and the purification of manufactured RBCs [198], [357], [358].

In contrast, the contribution of shape in sorting is less well documented. Initial work on spheroid particles in straight channels (i.e. without the presence of Dean forces) documented complex rotational behaviours of the non-spherical particles; prolate particles (elongated ellipsoid particles) and oblate particles (disc-like ellipsoid particles) showed rotations described as “kayaking”, “log-rolling” and “tumbling”, depending on their position in the flow and the strength of the inertial forces. When these particles focus within the flow, they tend to exhibit a stable rotation with prolate particles “tumbling” and oblate particles “log-rolling” [209], [359], [360]. By increasing the Reynolds number further, particles have been shown to align with the flow and rotate periodically or stop rotating altogether, though this behaviour has not been observed in all studies [209], [361]. Despite their rotational behaviour, it was documented that the longest dimension of a particle (rotational diameter) could be taken as a measurement equivalent to the diameter of a spherical particle [232]. Thus, by ignoring the shortest dimension, the behaviour of non-spherical and spherical particles showed a high correlation independent of their shape [232], [360], [362]. An exception to this behaviour has been shown for “h” shaped particles due to the lack of symmetry [196].

While the behaviour of rigid non-spherical beads has been extensively studied in straight channels, a distinct contrast is seen for that of curved channels. In a study testing four different shapes of beads, Roth confirmed the equivalent particle diameter could also be used in curved channels to give an indication of focusing position [363]. However, the study also mentioned that shape may play more of a role in curved channels as peanut-shaped beads and ellipsoidal particles of the same dimensions and volumes demonstrated different focusing positions [363]. Hafemann on the other hand, simulated the effects of particle shape in a curved channel [364]. In agreement with previous work, the authors demonstrate that prolate particles tumble in the flow while oblate particles log-roll around their shortest axis. As a result of this difference in rotational behaviour, the prolate particles were demonstrated to have a more stable focusing position than the oblate particles due to their alignment with the flow. In addition, an important point addressed in this work is the effect of the particles on the fluid velocity profile. For larger particles, simulation of the fluid profile was shown to be altered quite dramatically by the presence of particles, with spherical, oblate and prolate particles inducing the formation of secondary vortices towards the inner wall. For spherical particles, these vortices were suggested to stabilise the focusing at the inner wall. Both the large prolate and oblate particles also induced the formation of secondary vortices at the inner wall; however, these vortices were much larger and spanned a greater distance ranging over 1/4 of the channel width. The non-spherical particles subsequently focused further away from the inner wall, with the prolate particles being closest to the centreline. Both of these publications suggest that in Dean flow, particle shape has a larger contribution to the focusing position of particles within spiral channels.

Inertial microfluidics has also been successfully applied to a variety of non-spherical cells. Using a spiral channel with a trapezoidal shaped cross section, small and round *Caenorhabditis elegans* eggs were isolated from later development stages with a vermiform shape [365]. Keinan showed that sorting of budding yeast in serpentine channels could be used to identify different populations based on cell ages. In this work, characterisation was carried out using microscopy to analyse cell size and the number of budding scars – an indicator of cell age [343]. Yeast has also been separated based on shape into the different stages of the cell cycle, obtaining up to 94% purity for singlet cells and 31% purity for budding stages [232]. Of particular interest to this study are the works done on sperm and algae; organisms demonstrating elongated cell bodies with the presence of a flagellum. Interestingly, sperm are consistently shown to focus to the outer wall within spiral channel devices, showing good separation from deformable RBCs at a Reynolds number as low as 119.0 [366]–[369]. Feng hypothesised that this migration to the outer wall was a result of the flagellum affecting particle rotation within the flow and demonstrated that through the removal of the flagellum *via* sonication, deflagellated sperm heads focused closer to the inner wall. Microalgae on the other hand are highly heterogenous organisms, demonstrating both intra-strain and inter-species morphological differences. These morphological differences have been taken advantage of with trapezoidal and spiral channels to isolate different strains of microalgae, while a straight channel was used to sort different life cycle stages of flagellated Euglena gracilis [342], [344], [370]. In the latter study, Li demonstrated that within a high aspect ratio straight channel, longer and narrower cells focused towards the centreline of the channel, while rounder cells located to the walls. While inertial microfluidics has been applied to the sorting of non-spherical cells, often the role of shape is not addressed, or the equivalent particle diameter is used as a proxy for shape. Thus, the role of shape has not been addressed in isolation, i.e. for cells with similar rotational diameters but different aspect ratios.

With inertial microfluidics thus showing potential for both cell cycle analysis and the separation of heterogenous cell types, its application for separating the different cell cycle stages of *L. mexicana* was tested. As discussed in Section 4.2.7, a fairly high amount of overlap is seen between the morphologies of the different cell cycle stages, as a result of biological variation and it being a continuous process. It was also discussed that the best option for sorting was determined to be an aspect ratio cut off at 0.5; a 100% sorting rate would achieve 65.2% purity and a 5.8X enrichment of M/C cells. However, it is still uncertain as to what role aspect ratio plays in sorting. For this application, sorting based on the rotational diameter alone would be unable to isolate an individual cell cycle stage as early G1 and M/C cells have similar lengths, as do cells in later G1 and S phases. As curved channels have been suggested to result in different focusing patterns for different particle shapes, it was first sought to understand the behaviour of *L. mexicana* within flow, and the contribution of different morphological parameters to sorting. To achieve this, the morphology of *L. mexicana* was varied through chemical treatment (with flavopiridol, hydroxyurea and for deflagellation), and cell differentiation (Fig. 5.1), in an attempt to isolate the role of the flagellum, cell size, and cell shape in sorting. In this Chapter, all cell populations analysed were fixed with 4% PFA (see Section 2.2.1 for details) prior to inertial microfluidic analysis, unless explicitly stated otherwise. While fixation has been shown to affect the morphology of cells, the pressurisation of the microfluidic system increased the risk of both leaks and aerosolisation of the parasites, thereby increasing the risk of exposure. Due to the portable size of the microfluidic setup, sorting could be carried out within a class II microbiological safety cabinet (MSC); however, methods for analysing particle focusing behaviour are limited to bulky and expensive equipment which could not be used in this study in an MSC. Therefore, the focusing behaviour of fixed parasites was first analysed with a high-speed camera prior to work with live cells. The application of alternative techniques for analysing particle focusing behaviour is discussed more in Chapter 6.

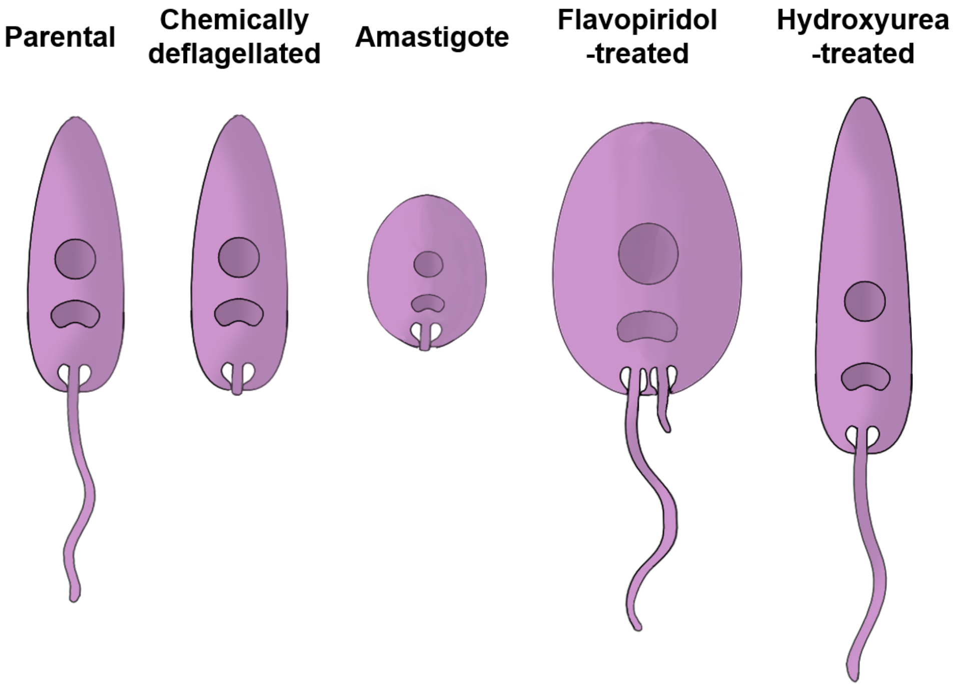

**Figure 5.1: Modified morphologies of *L. mexicana.***
Graphical representation of the different morphologies of *L. mexicana* achieved through chemical treatment and differentiation (see Section 2.1.2 for details). Variations in cell length, width and flagellum presence have been demonstrated. It should be noted that all populations demonstrated a certain amount of variation in terms of their dimensions, and that the average measurements of the parasite populations were represented. Image not to scale.

## 5.2 Results

### 5.2.1 Inertial microfluidics set up

The device that was first tested was a 6-turn Archimedean spiral with a height of 30 μm and a width of 170 μm (Fig. 5.2). This device has been validated in previous work, demonstrating that rigid 10 μm beads focus towards the inner wall at Reynolds numbers between 33 and 169, showing good separation with highly deformable RBCs focusing closer towards the outer wall of the channel [356]. For this channel, Equation 1.3 was used to calculate a $\lambda$ of 0.07 for a 4 μm spherical particle. As 99.2% of parental parasites are above this length, this would mean that, in theory, if sorting was driven by the rotational diameter, almost all cells in the parental population would have focused, like spherical beads, to the inner wall. In contrast, if particle width contributed to particle focusing, then this may have enabled wider M/C cells to focus while narrower cells would recirculate potentially enabling enrichment of M/C cells.

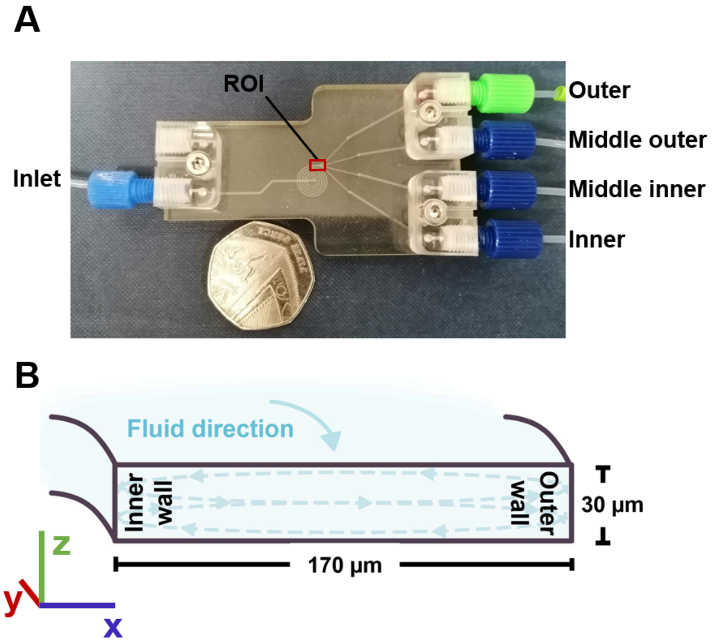

**Figure 5.2: Microfluidic design used for the separation of *L. mexicana.***
(A) An image of the microfluidic device used for sorting. The channel consisted of a 6 turn Archimedean spiral with one inlet and four outlets labelled as: the "outer" channel (the channel the furthest from the centre of the spiral), the "middle outer" channel, the "middle inner" channel and the "inner" channel (the outlet closest to the centre of the spiral). High-speed imaging of particle sorting was performed at the region of interest (ROI), prior to where the channel expanded into the outlets. (B) The channel cross section had a low aspect ratio (channel height < width) with a height of 30 µm and a width of 170 µm. The direction of the fluid as well as the Dean vortices (dashed lines) are shown. The height of the channel is marked as the z-direction (green), the width of the channel is on the x-axis (blue) while the length of the channel corresponds to the y-axis (red), as shown using the 3D axis.

### 5.2.2 *L. mexicana* displayed unusual focusing behaviours in comparison to spherical rigid particles.

As previously described, the rotational diameter (in this case a cell's length) has been shown to be equivalent to the diameter of a spherical bead in determining a particle's focusing position within a channel [232], [360]. In order to test whether this theory stands for *L. mexicana*, the focusing position of these cells was compared to that of similarly sized beads. IFC was first carried out on fixed *L. mexicana* as described in Section 2.2.5, which determined the average length of these cells to be 9.5 µm (Fig. 5.3A). The focusing position of these same cells was then compared to spherical beads with a diameter of 10 µm over a range of flow rates (see Section 2.4.1 for details). From these data, it was seen that *L. mexicana* behaved very differently from 10 µm beads (Fig. 5.3B and C). At Re = 33.3, the parasites recirculated across the entirety of the channel width. Increasing the Reynolds number to 83.3 resulted in a bimodal distribution with parasites aligning around 40 µm away from both the inner wall and outer wall. At Reynolds numbers $\geq$ 116.7, the vast majority of cells migrated to the outer wall, with a higher flow rate correlating to a tighter focusing band and a position closer to the outer wall. In contrast, 10 µm beads initially focused closer to the centreline of the channel, moving towards the inner wall with increasing Re. At both Re = 166.7 and 250.0 two focusing positions can be seen, which has been described as step wise focusing to a more stable equilibrium position [347], [371]. While the behaviour of the beads is in line with previous studies, the focusing behaviour of *L. mexicana* is unusual for two reasons. Firstly, considering the high heterogeneity in *L. mexicana's* morphology, a single focusing position was not expected, suggesting completely dominating forces acting independently of size/shape. Secondly, a focusing position at the outer wall is unusual as similarly sized 10 µm beads only focused towards the inner half of the channel.

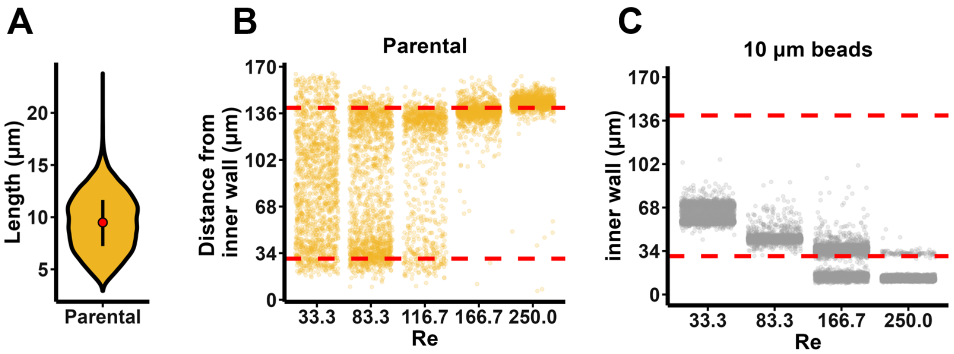

**Figure 5.3: The rotational diameter of fixed *L. mexicana* parasites is not equivalent to a sphere's diameter.**
(A) Fixed *L. mexicana* cells were analysed using IFC and their length measured. The red dot shows the mean (9.5 µm) and the black bar gives the 25th to 75th quartile range. The parental *L. mexicana* cells (B) or 10 µm beads (C) were analysed using a high-speed camera to assess the focusing position of individual particles within the 30 x 170 µm$^2$ channel over a range of Reynolds numbers (Re). Each point of the graph represents a single particle within the channel (n $\geq$ 965). Red dashed reference lines indicate a distance of 30 µm from both the inner and outer wall.

To ensure that this unusual focusing behaviour was not an artefact of cell fixation, and that using fixed cells was a true representation of the behaviour during sorting, the focusing of live *L. mexicana* parasites was tested. Live cells could not be analysed using the high-speed camera for safety reasons, therefore: sorting at Re = 250.0 was carried out in a class II MSC; the output from the four outlets were collected; cell counts were performed using a haemocytometer; and the samples analysed *via* microscopy. No cells were detected at either of the inner channel outlets (Fig. 5.4), a small proportion (9.8%) were found at the middle outer outlet, while the vast majority of cells focused to the outer wall (94.1%). From these data, three conclusions were inferred: i) the focusing position at the outer wall is stable and not an artefact of cell fixation, ii) live and fixed cells behave similarly in the tested channel design at Re = 250.0 and iii) something about the morphology and/or mechanical properties of *L. mexicana* is inducing migration to the outer wall, which is not seen for rigid spherical beads.

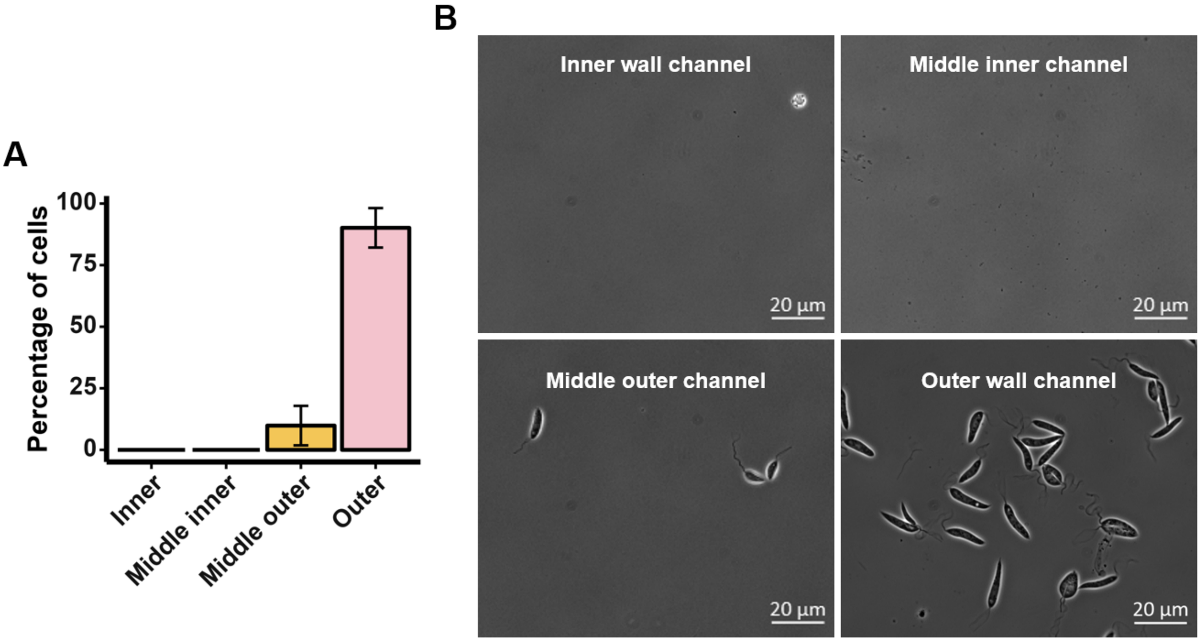

**Figure 5.4: Live *L. mexicana* focus to the outer wall at high Reynolds numbers.** Sorting of live parasites at Re = 250.0 was carried out in the 30 x 170 μm$^2$ channel in a class II microbiological safety cabinet. (A) The percentage of cells sorted into each outlet was calculated. The error bars show the standard deviation from the mean for two replicates. (B) The output from each of the four outlets was collected and imaged using microscopy. Scale bars: 20 μm.

### 5.2.3 Generation of flagellated beads

As previously mentioned, the presence of a flagellum has been described to cause particle focusing at the outer wall, in a spiral channel similar to the one used here [366], [367]. The authors showed that on removal of the flagellum, the cell bodies changed their behaviour and focused to the inner wall. If the focusing position of *L. mexicana* was similarly driven solely by the presence of a flagellum and thus resulted in all *L. mexicana* morphologies having the same equilibrium position at the outer wall, then separation of the different cell cycle stages of *L. mexicana* using only morphology would not be possible. Therefore, the role of the flagellum in the focusing position of fixed *L. mexicana* parasites was explored.

To isolate the role of the flagellum in sorting, an attempt was first made to flagellate a bead. This would have enabled a direct comparison between a particle with a known behaviour *vs* that of the same particle but with an added flagellum. Artificial flagellation of a bead has been achieved by Mori, who removed the flagella of *Chlamydomonas reinhardtii* using dibucaine HCl [372]. By adding polystyrene beads to the isolated flagella, spontaneous binding resulted in beads with a single flagellum in the majority of cases. For this work, using *Chlamydomonas reinhardtii* was unfeasible, thus it was tested whether the flagellum of *L. mexicana* could instead be isolated and bound to a bead. While protocols for flagellum isolation have previously been described for trypanosomes, freed flagella have not been reported to spontaneously bind to surfaces [373], [374]. However, it has been shown that through the interaction between biotin and streptavidin, full organelles could be pulled out of a lysate using streptavidin-coated beads [375]. By combining these two methods, it was hypothesised that an isolated flagellum with a biotinylated tip would bind to a streptavidin-coated bead.

To test this hypothesis, *L. mexicana* first had to be genetically modified to enable biotin expression on the flagellum tip. The axoneme capping structure (ACS) was identified as a protein localising solely to the flagellar tip [244], [376], which was confirmed though mNeonGreen tagging (Fig. 5.5A). As the TwinStrep II tag used in the organelle pull down experiment wasn't readily available, tagging of the ACS was instead carried out with MiniTurbo (see Section 2.1.2 for details). This proximity labelling enzyme is traditionally used in proteomic experiments to identify proteins interacting with the labelled target [145]. Here, however, it was hoped that by tagging the ACS, both the ACS and nearby proteins would be biotinylated, thereby increasing the total area expressing biotin for more robust binding to streptavidin-coated beads. Biotinylation of MiniTurbo expressing cells was carried out as explained in Section 2.3.1, after which the cells were washed ready for deflagellation. Two methods of deflagellation were trialled, either to maintain or to remove the cell membrane as it was unknown whether the membrane would act as a physical barrier and prevent the binding between the biotinylated ACS and the streptavidin-coated beads. After deflagellation using both methods, the resulting suspension (containing both the cell bodies and the removed flagella) was incubated with the beads for half an hour, with occasional agitation. Microscopy was used to assess the binding of the beads to flagella. While occasionally a bead and a flagellum would be positioned together (Fig 5.5B), the rarity of this event was concluded to be due to overlapping positions as opposed to true binding. In no scenario tested were the flagella shown to be bound to beads. While various parameters could have been adjusted to try and induce binding (such as obtaining a TwinStrepII tag, tagging a different protein, or optimising the deflagellation protocols), the time required to troubleshoot, and the uncertainty of the outcome instead encouraged a different approach to be taken to study the role of the flagellum in sorting.

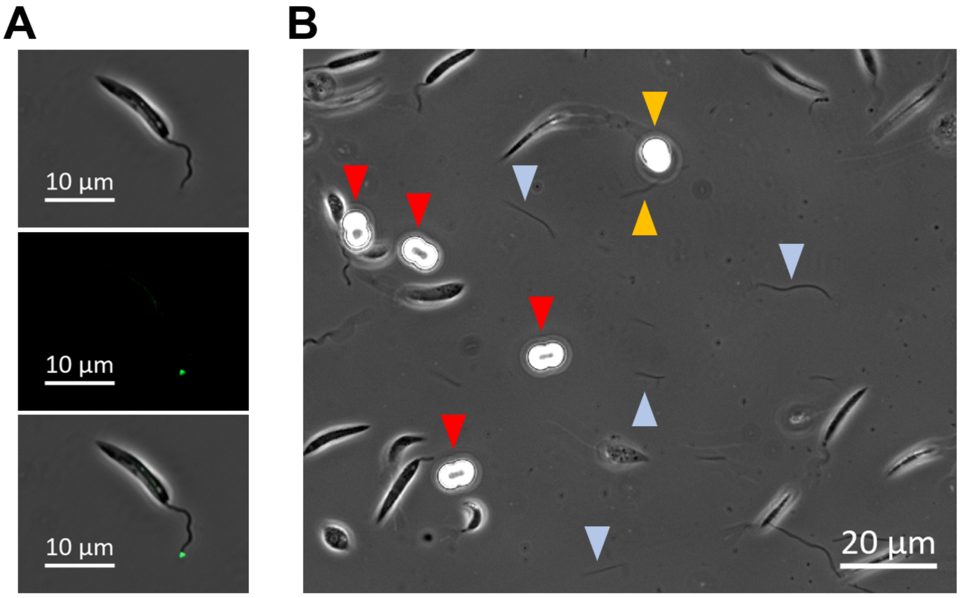

**Figure 5.5: Attempted flagellation of beads**
(A) An example of mNeonGreen fluorescence in the ACS:mNG cell line. A single cell was imaged by microscopy in BF (top) and fluorescence mode (middle), from which the corresponding composite image was generated (bottom). Scale bars: 10 µm. (B) The ACS:MiniTurbo cell line was incubated in biotin and deflagellated following the protocols outlined in Sections 2.1.2 and 2.3.1. The resulting suspension (containing a mixture of flagellated cells, cell bodies with sheared flagella and the separated flagella (blue arrowheads)), was incubated with streptavidin-coated beads (red arrowheads) and imaged by microscopy. A flagellum and a bead positioned in close proximity is identified with a gold arrowhead. Scale bar: 20 µm.

### 5.2.4 Focusing of non-flagellated *L. mexicana*

The next approach taken to assess the role of the flagellum was to remove the flagellum from the cell body and thus compare the focusing position of flagellated untreated *L. mexicana* C9T7 promastigotes (henceforth called the parental population) with the resulting deflagellated cells. Both chemical deflagellation (which maintained the cell membrane) and cell differentiation were carried out (see Section 2.1.2). Differentiation of promastigotes was used to generate axenic amastigotes, which are the mammalian infective form of the parasite. They are known to be smaller and naturally have a vestigial flagellum with only a small bulbous end protruding from a small cell body [301]. Due to the flagellum not being visible and thus presumed to have no effects on sorting, for convenience, this population is subsequently referred to as being non-flagellated. Details of cell population generation are found in Section 2.1.2.

Morphological characterisation was subsequently carried out by IFC on the resulting cell populations and compared to that of the parental cells. All cell populations were fixed with 4% PFA prior to IFC analysis (the chemically treated line was fixed prior to deflagellation) to ensure consistency with the inertial microfluidic analysis. This demonstrated that the deflagellated cell line had a morphology similar to the parental line when measuring the area, aspect ratio, length and width (Fig. 5.6). On average the parental cells were less than 0.5 μm longer and 0.3 μm narrower than the deflagellated line (lengths of 9.5 μm and 9.1 μm and widths of 3.3 μm and 3.6 μm, respectively). The high similarity in morphology is demonstrated by the receiver operating characteristic (ROC) curves and the corresponding area under the curve (AUC) values (Fig. 5.6iv and v); all the morphological parameters analysed using the ROC curves are close to the reference line, with the highest deviation in AUC values from 0.5 being width measurements at 0.62. In contrast, the amastigote cells were much smaller than the parental line (as demonstrated by an AUC of 0.11) at only 5.6 μm long, and had the highest aspect ratio at 0.63, which was almost twice that of the parental cells (0.35) (Fig. 5.6iii). Despite being shorter, these cells had a width comparable to that of parental cells with an AUC of 0.55 (Fig. 5.6iv and v).

In order to better understand the distribution of sizes within each cell population, cells were classified into short or wide and long or narrow, as previously carried out in Section 4.2.3. It can be seen in figure 5.6ii that the parental line and the deflagellated line had relatively similar proportions of each of the classifications, with deflagellated cells having an increase in the number of short and wide cells (9.5% *vs* 18.2%), and a decrease in the number of long and narrow cells (40.6% *vs* 30.6%). Amastigotes on the other hand were rarely long, with 80.0% being short and narrow and 18.4% being short and wide.

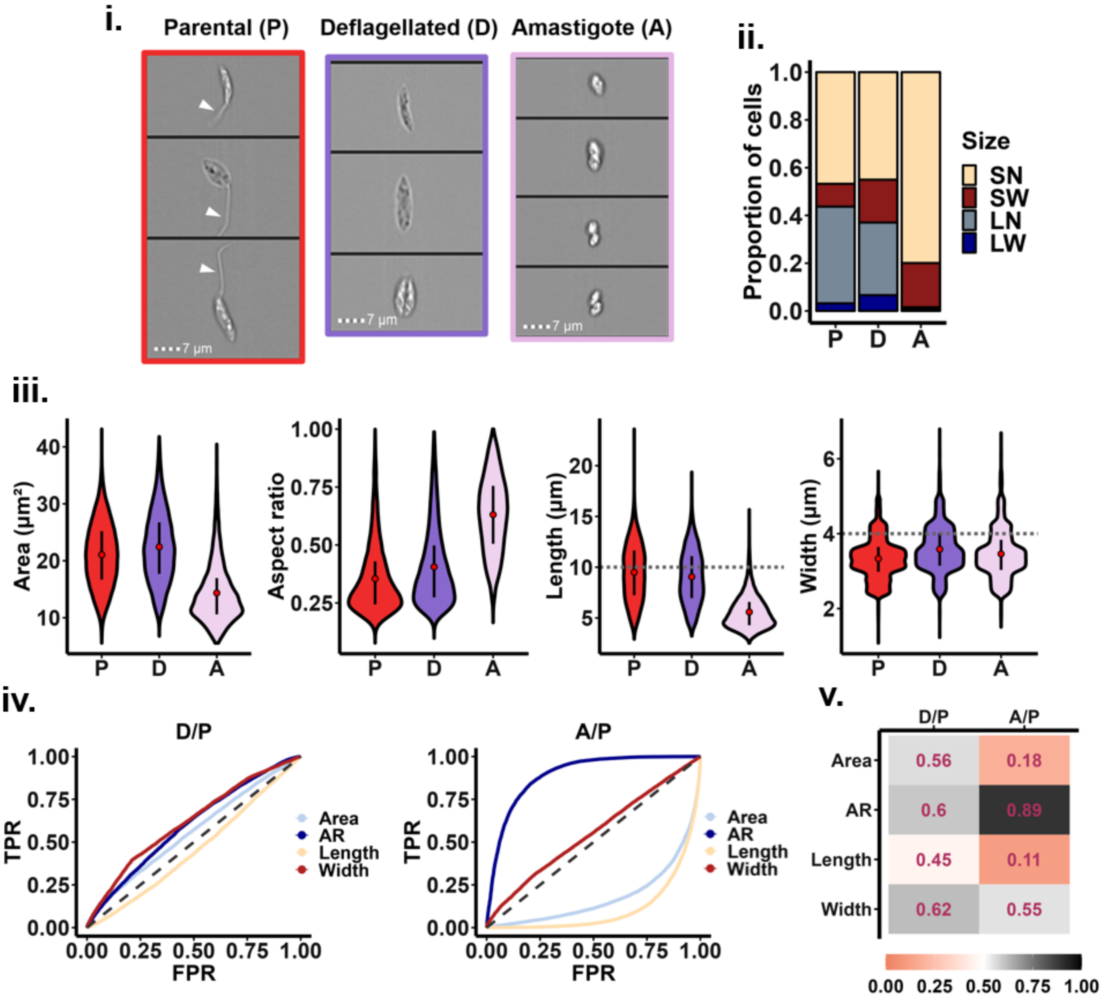

**Figure 5.6: Morphology of fixed and non-flagellated *L. mexicana*.**
The morphology of fixed parental (P), chemically deflagellated (D), and axenic amastigote (A) form parasites were analysed *via* IFC. (i.) Example BF images of the different populations, with flagella being identified with white arrowheads. Scale bars: 7 μm. (ii.) Morphological measurements were calculated for each cell population in IDEAS®, and the cells were subsequently classified based on their length and width measurements into short ($\leq$ 10 μm) and narrow ($<$ 4 μm) (SN), short and wide ($\geq$ 4 μm) (SW), long ($>$ 10 μm) and narrow (LN) and long and wide (LW) ($n \geq 12{,}962$). (iii.) The area, aspect ratio, length and width measurements were calculated for each population and plotted as a violin plot. The thresholds of 10 μm and 4 μm set on length and width are shown with dotted grey lines. The black bars show the 25th – 75th quartile range with the red dot showing the mean. (iv.) The distributions of morphological parameters of the deflagellated and amastigote populations (positive populations); were compared to that of the parental line (negative population). The grey dashed line indicates where the true positive rate (TPR) is equal to the false positive rate (FPR) and thus where there is no distinction in the distribution of measurements between the parental cell and the corresponding non-flagellated population. A curve close to the reference line indicates a similar distribution in measurements while the further the curve is from the reference line, the higher the deviation in distributions. (v.) From the ROC curves, the area under the curve (AUC) values were calculated and plotted as a heatmap. A score close to 0.5 (white) represents a distribution with a high similarity to the parental cell population, while a score closer to 0 (peach) or 1 (black) denotes a high deviation in the distribution of measurements. A value $<$ 0.5 or $>$ 0.5 indicates that the morphological measurements are smaller or larger than the parental cells, respectively.

Once characterised, the focusing behaviour of the non-flagellated parasites was then compared to that of the parental cells. The parental and the deflagellated populations had very similar focusing profiles, recirculating at lower Reynolds numbers and focusing to the outer wall with increasing Re. The deflagellated line showed slight differences at Re = 83.3 and 166.7 compared to the parental popuation, with no bimodal distribution and a wider focusing distribution, respectively; however, overall, the deflagellated population showed good correlation with the parental. The change in focusing positions may reflect the slight changes in width measurements between the two cell populations. In contrast, the smaller and rounder amastigotes showed a higher level of divergence compared to the parental population. At Re ≤ 166.7, these cells had a more typical focusing profile compared to beads; focusing close to the inner wall and moving slightly further away with increasing flow rates [201]. Interestingly, despite this typical focusing behaviour at intermediate Reynolds numbers, at Re = 250.0, amastigotes demonstrated a large shift in focusing position with > 50% of cells having migrated to the outer wall. This is the lowest proportion of cells focusing to the outer wall at Re = 250.0, suggesting that smaller and higher aspect ratio cells required a higher Reynolds number to migrate to the outer wall.

Additionally, a trend can be seen in the “minimum” and “maximum” focusing positions between the different flow rates - unfocused particles at Re = 33.3 (the parental and deflagellated populations) are found across almost the entire channel width, with the exception of $\sim$ 15 µm from either channel wall. By increasing the flow rate, this repulsion from the walls seemed to be at its maximum at a distance of 30 µm which is shown in figure 5.7 by the presence of red dashed lines. Focused cells which formed tight bands were able to cross this “barrier” to localise within $\sim$ 30 µm of either the inner or the outer wall. The presence of this “barrier” is also seen for 10 µm beads, which demonstrated two focusing positions – one within 30 µm of the inner wall, and the other at 30 µm away from the inner wall (Fig. 5.3C). Such a barrier force has been previously observed in high aspect ratio channels at the inner wall, but not reported for the outer wall [377].

From the data presented in figure 5.7, the following observations were made: 1) the presence of a flagellum had little effect on the focusing position of *L. mexicana.* 2) Instead, the size or shape of cells seemed to have a larger effect on focusing positions at Re ≤ 116.7. 3) Cells migrated to the outer wall in a size/shape-dependent manner, with smaller and less elongated cells requiring a higher Reynolds number to move to the outer wall. 4) At high flow rates (Re = 250.0), > 80% of parental and deflagellated cells and > 40% of amastigotes focused within the same 17 μm region $\sim$ 25 μm from the wall, overcoming differences in morphology. 5) Cells experienced a repulsion from the walls at intermediate Re which was overcome during particle focusing.

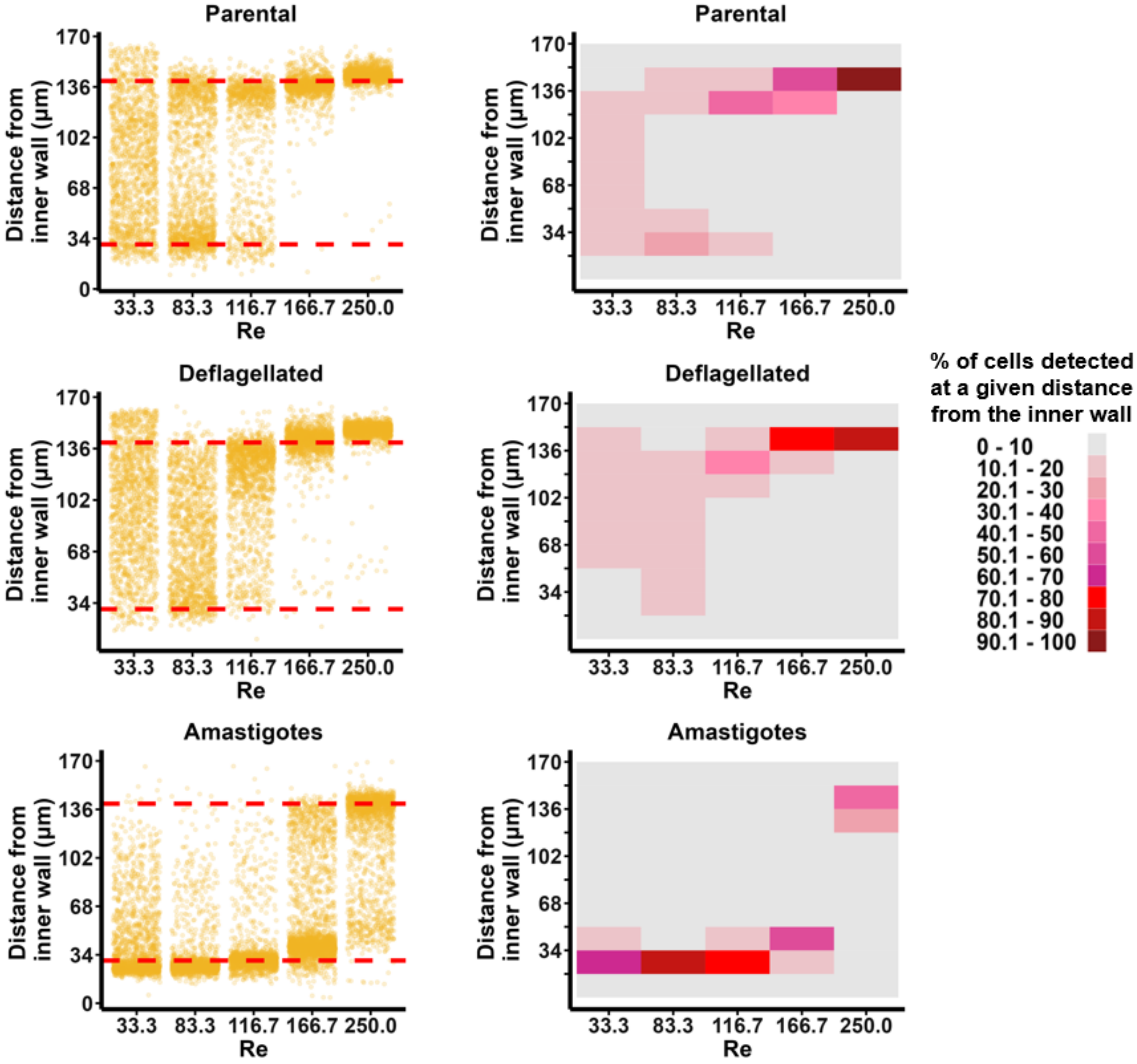

**Figure 5.7: Non-flagellated *L. mexicana* focus to the outer wall.**
Fixed deflagellated and amastigote populations were analysed for their focusing position within a 30 x 170 μm$^2$ channel using a high-speed camera and compared to the parental population (data for the parental population is replotted from figure 5.3). A single representative replicate of three is shown (n $\geq$ 965 per flow rate, per replicate). (Left) Each dot corresponds to a the focusing position of a single cell at a variety of Reynolds numbers (Re). The red dashed lines indicate a position 30 μm away from both the inner and outer wall. (Right) The percentage of parasites focusing at a given distance from the inner wall was calculated (channel width was divided into 10 sections), with red zones highlighting a high focusing concentration with > 70% of cells found within a tenth of the channel width.

### 5.2.5 Role of shape on focusing

After demonstrating that the flagellum had minimal effects on the focusing position of *L. mexicana*, attention was turned to the role of shape. There is a lack of research regarding the role of cell shape in curved channels; thus, to be able to sort *L. mexicana* based on their width or aspect ratio, a better understanding of the role of shape is first needed. As is typically carried out in the literature, rigid beads were first analysed to understand the behaviour of model particles, with non-spherical beads being compared to spherical beads with equivalent diameters (Fig. 5.8). The aspect ratios of the non-spherical beads were calculated from the given dimensions and were in the range of 0.63 – 0.81; outwith the range of the cells analysed (0.35 - 0.63). A wider range of aspect ratios would have been tested but a limitation was imposed by the sizes of beads commercially available. Thus, three different sizes of both pear-shaped beads and peanut-shaped beads were tested for their focusing position. The pear-shaped beads generally showed good correlation with spherical beads – focusing was first seen towards the inner wall at lower flow rates, the increase of which caused lateral migration away from the wall. At higher flow rates, non-spherical beads migrated further away from the inner wall than spherical beads. When looking at the spherical beads, an increase in the particle size (from 3 µm to 5 µm in diameter) resulted in a focusing position closer to the inner wall. This was also seen for pear-shaped beads until Re = 250.0 where all sizes demonstrated the same focusing position (a median of 56.4 µm away from the inner wall ± 2.6 µm).

For peanut-shaped beads, a similar behaviour was seen for particles ≤ 6.3 µm in length; at lower Reynolds numbers peanut-shaped beads behaved similarly to size matched spherical beads until Re = 250.0 where the peanut-shaped beads migrated further away from the inner wall. Again, both sizes of peanut-shaped beads had highly similar focusing positions, with a median of 99.15 µm away from the inner wall ± 1.65 µm. Interestingly, at Re = 250.0, despite having as little as 0.3 µm difference in size, 85% of the peanut-shaped beads ≤ 6.3 µm in length moved past the centreline of the channel in comparison to < 1% of pear-shaped beads. Finally for the largest spherical and peanut-shaped beads of 8 µm and 5.1 x 7.7 µm$^2$, respectively (with particle confinement ratios of 0.16 and 0.15, as calculated using Equation 1.3), a critical threshold seemed to have been reached in terms of size, where the particles were unable to move away from the inner wall. It can be noted that both the diameter of the 8 µm beads and the length of the 5.1 x 7.7 $\mu m^2$ beads exceeded ¼ (7.5 µm) of the channel height.

From these results, it was demonstrated that both particle shape and size contributed to the focusing position of beads. Particularly at higher flow rates, non-spherical particles migrated further from the inner wall than spherical beads at equivalent flow rates. It can also be seen that shape, outwith just length and width measurements, contributed to inertial focusing with both pear- and peanut-shaped beads having similar dimensions but different focusing positions, in line with the work of Roth [363]. Finally, the role of shape was seen to overcome differences in size, with similarly shaped, but differently sized particles aligning to highly similar positions within the channel.

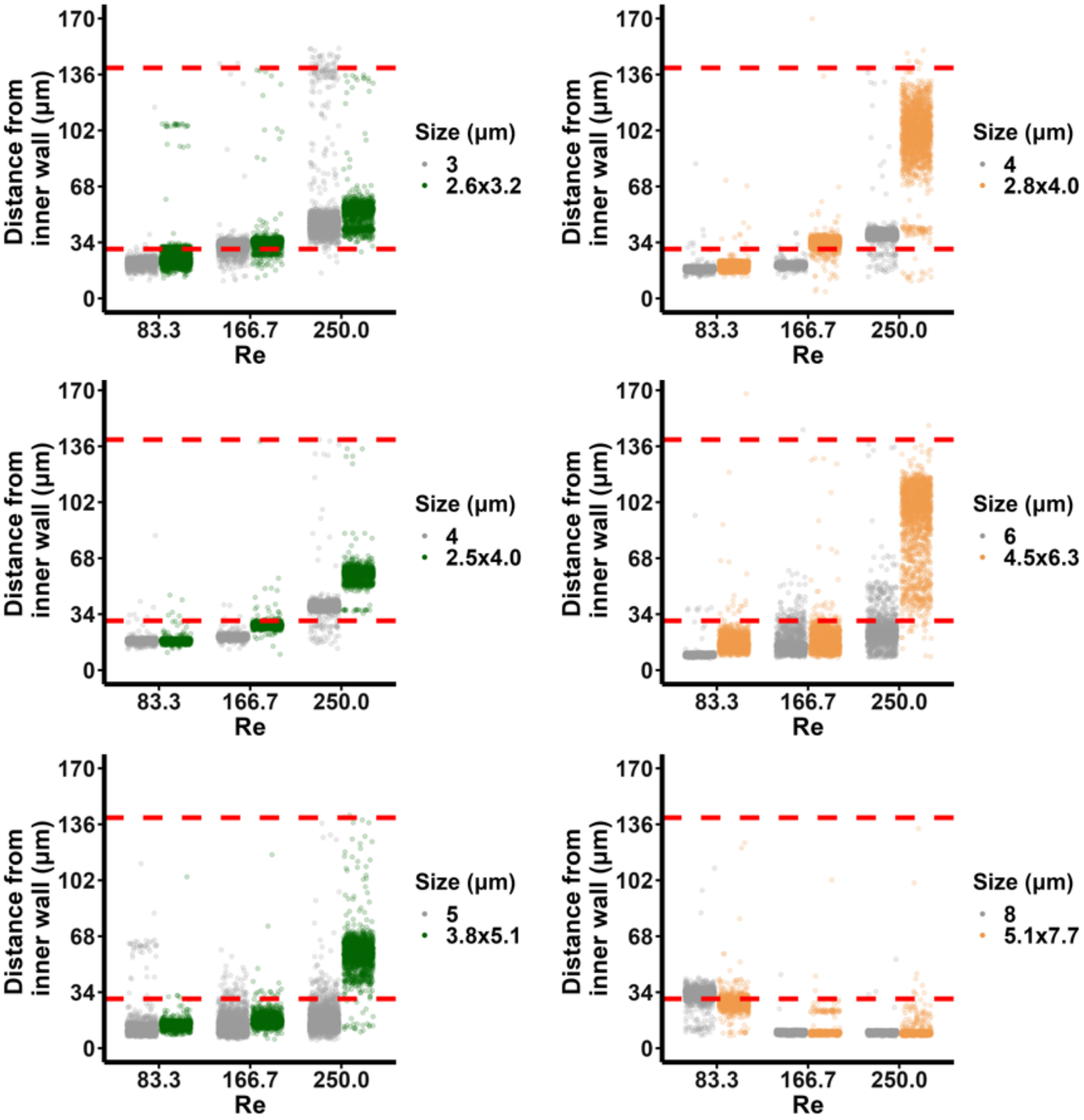

**Figure 5.8: Non-spherical beads undergo a higher level of lateral migration compared to spherical beads**

The focusing position of spherical beads was compared to that of non-spherical beads, where the longest measurement of the non-spherical bead matched that of the diameter of the spherical bead. Beads were analysed at various Reynolds numbers (Re) in a 30 x 170 µm$^2$ spiral channel using a high-speed camera, with each dot on the graphs representing an individual particle. (Left) Pear-shaped beads (green) with sizes of 2.6 x 3.2 µm$^2$, 2.5 x 4.0 µm$^2$, and 3.8 x 5.1 µm$^2$ were compared to that of spherical beads (grey) with diameters of 3, 4 and 5 µm, respectively. (Right) Peanut-shaped beads (orange) with sizes of 2.8 x 4.0 µm$^2$, 4.5 x 6.4 µm$^2$, and 5.1 x 7.7 µm$^2$ were compared to spherical beads with diameters of 4, 6 and 8 µm beads, respectively. Red dashed reference lines indicate positions 30 µm away from both the inner and outer wall.

While rigid, non-spherical beads were shown to migrate further away from the inner wall than their spherical counterparts, no beads tested were shown to behave similarly to *L. mexicana* with focusing positions at the outer wall. Therefore, in order to understand the role of shape in the focusing behaviour of *L. mexicana*, parental cells were chemically treated with the cell cycle synchronising drugs flavopiridol and hydroxyurea to produce populations with modified morphologies (Fig. 5.9). Traditionally, flavopiridol and hydroxyurea are used to synchronise different *Leishmania spp.* at G2/M and G1/S, respectively [133], [139], [160], [378]; however, cells continue to produce proteins while arrested, thus growing in size resulting in the morphological changes seen. The data were collected with the assistance of Sulochana Omwenga who both prepared and fixed the flavopiridol- and hydroxyurea-treated cells and quantified their DNA using IFC, while I carried out all data analysis (see Sections 2.1.2 and 2.2.5 for details).

DNA quantification showed that flavopiridol-treated cells had an increased percentage of cells with 4C DNA (G2/M/C in figure 5.9C) while the hydroxyurea-treated cells showed similar proportions in all cell cycle stages compared to control cells, indicating that synchronisation was not achieved. Despite this, morphological changes were still seen for both methods of treatments (Fig. 5.9D-F). Flavopiridol-treated cells were shown to be the largest cells by area (AUC of 0.89 compared to the parental cells), with a similar average length to the parental parasites (10.0 μm *vs* 9.5 μm, respectively, with an AUC of 0.54) but an increased width (4.9 μm *vs* 3.3 μm and an AUC of 0.92) and subsequently higher aspect ratio (0.51 *vs* 0.35 and an AUC of 0.74) (Fig 5.9D-F). Hydroxyurea-treated cells on the other hand, were longer (at 11.8 μm; AUC of 0.69) and wider (4.0 μm; AUC of 0.79) than the parental population, but as demonstrated by the ROC curve, had an almost indistinguishable distribution for their aspect ratios, with an AUC of 0.48 (Fig. 5.9D-F). Similarly to the deflagellated cells, the flavopiridol- and hydroxyurea treated cells were also classified based on their size distributions into SN, SW, LN and LW (Fig. 5.9B). The flavopiridol-treated cells were shown to be predominantly wide (48.8% as SW and 33.5% as LW), and thus had a reduced proportion of narrow cells (6.2% as SN and 11.5% as LN). In comparison, hydroxyurea-treated cells were predominantly long (40.0% LN and 28.9% LW) with only a total of 31.1% being short compared to 54.2% of parental cells. Thus, through chemical treatment, cell populations that were a similar length but wider (flavopiridol-treated cells), and the same aspect ratio but longer and wider (hydroxyurea-treated cells) were generated.

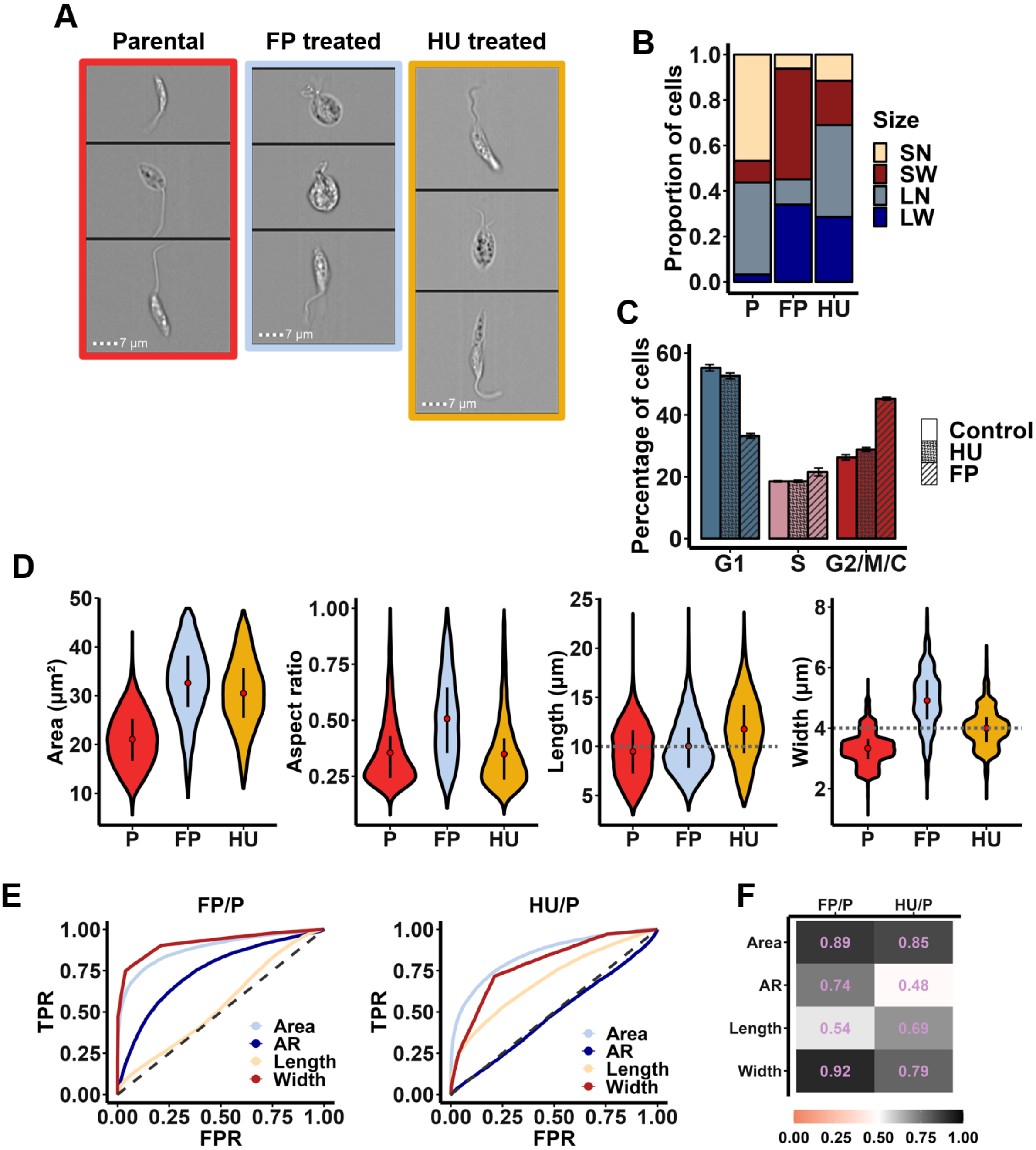

**Figure 5.9: Modified morphologies of L. mexicana**
(A) Example IFC images of fixed parental (P), flavopiridol-treated (FP) and hydroxyurea-treated (HU) cells. Scale bars: 7 µm. (B) The populations were classified based on their length and width measurements into short (S; ≤ 10 µm) or long (L; > 10 µm), and narrow (N; < 4 µm) or wide (W; ≥ 4 µm). The proportion of cells in each size classification was then calculated for each cell population. (C) DNA quantification was carried out for each cell population through propidium iodide staining. The DNA intensity profiles were analysed using IFC and the percentages of cells in each stage of the cell cycle were calculated using FCS Express's multicycle feature. (D) The measured area, aspect ratio, length, and width distributions of the P, FP, or HU populations. The black bars show the 25th - 75th percentile, and the mean is shown as the red dot. (E) Receiver operating characteristic curves were calculated from the distributions of each size measurement. The FP and HU populations were classified as the positive population and compared to the parental cells (the negative population). The grey dashed lines indicate where the true positive rate (TPR) is equal to the false positive rate (FPR), and thus morphological

parameters which lie close to the dashed line show little differences in distribution between the parental and drug-treated populations. The further the curves lie from the grey dashed line, the more different the distributions. (F) From the ROC curves, the area under the curve (AUC) values were calculated. An AUC value close to 0.5 indicates that there is little deviation in distributions between the drug treated cells and the parental cells. Values closer to 0 or 1 denote distributions with a high deviation from the parental population, with values > 0.5 (grey) indicating that the measurement is higher for the drug treated cells than for parental cells, while a value < 0.5 (peach) shows that the drug treated cells measured less than the parental cells. n > 12,962.

The flavopiridol- and hydroxyurea-treated cells were analysed for their focusing position within the 30 x 170 μm$^2$ channel and compared to the data from the parental line (Fig. 5.10). At low Reynolds numbers (Re $\leq$ 116.7), the wider flavopiridol-treated cells recirculated within the channel and did not have a definitive focusing position. At Re = 166.7, > 80% of the flavopiridol-treated population were located at the outer half of the channel; however, compared to both the parental, fewer hydroxyurea-treated cells were found within 30 μm of the outer wall. At the highest flow rate (Re = 250.0), these wider and higher aspect ratio cells reached the same focusing position of the parental cells, within 30 μm of the outer wall. For these cells, very little focusing was seen at the inner wall, with a focusing pattern more similar to that of deflagellated cells (Fig. 5.7). Hydroxyurea-treated cells on the other hand showed a distribution more similar to that of the parental cells: cells recirculated at Re = 33.3, had a bimodal distribution at Re = 83.3 and 116.7, and moved to the outer wall at $\geq$ 166.7.

The data presented thus far in Chapter 5 suggest that shape plays a large role in the focusing of *L. mexicana*; none of the morphologies tested had the typical focusing profile of beads, even for the roundest cells (amastigotes) tested which still focussed to the outer wall at Re = 250.0. Below a certain size threshold ($\sim$ 7.5 μm), at lower flow rates particles were able to focus towards the inner wall. Above that threshold, more elongated cells (i.e. with a lower aspect ratio) such as hydroxyurea-treated and parental cells (both with an aspect ratio of 0.35) were able to focus to both the inner and outer wall, while particles with a higher aspect ratio such as deflagellated and flavopiridol-treated cells (aspect ratios of 0.41 and 0.51, respectively) were unable to focus towards the inner wall. Instead these longer cells were found more evenly spread throughout the channel at a lower flow rates before focusing to the outer wall at higher Reynolds numbers.

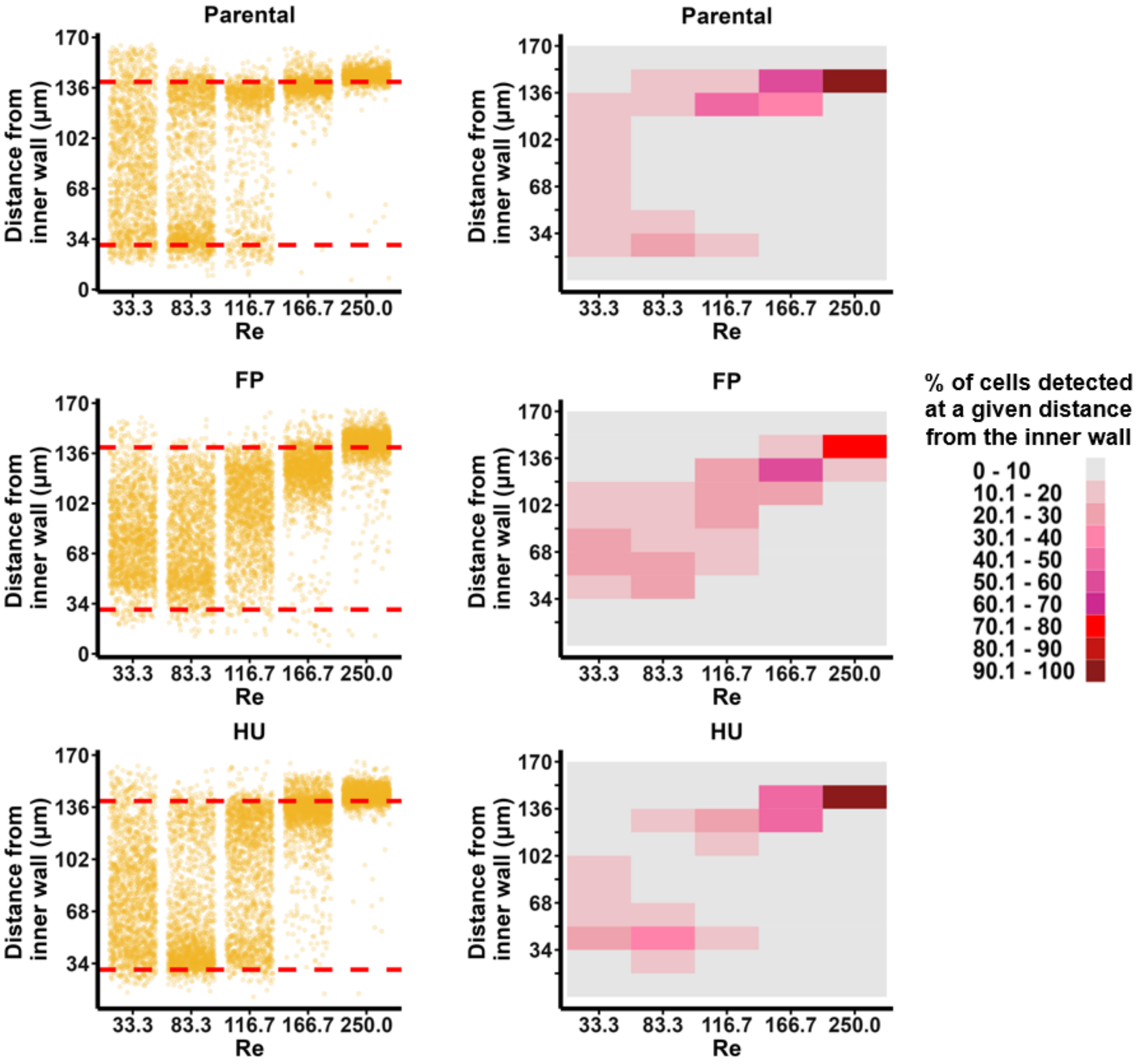

**Figure 5.10: Different shapes of *L. mexicana* focus to the outer wall**
Fixed, flavopiridol-treated (FP) and hydroxyurea-treated (HU) cells were analysed for their focusing position and compared to the focusing data of the parental population replotted from figure 5.3. (Left) The focusing position of individual cells within the 30 x 170 µm$^2$ channel was analysed using high-speed imaging at a variety of Reynolds numbers (Re). A single representative replicate of three is shown (n > 1065 per flow rate, per replicate). The red dashed reference lines indicate a position 30 µm away from both the inner and outer wall. (Right) The data from the dot plots was quantified to show the percentage of cells distributed across the channel width. For each flow rate, the channel was divided into 10 sections corresponding to a width of 17 µm. Each section was colour-coded (on a scale of 0-100 ) according to the percentage of cells falling within that section.

From figure 5.7, it was demonstrated that smaller and rounder amastigotes that focused predominantly located to the inner wall while focused cells with longer morphologies mainly located to the outer wall. It was therefore unexpected that at Re = 83.3, a higher proportion (> 50%) of the hydroxyurea-treated cells (a population with very few small and round cells) would have a focusing position at the inner wall (Fig. 5.10). Hundreds of high-speed images of each cell population were subsequently analysed to better understand the focusing behaviour of these different morphologies. From these images, elongated cells (in both the parental and hydroxyurea-treated populations) were shown to have two different orientations within the channel; cells at the inner wall predominantly orientated perpendicular to the channel wall, while cells focusing to the outer wall had an orientation aligned with the flow (Fig. 5.11A and C). Wider flavopiridol-treated cells on the other hand showed a variety of orientations, making patterns much more difficult to identify (Fig. 5.11B). It was therefore concluded that cell orientation was directly related to a cell's focusing position, and that cells with both a high confinement and a low aspect ratio were capable of focusing to both the inner and outer wall.

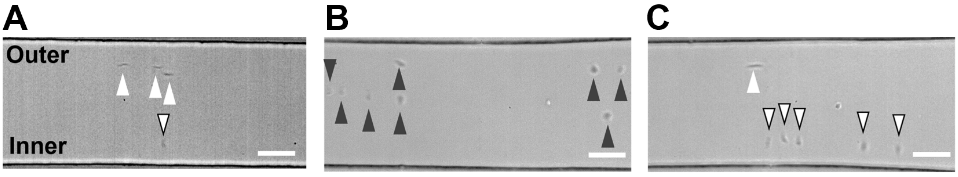

**Figure 5.11: *L. mexicana* will align in different orientations in different lateral positions within the channel.**
Fixed parental (A), flavopiridol-treated (B) and hydroxyurea-treated (C) *L. mexicana* parasites were imaged with a high-speed camera during sorting at Re = 83.3 within a 30 x 170 $\mu m^2$ channel. White arrowheads indicate cells which focused to the outer wall in an orientation aligned with the flow, white arrows with a black outline indicate cells which focused to the inner wall and are orientated perpendicular to the wall, while black arrows indicate cells with undefined orientations.

From the results shown in figure 5.7, it was demonstrated that short (both SW and SN) amastigotes focused to the inner wall at Re = 83.3 and 116.7. However, it was also shown through high-speed imaging that at a Reynolds number of 83.3, elongated cells were also able to focus to the inner wall. These contradicting results, along with the high heterogeneity seen within each population therefore made it difficult to understand how the morphology of individual cells related to their focusing position. Therefore, live parental cells were sorted into each of the four outlets and the morphology of each sorted population was measured *via* IFC, thus enabling the morphology of cells focusing within each ¼ of the channels width to be analysed. For this, a Reynolds number of 116.7 was selected: here, the parasites showed a bimodal distribution, with the majority of cells focusing to the outer wall. It was thus hypothesised that the high proportion of elongated cells would have migrated to the outer wall, and short cells (similar to amastigotes) would focus to the inner wall, thereby enriching for short and wide cells (as well as short and narrow cells), indicative of cells in the M/C stage of the cell cycle.

Thus, parental cells were sorted at Re = 116.7, the outlets were collected, and counts performed to obtain the distribution of cells across the channel (see Section 2.4.1 for details). From figure 5.12A, it can be seen that, like the data from the high-speed camera, the highest proportion of cells (37.8%) focus to the outer wall. However, the other 62.2% is spread more evenly across the other outlets. This variation in results may be due to differences in the cells size or shape, or changes in their mechanical properties (i.e. deformability) as a result of cell fixation. Looking at the cells within the channels, it was first assessed whether sorting at this Reynolds number had any effect on morphology. To achieve this, the data from all of the outlets were pooled to analyse the entire population of sorted cells. The area, aspect ratio, length and width of the sorted cells was then compared to the unsorted control cells. Visual inspection of the cells within each of the populations showed no obvious aberrations in morphology (e.g. an enlarged vacuole which is indicative of cell stress, such as was seen in Section 3.2.3 on the addition of cell dyes) (Fig. 5.12B). Morphological analysis demonstrated that the control cells and sorted cells had highly similar morphologies, with the sorted cells being slightly shorter and wider, as demonstrated by AUC values of 0.47 and 0.53, respectively, resulting in a higher aspect ratio (AUC of 0.54) (Fig. 5.12C and D). However, these values are still very close to 0.5, indicating that sorting had minimal effect on morphology.

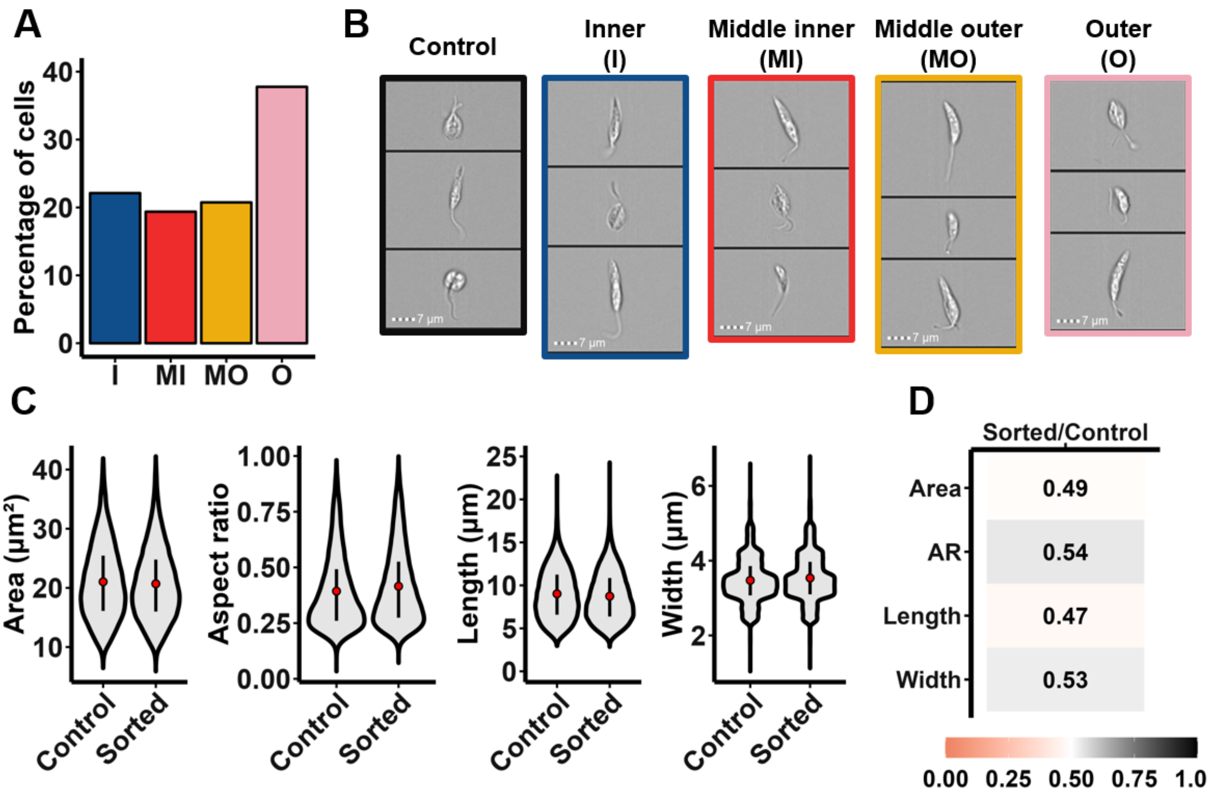

**Figure 5.12: Inertial sorting of live *L. mexicana* at Re = 116.7 had minimal effects of cell morphology.**
Live parental *L. mexicana* were sorted at a flow rate of 0.7 ml.min$^{-1}$ (Re = 116.7) using a 30 x 170 µm$^2$ spiral channel, and the cells from the outlets were collected. (A) Cell counts were performed on the sorted populations to obtain the percentage of cells found at the inner (I), middle inner (MI), middle outer (MO) and outer (O) outlets. The cells within the unsorted control population and each of the outlets were analysed by IFC, with (B) showing example images from each population. Scale bars: 7 µm. (C) The analysed data from each of the outlets were pooled to comprise the "sorted" population. The area, aspect ratio (AR), length and width of the sorted cells was then compared to the unsorted control population. The black bars show the 25th - 75th quartile ranges, and the red dots shows the mean values (n > 18,539). (D) The distributions of the control and sorted populations were compared, and the area under the curve (AUC) values were calculated and plotted as a heatmap. An AUC value close to 0.5 (white) indicates that there was little deviation in distributions between the sorted cells and the unsorted control cells. Values closer to 0 (peach) or 1 (black) denote distributions with a high deviation from the control population, with values > 0.5 indicating that the measurement is higher for the sorted cells than for control cells, while a value < 0.5 shows that the sorted cells measured less than the control cells.

When the morphology of cells in each of the sorted outlets was analysed, trends were seen that indicated shape-based sorting. Both the area and length of cells increased with increasing distance from the inner channel, while aspect ratio decreased (Fig. 5.13i and ii). Interestingly, the largest change in the distribution of morphologies (when compared to the control population) was seen for aspect ratio at the inner wall (AUC of 0.63), adding to the evidence that aspect ratio plays a role in sorting. This corresponds to SW cells seeing the largest enrichment from 14.1% to 24.8% (75.4% increase compared to the control) (Fig. 5.13iii). Additionally, an enrichment of long cells was seen at the outer wall, with 52% of all LN and 48% of all LW cells being collected in the outer channel (Fig. 5.13iv). While enrichment of the different sizes was seen across the channel, the purity of the enriched populations was still low, with the highest purity being for SN cells at the inner wall (purity of 57.0% compared to the control cells at 49.7%). For SW cells, the purity was low, with 75.2% of cells at the inner wall having alternative morphologies. This suggests that while SW cells may have a predilection for the inner wall, all morphologies were still able to recirculate and distribute across the channel. Thus, while these data give further evidence that shape, along with size are contributing to the focusing position of cells in curved channels, further aspects of cell composition are likely affecting cell rotation and causing particles to recirculate across the channel.

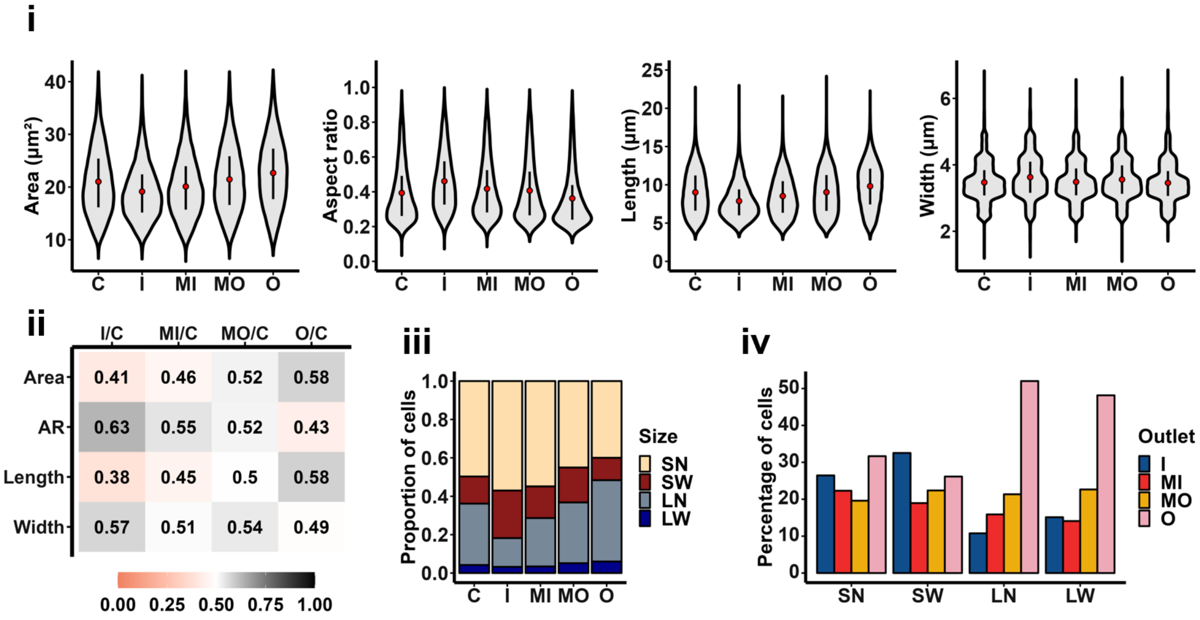

|  | I/C | MI/C | MO/C | O/C |
|---|---|---|---|---|
| Area | 0.41 | 0.46 | 0.52 | 0.58 |
| AR | 0.63 | 0.55 | 0.52 | 0.43 |
| Length | 0.38 | 0.45 | 0.5 | 0.58 |
| Width | 0.57 | 0.51 | 0.54 | 0.49 |

**Figure 5.13: Sorting of live *L. mexicana* enriches for short and wide cells.**
Live parental *L. mexicana* parasites were sorted at a flow rate of 0.7 ml.min$^{-1}$ (Re = 116.7) in a 30 x 170 µm$^2$ spiral channel. The unsorted control (C) and the sorted populations were collected at the inner (I), middle inner (MI), middle outer (MO) and outer (O) outlets and their morphologies analysed by IFC. (i.) The area, aspect ratio, length, and width distributions were plotted for each population. The black bars show the 25th – 75th percentile ranges of the data while the red dots show the means ($n \geq 18{,}539$). (ii.) The distributions in area, aspect ratio (AR), length and width measurements were then compared for the cells in each outlet to the unsorted control, and the corresponding area under the curve (AUC) was plotted. An AUC value close to 0.5 indicates that there is little deviation in distributions between the sorted and control cells. Values closer to 0 or 1 denote distributions with a high deviation from the control population, with values > 0.5 (grey) indicating that the measurement is higher for the sorted cells than for control cells, while a value < 0.5 (peach) shows that the sorted cells measured less than the control cells. (iii.) Using the cell length and width measurements obtained from IFC, cells were classified based on their size into short (S; ≤ 10 µm in length) or long (L; > 10 µm in length) and narrow (N; < 4 µm in width) or wide (W; $\geq$ 4 µm in width). The proportion of cells in each category was plotted for each outlet. (iv.) The percentage of each size category found in each outlet was calculated ($n \geq 18{,}539$).

When considering all particles tested, various conclusions regarding the role of shape in focusing can be drawn from the data (Fig. 5.14). Firstly, within this device, all beads behaved as expected showing focusing positions towards the inner wall, with peanut-shaped beads having a focusing position further away from the inner wall than any other bead shape or size (Fig. 5.8) [201], [363]. Additionally, in the literature it has been demonstrated that in straight channels, beads and cells with similar rotational diameters behave similarly [200], [231]. However, here it is evident that in curved channels, this is not the case. While cell populations of similar sizes had similar focusing patterns within the channel (e.g. parental *vs* deflagellated populations), the cells did not behave like beads. Flavopiridol-treated cells and spherical beads both had lengths of 10 µm, but different widths (5 µm *vs* 10 µm, respectively); however, the flavopiridol-treated cells were unable to localise to an equilibrium position at the inner wall, and instead displayed a tight focusing position to the outer wall at higher flow rates. 10 µm beads, on the other hand, showed the opposite behaviour, focusing to the inner wall at all flow rates tested, with no focusing to the outer wall. A similar deviation in behaviour was seen between beads and cells with equivalent lengths and widths. Amastigotes (with a width of 3.4 µm and a length of 5.5 µm) focused to the inner wall at low flow rates (Fig. 5.7), as did 3.8 x 5.1 µm$^2$ pear-shaped beads (Fig. 5.8); however, at high flow rates, the amastigotes were able to migrate to the outer wall, unlike the equivalently sized beads. The amastigote cells were the only cells tested which showed a predominant focusing position at the inner wall at the flow rates tested. This may be due to their increased aspect ratio, or due to their smaller length (corresponding to a particle confinement ratio of 0.11 *vs* 0.19 for parental cells). Additionally, they were the only cell type tested which had a length of < ¼ of the channel height. This was shown to be an important threshold as both spherical and non-spherical beads > ¼ of the channel height were unable to move away from the inner wall, even at the highest flow rates tested (Fig. 5.3 and 5.8).

| | **Parasites** | | | | | **Spherical beads** | | | | | | **Non-spherical beads** | | | | | |
|---|---|---|---|---|---|---|---|---|---|---|---|---|---|---|---|---|---|
| **Cell/bead type** | **P** | **D** | **A** | **FP** | **HU** | | | | | | | **Pear-shaped** | | | **Peanut-shaped** | | |
| **Length** | 9.5 | 9.1 | 5.6 | 10.0 | 11.8 | 3.0 | 4.0 | 5.0 | 6.0 | 8.0 | 10 | 3.2 | 4.0 | 5.1 | 4.0 | 6.3 | 7.7 |
| **Width** | 3.3 | 3.6 | 3.5 | 4.9 | 4.00 | 3.0 | 4.0 | 5.0 | 6.0 | 8.0 | 10 | 2.6 | 2.5 | 3.8 | 2.8 | 4.5 | 5.1 |
| **AR** | 0.35 | 0.41 | 0.63 | 0.51 | 0.35 | 1.00 | 1.00 | 1.00 | 1.00 | 1.00 | 1.00 | 0.81 | 0.63 | 0.75 | 0.70 | 0.71 | 0.66 |
| **Focus to IW** | Y | N | Y | N | Y | Y | Y | Y | Y | Y | Y | Y | Y | Y | Y | Y | Y |
| **Focus to OW** | Y | Y | Y | Y | Y | N | N | N | N | N | N | N | N | N | Y | Y | N |

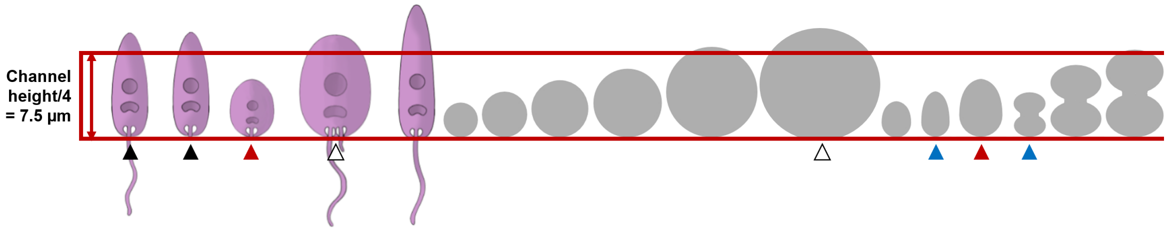

**Figure 5.14: Summary of focusing behaviour of *L. mexicana* populations and beads.** The average length (µm), width (µm), and aspect ratio (AR) of parental (P), deflagellated (D), amastigote (A), flavopiridol-treated (FP) and hydroxyurea-treated (HU) parasites, along with spherical and non-spherical beads are given. A green yes (Y) or a red no (N) demonstrates whether > 70% of particles did or did not focus within 34 µm of the inner (IW) or outer wall (OW) at at least one Reynolds number. A light green Y demonstrates where > 70% of particles located within the inner or outer half of the channel but further than 34 µm from either wall. A graphical representation is given to demonstrate the sizes of the different particles analysed, in relation to ¼ of the height of the channel. The arrows identify particles with equivalent length measurements, including parental and deflagellated cells (black arrows); amastigotes and pear-shaped beads (red arrows); flavopiridol-treated cells and 10 µm beads (white arrows); and pear-shaped and peanut-shaped beads (blue arrows).

### 5.2.6 Role of confinement on focusing

To test the relationship between particle size within the channel (confinement) and focusing position within the channel, the parental population was analysed within a channel with a larger cross section (60 x 360 μm$^2$). By maintaining the proportions of the channel, the Reynolds number and the Dean number could be matched between the smaller and larger devices. Thus, within the larger channel design, the only parameter which was changed was the confinement of the particle, enabling a direct comparison between devices. From figure 5.15, it can be seen that at a Reynolds number of 79.4, focusing occurred solely at the inner wall, which was never seen for parental cells in the 30 x 170 μm$^2$ channel (at the closest Reynolds number at 83.3). At Re = 119.0 and 158.7, particles had bimodal distributions, with cells focusing to both the inner and outer wall, and at Re $\geq$ 261.9, the focusing at the inner wall was lost with > 80% of particles being found within a 36 μm wide region at the outer wall. Interestingly, the parental cells demonstrated a focusing pattern most similar to amastigote cells within the 30 x 170 μm$^2$ device, being able to focus to the inner wall at Re ≤ 166.7 and with a sharp focusing position at the outer wall at Re = 250.0 (Fig. 5.7). However, in contrast, the parental cells were able to start focusing towards the outer wall at Reynolds numbers as low as 119.0 for the 60 x 360 μm$^2$ channel (occurred at Re = 83.3 in the smaller device). The ability to focus to the inner wall is thus most likely a result of the low particle confinement, with parental and amastigote cells having similar particle confinement ratios of 0.09 *vs* 0.1, respectively. Similarly, both the amastigotes and the parental cells are < ¼ of the channel height in the corresponding devices, suggesting that a lower particle confinement and a length < ¼ channel height is required for particles to focus to the inner wall. As with all the cell lines tested, the parental cells in the 60 x 360 μm$^2$ device focused to the outer wall, conserving the theory that a low aspect ratio aids in particle migration to the outer wall. Additionally, the same “barrier” force is seen between both devices, which is positioned around $\sim$ 60 μm away from the channel walls in the larger device (Fig. 5.15A). Again, this also happens to be the height of the channel.

These data thus conform with the hypothesis that there is a critical threshold on the length, below which particles are able to focus towards the inner wall, as well as with the hypothesis that a low aspect ratio assists particle migration to the outer wall.

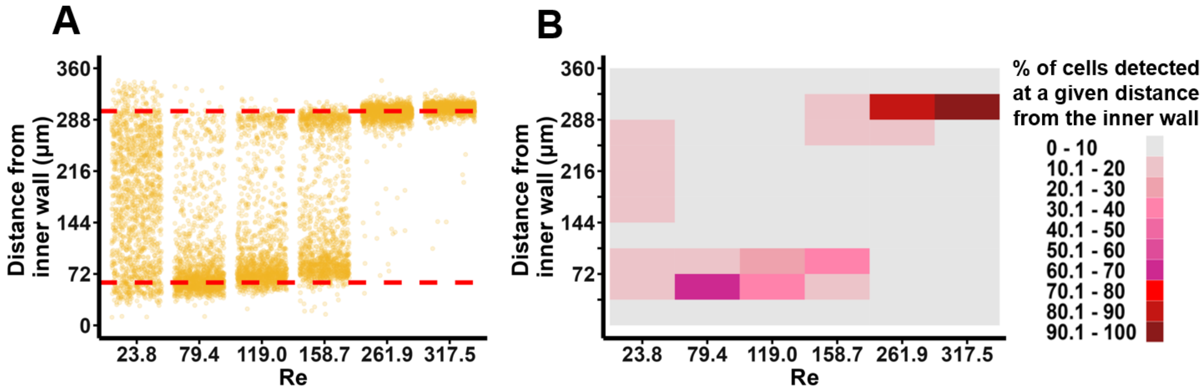

**Figure 5.15: Fixed parental *L. mexicana* focus to the outer channel in a larger device.** Fixed *L. mexicana* cells were analysed for their focusing position in a channel with a cross section 60 x 360 µm$^2$. (A) The focusing position of individual cells over a range of Renolds numbers (Re) within the microfluidic channel as analysed using a high-speed camera. The red dashed lines indicate a position 60 µm away from both the inner and outer wall (n > 1,500). (B) The data from (A) was quantified to show the distribution of cells along the channel width. For each flow rate, the channel width was divided into 10 sections; each section corresponds to a distance of 36 µm and was colour-coded (on a scale of 0-100) according to the percentage of cells falling within that section. Red boxes indicate a region with > 70% of particles focusing within a 36 µm region.

### 5.2.7 Analysis of fluid behaviour within the microfluidic chip

As has been demonstrated in the literature, non-spherical particles are able to affect the fluid flow profile, thought to result in particles moving further away from the inner wall [364]. It has also been shown that in curved channels at De $\geq$ 30.2, the formation of secondary Dean vortices are able to trap both rigid spherical beads and deformable RBCs at the outer wall [379]. Therefore, it was hypothesised that the low aspect ratio of these parasites (all cell populations tested had an average aspect ratio ≤ 0.63) altered their rotation within the flow, deforming the fluid profile to induce the formation of secondary Dean vortices, thus causing an equilibrium position at the outer wall. According to the work done by Nivedita [379], a higher Dean number must be achieved in channels with lower aspect ratios (as opposed to channels with higher aspect ratios) before secondary vortices are able to form. Nivedita demonstrated that in a channel with an aspect ratio of 1:5, secondary Dean vortices were first detected at De > 39. In the 30 x 170 µm$^2$ channel (aspect ratio of 1:6), the highest Reynolds number used was Re = 250.0, corresponding to a Dean number of 28.6 which is below the theoretical threshold for the formation of secondary Dean vortices. Thus, if the parasites are capable of deforming the flow, this may explain why parasites and not rigid spherical beads focus to the outer wall.

In order to test this hypothesis, an attempt was made to replicate the experiments carried out by Nivedita to visualise the flow profile within the 30 x 170 μm$^2$ channel [379]. Fluorescein dye in concentrations between 1 μm and 26.6 μm was pumped into the channel in the reverse direction; by adding fluorescein in through the inner channel outlet and PBS through the middle inner outlet, the recirculation of the fluorescein dye across the channel could be imaged (Fig. 5.16; see Section 2.4.1 for details).

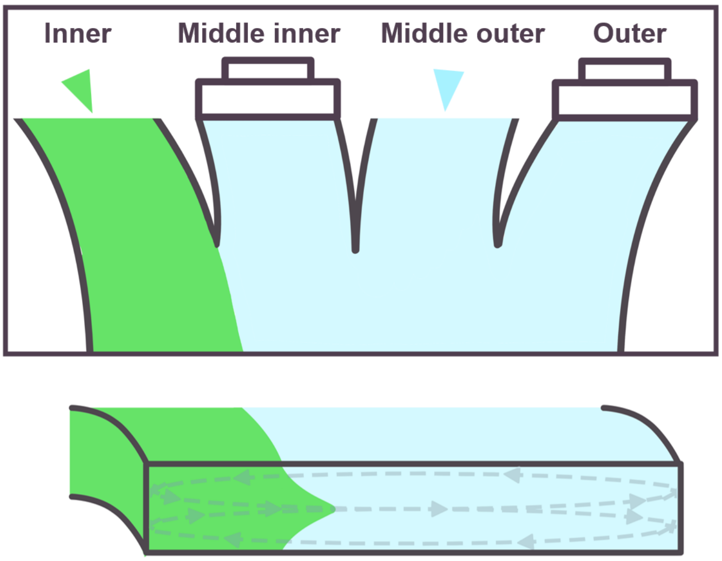

**Figure 5.16: Representation of fluorescein injection into channel.**
A graphical representation of injecting fluorescein dye (green) and PBS (blue) into the 30 x 170 μm$^2$ channel, from a top-down view of the channel (top) and an example from the cross section (bottom). Fluorescein was added into the inner most outlet (inner) as represented with the green arrowhead, while PBS was injected into the middle outer outlet (middle outer) as shown with the blue arrowhead. The other two outlets were sealed off to prevent back flow of the fluid. The Dean vortices are represented by the dashed grey lines.

Here, prior to using confocal microscopy (as was carried out in the literature to image the z-plane), the setup was first tested and optimised with an inverted fluorescence microscope. Figure 5.17 shows example images of the fluorescein dye within each of the 6 turns of the spiral channel at Re = 83.3 along with their corresponding intensity profiles. From these data, the flow can be seen to change throughout each rotation of the channel. In the first rotation, a sharp streak of fluorescence was seen at the inner wall (Fig. 5.17A). In the second and third rotations (Fig. 5.17B and C, respectively), the fluorescence had moved into the centre of the channel before shifting almost entirely to the outer wall. At the fourth and fifth rotation, the intensity was strongest again at the inner wall and then redistributed throughout the channel. At the final turn, the fluorescein was strongest at the outer wall; however, from these data the fluid profile is unable to be discerned due to the bottom-up view of a single focal plane of the channel.

Thus, in order to analyse the flow in the channel cross section, the experiment was repeated but analysed using a confocal microscope to image through the z-plane of the device. To ensure that the entire depth of the channel was captured, an in-focus plane of the channel was first found which was set as the “centre”. The microscope was then set to capture between a set number of images through a defined distance (distances of between 25 and 50 µm were tested) above and below that centre focal plane. Unfortunately, despite testing a multitude of settings (e.g. modifying the intensity of the lasers, the concentration of the dye, the exposure time and the amount of gain) and even different confocal microscopes, fluorescent signal was detected through the entire depth imaged, and not just within the 30 µm of the channel itself. It was hypothesised that the fluorescence of the dye was too bright and too widespread throughout the channel and was therefore giving too much background noise. Thus, the flow profile within the channel was unable to be imaged.

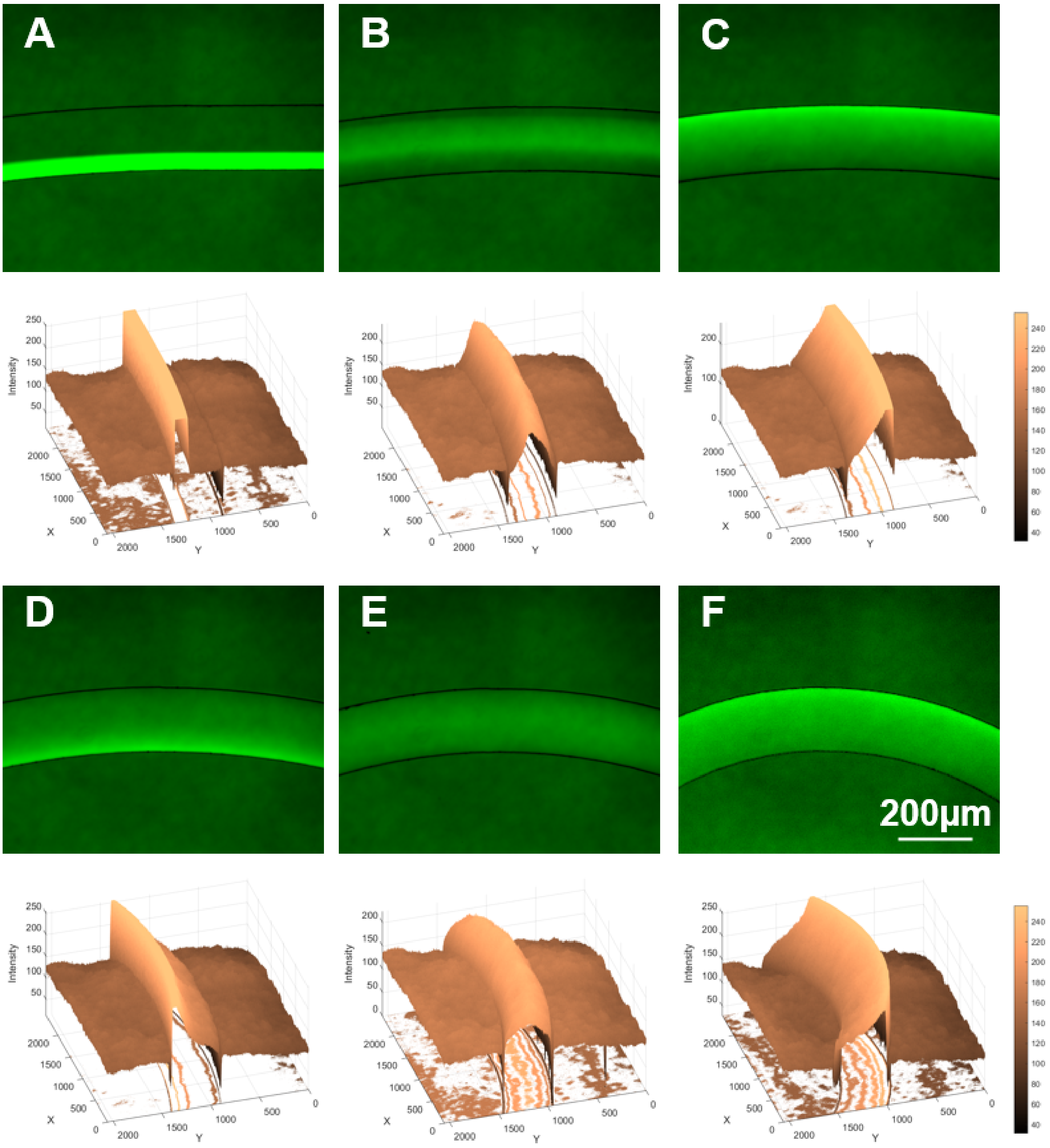

**Figure 5.17: Optimisation of flow profile analysis using fluorescein dye.**
In the 30 x 170 µm$^2$ channel, fluorescein was injected into the inner most outlet channel at a concentration of 26.6 µM at a flow rate of 0.125 ml.min$^{-1}$ using a hydraulic pump. Similarly, PBS was pumped at 0.375 ml.min$^{-1}$ into the middle outer outlet. The other two outlet channels were blocked to prevent the backflow of fluid. (A-F) After the flow within the device had equilibrated, each of the six rotations of the channel were imaged, starting at the outer rotation of the channel, using an inverted fluorescence microscope and acquired using Zen Blue software. Scale bars: 200 µm. The corresponding intensity profiles were generated in MATLAB and are shown below each fluorescence image.

In order to reduce the level of fluorescence within the channel, and thus reduce the permeation of the fluorescence throughout the plastic of the device, it was tested whether the z-position of beads could be analysed instead of fluorescein. As beads have a much smaller area of fluorescence than the fluorescein dye, the background noise was hypothesised to be minimal in comparison, and using small beads which did not focus in the channel may have enabled the visualisation of the flow. To test whether spherical beads could be imaged in 3D within the device, larger beads of both 3 and 5 μm in diameter were first imaged in the device at different flow rates using a confocal microscope. While high intensity fluorescence signals were detected at a single point on the channel x-axis for each flow rate (Fig. 5.17), again, fluorescence signal was detected throughout the entire 50.5 μm imaged, instead of just the 30 μm of the channel (Fig. 5.18). Therefore, the flow profile within the device used was not able to be determined and had to be inferred from the literature.

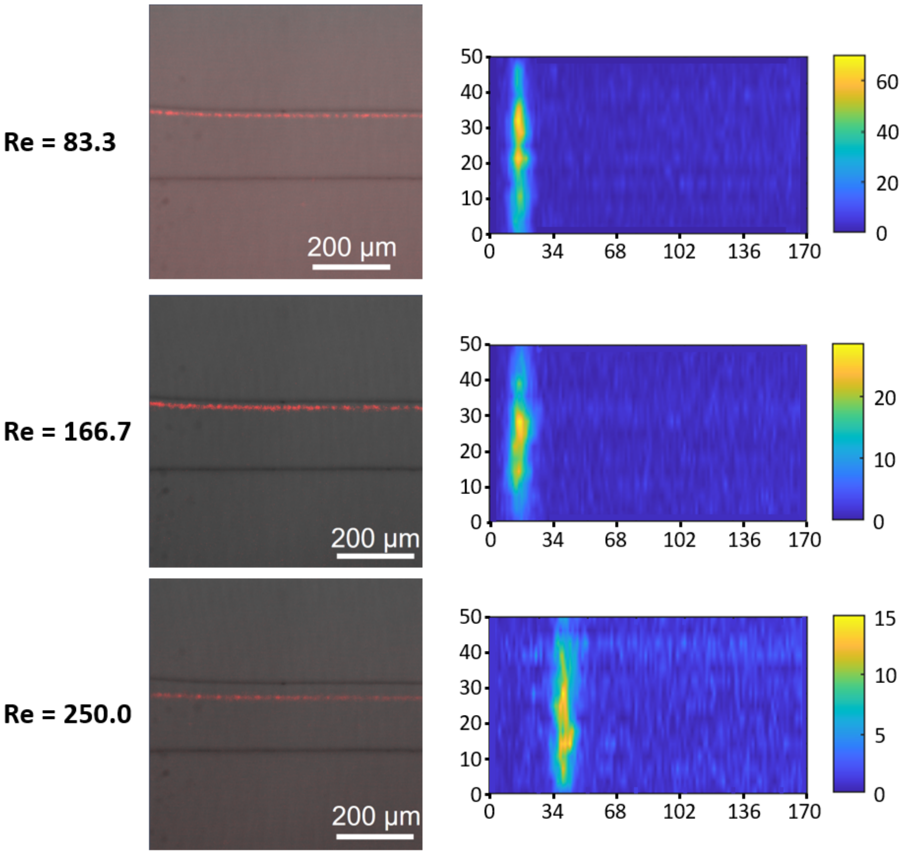

**Figure 5.18: Z-plane imaging displays high background fluorescence.**
5 μm red fluorescent beads were injected the 30 x 170 μm$^2$ channel at Re = 83.3 (top), 166.7 (middle) and 250.0 (bottom). Left: single composite images of the channel and the red fluorescent streak of the beads. Scale bars: 200 μm. Right: the corresponding reconstructed z-stack of the focusing of beads. Z-stack images were acquired using a spinning disk confocal microscope in the Zen Blue software for which 15 slices were imaged every 3.6 μm, thus spanning 50.5 μm in depth. Images were extracted and analysed in MATLAB where the area spanning the channel width was identified, background removed, and the intensity plotted (see Section 2.4.2 for details). The resulting heatmaps show the depth (μm) of the channel imaged on the y-axis, the width (μm) of the channel along the x-axis and the colour shows the intensity of the pixels.

As the fluid profile was unable to be determined though imaging of the z-plane, it was hypothesised that if *L. mexicana* cells were deforming the fluid flow resulting in secondary Dean vortices, that beads would also be trapped in the same secondary vortices and focus to the same lateral position as the cells. A mixture of fixed parental *L. mexicana* parasites and 5 µm beads were subsequently analysed for their focusing position within the 30 x 170 $\mu m^2$ device at Re = 166.7. From the data obtained, it was seen that there were two separate populations of particles, one focusing to the inner wall and one focusing to the outer wall (Fig. 5.19). Analysis of the brightness of the particles, and inspection of the corresponding images revealed that the darker 5 µm beads focussed to the inner wall, while the lighter parental cells focused to the outer wall. The focusing behaviour of both particles matched the focusing position of when they were analysed separately, indicating that the presence of the *L. mexicana* parasites did not affect the behaviour of the beads and vice versa. These results however cannot confirm or refute the theory of the formation of secondary Dean vortices as it is possible that either no vortices are forming and thus the beads focus to the inner wall, or that there are secondary vortices forming but that the beads do not get trapped within these vortices. While this may be the case, these results also highlight the potential for shape-based separation, isolation and/or concentration of non-spherical particles, with 94.1% of *L. mexicana* cells focusing to the outer half of the channel, and 99.8% of beads focusing to the inner half of the channel. Such an application may be the isolation of pathogens from water [228].

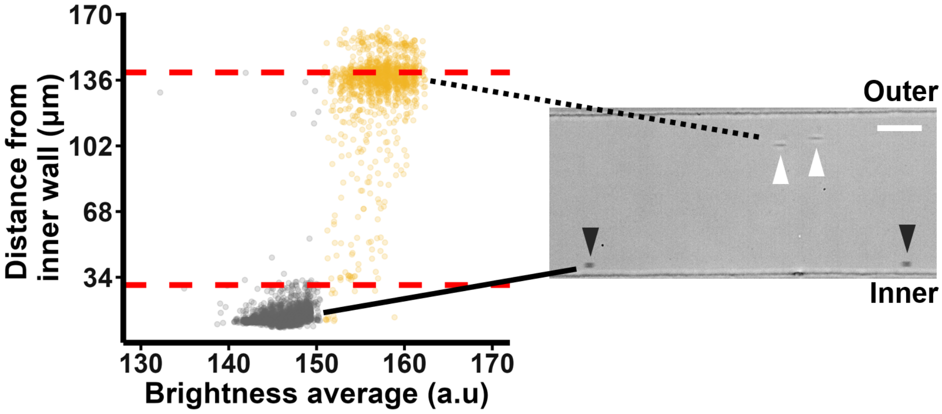

**Figure 5.19: *L. mexicana* and beads have highly different focusing positions.** A mixture of fixed *L. mexicana* parental cells and beads with a diameter of 5 µm were imaged with a high-speed camera during focusing within a 30 x 170 µm$^2$ channel at Re = 166.7. The particles were plotted based on their distance from the inner wall *vs* their brightness, with 5 µm beads (grey) being identified as having a brightness as ≤ 150 arbitrary units (a.u) and *L. mexicana* cells (gold) as having a brightness of > 150 a.u. The red dashed reference lines indicate positions 30 µm from the inner and outer walls. An example image containing particles from within these two populations are shown on the right-hand side. *L. mexicana* cells focusing to the outer wall are shown by the black dotted line and indicated in the image using white arrowheads, while 5 µm beads from the population of particles focusing to the inner wall are shown with the solid black line, with individual particles being highlighted with black arrowhead. Scale bar: 20 µm.

## 5.3 Discussion and conclusions

In this Chapter, it was aimed to take advantage of the morphological changes seen in *L. mexicana* to achieve a shape-based method of cell cycle synchronisation. It was demonstrated in Section 4.2.7 that while there is a fairly high amount of overlap in morphology between the different cell cycle stages, the M/C cells proved to be the most morphologically distinct, with an average length of 7.5 µm, a width of 4.3 µm and an aspect ratio of 0.56. By defining a cut off of cells with an aspect ratio of $\geq$ 0.5, a 65.2% purity of M/C cells and a 5.8X enrichment could hypothetically be achieved. However, the role of cell shape in inertial microfluidics had not been well studied in curved channels, with cell length being the primary differentiating factor driving separation. As M/C cells overlap with early G1 cells in terms of length, sorting based on the length would be unsuitable to achieve a pure population. Thus, a better understanding of the relationship between cell shape and inertial microfluidic focusing position was sought. To achieve this, four different morphologies of *L. mexicana* were generated and compared to that of the parental line - chemically deflagellated cells, differentiated amastigotes, flavopiridol-treated cells and hydroxyurea treated-cells. IFC enabled high-throughput and robust morphological analysis of the generated cell populations, such that the flagellation status, aspect ratio, length and width of cells were analysed for their contribution to inertial microfluidic sorting.

### Effect of the flagellum on the focusing position

Initial tests with the parental cell population demonstrated that the elongated prolate-like parental *L. mexicana* parasites had a focusing position towards the outer wall at Reynolds numbers as low as 83.3. In the literature, a preferential focusing position at the outer wall is unusual, with spherical particles, non-spherical particles and cells predominantly focusing to different places at the inner wall [201], [362], [380]. While there are a variety of circumstances which cause particles to migrate to the outer wall [198], [357], [379], [381], [382], the most relevant to this study was the work carried out by Feng who demonstrated that flagellated sperm cells focused to the outer wall while beads and RBC focus to the inner wall [366]. They oberved that the flagellum altered particle rotation, and that by removing the flagellum the cell bodies focused to the inner wall. In contrast, here the flagellum of *L. mexicana* was shown to have little effect on particle focusing with similarly sized and shaped deflagellated cells also migrating to the outer wall. There are two possible explanations for this discrepancy with the literature. Firstly, it is possible that both the elongated cell shape and the presence of the flagellum are having the same effect of stabilising the rotation of the cells within the flow, causing them to migrate to the outer wall. Thus, by removing the flagellum, the elongated shape would maintain their focusing position at the outer wall. In contrast, the cell bodies of sperm are rounder and thus the loss of the flagellum may have altered their rotation resulting in focusing to the inner wall. This hypothesis is substantiated by the high-speed imaging demonstrating that *L. mexicana* cells have a stable rotation at the outer wall and align with the flow. The second possibility is that the sonication of the spermatozoa to remove their flagella is also having an effect on the cell morphology, which in turn affects their focusing position.

### Effect of cell confinement and shape on focusing position

As the flagellum was shown to have little effect on the focusing position, the role of cell size and shape was next tested using spherical and non-spherical beads as well as *L. mexicana* cells with different morphologies. From this work, a variety of observations regarding the role of shape were made. i.) The diameter of a bead is not equivalent to the length of *L. mexicana* parasites in terms of determining focusing position, with all parasites and beads having highly different focusing positions. ii.) Cells with the highest aspect ratios (amastigote cells and flavopiridol-treated cells) required a higher Reynolds number to form a sharp focusing position at the outer wall, compared with lower aspect ratio cells. iii) When sorting live cells, it was seen that higher aspect ratio cells showed the highest enrichment at the inner wall while lower aspect ratio cells were enriched at the outer wall. iv.) Particles with the same aspect ratio but different dimensions did not focus to the same location. This was seen between both bead and *L. mexicana* samples. v.) A low particle confinement ($\lambda \leq 0.11$) within the channel enabled particles to focus towards the inner wall at lower flow rates. Similarly, these particles were shown to have a length of < ¼ of the channel height. On the other hand, particles with a higher confinement ($\lambda \geq 0.18$), or a length of > ¼ of the channel height, did not focus at the inner wall at any flow rate tested. vi.) The exception to this was highly elongated cell types (hydroxyurea-treated and parental) which focused to both the inner and outer wall at lower flow rates, as a function of particle rotation. Long cells orientated either perpendicularly to the walls at the inner wall or aligned with the flow at the outer wall. Rounder cells on the other hand did not show any trends in terms of their orientation and demonstrated a higher level of recirculating within the flow. vii.) At high flow rates, all cells, regardless of shape or size, focused to the same position within the channel $\sim$ 30 µm from the outer wall. No beads demonstrated this focusing position, even when mixed with cells.

From these observations, it is evident that the focusing behaviours of particles, particularly non-spherical cells, is highly complex. These data have demonstrated that both cell length and aspect ratio contribute to determining the equilibrium position of a particle. At low flow rates, particle confinement seems to be responsible for particles focusing at the inner wall; cells with a length < ¼ of the channel height focused towards the inner wall. Increasing the length of particles past this threshold increased the likelihood that cells will be distributed throughout the channel width. At higher flow rates, shape seemed to be the largest factor in determining focusing position, with elongated cells focusing towards the outer wall. At the highest flow rate tested, all cells showed a conserved focusing position at the outer wall, regardless of differences in cell length. This was thought to be due to the non-spherical nature of the cells altering their rotation compared to spherical particles, as elongated cells were shown to align with the flow at the outer wall.

While particle confinement and aspect ratio affect particle focusing, they cannot explain all of the behaviours seen. For example, of all beads tested, peanut-shaped beads (with a length ≤ 6.3 μm) focused closest to the outer wall, despite having an aspect ratio of $\sim$ 0.7. Furthermore, while enrichment of SW and LN cells was seen during the live sort, the purity of these populations was low, with all outlets having a mixture of different sizes. This suggests that cells are predominantly recirculating throughout the channel rather than focusing based on their size or shape. Instead, other aspects of cells' morphology may be preventing their stable rotation within the flow, for example, the surface texture of the cells. In *L. mexicana*, it is known that the surface of the cells is not smooth and instead has ridges in a chiral shape which help the cells to swim in a stable manner [383]. These ridges may be causing the flow around the cell to be turbulent at lower flow rates, to prevent a stable rotation and result in cells recirculating. It has also been shown that cell deformability affects a particles rotation within the flow which may be the cause for these particles migrating to the outer wall [196], [356]. An attempt was made to analyse the deformability of these parasites, although due to their elongated shape it was difficult to draw any conclusions from the data. However, there seemed to be minimal differences in the focusing behaviour between live and fixed cells, and as fixation is known to affect cell deformability, the effect of cell deformability was thought to be minimal. Interestingly, it is thought that deformable particles alter their shape as a result of the shear forces, taking on a more prolate morphology [196]. It has been shown that instead of rotating, these particles "tank-tread" and thus maintain this elongated shape within the flow. It is therefore possible that the deformable particles and the elongated *L. mexicana* cells experience the same behaviour in the flow, with a non-rotating elongated shape causing migration to the outer wall.

While there are many aspect of a cells morphology which may contribute to the complex focusing behaviours seen within inertial microfluidic devices, this work, along with the literature has indicated that these morphological features likely affect cell rotation which directly relates to their focusing position [364], [366]. Future work into understanding the relationship between cell rotational behaviours within curved channels may provide a better understanding of how and where cells focus within such microfluidic devices.

### Cell cycle separation

In terms of sorting the different morphologies for cell cycle synchronisation, the largest enrichment was seen for SW cells from 14.1 to 24.8%, a morphology indicative of cells in M/C phase. The low enrichment is hypothesised to be due to a variety of reasons. Firstly, as discussed, the complex behaviours in the device made shape-based separation difficult. This was exacerbated by the high amount of overlap between the morphologies of the different stages of the cell cycle, with both early G1 cells and M/C cells having similar lengths, but different widths. Furthermore, the behaviour of fixed cells was predominantly analysed, which was previously shown to cause cells to shorten and widen, thereby increasing the proportion of SW cells and reducing the size difference between cell types. In contrast, when working with live cells, a high number of sorted cells was required for ImageStream analysis (> $4 \times 10^6$ cells.ml$^{-1}$ per outlet). With a single microfluidic channel (i.e., not multiplexed) at a flow rate of 0.7 ml.min$^{-1}$ this took $\sim$ 46 minutes of continual sorting, excluding time for processing the collected outlets for ImageStream analysis as well as refilling the 10 ml syringe. Thus, lengthy processing times may have caused cells to progress through the cell cycle from their initial time of sorting, adding to the heterogeneity seen in the sorted sample.

Further work would be beneficial to achieve a higher level of purity in sorting the different cell cycle stages of *L. mexicana.* Firstly, quantification of the DNA content of the sorted cells would enable a better understanding of how the different cell cycle stages were being sorted, as well as an indication of synchronisation purity. Increasing the speed of sorting (i.e. by channel multiplexing) would reduce the possibility of cells progressing through the cell cycle. Alternatively, developing a portable method of analysing the sorting of live cells during focusing would enable the investigation of particle behaviour without any time constraints. Channel design could be improved to achieve a higher level of separation: in both the 30 x 170 μm$^2$ and the 60 x 360 μm$^2$ channel, *L. mexicana* with $\lambda \leq 0.12$ (based on cell length) focused towards the inner wall, while cells above this threshold had a higher tendency to recirculate. From the data presented in Section 4.2.3, M/C cells had an average length of 7.4 μm ($\lambda = 0.15$), suggesting that the majority of M/C were above this size threshold and would recirculate within the channel. Instead, a channel with a height of 36 μm and a width of 220 μm would give a $\lambda = 0.12$ for M/C cells and a $\lambda = 0.16$ for cells > 10 μm in length. This therefore may enable the M/C cells to focus towards the inner wall with longer G1 and S cells recirculating throughout the width of the channel, or focused towards the outer wall. Alternatively, a straight channel with a high confinement may provide a better means for separating based on cell aspect ratio/rotational diameter, as demonstrated by Li [344].

While the results here showed a low enrichment of the different cell cycle stages, it was demonstrated that all morphologies of *L. mexicana* cells could be concentrated within a 34 μm region at the outer wall at high flow rates. Such a highly specific focusing position of non-spherical and highly heterogeneous cells is a unique behaviour, and as far as I am aware, has not previously been documented for curved inertial microfluidic devices. For *Leishmania*, this may have applications in diagnostics i.e. to isolate the pathogens from blood, serum or wound exudate samples or for sample processing, such as separating isolated flagella from cell bodies (either with or without flagella). This ability to concentrate cells at a particular location, regardless of shape, may also have applications in other fields, such as the concentration of pathogens from water [228], [384].

## Chapter 6

# High-speed detection of *Leishmania* in microfluidic devices

## Highlights

- Event-based cameras provide a low-cost and portable alternative to traditional high-speed imaging, without the need for pulsed light.
- Such cameras were capable of tracking particles up Reynolds numbers of 158.7 and detecting particles up to Re = 250.0.
- A proof-of-concept high-speed portable imaging system is demonstrated, using a 3D printed microscope. All data collection, visualisation and analysis being performed on a standard laptop.

## Published work:

J. Howell, T.C. Hammarton, Y. Altmann and M. Jimenez, **High-speed particle detection and tracking in microfluidic devices using event-based sensing** *Lab on a Chip*. (2020). 20(16), pp.3024-3035. https://doi.org/10.1039/D0LC00556H. [385]

Data was partially presented at the conference:

1. J. Howell, N. Hall, T. C. Hammarton, Y. Altmann, M. Jimenez. **Event-based sensing for flow cytometry**. (May 2023), *CYTO23*, Montreal, Canada.

## 6.1 Introduction

As discussed in previous chapters, analysing fixed cells during sorting has the caveat that such chemical treatment alters morphology, thereby increasing the proportion of short and wide cells. This makes enriching for the naturally short and wide mitotic population of interest more difficult as it reduces the size differences between the different cell cycle stages. In contrast, while live cells could be analysed post-sort, the length of time it took to sort a sufficient quantity of cells for morphological analysis may have reduced the validity of the results as the morphology of live cells can change rapidly, in addition to making it unfeasible to do large scale iterative testing. As a full imaging system was too large to fit within a biological safety cabinet for the high-speed analysis of live cells, we sought to develop a portable, high-speed method of particle tracking for the analysis of live cells.

With the advancement of technology, sensors, lenses, and processors are getting smaller, cheaper and more accessible. This has given rise to research into portable imaging technologies for applications such as handheld microscopes for surgical imaging [386], transportable microscopes for use in remote locations [387], wearable microscopes such as that used to image brain activity in live animals [388], and small wireless microscopes for use in enclosed spaces (i.e. in a cell incubator) [389]. Three main areas have been adapted to enable portability:

- miniaturising the body of the microscope,
- reducing the size or the number of lenses, with studies often using a combination of the three [390].
- using smart phones as processors and/or sensors,

One of the most common methods for miniaturising microscopes is to use commercially available and small footprint optics and sensors housed within 3D printed parts. 3D printed microscopes are highly attractive due to being completely customisable, and the capacity to share designs. As such, a plethora of microscopes have been developed, from simple fluorescence microscopes costing $\sim$ £100, to complex, laboratory grade microscopes with automated focusing and slide scanning, enabled by a motorised stage at only 15 cm high [391]–[393]. Such microscopes have shown promise in the field, being capable of diagnosing tropical diseases such as sickle cell disease [394], identifying and classifying parasitic infections in stool samples [395], and detecting *Mycobacterium tuberculosis* growth in culture [396]. Furthermore, their quality and application is comparable to traditional microscopes, as is demonstrated by their use for single molecule detection [397], time-lapse imaging [398], and super resolution imaging with a resolution in the nm ranges [399], [400].

While 3D printed microscopes typically use commercially available objective lenses, studies have demonstrated miniaturised microscopes using low cost and smaller objective lenses, and even lens-free devices can reduce the size of microscopes. Commercially available objective lenses typically use a combination of multiple and specifically distanced glass lenses to correct for aberrations in focus and colour bleeding. Christopher et al, demonstrated the use of low-cost and in-house 3D printed lenses capable of imaging both in brightfield and fluorescence modes [401]. Gradient refractive index (GRIN) lenses are much smaller (mm range) than conventional lenses and were originally designed to be flat to transfer an image to an optical fibre such as for endoscopes [402]. These have also shown potential in wearable mini microscopes such as for imaging the activity of neural cells in live mice [403], [404]. Lens free devices on the other hand provide a low-cost method of imaging with a large field of view (FOV). Such devices typically direct incoherent light through a pinhole or a GRIN lens to illuminate a sample directly above a sensor, producing holographic images of the sample. While the lack of lens prevents any magnification, the imaging of microparticles is achieved due to close proximity of the sensor and the sample, with high spatial resolution (i.e. 1.55 μm) being achieved through mechanical techniques such as sequentially angling the illumination or computationally during image reconstruction [405], [406]. This enables a highly compact microscope as small as 5.8 cm high for applications such as tracking the motility of many organisms on a slide, characterising homogenous populations of cells, and detection of pathogens in water [407]–[410].

The last technique to be discussed is the use of mobile phones for portable microscopy. Mobile phones serve as a highly convenient method of both imaging and image processing, due to being inherently portable, wireless, having powerful processors and containing good quality sensors and lenses. Typically phone microscopes consist of a structure to hold a phone's camera above a sample which is illuminated by a LED, enabling phones to achieve brightfield, darkfield, phase contrast, fluorescence, and quantitative imaging, depending on the addition of suitable filters, lenses, and mirrors [411]. Various groups have developed custom phone apps for viewing images, image processing and even machine learning for automated cell counting [412], [413]. As mentioned previously, often these three techniques are used together, with the lens free systems and smart phones being housed within 3D printed parts, and smart phones acting as sensors or used for image processing for lens-free holographic imaging [407], [414]–[418].

While there is a vast amount of research having been carried out into portable systems, there is a paucity in studies into portable high-speed imaging, resulting from two main limiting factors. Firstly, while high frame rates up to 2250 fps have been achieved in portable systems, these typically use a continuous light source which have the downside of introducing motion blur into an image [419]. Pulsed light on the other hand is traditionally used with high-speed imaging as it reduces motion blur; however, the introduction of strobes increases the size of the device and reduces portability. Secondly, capturing images at such a high frame rate generates a massive amount of data which requires transfer to a processor. In order to cope with the high volume of data transfer in a low latency manner, powerful (and thus bulky) processors are needed, again, reducing the portability of high-speed imaging systems. To overcome these limitations, event-based cameras (of neuromorphic vision sensors) were tested as a replacement for traditional frame-based cameras, to achieve a truly portable, motion blur-free method of high-speed particle imaging.

The first neuromorphic sensors were developed in 1991 by Mahowald and Mead, who described a silicon retina designed to mimic the cells in human eye and their mechanisms of detecting light and processing the corresponding information [420]. In contrast to traditional frame based cameras which record data from every pixel simultaneously to create an image, the pixels of event-based cameras respond independently and asynchronously to each other, responding only when a change in light intensity is detected [421]. In this way, event-based cameras only capture information regarding moving objects. When a pixel detects such a change, it records an event consisting of the x and y coordinate of the pixel, the time stamp, and the polarity of the event – an increase in light intensity is recorded as a positive event while a decrease in intensity records a negative event (Fig. 6.1A). For a pixel to record an event, the change in light intensity must be greater than a user defined threshold. An example of the behaviour of a single pixel is given in figure 6.1B; initially the intensity increases rapidly over time, crossing the threshold of intensity six times resulting in six positive events. After this point, the intensity of light begins to decrease slowly, crossing two thresholds to give two negative events before a spike in intensity for a final positive event. Note that when no threshold is crossed, no event is recorded. In order to visualise the captured data in a meaningful way, frames are reconstructed from the events using a user defined accumulation time e.g. 10 ms. Within a 10 ms timeframe, if a pixel has recorded two positive events and then a negative event, then the most recent event captured (in this instance the negative event) will be displayed. In this way, each pixel will either be coloured white if the last event was positive, grey if no event within that timeframe was recorded, or black if the last event was negative; thus, an image can be generated (Fig. 6.1C). The frame rate must also be defined, which is the number of integration windows within a second. If the frame rate is equivalent to the accumulation time (e.g. a frame rate of 100 generates a new frame every 1/100 s which is equivalent to 10 ms) then every event will be displayed once, termed full accumulation. If the accumulation time is higher than the number of frames, then an event will be displayed multiple times, while a lower accumulation time will result in some events never being displayed.

As event-based cameras do not record frames, they are thus not limited in their speed of data acquisition in the same as traditional cameras. The frame rate of traditional cameras typically relies of a variety of factors, such as exposure time, processing times, and data storage. As every pixel captures data simultaneously, data from every pixel must also be processed and stored simultaneously, resulting in a higher demand of the hardware. In contrast, as event-based cameras only transfer data from pixels which have been activated, the data can be processed much more quickly. Instead, the pixels of event-based cameras are limited by a refractory period, defined as the time taken for a pixel reset, during which time a pixel is unable to be activated. While this depends on the number of events being recorded, for the early sensor, the refractory period is less than 50 μs; however, for newer sensors these were estimated to be down to 5.8 μs, enabling frame rates of > 200,000 fps [422].

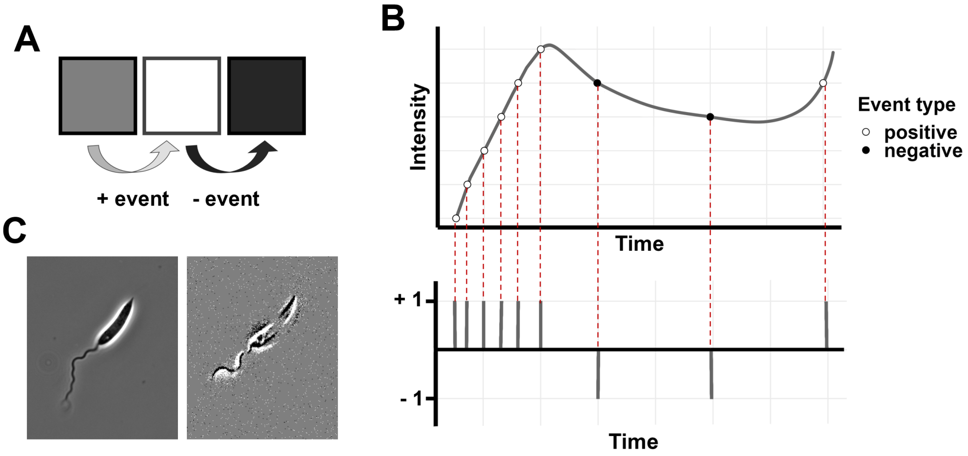

**Figure 6.1: Event-based sensors capture individual events rather than frames.** The theory behind event-based sensors is demonstrated here. (A) When a change in light intensity crosses a set threshold, an event is recorded. An increase in light intensity causes a positive event (+1) and is demonstrated with a white pixel. In contrast a decrease in intensity corresponds with a negative event (-1) and a black pixel. If no change in intensity is seen, then the pixel will be grey. (B) A graphical representation of a single pixel's response to changes in light intensity is shown. Each point in the plot represents when the threshold of intensity has been crossed, causing an event to be recorded. Image adapted from [423]. An example of the output is shown in (C). On the left is an image of a *L. mexicana* promastigote taken with a standard CMOS camera, while on the right is a reconstructed image of a swimming cell captured with an event-based camera

Due to pixels firing asynchronously and only being active when sufficiently stimulated, event-based cameras offer an affordable, high-speed, low latency, low power and high dynamic range method of imaging. This makes them a highly attractive tool, and since their commercialisation in 2008 [421], their applications have become more widespread, particularly in industrial and engineering environments such as for robotics development [424]–[428], mechanical fault detection [429]–[431], surveillance [432]–[434], autonomous driving [435], [436] and space research [437]–[440]. Their benefit for tracking particles in flow has also been demonstrated, having been used primarily for particle tracking velocimetry (PIV) – a technique used to measure the velocity of water or air by tracking the movement of suspended neutrally buoyant particles (e.g. hollow glass spheres and helium air bubbles, respectively) [441]–[445]. Willert and Klinner (2022) demonstrated that event-based cameras have a considerable number of advantages over traditional high-speed cameras when measuring the motion of disturbed particles in water; they were particularly tolerant to visual artefacts such as a high background intensity, spatial variations in intensity and scattered light from the laser [446]. Some disadvantages were also noted, such as an increased latency with an increased number of events and the lack of detection of slow-moving particles. These disadvantages are addressed in a later publication by Willert by implementing a pulsed illumination system [447]. In addition, micro-PIV (PIV using microparticles) was carried out by Ni et al, demonstrating the event-based camera's capability of high-speed imaging of slow moving particles under Brownian motion [444]. The compatibility of event-based cameras with microscopy has also been realised, having been used in single-molecule localisation microscopy [448], electron microscopy [449], [450], fluorescence active cell sorters [451], high-speed imaging [444], low-light microscopy [452], and a tool for autofocusing [453].

While event-based cameras offer a powerful tool for imaging microparticles, their applications for portable microscopy are limited to the work done by Berthelon (2018) during his PhD, who aimed to develop a portable event-based system for imaging red blood cells flowing within blood vessels to improve research into haemorrhagic shock [454]. Here, Berthelon used an event-based camera with a microscope to image the circulatory system of cremaster muscles in male mice, where the number, velocity and density of RBCs were analysed to calculate the perfusion rate before and after induced haemorrhagic shock (the lowering of the total blood volume within the mouse by removal with a syringe). While a prototype of the device was made, its ability to image RBCs was not shown due to the device being developed in parallel to the experimental work.

In this chapter, the use of event-based cameras as a portable method for the high-speed imaging was explored for applications in inertial microfluidic imaging. During this work, proof of concept is given, demonstrating the first use of event-based cameras for the high-speed imaging of particles within microfluidic devices. Particle tracking was achieved to a Reynolds number of 158.7 and particle detection up to Re = 250.0. It was further demonstrated that particle fluorescence improved their detection. This work lead to a publication in Lab on Chip in 2020 [385].

## 6.2 Results

### 6.2.1 Characterisation of the event-based camera with beads in flow

In order to confirm that event-based cameras were indeed compatible with traditional microscopes, a single fluorescent 10 µm bead on a microscope slide was imaged in both BF and fluorescence mode using a traditional frame-based camera and the event-based camera

(Fig. 6.2). In order to capture the images with the event-based camera, the slide was moved to create events. Details of the experimental setup and image processing can be found in Sections 2.4.2 and 2.2.4, respectively. With a traditional camera, the bead appears as a dark outline of a circle against a lighter background in BF, and as a solid white circle against a black background in fluorescence mode. In BF, due to the bead appearing as a dark ring against a grey background, negative events are generated with positive events following in the wake. In contrast, in fluorescence mode the bead is lighter than the background; thus, the moving bead initially generates positive events in the direction of movement, followed by negative events. In both BF and fluorescence modes imaged with the event-based camera, the particles have a grey centre due to the uniformity in light intensity triggering no events. Additionally, a higher accumulation time (5,000 µs vs 500 µs) is required to reconstruct the image in BF mode so that the particle is clearly visible. This is due to the lower contrast between the particle and the background resulting in fewer pixels crossing the threshold to trigger an event during acquisition; thus, fewer events being recorded.

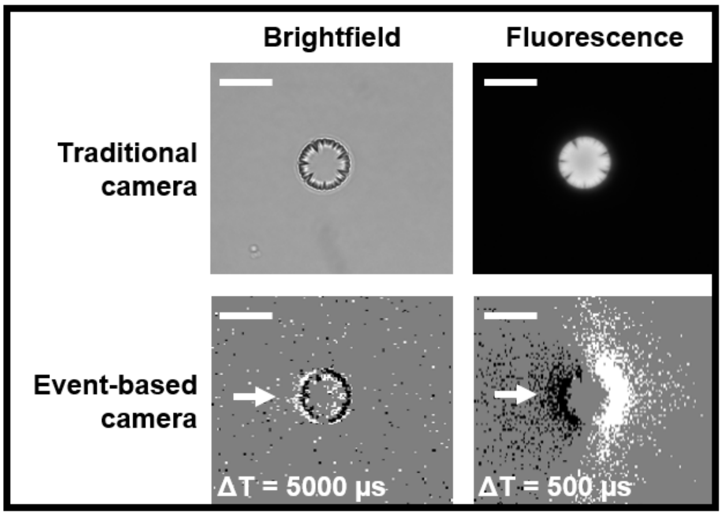

**Figure 6.2: BF vs fluorescence.**
Example images of a 10 µm red fluorescent bead on a microscope slide as captured by a standard CMOS camera (top row) and an event-based camera (bottom row). The event-based camera images were captured by moving the microscope stage so that the bead moved in the direction of the white arrows. Images captured in brightfield are shown on the left while fluorescent images are shown on the right. Scale bars: 10 µm. In order to reconstruct images from the individual events recorded by an event-based camera, signal processing is carried out post-acquisition to define the frame rate of the video along with the accumulation time (∆T). The ∆T corresponds to the time frame in which pixels maintain their polarity. An ∆T of 5,000 µs was used to display the image in BF while an ∆T of 500 µs was used for the fluorescence image.

On confirming that the event-based camera was capable of imaging objects on a slide, it was tested whether particles could be detected flowing within microfluidic channels (Fig. 6.3). Here, 10 μm beads in fluorescence mode were imaged at a low flow rate (Re = 4.0) within the 60 x 360 $\mu m^2$ channel, details of which can be found in Section 2.4.1. After data acquisition, image processing was carried out in MATLAB to extract a frame from the recording; in figure 6.3, different accumulation times are shown for the same frame, with the individual particles being similarly marked on all plots with red arrows. For an accumulation time that is too low, in this case 100 μs (Fig. 6.3A), not all particles are visible, with few negative events following the marked particles, showing each particle's trajectory. Increasing the accumulation time to 1,000 μs (Fig. 6.3B) resulted in more events being displayed per image; a larger area of positive events is seen with longer negative trails. Here, particles are clearly visible and distinct. In contrast, while all particles are visible using an accumulation time of 10,000 μs (Fig. 6.3C), the trails overlap making differentiation of the individual particles more difficult. Thus, an optimum accumulation time is necessary to achieve particle detection, without creating too much noise. Furthermore, as the number of events displayed per particle is related to both the strength of the signal (i.e. the number of events captured during acquisition) and the accumulation time, the accumulation time must therefore be set individually for each experiment in order to maximise the output.

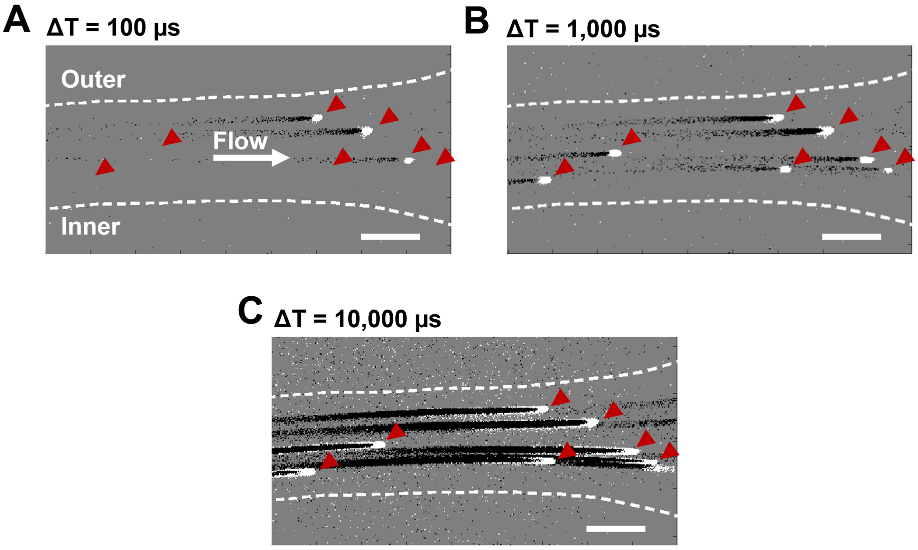

**Figure 6.3: Using accumulation time to track particle location.**
10 μm beads were recorded within a microfluidic channel with an event-based camera at Re = 4.0. A single frame from the recording was extracted using an accumulation time of 100 μs (A), 1,000 μs (B) and 10,000 μs (C). The dashed lines indicate the top and bottom of the channel, the position of each particle flowing in the channel has been identified with a red arrow, and the direction of flow is shown with a white arrowhead. Scale bars: 200 μm.

Next, the event-based camera was tested as a method for analysing particle focusing over a range of flow rates between 0.05 and 1.5 ml.min$^{-1}$ (Re = 4.0 – 158.7). 10 μm fluorescent beads were analysed within the 60 x 360 μm$^2$ channel, with particle focusing being recorded in both BF and fluorescence modes. Extensive signal processing was carried out by Dr Yoann Altmann to identify individual particles within the channel. A high frame rate (20k fps) and accumulation time was used to precisely identify the trajectory of at least 1,000 particles for each flow rate and thus their location within the channel, as well as to distinguish true events (beads within the channel) from background noise (Fig. 6.4A). Altmann extracted the position of the centre of each event while I subsequently plotted the data in R (Fig. 6.4B). At low flow rates, particles were detected across the width of the channel, getting closer to the inner wall with increasing flow rate. At Re = 39.7, a predominant focusing position was detected at the inner wall which was maintained up to a Re = 158.7. This is in line with the expected behaviour of particle focusing within this channel. The event-based camera was similarly tested and analysed for imaging in BF (Fig. 6.4C). For a Re $\leq$ 15.8, a similar distribution was seen between these two methods of illumination, with the percentage overlap calculating to be $\geq$ 77% and the lowest flow rate having the highest correlation. At Re > 15.8, the limit of detection was reached for BF illumination such that particles were unable to be detected. This was determined to be a result of the BF illumination and the high velocities of the particles decreasing the contrast of the particle with the background, and thus reducing the number of events being recorded for each particle. Finally, event-based particle detection was shown to be highly reproducible, with an overlap of > 89% between three replicates for BF mode and > 94% in fluorescence mode. This confirmed that event-based cameras are compatible with standard microscopes and do not need high powered strobes to achieve high-speed particle detection. Due to particle fluorescence having a higher intensity and subsequent contrast than BF illumination, detection in fluorescence mode is more sensitive and thus is the preferred method of illumination for particle detection with event-based cameras.

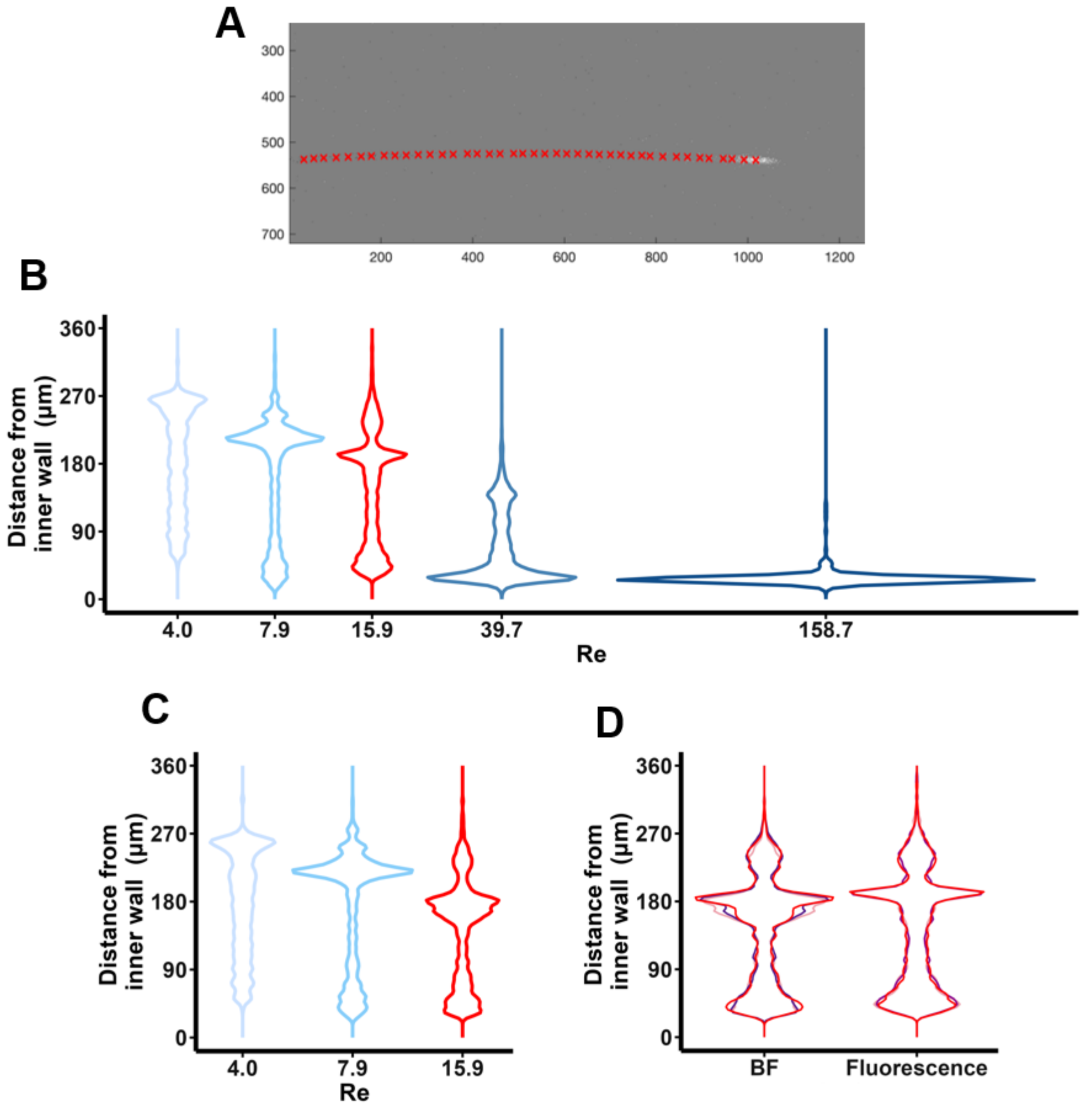

**Figure 6.4: Event-based cameras can detect particles in microfluidic channels at various flow rates.**
10 µm red fluorescent beads were injected into a 60 x 360 µm$^2$ channel at various flow rates and imaged using an event-based camera. (A) An example of the signal processing is shown; the trajectory of each particle flowing through the channel was analysed post-acquisition, as marked by red crosses. The axes represent the pixel coordinates of the image. $\sim$ 15 s videos of particle focusing at various flow rates were imaged in fluorescence mode (B) or BF (C) with the location of each particle across the width of the channel being plotted as a distribution. (D) Particle focusing distributions at Re = 15.9 (red) are compared between BF and fluorescence mode for each of three replicates (red, blue and pink) (*n* > 1,000).

### 6.2.2 Validation of the event-based camera as a method of high-speed particle analysis

After confirming that particles could be detected at high-speed using the event-based camera, the distribution of particles within the channel was subsequently compared to that of streak imaging using a Dino-Lite microscope, a commercially available tool for the portable imaging of particles in flow. Streak imaging uses a long exposure to capture the focusing trends of fluorescent particles within a channel; an area with many fluorescent particles localising to the same location appears as a fluorescent streak. $\sim$15 s videos of fluorescent particles were captured for a range of flow rates using streak imaging, details of which can be found in Section 2.4.2. For each flow rate, a single frame was extracted from each of three replicates which were stacked in MATLAB. This served three purposes: to average the intensity across the replicates, to reduce background noise and to enhance true signals. The stacked images are shown for three flow rates (Fig. 6.5A). At Re = 7.9, a faint signal is barely visible at the inner wall while at Re $\geq$ 39.7 a defined focusing position is clearly seen at the inner wall. From these images, the fluorescence distribution across the channel was extracted by averaging the pixel values in the x-direction (direction of the flow) within the denoted ROI. The subsequent intensity across the channel was plotted in figure 6.5B alongside the corresponding distributions as measured by the event-based camera. When comparing the two methods of detection, the same general trend was seen for particle distribution across the channel for all flow rates, with slight differences. Initially, at Re $\leq$ 7.9 a focusing position was detected by the event-based camera $\sim$ 220 μm from the inner wall which was not detected when using the Dino-Lite. This may have been a limit of detection with the Dino-Lite which may not have been sensitive enough to detect weak signals arising from a low number of particles focusing to a specific spot within the channel. Furthermore, for the Dino-Lite, a similar width of violin plot was seen between Re = 39.7 and 158.7, while a larger difference was seen for that of the event-based camera. Again, this may have been due to inaccuracies in imaging with a Dino-Lite. In a greyscale image, the maximum pixel intensity is 255, which corresponds to white. As particle focusing results in a high intensity streak, it is possible that the pixels were saturated and could not account for any further increase in fluorescence intensity, thereby giving a similar distribution between two flow rates. In contrast, as the event-based camera data was generated by detecting the number/proportion of particles across the channel, there was no limit to the number of particles detected and thus this provided higher resolution in terms of particle quantification than imaging with a Dino-Lite. These data have demonstrated for the first time that event-based sensing is a suitable method of particle detection and tracking within microfluidic systems.

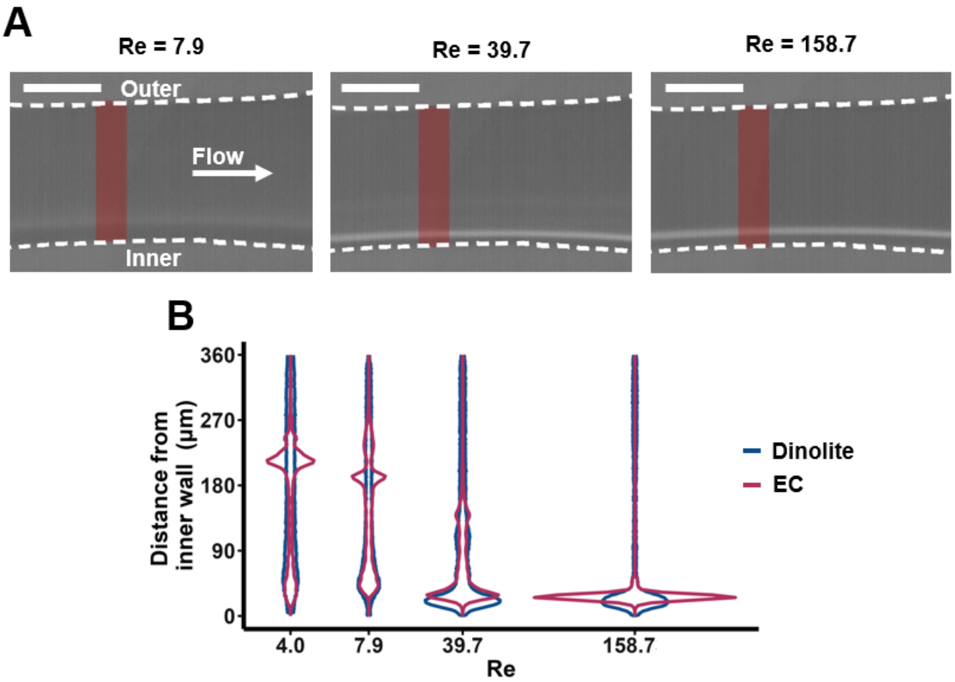

**Figure 6.5: Event-based cameras measure a similar particle distribution to Dino-Lite-based streak imaging.**
A Dino-Lite camera was used to record ∼15 s videos in triplicate of 10 μm fluorescent beads flowing within a 60 x 360 $\mu m^2$ channel at various Reynolds numbers (Re). From these videos, frames were extracted and processed according to Section 2.4.2 to give the images in (A). The inner and outer channel walls are marked with dashed lines, the ROI is shown with a red band and the flow direction is demonstrated with the white arrow. (B) From these images, the intensity within the ROI was averaged across the x-axis (flow direction) and the resulting distribution of intensity across the channel was plotted alongside the data previously plotted for the event-based camera distribution. Scale bars: 100 μm .

Thus far it has been shown that event-based cameras provide comparable results to traditional methods of particle focusing analysis when tracking the particle's trajectory. While this method of signal processing is sensitive and specific, tracking individual particles requires complex and lengthy signal processing. However, a similar effect can be achieved much more quickly through extracting only the positive events from the event-based camera data. Due to the nature of this processing, positive events generated from noise will also be captured within these data; however, the high number of beads within the channel (over 1,000 per Reynolds number, as analysed by Altmann) corresponds to a high proportion of true positive events, reducing the impact of the noise. An example of such processing is shown in figure 6.6, replotting the data given in figure 6.5; the positive events from a ROI were extracted and the position of each event within the channel was plotted as a function of time using a 3D histogram in MATLAB. The colour and the height of the plot corresponds to the proportion of events within a specific bin. These plots demonstrate the same trends as the tracked data – at

Re = 4.0, the signal is spread across the width of the channel. At Re = 7.9 and 15.9, two distinct focusing positions can be seen, one close to the inner wall and a second towards the centre of the channel. Increasing the Reynolds number further caused particles to migrate to the inner wall with the sharpest focusing position at Re = 158.7. The remaining events-based camera data have been processed in this way.

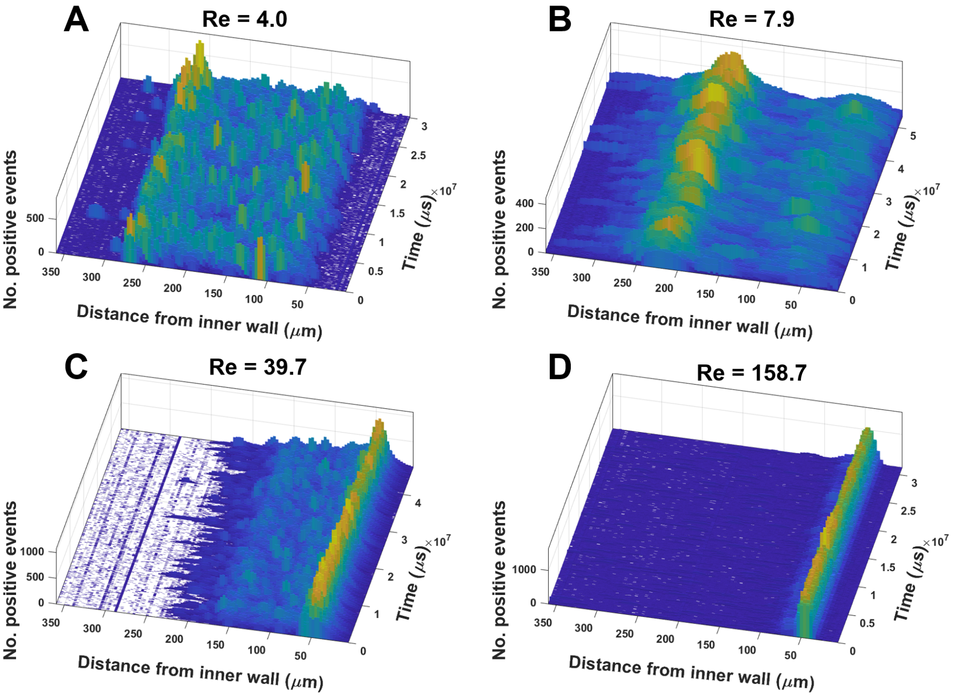

**Figure 6.6: Focusing trends can be shown by extracting the positive events in event-based camera data.**
Event-based camera data requires signal processing prior to visualisation. The data shown here is the same as that plotted in figure 6.5, where 10 µm beads were imaged using an event-based camera at various flow rates within a 60 x 360 µm$^2$ channel. The positive events were extracted from a ROI within the channel and their position was plotted as a function of time using 3D histograms. Reynolds numbers (Re) between 4.0 – 158.7 were analysed (A-E).

### 6.2.3 Event-based cameras for analysing the focusing position of *L. mexicana*

Here, it was demonstrated that the events-based camera is a suitable method of analysing 10 µm beads at flow rates up to Re = 158.7. However, the overall aim was to use event-based sensing to the assess the focusing behaviour of live *L. mexicana* parasites within the 30 x 170 µm$^2$ channel at Reynolds numbers up to 250.0. Prior to the use of cells, it was first tested whether beads of a similar size were capable of being detected up to the desired flow rate. Spherical 5 µm fluorescent beads were first tested within the 30 x 170 µm$^2$ channel, being a similar size to mitotic *L. mexicana* promastigotes (Fig. 6.7). Due to the smaller size of the channel, a higher-powered objective lens with a higher numerical aperture could be used thus increasing the resolution of the image. To note, the next generation of event-based cameras was used here, details of which are found in Section 2.4.2. These two factors together provided increased resolution and sensitivity for particle detection. The distribution of 5 μm beads across the channel was compared between the event-based camera and traditional high-speed particle tracking. For both methods of detection, the beads were seen to focus tightly towards the inner wall at Re = 83.3 and move further from the wall with increasing Reynolds number. A slight discrepancy in focusing position was seen between the two methods, with the largest difference being seen for Re = 250.0. The average focusing positions as measured by the high-speed camera and event-based camera were $\sim$ 18 μm and 37 μm away from the inner wall, respectively (Fig. 6.7A and D). This difference was more likely to be a result of variation in the experiment rather than the event-based camera incorrectly measuring particle localisation, for example, due to differences in how the channel was aligned during imaging, slight movement of the channel between testing or an unnoticed piece of debris affecting particle focusing. Despite the differences in positioning, the event-based camera achieved particle detection up to Re = 250.0, confirming that event-based cameras have the capacity to measure *L. mexicana* at flow rates where they have migrated to the outer wall.

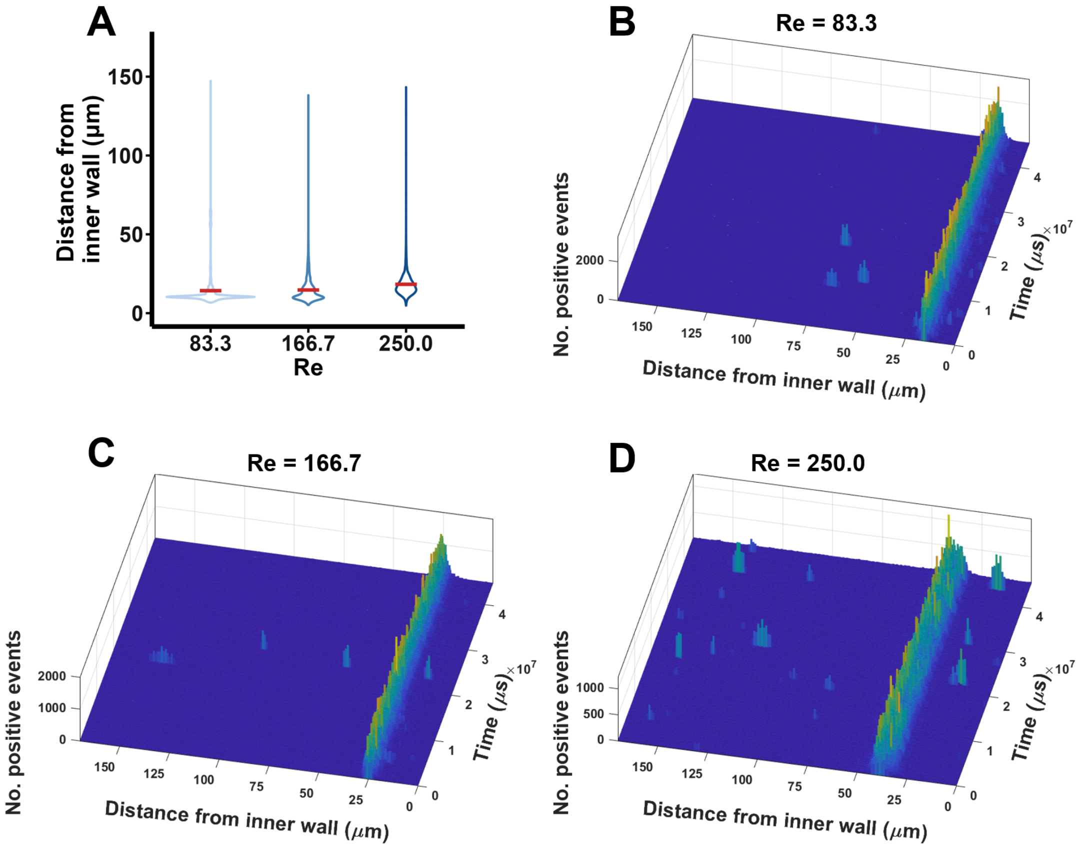

**Figure 6.7: Event-based cameras can detect particles up to Re = 250.0.** Spherical 5 µm fluorescent beads were analysed for their focusing position within a 30 x 170 µm$^2$ channel. The distribution of particles at various Reynolds numbers (Re) was compared between a high-speed camera (A) and an event-based camera (B-D). For the event-based camera, $\sim$ 15 s videos of particle focusing were recorded. The positive events were extracted from the videos in MATLAB and plotted as 3D histograms – the position and number of the events was plotted over time.

Previously it has been demonstrated that the event-based camera was unable to detect particles in BF above a Reynolds number of 15.9 due to having a lower contrast than fluorescent particles. As live *L. mexicana* are not naturally fluorescent, and the addition of dyes have the potential to affect cell morphology and mechanical properties, the analysis of *L. mexicana* in BF is preferred. It was therefore tested whether the improved set up (a smaller inertial microfluidic device, a higher-powered objective lens and a higher resolution event-based camera) could detected particles in BF at higher Reynolds numbers. Initially, peanut-shaped beads of 5.1 x 7.7 µm$^2$ were analysed for their focusing position within the channel using the event-based camera. These beads typically formed two focusing positions at Re = 33.3 and a single focusing position closer to the wall at Re = 83.3 (Fig. 6.8A). Similar to analysing particle focusing in BF using the previous setup, a Re $\leq$ 33.3 was out with the limit of detection for the event-based camera, as demonstrated by the few number of positive events which were randomly distributed across the channel (Fig. 6.8B). At Re = 83.3, even fewer events were detected (Fig. 6.8C). Thus, even with the improved setup, the event-based camera was unable to detect particles in BF at the desired flow rate. A similar result was obtained when fixed *L. mexicana* were imaged in BF using the event-based camera.

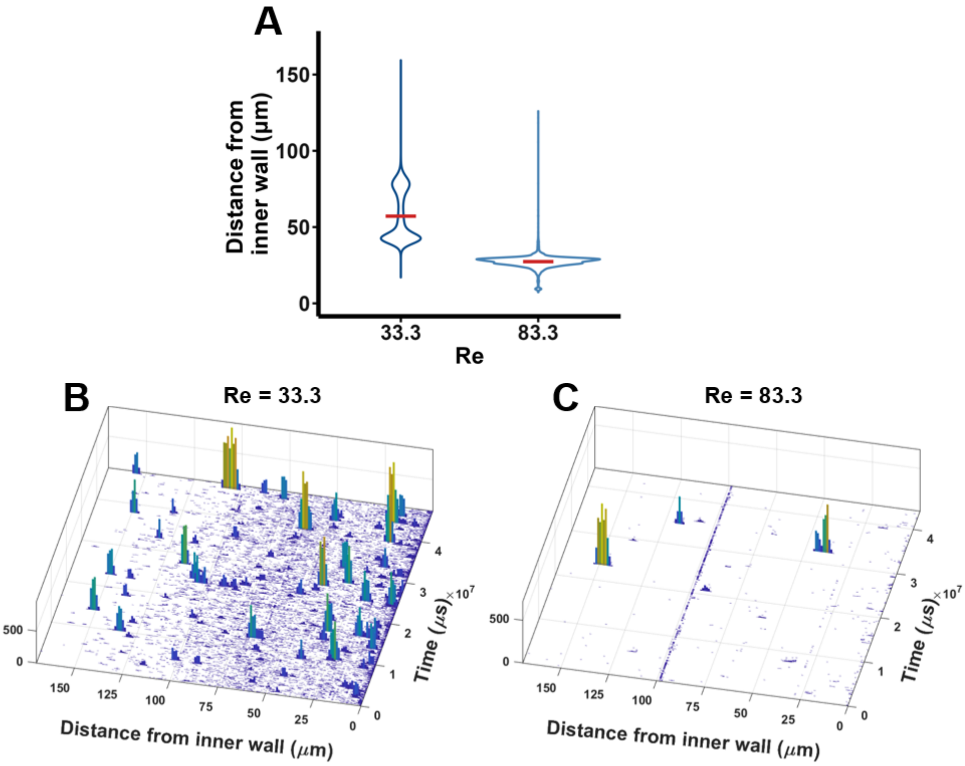

**Figure 6.8: Peanut shaped particles were unable to be detected at high flow rates.** 5.3 x 7.7 µm$^2$ peanut-shaped beads were analysed for their focusing position at Reynolds numbers (Re) of 33.3 and 83.3 within the 30 x 170 µm$^2$ using a high-speed camera (A) and the higher resolution event-based camera (B and C). For the event-based camera data, the positive events were extracted in MATLAB and their position within the channel was plotted as a 3D histogram over time.

While BF was the preferred option for illumination, its lower levels of particle detection prevented its use for *L. mexicana* analysis. Therefore, it was tested whether the induction of fluorescence would improve their detection by event-based sensing (Fig. 6.9). Various methods were tested to induce the expression of fluorescence in *L. mexicana* parasites. Firstly, cells were genetically modified to endogenously express mNG fused to their glucose transporter A protein (THT2A), which is found in the cells' pellicular membrane [244]. This resulted in cells with a stable and uniform fluorescence; however, the intensity of the fluorescence was low, requiring the highest laser power (200 mW) for visualisation purposes (Fig. 6.9A). These mNG:THT2A cells were first analysed on a slide with the event-based camera, in both BF and fluorescence. While the BF illumination provided clear images of the cells using a relatively low accumulation time ($\Delta T$ = 1,000 μs) (Fig. 6.9D), fluorescence illumination on the other hand required a higher accumulation time ($\Delta T$ = 5,000 μs) and the shape of the cells was lost (Fig. 6.9E). As discussed earlier in this Chapter, the length of the accumulation time required for image reconstruction is related to the strength of the signal being recorded – the higher the contrast of the object, the more events are acquired and the lower the accumulation time necessary to reconstruct an appropriate image. Therefore, as a higher accumulation time was required for imaging in fluorescence mode than in BF, this suggested that the mNG:THT2A expression provided a lower level of contrast than the BF imaging and would thus be unable to be detected during microfluidic sorting. Instead of transgenic fluorescence, different dyes were tested for the labelling of *L. mexicana*. Initially MemGlow™ 640 was selected as it reportedly binds to the cellular plasma membrane in both live and dead cells [455]. When staining *L. mexicana* however, it provided inconsistent labelling with the majority of cells ($\sim$74%) having a low level of fluorescence while a small proportion stained very brightly (Fig. 6.9B). Both live and fixed cells were tested and the same pattern of expression was seen. Finally, MitoTracker™ Deep Red FM (MitoTracker), a dye developed to stain active mitochondria was analysed. This dye was obtained from the Gluenz lab and was found to stain the entirety of the cell with a high level of fluorescence (Fig. 6.9C). This dye was thus selected for further testing.

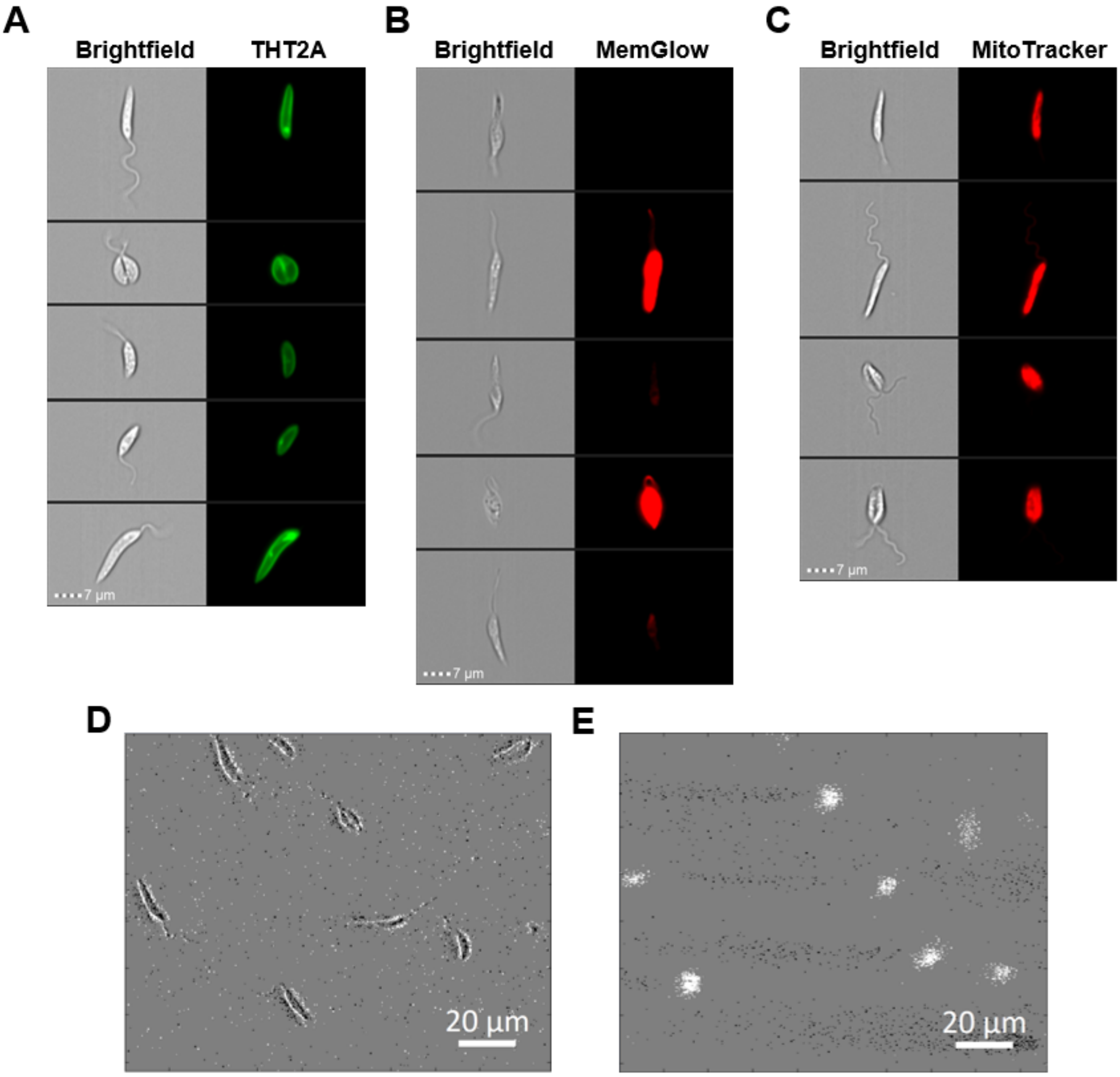

**Figure 6.9: Generation of fluorescent *L. mexicana* for EC-based detection.**
Live *L. mexicana* promastigotes were genetically modified to express mNG:THT2A, or stained with MemGlow™ 640 or MitoTracker™ Deep Red FM. Their corresponding fluorescence was analysed via imaging flow cytometry (A-C). The brightfield images are shown on the left while images of fluorescence localisation are on the right for each dye. Scale bars: 7 µm .mNG:THT2A expressing cells were seeded onto a microscope slide and analysed using an event-based camera in brightfield (D) or fluorescence mode (E) using a 63X objective. The microscope stage was moved while the videos were being recorded for the events to be generated. Scale bars: 20 µm.

Prior to testing cells within the microfluidic device, it was first confirmed that cells were sufficiently stained with MitoTracker for detection. As a note, fixed cells were used here as the sorting and the event-based camera imaging was carried out outside of a MSC for testing with a standard inverted microscope (as opposed to a portable microscope for use within the MSC). Cells were first fixed with 4% PFA for 15 minutes and stained with MitoTracker according to Section 2.2.3. The fluorescence of these cells was confirmed using microscopy - while the fluorescence may be very bright on the ImageStream, the same is not necessarily true for microscopy due to the use of different objective lenses and methods of fluorescence excitation. While using the same imaging setup as would be used for sorting analysis, the cells appeared bright and were clearly visible (Fig. 6.10A). To validate whether the MitoTracker-stained cells would be visible within the microfluidic device and to confirm the sorting patterns of the stained cells, streak imaging was performed using the standard microscope camera. Streak images were captured in triplicate of the sorting of the stained cells at various flow rates (see Section 2.4.2. For each flow rate, the images were extracted from Zen lite imaging software and processed in MATLAB, where the background was subtracted and the replicates were stacked into a single image (Fig. 6.10B). The distribution of fluorescent signal across the channel was subsequently extracted from the ROI marked in these images in MATLAB as outlined in Section 2.4.2 and plotted as a violin distribution in figure 6.10C. From the images, streaks made by the focusing of cells can be seen in all flow rates tested. At Re = 83.3, a streak is seen towards the inner wall, which shifts towards the outer wall at Re = 166.7 in a wide focusing position before focusing sharply at Re = 250.0. From the distribution plots in figure 6.10C, it can be seen that at Re = 83.3, a slight bimodal distribution can be seen with an increase in fluorescence towards both the inner and outer wall. At Re = 166.7, a spread of fluorescence is seen across the channel with a predominant localisation towards the outer wall. Finally, at Re = 250.0, a sharp fluorescence peak is seen at the outer wall. In all flow rates, a small spike in fluorescence was seen around the middle of the channel – this was most likely caused by the small piece of debris (or a single cell) which was stuck in the channel and was visible within the ROI. These results are consistent with focusing behaviour of *L. mexicana* as analysed in Section 5.2.5.

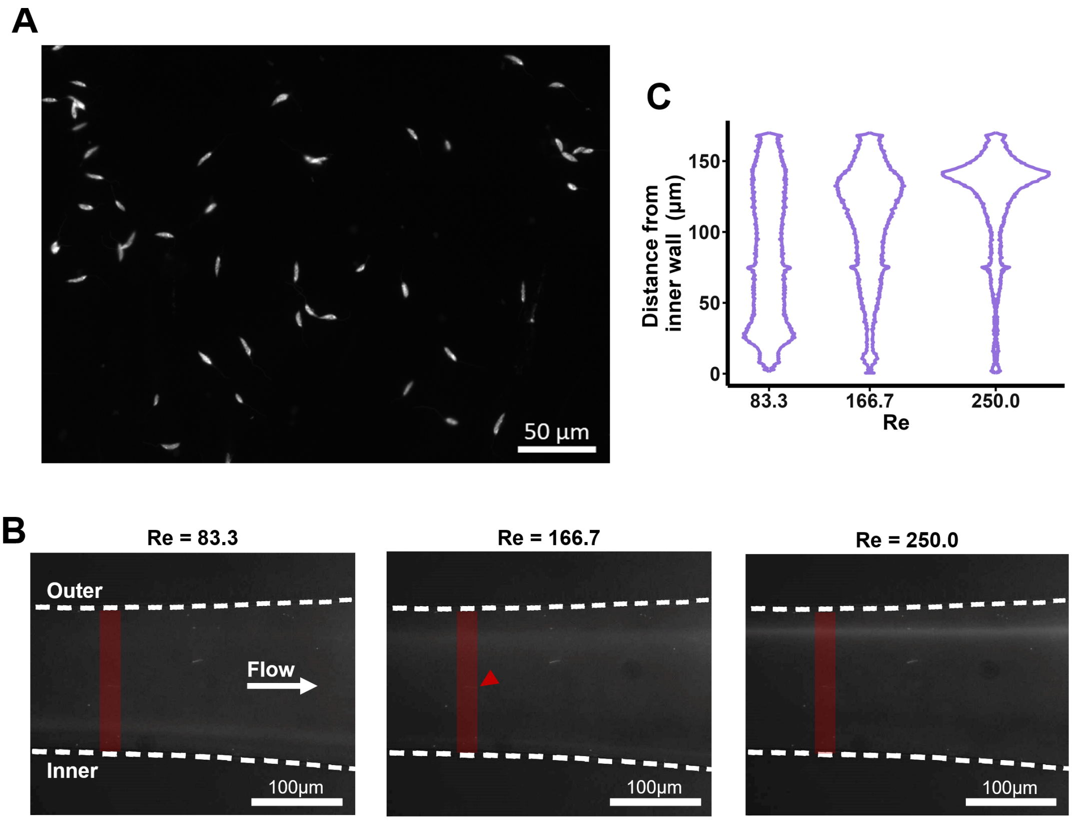

**Figure 6.10: MitoTracker-stained cells can be detected via microscopy imaging.** (A) Cells were fixed and stained with MitoTracker according to Sections 2.2.1 and 2.2.3 and subsequently imaged on a slide on an inverted microscope. The image was taken using a 20X objective lens in fluorescence mode using Zen Blue. Scale bar: 50 µm .These cells were then sorted within the 30 x 170 µm$^2$ channel at various flow rates and analysed by streak imaging in triplicate. (B) Image processing was performed in MATLAB to stack the images from the three replicates and identify a ROI (red rectangle) within the channel. The dashed lines show the inner and outer walls of the channel, the white arrow shows the direction of the flow, the red arrowhead identifies debris within the channel and the scale bar represents 100 µm. (C) The average intensity across the ROI was taken and plotted as a violin plot.

Having confirmed that MitoTracker-stained cells were capable of being imaged using streak imaging, it was therefore tested whether same the experimental setup could be used with the event-based camera for particle detection. Unfortunately, when these experiments were replicated and analysed as outlined above, only noise was detected for all flow rates analysed, with no region across the channel with an increased number of events (Fig. 6.11). This suggests that even stained with MitoTracker, the level of fluorescence of the individual cells was still too low to trigger an event. From these results, it was thus determined that event-based sensing was unsuitable for the analysis of live *L. mexicana* at sufficient flow rates with the current experimental design.

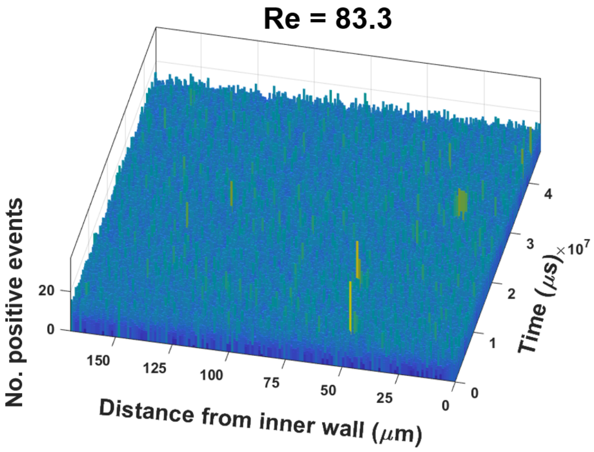

**Figure 6.11: ECs are unable to detect MitoTracker stained *L. mexicana* in flow.**
*L. mexicana* cells were fixed and stained with MitoTracker according to section 2.2.1 and 2.2.3 ∼15 s videos of particle focusing was recorded in triplicate using the higher resolution event-based camera. The positive events were extracted in MATLAB and their position across the width of the channel was plotted against time in a 3D histogram.

### 6.2.4 Event-based camera as a portable method of high-speed imaging

While the use of event-based cameras to track *Leishmania* within this microfluidic system was unfeasible at the desired flow rates, these high-speed detectors still present as a novel tool for many other areas of *Leishmania*, biological and microfluidic research. One such potential application is the tracking of flagellum wave forms to understand mechanics of cell motility. Such work traditionally uses videomicroscope to capture videos at over 200 fps, and has provided insight into the molecules controlling the type of flagellar beat propagated [456], how cell body shape correlates to directional motility [383], and how sperm cells steer [457]. To provide proof of concept, videos were captured of individual *L. mexicana* promastigotes swimming, from which the motion of the flagellum is clearly distinguishable (Fig. 6.12).

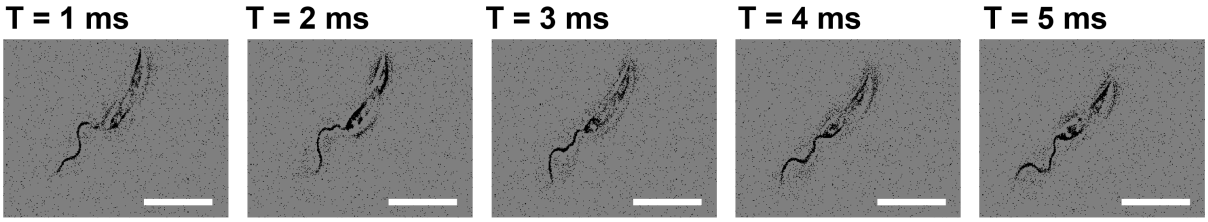

**Figure 6.12: Event-based cameras have applications in other areas of *L. mexicana* research.**
Live *L. mexicana* were seeded onto a microscope slide and their swimming behaviour imaged with an event-based camera at 63X magnification. Signal processing was carried out in MATLAB to set the frame rate to 1k fps and to extract the negative events. Example images are shown of the flagellar beating over the course of 5 ms.

Finally, to provide proof of concept for the use of event-based cameras as a portable method of high-speed imaging, an event-based camera was fitted to a Portable Upgradeable Modular and Affordable (PUMA) 3D printed microscope, developed by Tadrous and built in-house by Dr Yoann Altmann and Dr Melanie Jimenez (Fig. 6.13) [458]. The full set-up including the camera measured around 17.5 × 12.5 × 33.1 cm and weighed less than 600 *g*, making it suitable for use within a microbiological safety cabinet (Fig. 6.13A). Using the outlined setup, 10 μm beads were recorded moving on a microscopy slide. The data from the event-based cameras were both captured and analysed using a standard laptop, demonstrating both a functional microscope as well as a fully portable system (Fig. 6.13B).

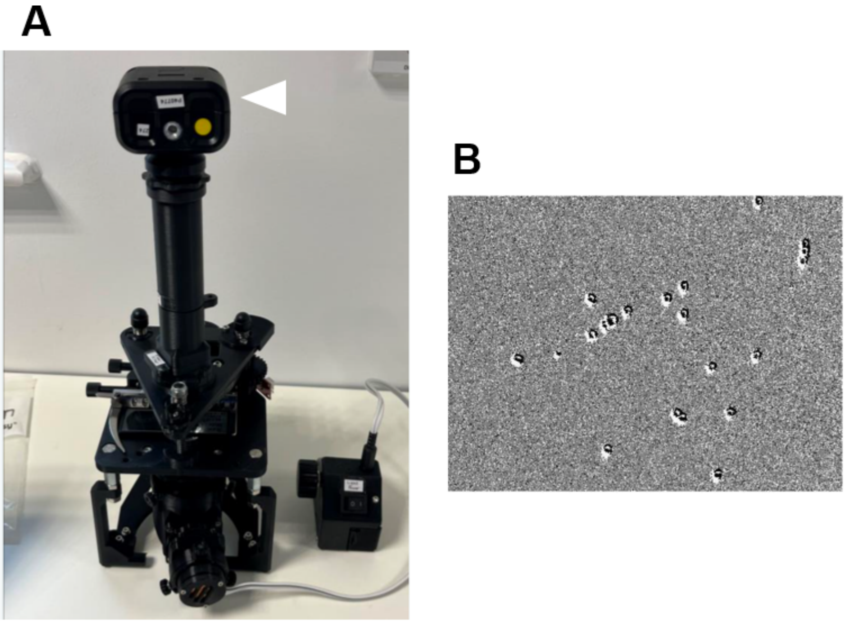

**Figure 6.13: Event-based cameras are compatible with portable microscopes.**
(A) Photograph of an event-based camera connected to a Portable Upgradeable Modular and Affordable 3D printed microscope. The white arrowhead identifies the event-based camera. (B) Example image of data collected using the outlined microscope set-up. 10 μm spherical polystyrene beads were seeded onto a microscope slide and were imaged in BF mode using the event-based camera. The microscope slide was moved in order to create the events, and the data was analysed in MATLAB in order to reconstruct the image. The work presented here was carried out by Sulaf Bakrou.

## 6.3 Discussion and conclusions

From the work carried out in Chapter 5, it was evident that small changes in the morphology of *L. mexicana* parasites resulted in different focusing trends within inertial microfluidic devices. One of the caveats to this work was that fixed cells had to be used when carrying out high-speed particle analysis due to the risk of potential exposure when using the pressurised microfluidic system, which is known to affect cell morphology and deformability. Thus, the analysis of fixed cells may not provide a true representation when sorting on the cell cycle of *L. mexicana*. A portable method of high-speed imaging was therefore sought in order to carry out particle analysis within inertial microfluidic devices on live cells. To achieve this, event-based cameras were employed to replace the traditional high-speed CMOS camera, offering a cheaper, less data heavy, low latency and easier data processing alternative. While event-based cameras are widely used in robotics and surveillance, their applications with microscopy and in biomedical settings are limited. Thus, in this Chapter, a novel application is demonstrated for event-based cameras for the imaging of microparticles within inertial microfluidic systems as well as a suggested application for its use in biomedical research.

In order to use event-based cameras for high-speed imaging of *L. mexicana* within inertial microfluidic devices, the setup was first validated with beads and compared to results from a portable Dino-Lite microscope. It was demonstrated that fluorescent particles provided a higher level of sensitivity, due to the increased contrast between the particles and the background, enabling trajectory of 10 μm beads to be tracked at Re = 158.7 in fluorescence mode, but only Re = 15.9 in BF. While tracking of particles was achieved to Re = 158.7, particle detection was achieved up to Re = 250.0 for fluorescent 5 μm particles, demonstrating focusing positions in-line with that captured using high-speed particle detection. This validates the suitability of event-based cameras for high-speed particle detection without the need for a pulsed light source.

Unfortunately, at the flow rates tested ($Re \geq 33.3$) *L. mexicana* cells were unable to be detected during inertial focusing with the event-based camera, even with induced fluorescence. As streak imaging was still able to be performed on the MitoTracker stained cells, this suggested that the dye was too faint to generate an event. Potential improvements to the system to increase the detection of *L. mexicana* within these devices could include the use of different dye for higher contrast and using higher power and more sensitive objective lenses.

While the current system was unsuitable for the desired application, proof of concept for a portable high-speed imaging system was demonstrated. For the first time, a frame rate of 20k fps could be achieved in a system without the use of a strobe, all collected and analysed on a standard laptop. Furthermore, visualisation of the high-speed imaging was performed in real time, providing feedback on the data being collected. Here, the microscope used was only to image particles in BF and dark-field (on the addition of 3D printed filters); however, as fluorescent particles provide a higher level of detection, a next step would be to test the event-based camera with a portable fluorescence microscope as well as apply the microscope for inertial microfluidic imaging. While Berthelon also suggested the use of an event-based camera as a portable method of imaging microvasculature [454], as far as I am aware, this is the first demonstration of a functioning portable microscope using event-based sensing.

Thus, here it has been demonstrated that event-based cameras hold much potential for inertial microfluidic analysis, biomedical research and portable microscopy and it is hoped that this work can provide such research groups with a more accessible alternative to traditional high-speed microscopy.

## Chapter 7

# Conclusions and future outlook

As outlined in Section 1.2, the cell cycle has demonstrated much promise as a target for drug development for the treatment of leishmanial diseases – halting a cell's progression through this essential process prevents its replication and thus its ability to cause disease. The high heterogeneity and non-canonical methods of cellular control of *Leishmania* parasites makes it difficult to identify and understand the role of proteins involved in cell cycle progression, highlighting the need for tools to both better understand the cell cycle, as well as robust methods of cell cycle synchronisation. In this thesis, it was tested whether inertial microfluidics could be used as a chemical free, high-throughput and passive method of cell cycle synchronisation, relying purely on the mechanical properties of these parasites as the basis of separation. In pursuit of this aim, significant contributions to both the field of *Leishmania* research and inertial microfluidics were made, as well as achieving enrichment of subsets of cells with particular cell cycle-related morphologies.

### IFC analysis of the cell cycle of *L. mexicana*

The first objective was to better understand how the morphology of *L. mexicana* related to its stage in the cell cycle and to identify physical biomarkers to distinguish the different stages. As morphology was a key component of this work, traditional methods of cell cycle analysis were insufficient as these require cell fixation (which was demonstrated to affect cell morphology), were low throughput and time consuming, or had a low resolution for distinguishing the different stages. Therefore, a novel method of analysing the cell cycle of *L. mexicana* parasites was developed. While there are a plethora of dyes which stain DNA in mammalian cells, many of these same dyes were shown to be non-quantitative in live *L.*

*mexicana*. After much optimisation, a staining protocol was developed using DCO. By combining this protocol with imaging flow cytometry (IFC), a high-throughput method of cell cycle analysis was developed to simultaneously assess both DNA and morphology.

From these data, morphological parameters associated with the individual cell cycle stages were identified, enabling thresholds of 10 μm in length and 4 μm in width to be defined as indicators of cell cycle stage. Furthermore, width and aspect ratio measurements were shown to have the highest correlation to a particular stage in the cell cycle - for cells in M/C. In addition, the application of the developed protocol was applied to *L. mexicana* promastigotes tagged with mNG:KINF, and through the automatic characterisation of cells based on their mNG:KINF fluorescence, along with the manual classification of cells with two flagella, the elusive G2 stage of *L. mexicana's* cell cycle was defined along with a population of newly divided daughter cells. Cell cycle stages down to 10 minutes in a 12.4 hour cell cycle could be resolved, due to the high number of cells capable of being analysed by IFC. This new method of cell cycle analysis was shown to give comparable results to traditional methods of analysis, in terms of the proportions and timings of cells in each of the cell cycle stages [125], [337]. However, here, the analysis was carried out at a much higher scale, with > 400 cells being analysed per cell cycle population, with the smallest population being only 1.7% of the total number of cells. Additionally, 6 cell cycle stages were capable of being automatically identified using IFC (very early G1, early G1, late G1/early S, late S/G2, mitotic and post-mitotic) resulting in a high resolution of analysis. IFC therefore proved to be a highly useful tool for the morphological characterisation of *L. mexicana*, overcoming traditional limitations of low *n* numbers and lengthy analysis times for a high-throughput and in-depth characterisation of different populations.

While this work provided in depth analysis of *L. mexicana's* cell cycle, one of the caveats (as discussed previously in Section 3.2.3) is that the addition of chemicals, including DNA dyes such as DCO, can introduce artefacts into the cells and affect normal cellular function. Therefore, there is a movement towards label-free techniques of cellular analysis. For IFC, this has been achieved by training machine learning and/or AI modules on the BF images of pre-classified data sets to identify populations of interest. This technique has previously been applied to classify Jurkat cells into the different cell cycle stages [268]. Here, prior to the discovery of DCO as a quantitative DNA dye, machine learning was applied (with the help of

Prabhjoat Chana from Amis® Corporation) to *L. mexicana* cells to attempt to similarly classify cells based on their BF images. Due to the relatively low resolution of the images, the overlap in morphology between different cell cycle stages (e.g. identification of one flagella *vs* two) and the high level of technical variation (e.g. cells rotating in the flow and imaged end on or side on, and cells crossing through multiple focal planes), robust classification was not achieved. This may however have been improved with the use of the rigorous data processing strategy (not defined at the time of analysis) and an increase in the number of cells used in the training set. While the use of machine learning for such cell cycle analysis is complex, automatic classification of cells in this way may have higher success in applications such as for the life cycle classification of *L. mexicana* cells, where cell morphologies are more distinct [301].

While protocols were developed for the cell cycle analysis of *L. mexicana*, such protocols may also have applications in other areas of *L. mexicana* research, and the study of other protozoa. As previously mentioned in Section 4.1, cell cycle analysis and morphological measurements are often employed in a variety of studies, such as the functional assessment of proteins, drug toxicity assays and life cycle analysis. While the relatively low resolution of IFC means that it will not replace microscopy, the ability to accurately measure the morphology of thousands of cells and generate a picture of a population as a whole, is highly beneficial. IFC enables the identification of rare populations and events which may be missed during microscopy analysis (particularly for gene knockout or knockin experiments analysing temporally and/or spatially specific proteins), provides an accurate quantification of subpopulations without lengthy data processing times and enables many conditions to be simultaneously analysed and compared. Thus, IFC holds a massive amount of potential for the morphological analysis of many non-spherical cell types where traditional methods of analysis are unsuitable. It is hoped that this thesis exemplifies the extensive range of features and capabilities of IFC and encourages a new standard for morphological analysis.

### Inertial microfluidic sorting of *L. mexicana*

From such IFC characterisation of the cell cycle, it was determined that sorting cells based on cell width or aspect ratio would achieve the greatest purity of M/C cells during inertial microfluidic sorting. However, in literature it has been demonstrated, predominantly in straight channels, that only a particle’s longest dimension affected the focusing position of particles during sorting, and that the width and thus aspect ratio were irrelevant [232], [362], [459]. Sorting on length alone would be insufficient to separate the cell cycle stages of *L. mexicana* as both early G1 cells and M/C cells are short, and late G1 and S phases are long. However, more recent work has suggested that in curved channels, the shape of a particle may play a more prominent role in sorting, yet this theory had not been explored for the separation of cells. It was thus attempted to understand the contribution of individual aspects of *Leishmania's* morphology in particle focusing in order to use this knowledge to guide the sorting of the different stages of the cell cycle. For this, various different morphologies of *L. mexicana* were generated, using chemical treatment and cell differentiation.

First an attempt was made to isolate the role of the flagellum in the focusing behaviour of *L. mexicana*, which, in previous work, has been reported to alter the rotation of sperm cells in flow and cause a focusing position to the outer wall [366]. Here, removal of cell flagella (but maintaining cell morphology), had minimal effect on the focusing position of cells. Informed by the behaviours of the parasites with modified morphologies, it was thus concluded that differences in cell shape resulted in altered rotational behaviours in a similar manner to how flagella altered the rotation of sperm cells, thus causing the same focusing position to the outer wall. Interestingly, deformable particles are also one of the few the cell types which also have a focusing position to the outer wall [196], [356], [366]. These particles have been described to, instead of rotating in the flow, “tank-tread” in a deformed shape under high shear stress [196]. This hypothesis that an elongated shape and an altered rotation cause migration the outer wall could also be applied to the focusing of deformable particles. Therefore, future work into understanding the rotational behaviour of cells in flow will be key in predicting how cells will focus within inertial microfluidic devices.

Typically the rotation of individual particles within inertial microfluidic devices is achieved by high-speed imaging to analyse the orientation of particles across multiple frames [459]. Here however, such high-speed imaging was attempted; however, a suboptimal imaging setup, and the high flow rates used for the sorting experiments prevented an individual cell from being imaged multiple times. Alternative methods of analysing the rotation of particles within channels includes numerical simulation experiments [209] or the use of asymmetrically-bound fluorescent probes on the surface of non-spherical particles [460].

As the flagella did not cause the unusual focusing behaviour, attention was turned to the role of cell shape. Here, various cell populations were generated to modify components of the shape of parental *L. mexicana* parasites. This included differentiation to amastigotes, and treatment with the cell cycle synchronising drugs hydroxyurea and flavopiridol. While these drugs were used to modify the morphology of the parental cells, it was hoped that by chemically enriching cells at a single cell cycle stage, that the morphological variation associated with the different cell cycle stages would thus be reduced. As such, this would result in a "model" population of cells with a lower complexity to emphasise focusing behaviours associated with a particular morphology. As demonstrated by IFC analysis however, the incomplete synchronisation of these cells still resulted in populations with high amounts of variation. Synchronisation was also attempted using FACS but the numbers of cells recovered after such sorting were too low for inertial microfluidic analysis.

From analysing the focusing behaviour of these populations within curved microfluidic channels, it was demonstrated that over a range of flow rates, these parasites still had highly different focusing trends compared to that of rigid spherical beads with an equivalent diameter. Particularly at higher flow rates, all populations of cells tested focused to the same place at the outer wall at at least one flow rate tested. While using cells to model different features of *L. mexicana's* shape was beneficial in understanding focusing behaviours, the heterogeneity and complexity of these cells made it difficult to draw definitive correlations. Therefore, to better understand the contributions of cell shape and texture, future experiments could look at the use of non-rigid model particles or numerical simulation experiments.

Typically, rigid spherical beads are used as model particles for sorting; however, these are highly different to cells, having a smooth surface, no deformability and an even shape, and as demonstrated here, were unable to replicate the behaviour of the cells. In recent years, hydrogel beads have become popular particles for inertial microfluidic analysis due to their high level of customisability in terms of their size, shape and composition, enabling properties of cell (e.g. cell deformability) to be mimicked. Such particles have been generated with a wide range of complex shapes, such as tear-drop, snowflake, acorn, and spikey particles [461]. While no such particles are commercially available, their manufacture in house would enable the design of particles more closely resembling *L. mexicana* cells. Alternatively, simulation experiments, like that performed by Hafemann [364], could be performed to model the behaviour of highly elongated particles within a curved channel. An attempt to achieve this was carried out through a collaboration; however, the work proved highly complex and was not completed before the submission of this thesis. Such experiments may provide a greater level of understanding of the behaviour of *L. mexicana* within curved inertial microfluidic channels to improve device design for increased cell cycle enrichment.

Despite cells migrating to the same place at higher flow rates, at lower Reynolds numbers shape-based sorting was demonstrated, seeing an enrichment of 1.8X for short and wide cells; a morphology that was shown to correspond with cells in M/C phases. To ensure that this cell cycle stage was indeed enriched, the next step would be to perform cell cycle analysis on the sorted outlet populations. While an enrichment was seen, the purity was still too low to compete with existing methods of cell cycle synchronisation, with all sizes and shapes of the parental *L. mexicana* being found in all the outlets. This may be a result of the cells not finding stable focusing positions within the flow and instead predominantly recirculating throughout the width of the channel. This could be due to other factors of the cells' morphology affecting their rotation, such as an uneven surface texture or a curvature in the cell shape [383]. Similarly as above, model particles (such as hydrogels with complex surface topographies) [462] and simulation experiments maybe useful in deducing the contribution of such features in sorting.

From the experiments carried out here, a low enrichment of short and wide cells was achieved. To improve the enrichment, the channel design could be optimised. It was demonstrated that, at lower flow rates in both the smaller and larger channel, a lower confinement (achieved with smaller cells, or an increased channel size) better enabled cells to focus towards the inner wall. Additionally, from both the analysis of modified populations and the sort of live parental populations, it was seen that elongated cells seemed to preferentially focus towards the outer wall. Therefore, it was hypothesised that a channel with a height of 36 μm and a width of 220 μm would enable short cells with a low confinement (including the M/C population) to focus to the inner wall, while higher confinement long cells would focus to the outer wall. However, as previously mentioned in Section 4.2.7, sorting based on cell length alone would sort both early G1 and M/C cells into the same outlet. Alternatively, a different channel design, for example, a straight channel like the one employed by Li et al., may provide an increased enrichment [344].

At higher flow rates, no enrichment of populations was seen, as all cells (both within a single population and the populations with altered morphologies) focused to a single conserved position at the outer wall. While the single focusing position at the outer wall was not beneficial for the isolation of the different cell cycle stages, this mechanism may be highly beneficial for alternative applications, particularly as the typical focusing of spherical particles at the inner wall is still maintained. Such applications may include the removal of substances from a liquid or for the continual concentration of particles, i.e. the isolation of parasites from water [228], [384] and particle concentration for manufacturing purposes [463].

### Portable high-speed imaging using event-based cameras

One of the caveats noted in the sorting of *L. mexicana* was that high-speed imaging had to be carried out on fixed cells due to the requirement of handing live cells within a microbiological safety cabinet (MSC). Fixation was shown in Chapter 3 to affect cell morphology, and it is known to affect cell deformability, both of which affect cell migration within inertial microfluidic channels, and potentially provide different results to live cells. Therefore Chapter 6 explored whether event-based cameras could be used as a method of high-speed imaging, requiring no pulsed light and minimal computer processing power in comparison to traditional high-speed imaging. The reduction in bulky equipment thus enabled a portable system for use in an MSC. It was demonstrated that while event-based cameras were capable of tracking particles (both in brightfield and fluorescence mode) at low Reynolds numbers ($Re \leq 15.9$), a decrease in the contrast of particles at higher flow rates prevented their detection. Increasing the contrast of beads with fluorescence was shown to be highly effective in improving their detection up to $Re = 250.0$; however, the maximum fluorescence that was achieved in *L. mexicana* cells was still too low for detection, even at Reynolds numbers as low as 33.3. While its use for tracking the focusing behaviour of live *L. mexicana* within inertial microfluidic devices was unfeasible, event-based cameras hold much potential in the field of both inertial microfluidic and *Leishmania* analysis, offering a portable, low power, low latency, low data usage method of high-speed imaging. Future work would focus on continuing the development of a fully functional portable, 3D-printed microscope using the event-based camera for particle analysis.

### Overview

Thus, throughout this work, while cell cycle synchronisation using inertial microfluidics was not achieved, significant contributions have been made towards *Leishmania* and inertial microfluidic research. New methodologies were developed for use in both fields, as well as providing experimental data towards the fundamental understanding of *L. mexicana’s* cell cycle and the focusing of non-spherical cells in curved inertial microfluidic devices.

# Bibliography

[1] WHO, *Leishmaniasis*, `https://www.who.int/data/gho/data/themes/topics/gho-ntd-leishmaniasis`, Web Page, [Online; 26-Feb-2024], 2021.

[2] L. Remadi, N. Haouas, D. Chaara, *et al.*, “Clinical presentation of cutaneous leishmaniasis caused by *Leishmania major*,” *Dermatology*, vol. 232, no. 6, pp. 752–759, 2017.

[3] I. Abadías-Granado, A. Diago, P. A. Cerro, A. M. Palma-Ruiz, and Y. Gilaberte, “Cutaneous and mucocutaneous leishmaniasis,” *Actas Dermo-Sifiliográficas (English Edition)*, vol. 112, no. 7, pp. 601–618, 2021.

[4] A. V. Ibarra-Meneses, A. Corbeil, V. Wagner, C. Onwuchekwa, and C. Fernandez-Prada, “Identification of asymptomatic *Leishmania* infections: A scoping review,” *Parasit Vectors*, vol. 15, no. 1, p. 5, 2022.

[5] S. Mann, K. Frasca, S. Scherrer, *et al.*, “A review of leishmaniasis: Current knowledge and future directions,” *Curr Trop Med Rep*, vol. 8, no. 2, pp. 121–132, 2021.

[6] R. Molina, M. Jiménez, J. García-Martínez, *et al.*, “Role of asymptomatic and symptomatic humans as reservoirs of visceral leishmaniasis in a Mediterranean context,” *PLoS Negl Trop Dis*, vol. 14, no. 4, e0008253, 2020.

[7] A. K. Kushwaha, B. M. Scorza, O. P. Singh, *et al.*, “Domestic mammals as reservoirs for *Leishmania donovani* on the Indian subcontinent: Possibility and consequences on elimination,” *Transbound Emerg Dis*, vol. 69, no. 2, pp. 268–277, 2022.

[8] H. Medkour, B. Davoust, F. Dulieu, *et al.*, “Potential animal reservoirs (dogs and bats) of human visceral leishmaniasis due to *Leishmania infantum* in French Guiana,” *PLoS Negl Trop Dis*, vol. 13, no. 6, e0007456, 2019.

[9] L. Zhuang, J. Su, and P. Tu, “Cutaneous leishmaniasis presenting with painless ulcer on the right forearm: A case report,” *World J Clin Cases*, vol. 10, no. 7, pp. 2301–2306, 2022.

[10] A. Woodland, R. Grimaldi, T. Luksch, *et al.*, “From on-target to off-target activity: Identification and optimisation of *Trypanosoma brucei* GSK3 inhibitors and their characterisation as anti-*Trypanosoma brucei* drug discovery lead molecules,” *ChemMedChem*, vol. 8, no. 7, pp. 1127–1137, 2013.

[11] S. D. Lawn, J. Whetham, P. L. Chiodini, *et al.*, “New world mucosal and cutaneous leishmaniasis: An emerging health problem among British travellers,” *QJM*, vol. 97, no. 12, pp. 781–788, 2004.

[12] T. V. Piscopo and C. Mallia Azzopardi, “Leishmaniasis,” *Postgrad Med J*, vol. 83, no. 976, pp. 649–657, 2007.

[13] E. Torres-Guerrero, M. R. Quintanilla-Cedillo, J. Ruiz-Esmenjaud, and R. Arenas, “Leishmaniasis: A review,” *F1000Res*, vol. 6, pp. 750–750, 2017.

[14] A. C. Costa-da-Silva, D. O. Nascimento, J. R. M. Ferreira, *et al.*, “Immune responses in leishmaniasis: An overview,” *Trop Med Infect Dis*, vol. 7, no. 4, p. 54, 2022.

[15] Anon, “Urbanization: An increasing risk factor for leishmaniasis,” *Wkly Epidemiol Rec*, vol. 77, no. 44, pp. 365–370, 2002.

[16] WHO, *Leishmaniasis - magnitude of the problem*, `https://www.who.int/leishmaniasis/burden/magnitude/burden_magnitude/en/`, Web page, [Online; accessed 26-Aug-2020].

[17] E. Y. Osorio, A. Uscanga-Palomeque, G. T. Patterson, *et al.*, “Malnutrition-related parasite dissemination from the skin in visceral leishmaniasis is driven by PGE2-mediated amplification of CCR7-related trafficking of infected inflammatory monocytes,” *PLoS Negl Trop Dis*, vol. 17, no. 1, e0011040, 2023.

[18] S. Rijal, S. Koirala, P. Van der Stuyft, and M. Boelaert, “The economic burden of visceral leishmaniasis for households in Nepal,” *Trans R Soc Trop Med Hyg*, vol. 100, no. 9, pp. 838–41, 2006.

[19] G. Grifferty, H. Shirley, J. McGloin, J. Kahn, A. Orriols, and R. Wamai, “Vulnerabilities to and the socioeconomic and psychosocial impacts of the leishmaniases: A review,” *Res Rep Trop Med*, vol. 12, pp. 135–151, 2021.

[20] C. A. Gómez-Ponce, E. Pérez-Barragán, D. M. Méndez-Palacios, K. O. Ramírez-Romero, and S. Pérez-Cavazos, “Emerging infectious diseases and migration: A case of leishmaniasis in northern Mexico,” *The Lancet Infectious Diseases*, vol. 23, no. 6, pp. 648–650, 2023.

[21] F. Z. Talbi, N. Nouayti, H. El Omari, *et al.*, “Thematic maps of the impact of urbanization and socioeconomic factors on the distribution of the incidence of cutaneous leishmaniasis cases in Sefrou Province, Central North of Morocco (2007-2011),” *Interdiscip Perspect Infect Dis*, vol. 2020, p. 8 673 091, 2020.

[22] J. M. Curtin and N. E. Aronson, “Leishmaniasis in the United States: Emerging issues in a region of low endemicity,” *Microorganisms*, vol. 9, no. 3, p. 578, 2021.

[23] A. Pavli and H. C. Maltezou, “Leishmaniasis, an emerging infection in travelers,” *Int J Infect Dis*, vol. 14, no. 12, e1032–e1039, 2010.

[24] C. F. Clarke, K. K. Bradley, J. H. Wright, and J. Glowicz, “Case report: Emergence of autochthonous cutaneous leishmaniasis in northeastern Texas and southeastern Oklahoma,” *Am J Trop Med Hyg*, vol. 88, no. 1, pp. 157–61, 2013.

[25] M. de Almeida, Y. Zheng, F. Nascimento, *et al.*, “Cutaneous leishmaniasis caused by an unknown *Leishmania* strain, Arizona, USA,” *Emerg Infect Dis*, vol. 27, no. 6, p. 1714, 2021.

[26] M. Douvoyiannis, T. Khromachou, N. Byers, J. Hargreaves, and H. W. Murray, “Cutaneous leishmaniasis in North Dakota,” *Clin Infect Dis*, vol. 59, no. 5, e73–e75, 2014.

[27] S. M. Reuss, M. D. Dunbar, M. B. Calderwood Mays, *et al.*, “Autochthonous *Leishmania siamensis* in horse, Florida, USA,” *Emerging infectious diseases*, vol. 18, no. 9, pp. 1545–7, 2012.

[28] P. M. Schantz, F. J. Steurer, Z. H. Duprey, *et al.*, “Autochthonous visceral leishmaniasis in dogs in North America,” *J Am Vet Med Assoc*, vol. 226, no. 8, pp. 1316–1322, 2005.

[29] C. Maia, C. Conceição, A. Pereira, *et al.*, “The estimated distribution of autochthonous leishmaniasis by *Leishmania infantum* in Europe in 2005–2020,” *PLoS Negl Trop Dis*, vol. 17, no. 7, e0011497, 2023.

[30] WHO, *Leishmaniasis: Status of endemicity of cutaneous leishmaniasis*, `https://www.who.int/data/gho/data/themes/topics/gho-ntd-leishmaniasis`, Web Page, [Online; accessed 17-Dec-2023], 2022.

[31] V. Tunalı and A. Özbilgin, “Knock, knock, knocking on Europe’s door: Threat of leishmaniasis in Europe with a focus on Turkey,” *Curr Res Parasitol Vector Borne Dis*, vol. 4, p. 100 150, 2023.

[32] R. Rocha, A. Pereira, and C. Maia, “Non-endemic leishmaniases reported globally in humans between 2000 and 2021-a comprehensive review,” *Pathogens*, vol. 11, no. 8, p. 921, 2022.

[33] UNWOT, *Global and regional tourism performance*, `https://www.unwto.org/tourism-data/global-and-regional-tourism-performance`, Web Page, [Online; accessed 18-Dec-2023], 2022.

[34] A. K. Boggild, E. Caumes, M. P. Grobusch, *et al.*, “Cutaneous and mucocutaneous leishmaniasis in travellers and migrants: A 20-year GeoSentinel Surveillance Network analysis,” *J Travel Med*, vol. 26, no. 8, taz055, 2019.

[35] G. Van der Auwera, L. Davidsson, P. Buffet, *et al.*, “Surveillance of leishmaniasis cases from 15 European centres, 2014 to 2019: A retrospective analysis,” *Eurosurveillance*, vol. 27, no. 4, p. 2 002 028, 2022.

[36] E. Schwartz, C. Hatz, and J. Blum, “New world cutaneous leishmaniasis in travellers,” *Lancet Infect Dis*, vol. 6, no. 6, pp. 342–349, 2006.

[37] W. S. Al-Salem, D. M. Pigott, K. Subramaniam, *et al.*, “Cutaneous leishmaniasis and conflict in Syria,” in *Emerg Infect Dis*. United States, 2016, vol. 22.

[38] R. Du, P. J. Hotez, W. S. Al-Salem, and A. Acosta-Serrano, “Old world cutaneous leishmaniasis and refugee crises in the Middle East and North Africa,” *PLoS Negl Trop Dis*, vol. 10, no. 5, e0004545, 2016.

[39] I. S. Koltas, F. Eroglu, D. Alabaz, and S. Uzun, “The emergence of *Leishmania major* and *Leishmania donovani* in southern Turkey,” *Trans R Soc Trop Med Hyg*, vol. 108, no. 3, pp. 154–8, 2014.

[40] A. Özbilgin, G. Gencoglan, V. Tunali, *et al.*, “Refugees at the crossroads of continents: A molecular approach for cutaneous leishmaniasis among refugees in Turkey,” *Acta Parasitol*, vol. 65, no. 1, pp. 136–143, 2020.

[41] C. M. Jones and S. C. Welburn, “Leishmaniasis beyond East Africa,” *Front Vet Sci*, vol. 8, p. 618 766, 2021.

[42] H. El Omari, A. Chahlaoui, F. Z. Talbi, K. E. Mouhdi, and A. El Ouali Lalami, “Impact of climatic factors on the seasonal fluctuation of leishmaniasis vectors in central Morocco (Meknes Prefecture),” *Can J Infect Dis Med Microbiol*, vol. 2020, p. 6 098 149, 2020.

[43] M. Maroli, L. Rossi, R. Baldelli, *et al.*, “The northward spread of leishmaniasis in Italy: Evidence from retrospective and ongoing studies on the canine reservoir and phlebotomine vectors,” *Trop Med Int Health*, vol. 13, no. 2, pp. 256–264, 2008.

[44] M. Gramiccia and L. Gradoni, “The current status of zoonotic leishmaniases and approaches to disease control,” *Int J Parasitol*, vol. 35, no. 11, pp. 1169–1180, 2005.

[45] D. Fischer, P. Moeller, S. M. Thomas, T. J. Naucke, and C. Beierkuhnlein, “Combining climatic projections and dispersal ability: A method for estimating the responses of sandfly vector species to climate change,” *PLoS Negl Trop Dis*, vol. 5, no. 11, e1407, 2011.

[46] L. K. Koch, J. Kochmann, S. Klimpel, and S. Cunze, “Modeling the climatic suitability of leishmaniasis vector species in Europe,” *Sci Rep*, vol. 7, no. 1, p. 1332, 2017.

[47] C. González, O. Wang, S. E. Strutz, C. González-Salazar, V. Sánchez-Cordero, and S. Sarkar, “Climate change and risk of leishmaniasis in North America: Predictions from ecological niche models of vector and reservoir species,” *PLoS Negl Trop Dis*, vol. 4, no. 1, e585–e585, 2010.

[48] W. B. Group, “Climate risk country profile: Morocco,” Report, 2021.

[49] K. Kholoud, S. Denis, B. Lahouari, M. A. El Hidan, and B. Souad, “Management of leishmaniases in the era of climate change in Morocco,” *Int J Environ Res Public Health*, vol. 15, no. 7, p. 1542, 2018.

[50] H. Goto and J. A. L. Lindoso, “Current diagnosis and treatment of cutaneous and mucocutaneous leishmaniasis,” *Expert Rev Anti Infect Ther*, vol. 8, no. 4, pp. 419–433, 2010.

[51] H. Fikre, E. Teklehaimanot, R. Mohammed, *et al.*, “Atypical mucocutaneous leishmaniasis presentation mimicking rectal cancer,” *Case Rep Infect Dis*, vol. v.2023, p. 2 768 626, 2023.

[52] A. Schwing, C. Pomares, A. Majoor, L. Boyer, P. Marty, and G. Michel, “*Leishmania* infection: Misdiagnosis as cancer and tumor-promoting potential,” *Acta Tropica*, vol. 197, p. 104 855, 2019.

[53] K. Sikorska, M. Gesing, R. Olszański, A. Roszko-Wysokińska, B. Szostakowska, and K. Van Damme-Ostapowicz, “Misdiagnosis and inappropriate treatment of cutaneous leishmaniasis: A case report,” *Trop Dis Travel Med Vaccines*, vol. 8, no. 1, p. 18, 2022.

[54] A. H. Tripathi, P. H. Tripathi, and A. Pandey, “Chapter 9 - evaluation of biomarkers to monitor therapeutic intervention against visceral leishmaniasis,” in *Pathogenesis, Treatment and Prevention of Leishmaniasis*, M. Samant and S. Chandra Pandey, Eds. Academic Press, 2021, pp. 161–182.

[55] P. Srivastava, A. Dayama, S. Mehrotra, and S. Sundar, “Diagnosis of visceral leishmaniasis,” *Trans R Soc Trop Med Hyg*, vol. 105, no. 1, pp. 1–6, 2011.

[56] CDC, *Leishmaniasis: Resources for health professionals*, `https://www.cdc.gov/parasites/leishmaniasis/health_professionals/index.html`, Web Page, [Online; accessed 18-Dec-2023], 2023.

[57] H. J. de Vries, S. H. Reedijk, and H. D. Schallig, “Cutaneous leishmaniasis: Recent developments in diagnosis and management,” *Am J Clin Dermatol*, vol. 16, no. 2, pp. 99–109, 2015.

[58] A. Q. Sousa, M. M. Pompeu, M. S. Frutuoso, J. W. Lima, J. M. Tinel, and R. D. Pearson, “Press imprint smear: A rapid, simple, and cheap method for the diagnosis of cutaneous leishmaniasis caused by *Leishmania (Viannia) braziliensis*,” *Am J Trop Med Hyg*, vol. 91, no. 5, pp. 905–7, 2014.

[59] S. L. Croft, S. Sundar, and A. H. Fairlamb, “Drug resistance in leishmaniasis,” *Clin Microbiol Rev*, vol. 19, no. 1, pp. 111–26, 2006.

[60] K. Katakura, S. I. Kawazu, C. Sanjyoba, *et al.*, “*Leishmania* mini-exon genes for molecular epidemiology of leishmaniasis in China and Ecuador,” *Tokai J Exp Clin Med*, vol. 23, no. 6, pp. 393–9, 1998.

[61] D. N. Lockwood and S. Sundar, “Serological tests for visceral leishmaniasis,” *BMJ (Clinical research ed.)*, vol. 333, no. 7571, pp. 711–2, 2006.

[62] S. Sundar, S. G. Reed, V. P. Singh, P. C. Kumar, and H. W. Murray, “Rapid accurate field diagnosis of Indian visceral leishmaniasis,” *Lancet*, vol. 351, no. 9102, pp. 563–5, 1998.

[63] V. K. Agrawal, “Field adaptable tests for kala-azar,” *Med J Armed Forces India*, vol. 62, no. 2, pp. 178–9, 2006.

[64] C. Abeijon, O. P. Singh, J. Chakravarty, S. Sundar, and A. Campos-Neto, “Novel antigen detection assay to monitor therapeutic efficacy of visceral leishmaniasis,” *Am J Trop Med Hyg*, vol. 95, no. 4, pp. 800–802, 2016.

[65] C.-h. Gao, Y.-t. Yang, F. Shi, J.-y. Wang, D. Steverding, and X. Wang, “Development of an immunochromatographic test for diagnosis of visceral leishmaniasis based on detection of a circulating antigen,” *PLoS Negl Trop Dis*, vol. 9, no. 6, e0003902, 2015.

[66] A. C. Vallur, Y. L. Tutterrow, R. Mohamath, *et al.*, “Development and comparative evaluation of two antigen detection tests for visceral leishmaniasis,” *BMC Infec Dis*, vol. 15, no. 1, p. 384, 2015.

[67] F. Frézard, C. Demicheli, and R. R. Ribeiro, “Pentavalent antimonials: New perspectives for old drugs,” *Molecules*, vol. 14, no. 7, pp. 2317–36, 2009.

[68] WHO, “Control of the leishmaniases: Report of a meeting of the WHO expert committee on the control of leishmaniases,” Report, 2010.

[69] M. C. Oliveira, R. F. B. d. Amorim, R. d. A. Freitas, and A. d. L. L. Costa, “A fatal case of mucocutaneous leishmaniasis after pentavalent antimonial use,” *Rev Soc Bras Med Trop*, vol. 38, no. 3, pp. 258–260, 2005.

[70] F. Chappuis, S. Sundar, A. Hailu, *et al.*, “Visceral leishmaniasis: What are the needs for diagnosis, treatment and control?” *Nat Rev Microbiol*, vol. 5, no. 11, pp. 873–882, 2007.

[71] K. Rai, B. Cuypers, R. Bhattarai Narayan, *et al.*, “Relapse after treatment with miltefosine for visceral leishmaniasis is associated with increased infectivity of the infecting *Leishmania donovani* strain,” *mBio*, vol. 4, no. 5, 10.1128/mbio.00611–13, 2013.

[72] C. V. David and N. Craft, “Cutaneous and mucocutaneous leishmaniasis,” *Dermatol Ther*, vol. 22, no. 6, pp. 491–502, 2009.

[73] A. C. Pinheiro and M. V. N. de Souza, “Current leishmaniasis drug discovery,” *RSC Med Chem*, vol. 13, no. 9, pp. 1029–1043, 2022.

[74] S. Pradhan, R. A. Schwartz, A. Patil, S. Grabbe, and M. Goldust, “Treatment options for leishmaniasis,” *Clin Exp Dermatol*, vol. 47, no. 3, pp. 516–521, 2022.

[75] N. M. Ikeogu, G. N. Akaluka, C. A. Edechi, *et al.*, “*Leishmania* immunity: Advancing immunotherapy and vaccine development,” *Microorganisms*, vol. 8, no. 8, p. 1201, 2020.

[76] R. Velez and M. Gállego, “Commercially approved vaccines for canine leishmaniasis: A review of available data on their safety and efficacy,” *Trop Med Int Health*, vol. 25, no. 5, pp. 540–557, 2020.

[77] A. J. Pollard and E. M. Bijker, “A guide to vaccinology: From basic principles to new developments,” *Nat Rev Immunol*, vol. 21, no. 2, pp. 83–100, 2021.

[78] A. Khamesipour, Y. Dowlati, A. Asilian, *et al.*, “Leishmanization: Use of an old method for evaluation of candidate vaccines against leishmaniasis,” *Vaccine*, vol. 23, no. 28, pp. 3642–3648,

[79] A. Selvapandiyan, R. Dey, S. Gannavaram, *et al.*, “Immunity to visceral leishmaniasis using genetically defined live-attenuated parasites,” *J Trop Med*, vol. 2012, p. 631 460, 2012.

[80] M. Osman, A. Mistry, A. Keding, *et al.*, “A third generation vaccine for human visceral leishmaniasis and post kala azar dermal leishmaniasis: First-in-human trial of ChAd63-KH,” *PLoS Negl Trop Dis*, vol. 11, no. 5, e0005527, 2017.

[81] B. M. Younis, M. Osman, E. A. G. Khalil, *et al.*, “Safety and immunogenicity of ChAd63-KH vaccine in post-kala-azar dermal leishmaniasis patients in Sudan,” *Mol Ther*, vol. 29, no. 7, pp. 2366–2377, 2021.

[82] K. Stuart, R. Brun, S. Croft, *et al.*, “Kinetoplastids: Related protozoan pathogens, different diseases,” *J Clin Invest*, vol. 118, no. 4, pp. 1301–10, 2008.

[83] P. Anuntasomboon, S. Siripattanapipong, S. Unajak, *et al.*, “Identification of a unique conserved region from a kinetoplastid genome of *Leishmania orientalis* (formerly named *Leishmania siamensis*) strain PCM2 in Thailand,” *Sci Rep*, vol. 13, no. 1, p. 19 644, 2023.

[84] L. Simpson, “The genomic organization of guide RNA genes in kinetoplastid protozoa: Several conundrums and their solutions,” *Mol Biochem Parasitol*, vol. 86, no. 2, pp. 133–141, 1997.

[85] V. Y. Yurchenko, E. M. Merzlyak, A. A. Kolesnikov, L. P. Martinkina, and Y. Y. Vengerov, “Structure of *Leishmania* minicircle kinetoplast DNA classes,” *J Clin Microbiol*, vol. 37, no. 5, pp. 1656–7, 1999.

[86] E. Gluenz, J. L. Höög, A. E. Smith, H. R. Dawe, M. K. Shaw, and K. Gull, “Beyond 9+0: Noncanonical axoneme structures characterize sensory cilia from protists to humans,” *FASEB J*, vol. 24, no. 9, pp. 3117–3121, 2010.

[87] R. J. Wheeler, E. Gluenz, and K. Gull, “Basal body multipotency and axonemal remodelling are two pathways to a 9+0 flagellum,” *Nat Commun*, vol. 6, no. 1, p. 8964, 2015.

[88] J. D. Sunter, R. Yanase, Z. Wang, *et al.*, “*Leishmania* flagellum attachment zone is critical for flagellar pocket shape, development in the sand fly, and pathogenicity in the host,” *Proc Natl Acad Sci U S A*, vol. 116, no. 13, p. 6351, 2019.

[89] A. Ambit, N. Fasel, G. H. Coombs, and J. C. Mottram, “An essential role for the *Leishmania major* metacaspase in cell cycle progression,” *Cell Death Differ*, vol. 15, no. 1, pp. 113–122, 2008.

[90] R. J. Wheeler, J. D. Sunter, and K. Gull, “Flagellar pocket restructuring through the *Leishmania* life cycle involves a discrete flagellum attachment zone,” *J Cell Sci*, vol. 129, no. 4, pp. 854–67, 2016.

[91] C. Halliday, R. Yanase, C. M. C. Catta-Preta, *et al.*, “Role for the flagellum attachment zone in *Leishmania* anterior cell tip morphogenesis,” *PLOS Pathogens*, vol. 16, no. 10, e1008494, 2020.

[92] J. D. Sunter and K. Gull, “The flagellum attachment zone: ’the cellular ruler’ of trypanosome morphology,” *Trends Parasitol*, vol. 32, no. 4, pp. 309–324, 2016.

[93] S. M. Landfear, “New vistas in the biology of the flagellum-*Leishmania* parasites,” *Pathogens*, vol. 11, no. 4, p. 447, 2022.

[94] S. Vaughan and K. Gull, “Basal body structure and cell cycle-dependent biogenesis in *Trypanosoma brucei*,” *Cilia*, vol. 5, no. 1, p. 5, 2016.

[95] M. A. Erlandson, U. Toprak, and D. D. Hegedus, “Role of the peritrophic matrix in insect-pathogen interactions,” *J Insect Physiol*, vol. 117, p. 103 894, 2019.

[96] P. A. Bates, “Transmission of *Leishmania* metacyclic promastigotes by phlebotomine sand flies,” *Int J Parasitol*, vol. 37, no. 10, pp. 1097–1106, 2007.

[97] M. E. Rogers, M. L. Chance, and P. A. Bates, “The role of promastigote secretory gel in the origin and transmission of the infective stage of *Leishmania mexicana* by the sandfly *Lutzomyia longipalpis*,” *Parasitology*, vol. 124, no. Pt 5, pp. 495–507, 2002.

[98] A. Dostálová and P. Volf, “*Leishmania* development in sand flies: Parasite-vector interactions overview,” *Parasit Vectors*, vol. 5, no. 1, p. 276, 2012.

[99] I. V. Coutinho-Abreu, J. Oristian, W. de Castro, *et al.*, “Binding of *Leishmania infantum* lipophosphoglycan to the midgut is not sufficient to define vector competence in *Lutzomyia longipalpis* sand flies,” *mSphere*, vol. 5, no. 5, 2020.

[100] P. F. P. Pimenta, S. J. Turco, M. J. McConville, P. G. Lawyer, P. V. Perkins, and D. L. Sacks, “Stage-specific adhesion of *Leishmania* promastigotes to the sandfly midgut,” *Science*, vol. 256, no. 5065, pp. 1812–1815, 1992.

[101] I. V. Coutinho-Abreu, T. D. Serafim, C. Meneses, S. Kamhawi, F. Oliveira, and J. G. Valenzuela, “Distinct gene expression patterns in vector-residing *Leishmania infantum* identify parasite stage-enriched markers,” *PLoS Negl Trop Dis*, vol. 14, no. 3, e0008014, 2020.

[102] S. M. Gossage, M. E. Rogers, and P. A. Bates, “Two separate growth phases during the development of *Leishmania* in sand flies: Implications for understanding the life cycle,” *Int J Parasitol*, vol. 33, no. 10, pp. 1027–34, 2003.

[103] M. Rogers, “The role of *Leishmania* proteophosphoglycans in sand fly transmission and infection of the mammalian host,” *Front Microbiol*, vol. 3, p. 223, 2012.

[104] Y.-D. Stierhof, P. A. Bates, R. L. Jacobson, *et al.*, “Filamentous proteophosphoglycan secreted by *Leishmania* promastigotes forms gel-like three-dimensional networks that obstruct the digestive tract of infected sandfly vectors,” *Eur J Cell Biol*, vol. 78, no. 10, pp. 675–689, 1999.

[105] P. A. Bates, “Revising *Leishmania’s* life cycle,” *Nat Microbiol*, vol. 3, no. 5, pp. 529–530, 2018.

[106] G. van Zandbergen, M. Klinger, A. Mueller, *et al.*, “Cutting edge: Neutrophil granulocyte serves as a vector for *Leishmania* entry into macrophages1,” *J Immun*, vol. 173, no. 11, pp. 6521–6525, 2004.

[107] D. Liu and J. E. Uzonna, “The early interaction of *Leishmania* with macrophages and dendritic cells and its influence on the host immune response,” *Front Cell Infect Microbiol*, vol. 2, p. 83, 2012.

[108] P. E. Kima, “The amastigote forms of *Leishmania* are experts at exploiting host cell processes to establish infection and persist,” *Int J Parasitol*, vol. 37, no. 10, pp. 1087–1096, 2007.

[109] M. J. McConville, D. de Souza, E. Saunders, V. A. Likic, and T. Naderer, “Living in a phagolysosome; metabolism of *Leishmania* amastigotes,” *Trends Parasitol*, vol. 23, no. 8, pp. 368–375, 2007.

[110] B. Alberts, A. Johnson, J. Lewis, M. Raff, K. Roberts, and P. Walter, *Molecular Biology of the Cell: An Overview of the Cell Cycle*, 4th edition. New York: Garland Science, 2002.

[111] S. Fulda, A. M. Gorman, O. Hori, and A. Samali, “Cellular stress responses: Cell survival and cell death,” *Int J Cell Biol*, vol. v.2010, pp. 1–23, 2010.

[112] A. Terhorst, A. Sandikci, C. A. Whittaker, *et al.*, “The environmental stress response regulates ribosome content in cell cycle-arrested *S. cerevisiae*,” *Front cell dev biol*, vol. 11, p. 1 118 766, 2023.

[113] B. Alberts, A. Johnson, J. Lewis, M. Raff, K. Roberts, and P. Walter, “Molecular biology of the cell: Intracellular control of cell-cycle events,” in 4th edition. New York: Garland Science, 2002.

[114] K. J. Barnum and M. J. O’Connell, “Cell cycle regulation by checkpoints,” *Methods Mol Biol*, vol. 1170, pp. 29–40, 2014.

[115] Y. Wang, P. Ji, J. Liu, R. R. Broaddus, F. Xue, and W. Zhang, “Centrosome-associated regulators of the G2/M checkpoint as targets for cancer therapy,” *Mol Cancer*, vol. 8, no. 1, p. 8, 2009.

[116] L. Hixon and A. Gualberto, “The control of mitosis,” *FBL*, vol. 5, no. 3, pp. 50–57, 2000.

[117] B. D. Dynlacht, “Regulation of transcription by proteins that control the cell cycle,” *Nature*, vol. 389, no. 6647, pp. 149–152, 1997.

[118] Y. Liu, S. Chen, S. Wang, *et al.*, “Transcriptional landscape of the human cell cycle,” *Proc Natl Acad Sci U S A*, vol. 114, no. 13, pp. 3473–3478, 2017.

[119] S. Basu, J. Greenwood, A. W. Jones, and P. Nurse, “Core control principles of the eukaryotic cell cycle,” *Nature*, vol. 607, no. 7918, pp. 381–386, 2022.

[120] G. M. Cooper, *The eukaryotic cell cycle*, 2000.

[121] L. Ding, J. Cao, W. Lin, *et al.*, “The roles of cyclin-dependent kinases in cell-cycle progression and therapeutic strategies in human breast cancer,” *Int J Mol Sci*, vol. 21, no. 6, p. 1960, 2020.

[122] T. Otto and P. Sicinski, “Cell cycle proteins as promising targets in cancer therapy,” *Nat Rev Cancer*, vol. 17, no. 2, pp. 93–115, 2017.

[123] M. Loddo, S. R. Kingsbury, M. Rashid, *et al.*, “Cell-cycle-phase progression analysis identifies unique phenotypes of major prognostic and predictive significance in breast cancer,” *British Journal of Cancer*, vol. 100, no. 6, pp. 959–970, 2009.

[124] J. Chakraborty and N. N. Das Gupta, “Mitotic cycle of the kala-azar parasite, *Leishmania donovani*,” *Microbiology*, vol. 28, no. 3, pp. 541–545, 1962.

[125] R. J. Wheeler, E. Gluenz, and K. Gull, “The cell cycle of *Leishmania*: Morphogenetic events and their implications for parasite biology,” *Mol Microbiol*, vol. 79, no. 3, pp. 647–662, 2011.

[126] A. Ambit, K. L. Woods, B. Cull, G. H. Coombs, and J. C. Mottram, “Morphological events during the cell cycle of *Leishmania major*,” *Eukaryotic Cell*, vol. 10, no. 11, p. 1429, 2011.

[127] M. Hair, R. Yanase, F. Moreira-Leite, *et al.*, “Whole cell reconstructions of *Leishmania mexicana* through the cell cycle,” *PLoS Pathog*, vol. 20, no. 2, p. 1 012 054, 2024.

[128] L. Simpson, “Effect of acriflavin on the kinetoplast of *Leishmania tarentolae*: Mode of action and physiological correlates of the loss of kinetoplast DNA,” *The Journal of cell biology*, vol. 37, no. 3, pp. 660–682, 1968.

[129] G. Cohen-Freue, T. R. Holzer, J. D. Forney, and W. R. McMaster, “Global gene expression in *Leishmania*,” *Int J Parasitol*, vol. 37, no. 10, pp. 1077–1086, 2007.

[130] L. Cortazzo da Silva, J. I. Aoki, and L. M. Floeter-Winter, “Finding correlations between mRNA and protein levels in *Leishmania* development: Is there a discrepancy?” *Front Cell Infect Microbiol*, vol. 12, p. 852 902, 2022.

[131] N. Baker, C. M. C. Catta-Preta, R. Neish, *et al.*, “Systematic functional analysis of *Leishmania* protein kinases identifies regulators of differentiation or survival,” *Nat Commun*, vol. 12, no. 1, p. 1244, 2021.

[132] C. Naula, M. Parsons, and J. C. Mottram, “Protein kinases as drug targets in trypanosomes and leishmania,” *Biochim Biophys Acta*, vol. 1754, no. 1-2, pp. 151–159, 2005.

[133] P. Hassan, D. Fergusson, K. M. Grant, and J. C. Mottram, “The CRK3 protein kinase is essential for cell cycle progression of *Leishmania mexicana*,” *Mol Biochem Parasitol*, vol. 113, no. 2, pp. 189–198, 2001.

[134] J. C. Mottram, K. G. McCready Bp Fau - Brown, K. M. Brown Kg Fau - Grant, and K. M. Grant, “Gene disruptions indicate an essential function for the LmmCRK1 cdc2-related kinase of *Leishmania mexicana*,” *Mol Microbiol*, vol. 22, no. 3, pp. 573–583, 1996.

[135] S. Wyllie, M. Thomas, S. Patterson, *et al.*, “Cyclin-dependent kinase 12 is a drug target for visceral leishmaniasis,” *Nature*, vol. 560, no. 7717, pp. 192–197, 2018.

[136] S. Monnerat, C. I. Almeida Costa, A. C. Forkert, *et al.*, “Identification and functional characterisation of CRK12:CYC9, a novel cyclin-dependent kinase (CDK)-cyclin complex in *Trypanosoma brucei*,” *PLOS ONE*, vol. 8, no. 6, e67327, 2013.

[137] L. A. T. Cleghorn, A. Woodland, I. T. Collie, *et al.*, “Identification of inhibitors of the *Leishmania* cdc2-related protein kinase CRK3,” *ChemMedChem*, vol. 6, no. 12, pp. 2214–2224, 2011.

[138] R. G. Walker, “Leishmania CRK3:CYC6 cyclin-dependent kinase as a drug target,” Thesis, 2008.

[139] K. M. Grant, M. H. Dunion, V. Yardley, *et al.*, “Inhibitors of *Leishmania mexicana* CRK3 cyclin-dependent kinase: Chemical library screen and antileishmanial activity,” *Antimicrob Agents Chemother*, vol. 48, no. 8, p. 3033, 2004.

[140] K. M. Grant, P. Hassan, J. S. Anderson, and J. C. Mottram, “The crk3 gene of *Leishmania mexicana*encodes a stage-regulated cdc2-related histone H1 kinase that associates with p12 cks1,” *J Biol Chem*, vol. 273, no. 17, pp. 10 153–10 159, 1998.

[141] R. G. Walker, G. Thomson, K. Malone, *et al.*, “High throughput screens yield small molecule inhibitors of *Leishmania* CRK3:CYC6 cyclin-dependent kinase,” *PLoS Negl Trop Dis*, vol. 5, no. 4, e1033–e1033, 2011.

[142] R. Chhajer, A. Bhattacharyya, N. Didwania, *et al.*, “*Leishmania donovani* Aurora kinase: A promising therapeutic target against visceral leishmaniasis,” *Biochim Biophys Acta*, vol. 1860, no. 9, pp. 1973–1988, 2016.

[143] N. G. Jones, E. B. Thomas, E. Brown, N. J. Dickens, T. C. Hammarton, and J. C. Mottram, “Regulators of *Trypanosoma brucei* cell cycle progression and differentiation identified using a kinome-wide RNAi screen,” *PLoS Pathogens*, vol. 10, no. 1, e1003886, 2014.

[144] S. Kramer, “Characterization of a PKA-like kinase from *Trypanosoma brucei.*,” Thesis, 2005.

[145] V. Geoghegan, J. B. T. Carnielli, N. G. Jones, *et al.*, “CLK1/CLK2-driven signalling at the *Leishmania* kinetochore is captured by spatially referenced proximity phosphoproteomics,” *Commun Biol*, vol. 5, no. 1, p. 1305, 2022.

[146] G. Marcianò, M. Ishii, O. O. Nerusheva, and B. Akiyoshi, “Kinetoplastid kinetochore proteins KKT2 and KKT3 have unique centromere localization domains,” *J Cell Biol*, vol. 220, no. 8, e202101022, 2021.

[147] A. Efstathiou and D. Smirlis, “*Leishmania* protein kinases: Important regulators of the parasite life cycle and molecular targets for treating leishmaniasis,” *Microorganisms*, vol. 9, no. 4, p. 691, 2021.

[148] K. A. Cunningham and C. S. Watson, “Cell cycle regulation, neurogenesis, and depression,” *Proc Natl Acad Sci U S A*, vol. 105, no. 7, pp. 2259–2260, 2008.

[149] C. Joseph, A. S. Mangani, V. Gupta, *et al.*, “Cell cycle deficits in neurodegenerative disorders: Uncovering molecular mechanisms to drive innovative therapeutic development,” *Aging and disease*, vol. 11, no. 4, pp. 946–966, 2020.

[150] T. Otto and P. Sicinski, “Cell cycle proteins as promising targets in cancer therapy,” *Nat Rev Cancer*, vol. 17, no. 2, pp. 93–115, 2017.

[151] A. Robbins Jonathan, S. Absalon, A. Streva Vincent, and D. Dvorin Jeffrey, “The malaria parasite cyclin H homolog PfCyc1 is required for efficient cytokinesis in blood-stage *Plasmodium falciparum*,” *mBio*, vol. 8, no. 3, e00605–17, 2017.

[152] P. Gavriilidis, A. Giakoustidis, and D. Giakoustidis, “Aurora kinases and potential medical applications of aurora kinase inhibitors: A review,” *J Clin Med Res*, vol. 7, no. 10, pp. 742–51, 2015.

[153] S. Goel, J. S. Bergholz, and J. J. Zhao, “Targeting CDK4 and CDK6 in cancer,” *Nat Rev Cancer*, vol. 22, no. 6, pp. 356–372, 2022.

[154] J. Bai, Y. Li, and G. Zhang, “Cell cycle regulation and anticancer drug discovery,” *Cancer Biol Med*, vol. 14, no. 4, pp. 348–362, 2017.

[155] X. H. Zhang, J. Hsiang, and S. T. Rosen, “Flavopiridol (alvocidib), a cyclin-dependent kinases (CDKs) inhibitor, found synergy effects with niclosamide in cutaneous T-cell lymphoma,” *J Clin Haematol*, vol. 2, no. 2, pp. 48–61, 2021.

[156] S. Cooper, “Rethinking synchronization of mammalian cells for cell cycle analysis,” *Cellular and Molecular Life Sciences CMLS*, vol. 60, pp. 1099–1106, 2003.

[157] M. A. Juanes, “Methods of synchronization of yeast cells for the analysis of cell cycle progression,” in *The Mitotic Exit Network: Methods and Protocols*, F. Monje-Casas and E. Queralt, Eds. New York, NY: Springer New York, 2017, pp. 19–34.

[158] U. Chandra, A. Yadav, D. Kumar, and S. Saha, “Cell cycle stage-specific transcriptional activation of cyclins mediated by HAT2-dependent H4K10 acetylation of promoters in *Leishmania donovani*,” *PLOS Pathogens*, vol. 13, no. 9, e1006615, 2017.

[159] M. S. da Silva, J. P. Monteiro, V. S. Nunes, *et al.*, “*Leishmania amazonensis* promastigotes present two distinct modes of nucleus and kinetoplast segregation during cell cycle,” *PLOS ONE*, vol. 8, no. 11, e81397, 2013.

[160] B. C. D. de Oliveira, L. H. C. Assis, M. E. Shiburah, *et al.*, “Synchronization of *Leishmania amazonensis* cell cycle using hydroxyurea,” in *Cell-Cycle Synchronization: Methods and Protocols*, Z. Wang, Ed. New York, NY: Springer US, 2022, pp. 127–135.

[161] P. Kapoor, M. Sachdeva, and R. Madhubala, “Effect of the microtubule stabilising agent taxol on leishmanial protozoan parasites in vitro,” *FEMS Microbiol Lett*, vol. 176, no. 2, pp. 429–35, 1999.

[162] J. D. Damasceno, C. A. Marques, D. Beraldi, *et al.*, “Genome duplication in *Leishmania major* relies on persistent subtelomeric DNA replication,” *eLife*, vol. 9, e58030, 2020.

[163] N. MINOCHA, D. KUMAR, K. RAJANALA, and S. SAHA, “Kinetoplast morphology and segregation pattern as a marker for cell cycle progression in *Leishmania donovani*,” *J Eukaryot Microbiol*, vol. 58, no. 3, pp. 249–253, 2011.

[164] A. d. O. Passos, L. H. C. Assis, Y. G. Ferri, V. L. da Silva, M. S. da Silva, and M. I. N. Cano, “The trypanosomatids cell cycle: A brief report,” in *Cell-Cycle Synchronization: Methods and Protocols*, Z. Wang, Ed. New York, NY: Springer US, 2022, pp. 25–34.

[165] S. J. Liliensiek, K. Schell, E. Howard, P. Nealey, and C. J. Murphy, “Cell sorting but not serum starvation is effective for SV40 human corneal epithelial cell cycle synchronization,” *Exp Eye Res*, vol. 83, no. 1, pp. 61–68, 2006.

[166] Z. Wang, “Cell cycle progression and synchronization: An overview,” in *Cell-Cycle Synchronization: Methods and Protocols*, Z. Wang, Ed. New York, NY: Springer US, 2022, pp. 3–23.

[167] C. Benz, F. Dondelinger, P. G. McKean, and M. D. Urbaniak, “Cell cycle synchronisation of *Trypanosoma brucei* by centrifugal counter-flow elutriation reveals the timing of nuclear and kinetoplast DNA replication,” *Sci Rep*, vol. 7, no. 1, p. 17 599, 2017.

[168] G. Banfalvi, “Overview of cell synchronization,” in *Cell Cycle Synchronization: Methods and Protocols*, G. Banfalvi, Ed. Totowa, NJ: Humana Press, 2011, pp. 1–23.

[169] N. Minocha, D. Kumar, K. Rajanala, and S. Saha, “Characterization of *Leishmania donovani* MCM4: Expression patterns and interaction with PCNA,” *PLOS ONE*, vol. 6, no. 7, e23107, 2011.

[170] M. E. Warkiani, A. K. P. Tay, G. Guan, and J. Han, “Membrane-less microfiltration using inertial microfluidics,” *Sci Rep*, vol. 5, no. 1, p. 11 018, 2015.

[171] T. R. Carey, K. L. Cotner, B. Li, and L. L. Sohn, “Developments in label-free microfluidic methods for single-cell analysis and sorting,” *Wiley Interdiscip Rev Nanomed Nanobiotechnol*, vol. 11, no. 1, e1529, 2019.

[172] D. R. Gossett, W. M. Weaver, A. J. Mach, *et al.*, “Label-free cell separation and sorting in microfluidic systems,” *Analytical and bioAnal Chem*, vol. 397, no. 8, pp. 3249–3267, 2010.

[173] C. W. Shields, C. D. Reyes, and G. P. López, “Microfluidic cell sorting: A review of the advances in the separation of cells from debulking to rare cell isolation,” *Lab Chip*, vol. 15, no. 5, pp. 1230–1249, 2015.

[174] S. Basu, H. M. Campbell, B. N. Dittel, and A. Ray, “Purification of specific cell population by fluorescence activated cell sorting (FACS),” *J Vis Exp*, vol. v.2010, no. 41, p. 1546, 2010.

[175] W. A. Bonner, H. R. Hulett, R. G. Sweet, and L. A. Herzenberg, “Fluorescence activated cell sorting,” *Rev Sci Instrum*, vol. 43, no. 3, pp. 404–409, 2003.

[176] B. A. Sutermaster and E. M. Darling, “Considerations for high-yield, high-throughput cell enrichment: Fluorescence versus magnetic sorting,” *Sci Rep*, vol. 9, no. 1, p. 227, 2019.

[177] J. R. Fromm, S. J. Kussick, and B. L. Wood, “Identification and purification of classical hodgkin cells from lymph nodes by flow cytometry and flow cytometric cell sorting,” *Am J Clin Pathol*, vol. 126, no. 5, pp. 764–80, 2006.

[178] X. Liao, M. Makris, and X. M. Luo, “Fluorescence-activated cell sorting for purification of plasmacytoid dendritic cells from the mouse bone marrow,” *J Vis Exp*, no. 117, p. 54 641, 2016.

[179] M. K. Malone, T. A. Ujas, K. M. Cotter, *et al.*, “FACS to identify immune subsets in mouse brain and spleen,” *Methods Mol Biol*, vol. 2616, pp. 213–229, 2023.

[180] Y. Zhang, H. Lei, and B. Li, “Refractive-index-based sorting of colloidal particles using a subwavelength optical fiber in a static fluid,” *Appl Phys Express*, vol. 6, no. 7, p. 072 001, 2013.

[181] A. Prasad and E. Alizadeh, “Cell form and function: Interpreting and controlling the shape of adherent cells,” *Trends Biotechnol*, vol. 37, no. 4, pp. 347–357, 2019.

[182] M. Antfolk, C. Magnusson, P. Augustsson, H. Lilja, and T. Laurell, “Acoustofluidic, label-free separation and simultaneous concentration of rare tumor cells from white blood cells,” *Anal Chem*, vol. 87, no. 18, pp. 9322–9328, 2015.

[183] S. A. Faraghat, K. F. Hoettges, M. K. Steinbach, *et al.*, “High-throughput, low-loss, low-cost, and label-free cell separation using electrophysiology-activated cell enrichment,” *Proc Natl Acad Sci U S A*, vol. 114, no. 18, pp. 4591–4596, 2017.

[184] P. Li and Y. Ai, “Label-free multivariate biophysical phenotyping-activated acoustic sorting at the single-cell level,” *Anal Chem*, vol. 93, no. 8, pp. 4108–4117, 2021.

[185] M. P. MacDonald, G. C. Spalding, and K. Dholakia, “Microfluidic sorting in an optical lattice,” *Nature*, vol. 426, no. 6965, pp. 421–424, 2003.

[186] V. Varmazyari, H. Habibiyan, H. Ghafoorifard, M. Ebrahimi, and S. Ghafouri-Fard, “A dielectrophoresis-based microfluidic system having double-sided optimized 3D electrodes for label-free cancer cell separation with preserving cell viability,” *Sci Rep*, vol. 12, no. 1, p. 12 100, 2022.

[187] X. Wang, S. Chen, M. Kong, *et al.*, “Enhanced cell sorting and manipulation with combined optical tweezer and microfluidic chip technologies,” *Lab Chip*, vol. 11, no. 21, pp. 3656–3662, 2011.

[188] N. Nitta, T. Sugimura, A. Isozaki, *et al.*, “Intelligent image-activated cell sorting,” *Cell*, vol. 175, no. 1, 266–276.e13, 2018.

[189] Y. Gu, A. C. Zhang, Y. Han, J. Li, C. Chen, and Y.-H. Lo, “Machine learning based real-time image-guided cell sorting and classification,” *Cytometry A*, vol. 95, no. 5, pp. 499–509, 2019.

[190] K. S. Lee, M. Palatinszky, F. C. Pereira, *et al.*, “An automated Raman-based platform for the sorting of live cells by functional properties,” *Nat Microbiol*, vol. 4, no. 6, pp. 1035–1048, 2019.

[191] D. Schraivogel, T. M. Kuhn, B. Rauscher, *et al.*, “High-speed fluorescence image-enabled cell sorting,” *Science*, vol. 375, no. 6578, pp. 315–320, 2022.

[192] M. Sesen and G. Whyte, “Image-based single cell sorting automation in droplet microfluidics,” *Sci Rep*, vol. 10, no. 1, p. 8736, 2020.

[193] H.-Y. Huang, T.-L. Wu, H.-R. Huang, *et al.*, “Isolation of motile spermatozoa with a microfluidic chip having a surface-modified microchannel,” *J Lab Autom*, vol. 19, no. 1, pp. 91–99, 2014.

[194] J. McGrath, M. Jimenez, and H. Bridle, “Deterministic lateral displacement for particle separation: A review,” *Lab Chip*, vol. 14, no. 21, pp. 4139–4158, 2014.

[195] D. Jiang, C. Ni, W. Tang, D. Huang, and N. Xiang, “Inertial microfluidics in contraction-expansion microchannels: A review,” *Biomicrofluidics*, vol. 15, no. 4, p. 041 501, 2021.

[196] H. Amini, W. Lee, and D. Di Carlo, “Inertial microfluidic physics,” *Lab Chip*, vol. 14, no. 15, pp. 2739–2761, 2014.

[197] M. E. Warkiani, B. L. Khoo, D. S.-W. Tan, *et al.*, “An ultra-high-throughput spiral microfluidic biochip for the enrichment of circulating tumor cells,” *Analyst*, vol. 139, no. 13, pp. 3245–3255, 2014.

[198] S. C. Hur, N. K. Henderson-MacLennan, E. R. B. McCabe, and D. Di Carlo, “Deformability-based cell classification and enrichment using inertial microfluidics,” *Lab Chip*, vol. 11, no. 5, pp. 912–920, 2011.

[199] G. Segré and A. Silberberg, “Behaviour of macroscopic rigid spheres in poiseuille flow part 2. experimental results and interpretation,” *J Fluid Mech*, vol. 14, no. 1, pp. 136–157, 1962.

[200] D. Di Carlo, D. Irimia, R. G. Tompkins, and M. Toner, “Continuous inertial focusing, ordering, and separation of particles in microchannels,” *Proc Natl Acad Sci U S A*, vol. 104, no. 48, pp. 18 892–18 897, 2007.

[201] J. M. Martel and M. Toner, “Particle focusing in curved microfluidic channels,” *Sci Rep*, vol. 3, no. 1, p. 3340, 2013.

[202] J. Zhang, W. Li, and G. Alici, “Inertial microfluidics: Mechanisms and applications,” in *Advanced Mechatronics and MEMS Devices II*, D. Zhang and B. Wei, Eds. Cham: Springer International Publishing, 2017, pp. 563–593.

[203] J. M. Martel and M. Toner, “Inertial focusing dynamics in spiral microchannels,” *Phys Fluids*, vol. 24, no. 3, p. 32 001, 2012.

[204] X. Wang, M. Zandi, C. C. Ho, N. Kaval, and I. Papautsky, “Single stream inertial focusing in a straight microchannel,” *Lab Chip*, vol. 15, no. 8, pp. 1812–21, 2015.

[205] A. A. S. Bhagat, S. S. Kuntaegowdanahalli, and I. Papautsky, “Enhanced particle filtration in straight microchannels using shear-modulated inertial migration,” *Phys Fluids*, vol. 20, no. 10, p. 101 702, 2008.

[206] C. Liu and G. Hu, “High-throughput particle manipulation based on hydrodynamic effects in microchannels,” *Micromachines*, vol. 8, no. 3, p. 73, 2017.

[207] J. Zhang, S. Yan, D. Yuan, *et al.*, “Fundamentals and applications of inertial microfluidics: A review,” *Lab Chip*, vol. 16, no. 1, pp. 10–34, 2016.

[208] Q. Zhao, D. Yuan, J. Zhang, and W. Li, “A review of secondary flow in inertial microfluidics,” vol. 11, no. 5, p. 461, 2020.

[209] T. Tohme, P. Magaud, and L. Baldas, *Transport of non-spherical particles in square microchannel flows: A review*, Electronic Article, 2021.

[210] D. Di Carlo, “Inertial microfluidics,” *Lab Chip*, vol. 9, no. 21, pp. 3038–3046, 2009.

[211] J. Zhou and I. Papautsky, “Fundamentals of inertial focusing in microchannels,” *Lab Chip*, vol. 13, no. 6, pp. 1121–1132, 2013.

[212] A. A. S. Bhagat, S. S. Kuntaegowdanahalli, and I. Papautsky, “Inertial microfluidics for continuous particle filtration and extraction,” *Microfluid Nanofluid*, vol. 7, no. 2, pp. 217–226, 2009.

[213] S. C. Hur, H. T. K. Tse, and D. Di Carlo, “Sheathless inertial cell ordering for extreme throughput flow cytometry,” *Lab Chip*, vol. 10, no. 3, pp. 274–280, 2010.

[214] H. Cha, H. A. Amiri, S. Moshafi, *et al.*, “Effects of obstacles on inertial focusing and separation in sinusoidal channels: An experimental and numerical study,” *Chemical Engineering Science*, vol. 276, p. 118 826, 2023.

[215] A. Farahinia, W. Zhang, and I. Badea, “Recent developments in inertial and centrifugal microfluidic systems along with the involved forces for cancer cell separation: A review,” *Sensors*, vol. 23, no. 11, p. 5300, 2023.

[216] A. Gangadhar and S. A. Vanapalli, “Inertial focusing of particles and cells in the microfluidic labyrinth device: Role of sharp turns,” *Biomicrofluidics*, vol. 16, no. 4, p. 044 114, 2022.

[217] G. Guan, L. Wu, A. A. Bhagat, *et al.*, “Spiral microchannel with rectangular and trapezoidal cross-sections for size based particle separation,” *Sci Rep*, vol. 3, no. 1, p. 1475, 2013.

[218] J. A. Kim, A. Kommajosula, Y. H. Choi, *et al.*, “Inertial focusing in triangular microchannels with various apex angles,” *Biomicrofluidics*, vol. 14, no. 2, p. 024 105, 2020.

[219] J. Palumbo, M. Navi, S. S. H. Tsai, J. K. Spelt, and M. Papini, “Lab on a rod: Size-based particle separation and sorting in a helical channel,” *Biomicrofluidics*, vol. 14, no. 6, p. 064 104, 2020.

[220] J. Zhou, P. V. Giridhar, S. Kasper, and I. Papautsky, “Modulation of aspect ratio for complete separation in an inertial microfluidic channel,” *Lab Chip*, vol. 13, no. 10, pp. 1919–1929, 2013.

[221] A. A. S. Bhagat, S. S. Kuntaegowdanahalli, and I. Papautsky, “Continuous particle separation in spiral microchannels using dean flows and differential migration,” *Lab Chip*, vol. 8, no. 11, pp. 1906–1914, 2008.

[222] N. Nivedita and I. Papautsky, “Continuous separation of blood cells in spiral microfluidic devices,” *Biomicrofluidics*, vol. 7, no. 5, pp. 54 101–54 101, 2013.

[223] H. Ramachandraiah, S. Ardabili, A. M. Faridi, *et al.*, “Dean flow-coupled inertial focusing in curved channels,” *Biomicrofluidics*, vol. 8, no. 3, pp. 034 117–034 117, 2014.

[224] T. Kwon, H. Prentice, J. D. Oliveira, *et al.*, “Microfluidic cell retention device for perfusion of mammalian suspension culture,” *Sci Rep*, vol. 7, no. 1, p. 6703, 2017.

[225] S. Kalyan, C. Torabi, H. Khoo, *et al.*, “Inertial microfluidics enabling clinical research,” *Micromachines*, vol. 12, no. 3, p. 257, 2021.

[226] M. E. Warkiani, A. K. P. Tay, B. L. Khoo, X. Xiaofeng, J. Han, and C. T. Lim, “Malaria detection using inertial microfluidics,” *Lab Chip*, vol. 15, no. 4, pp. 1101–1109, 2015.

[227] K. R. Ganz, L. Clime, J. M. Farber, N. Corneau, T. Veres, and B. R. Dixon, “Enhancing the detection of *Giardia* duodenalis cysts in foods by inertial microfluidic separation,” *Appl Environ Microbiol*, vol. 81, no. 12, pp. 3925–33, 2015.

[228] M. Jimenez and H. Bridle, “Microfluidics for effective concentration and sorting of waterborne protozoan pathogens,” *J Microbiol Methods*, vol. 126, pp. 8–11, 2016.

[229] M. Jimenez, B. Miller, and H. L. Bridle, “Efficient separation of small microparticles at high flowrates using spiral channels: Application to waterborne pathogens,” *Chem Eng Sci*, vol. 157, pp. 247–254, 2017.

[230] L. Ding, S. Razavi Bazaz, T. Hall, G. Vesey, and M. Ebrahimi Warkiani, “*Giardia* purification from fecal samples using rigid spiral inertial microfluidics,” *Biomicrofluidics*, vol. 16, no. 1, p. 014 105, 2022.

[231] W. C. Lee, A. A. S. Bhagat, S. Huang, K. J. Van Vliet, J. Han, and C. T. Lim, “High-throughput cell cycle synchronization using inertial forces in spiral microchannels,” *Lab Chip*, vol. 11, no. 7, pp. 1359–1367, 2011.

[232] M. Masaeli, E. Sollier, H. Amini, *et al.*, “Continuous inertial focusing and separation of particles by shape,” *Physical Review X*, vol. 2, no. 3, p. 031 017, 2012.

[233] T. Beneke, R. Madden, L. Makin, J. Valli, J. Sunter, and E. Gluenz, “A CRISPR Cas9 high-throughput genome editing toolkit for kinetoplastids,” *R Soc Open Sci*, vol. 4, no. 5, p. 170 095, 2017.

[234] M. Fiebig, S. Kelly, and E. Gluenz, “Comparative life cycle transcriptomics revises *Leishmania mexicana* genome annotation and links a chromosome duplication with parasitism of vertebrates,” *PLoS Pathog*, vol. 11, no. 10, e1005186, 2015.

[235] T. Beneke, F. Demay, E. Hookway, *et al.*, “Genetic dissection of a *Leishmania* flagellar proteome demonstrates requirement for directional motility in sand fly infections,” *PLOS Pathogens*, vol. 15, no. 6, e1007828, 2019.

[236] T. Beneke and E. Gluenz, “Leishgedit: A method for rapid gene knockout and tagging using crispr-cas9,” in *Leishmania: Methods and Protocols*, J. Clos, Ed. New York, NY: Springer New York, 2019, pp. 189–210.

[237] J. Howell, S. Omwenga, J. Melanie, and T. C. Hammarton, “Analysis of the *Leishmania mexicana* promastigote cell cycle using imaging flow cytometry provides new insights into cell cycle flexibility and events of short duration,” *bioRxiv*, p. 2023.07.24.550259, 2024.

[238] C. B. Bagwell, S. W. Mayo, S. D. Whetstone, *et al.*, “DNA histogram debris theory and compensation,” *Cytometry*, vol. 12, no. 2, pp. 107–118, 1991.

[239] P. S. Rabinovitch, “Chapter 18 DNA content histogram and cell-cycle analysis,” in *Method Cell Biol*, Z. Darzynkiewicz, J. Paul Robinson, and H. A. Crissman, Eds. Academic Press, 1994, vol. 41, pp. 263–296.

[240] P. N. Dean and J. H. Jett, “Mathematical analysis of DNA distributions derived from flow microfluorometry,” *J of Cell Biol*, vol. 60, no. 2, pp. 523–527, 1974.

[241] L. Bristiel, *Prophesee-matlab-scripts*, `https://github.com/prophesee-ai/prophesee-matlab-scripts`, Online Database, [Online; accessed 02-Apr-2024], 2020.

[242] R. J. Wheeler, E. Gluenz, and K. Gull, “The cell cycle of *Leishmania*: Morphogenetic events and their implications for parasite biology,” *Mol Microbiol*, vol. 79, no. 3, pp. 647–662, 2011.

[243] A. Yadav, U. Chandra, and S. Saha, “Histone acetyltransferase HAT4 modulates navigation across G2/M and re-entry into G1 in *Leishmania donovani*,” *Sci Rep*, vol. 6, pp. 27 510–27 510, 2016.

[244] C. Halliday, K. Billington, Z. Wang, *et al.*, “Cellular landmarks of *Trypanosoma brucei* and *Leishmania mexicana*,” *Mol Biochem Parasitol*, vol. 230, pp. 24–36, 2019.

[245] K. Nybo, “GFP imaging in fixed cells,” *BioTechniques*, vol. 52, no. 6, pp. 359–360, 2012.

[246] M. G. Paez-Segala, M. G. Sun, G. Shtengel, *et al.*, “Fixation-resistant photoactivatable fluorescent proteins for CLEM,” *Nat Methods*, vol. 12, no. 3, 215–8, 4 p following 218, 2015.

[247] S. Banerjee, A. Sen, P. Das, and P. Saha, "*Leishmania donovani* cyclin 1 (ldcyc1) forms a complex with cell cycle kinase subunit crk3 (ldcrk3) and is possibly involved in s-phase-related activities," *FEMS Microbiol Lett*, vol. 256, no. 1, pp. 75–82, 2006.

[248] R. Wheeler, "Kinetoplast and nuclear DNA staining in *Leishmania mexicana*," *figshare*, 2014.

[249] A. J. Hobro and N. I. Smith, "An evaluation of fixation methods: Spatial and compositional cellular changes observed by Raman imaging," *Vibrational Spectroscopy*, vol. 91, pp. 31–45, 2017.

[250] R. J. Wheeler, "Analyzing the dynamics of cell cycle processes from fixed samples through ergodic principles," *Mol Biol Cell*, vol. 26, no. 22, pp. 3898–903, 2015.

[251] L. Zhu, M. Rajendram, and K. C. Huang, "Effects of fixation on bacterial cellular dimensions and integrity," *iScience*, vol. 24, no. 4, p. 102 348, 2021.

[252] S. G. J. H. Al Kufi, J. Emmerson, H. Rosenqvist, C. M. M. Garcia, D. O. Rios-Szwed, and M. Wiese, "Absence of DEATH kinesin is fatal for *Leishmania mexicana* amastigotes," *Sci Rep*, vol. 12, no. 1, p. 3266, 2022.

[253] A. Hombach-Barrigah, K. Bartsch, D. Smirlis, *et al.*, "*Leishmania donovani* 90 kD heat shock protein – impact of phosphosites on parasite fitness, infectivity and casein kinase affinity," *Sci Rep*, vol. 9, no. 1, p. 5074, 2019.

[254] C. Mano, A. Kongkaew, P. Tippawangkosol, *et al.*, "Amphotericin B resistance correlates with increased fitness *in vitro* and *in vivo* in *Leishmania (Mundinia) martiniquensis*," *Front Microbiol*, vol. 14, p. 1 156 061, 2023.

[255] D. R. Stirling, M. J. Swain-Bowden, A. M. Lucas, A. E. Carpenter, B. A. Cimini, and A. Goodman, "CellProfiler 4: Improvements in speed, utility and usability," *BMC Bioinformatics*, vol. 22, no. 1, p. 433, 2021.

[256] R. J. Wheeler, "ImageJ for partially and fully automated analysis of trypanosome micrographs," in *Trypanosomatids: Methods and Protocols*, P. A. M. Michels, M. L. Ginger, and D. Zilberstein, Eds. New York, NY: Springer US, 2020, pp. 385–408.

[257] R. J. Wheeler, K. Gull, and E. Gluenz, "Detailed interrogation of trypanosome cell biology *via* differential organelle staining and automated image analysis," *BMC Biol*, vol. 10, no. 1, p. 1, 2012.

[258] K. M. McKinnon, “Flow cytometry: An overview,” *Curr Protoc Immunol*, vol. 120, pp. 5.1.1–5.1.11, 2018.

[259] K. H. Kim and J. M. Sederstrom, “Assaying cell cycle status using flow cytometry,” *Curr Protoc Mol Biol*, vol. 111, pp. 28.6.1–28.6.11, 2015.

[260] M. Shadab, B. Jha, M. Asad, M. Deepthi, M. Kamran, and N. Ali, “Apoptosis-like cell death in *Leishmania donovani* treated with kalsometm10, a new liposomal amphotericin b,” *PLoS One*, vol. 12, no. 2, e0171306, 2017.

[261] S. Kabani, M. Waterfall, and K. R. Matthews, “Cell-cycle synchronisation of bloodstream forms of *Trypanosoma brucei* using Vybrant DyeCycle Violet-based sorting,” *Mol Biochem Parasitol*, vol. 169, no. 1, pp. 59–62, 2010.

[262] M. H. Fox, “A model for the computer analysis of synchronous DNA distributions obtained by flow cytometry,” *Cytometry*, vol. 1, no. 1, pp. 71–77, 1980.

[263] J. V. Watson, S. H. Chambers, and P. J. Smith, “A pragmatic approach to the analysis of DNA histograms with a definable G1 peak,” *Cytometry*, vol. 8, no. 1, pp. 1–8, 1987.

[264] M. Capece, A. Tessari, J. Mills, *et al.*, “A novel auxin-inducible degron system for rapid, cell cycle-specific targeted proteolysis,” *Cell Death Diff*, vol. 30, no. 9, pp. 2078–2091, 2023.

[265] H. P. Easwaran, H. Leonhardt, and M. C. Cardoso, “Cell cycle markers for live cell analyses,” *Cell Cycle*, vol. 4, no. 3, pp. 453–5, 2005.

[266] M. J. Hendzel, Y. Wei, M. A. Mancini, *et al.*, “Mitosis-specific phosphorylation of histone H3 initiates primarily within pericentromeric heterochromatin during G2 and spreads in an ordered fashion coincident with mitotic chromosome condensation,” *Chromosoma*, vol. 106, no. 6, pp. 348–360, 1997.

[267] A. Ligasová, I. Frydrych, and K. Koberna, “Basic methods of cell cycle analysis,” *Int J Mol Sci*, vol. 24, no. 4, p. 3674, 2023.

[268] T. Blasi, H. Hennig, H. D. Summers, *et al.*, “Label-free cell cycle analysis for high-throughput imaging flow cytometry,” *Nat Commun*, vol. 7, no. 1, p. 10 256, 2016.

[269] M. E. K. Calvert, J. A. Lannigan, and L. F. Pemberton, “Optimization of yeast cell cycle analysis and morphological characterization by multispectral imaging flow cytometry,” *Cytometry A*, vol. 73A, no. 9, pp. 825–833, 2008.

[270] P. Eulenberg, N. Köhler, T. Blasi, *et al.*, “Reconstructing cell cycle and disease progression using deep learning,” *Nat Communs*, vol. 8, no. 1, p. 463, 2017.

[271] A. Filby, W. Day, S. Purewal, and N. Martinez-Martin, “The analysis of cell cycle, proliferation, and asymmetric cell division by imaging flow cytometry,” in *Imaging Flow Cytometry: Methods and Protocols*, N. S. Barteneva and I. A. Vorobjev, Eds. New York, NY: Springer New York, 2016, pp. 71–95.

[272] J. O. Patterson, M. Swaffer, and A. Filby, “An imaging flow cytometry-based approach to analyse the fission yeast cell cycle in fixed cells,” *Methods*, vol. 82, pp. 74–84, 2015.

[273] N. Azas, C. Di Giorgio, F. Delmas, M. Gasquet, and P. Timon-David, “*Leishmania infantum* promastigotes: Flow cytometry as a possible tool for assessing the effects of drugs on cellular functions,” *Exp Parasitol*, vol. 87, no. 1, pp. 1–7, 1997.

[274] E. D. Carlsen, Z. Jie, Y. Liang, *et al.*, “Interactions between neutrophils and *Leishmania braziliensis* amastigotes facilitate cell activation and parasite clearance,” *J Innate Immun*, vol. 7, no. 4, pp. 354–363, 2015.

[275] R. Dandugudumula, R. Fischer-Weinberger, and D. Zilberstein, “Morphogenesis dynamics in *Leishmania* differentiation,” *Pathogens (Basel, Switzerland)*, vol. 11, no. 9, p. 952, 2022.

[276] K. N. Gibson-Corley, M. M. Bockenstedt, H. Li, *et al.*, “An *in vitro* model of antibody-enhanced killing of the intracellular parasite *Leishmania amazonensis*,” *PLOS ONE*, vol. 9, no. 9, e106426, 2014.

[277] Z. Islek, F. Sahin, and M. H. Ucisik, “Novel dual-fluorescent flow cytometric approach for quantification of macrophages infected with *Leishmania infantum* parasites,” *Parasitology*, vol. 149, no. 1, pp. 44–50, 2022.

[278] I. B. Regli, K. Passelli, B. Martínez-Salazar, *et al.*, “TLR7 sensing by neutrophils is critical for the control of cutaneous leishmaniasis,” *Cell Reports*, vol. 31, no. 10, p. 107 746, 2020.

[279] C. Terrazas, S. Oghumu, S. Varikuti, D. Martinez-Saucedo, S. M. Beverley, and A. R. Satoskar, “Uncovering *Leishmania*-macrophage interplay using imaging flow cytometry,” *J Immunol Methods*, vol. 423, pp. 93–98, 2015.

[280] M. Jara, M. Berg, G. Caljon, *et al.*, “Macromolecular biosynthetic parameters and metabolic profile in different life stages of *Leishmania braziliensis*: Amastigotes as a functionally less active stage,” *PLOS ONE*, vol. 12, no. 7, e0180532, 2017.

[281] D. Tegazzini, R. Díaz, F. Aguilar, *et al.*, “A replicative *in vitro* assay for drug discovery against *Leishmania donovani*,” *Antimicrob Agents Chemother*, vol. 60, no. 6, pp. 3524–3532, 2016.

[282] R. M. Martin, H. Leonhardt, and M. C. Cardoso, “DNA labeling in living cells,” *Cytometry A*, vol. 67A, no. 1, pp. 45–52, 2005.

[283] H. A. Crissman and G. T. Hirons, “Chapter 13 staining of DNA in live and fixed cells,” in *Methods Cell Biol*, Z. Darzynkiewicz, J. Paul Robinson, and H. A. Crissman, Eds. Academic Press, 1994, vol. 41, pp. 195–209.

[284] P. J. Smith, N. Blunt, M. Wiltshire, *et al.*, “Characteristics of a novel deep red/infrared fluorescent cell-permeant DNA probe, DRAQ5, in intact human cells analyzed by flow cytometry, confocal and multiphoton microscopy,” *Cytometry*, vol. 40, no. 4, pp. 280–291, 2000.

[285] V. M. Borges, U. G. Lopes, W. De Souza, and M. A. Vannier-Santos, “Cell structure and cytokinesis alterations in multidrug-resistant *Leishmania (Leishmania) amazonensis*,” *Parasitol Res*, vol. 95, no. 2, pp. 90–96, 2005.

[286] L. Moulay, M. Robert-Gero, S. Brown, M. C. Gendron, and F. Tournier, “Sinefungin and taxol effects on cell cycle and cytoskeleton of *Leishmania donovani* promastigotes,” *Exp Cell Res*, vol. 226, no. 2, pp. 283–91, 1996.

[287] J. Tavares, M. Ouaissi, A. Ouaissi, and A. Cordeiro-da-Silva, “Characterization of the anti-*Leishmania* effect induced by cisplatin, an anticancer drug,” *Acta Tropica*, vol. 103, no. 2, pp. 133–141, 2007.

[288] W.-L. Yau, T. Blisnick, J.-F. Taly, *et al.*, “Cyclosporin A treatment of *Leishmania donovani* reveals stage-specific functions of cyclophilins in parasite proliferation and viability,” *PLoS Negl Trop Dis*, vol. 4, no. 6, e729, 2010.

[289] A. Eddaoudi, S. L. Canning, and I. Kato, “Flow cytometric detection of G0 in live cells by Hoechst 33342 and Pyronin Y staining,” in *Cellular Quiescence: Methods and Protocols*, H. D. Lacorazza, Ed. New York, NY: Springer New York, 2018, pp. 49–57.

[290] R. Fedr, Z. Kahounová, J. Remšík, M. Reiterová, T. Kalina, and K. Souček, “Variability of fluorescence intensity distribution measured by flow cytometry is influenced by cell size and cell cycle progression,” *Sci Rep*, vol. 13, no. 1, p. 4889, 2023.

[291] J. V. Forment and S. P. Jackson, “A flow cytometry-based method to simplify the analysis and quantification of protein association to chromatin in mammalian cells,” *Nat Protoc*, vol. 10, no. 9, pp. 1297–307, 2015.

[292] Q. Guo, X. X. Ke, S. X. Fang, *et al.*, “PAQR3 inhibits non-small cell lung cancer growth by regulating the NF-κB/p53/bax axis,” *Front Cell Dev Biol*, vol. 8, p. 581 919, 2020.

[293] C. M. Yuan, V. K. Douglas-Nikitin, K. P. Ahrens, G. R. Luchetta, R. C. Braylan, and L. Yang, “DRAQ5-based DNA content analysis of hematolymphoid cell subpopulations discriminated by surface antigens and light scatter properties,” *Cytometry B*, vol. 58B, no. 1, pp. 47–52, 2004.

[294] Z. Nerada, Z. Hegyi, Á. Szepesi, *et al.*, “Application of fluorescent dye substrates for functional characterization of ABC multidrug transporters at a single cell level,” *Cytometry A*, vol. 89, no. 9, pp. 826–834, 2016.

[295] E. Castanys-Muñoz, M. Pérez-Victoria José, F. Gamarro, and S. Castanys, “Characterization of an ABCG-like transporter from the protozoan parasite *Leishmania* with a role in drug resistance and transbilayer lipid movement,” *Antimicrob Agents Chemother*, vol. 52, no. 10, pp. 3573–3579, 2008.

[296] J. I. Manzano, R. García-Hernández, S. Castanys, and F. Gamarro, “A new ABC half-transporter in *Leishmania major* is involved in resistance to antimony,” *Antimicrob Agents Chemother*, vol. 57, no. 8, pp. 3719–30, 2013.

[297] M. Ouellette, D. Légaré, A. Haimeur, *et al.*, “ABC transporters in *Leishmania* and their role in drug resistance,” *Drug Resist Updat*, vol. 1, no. 1, pp. 43–8, 1998.

[298] P. Leprohon, D. Légaré, I. Girard, B. Papadopoulou, and M. Ouellette, “Modulation of *Leishmania* ABC protein gene expression through life stages and among drug-resistant parasites,” *Eukaryot Cell*, vol. 5, no. 10, pp. 1713–1725, 2006.

[299] L. H. Franco, S. M. Beverley, and D. S. Zamboni, “Innate immune activation and subversion of mammalian functions by *Leishmania* lipophosphoglycan,” *J Parasitol Res*, vol. 2012, p. 165 126, 2012.

[300] D. A. Campbell, S. Thomas, and N. R. Sturm, “Transcription in kinetoplastid protozoa: Why be normal?” *Microbes and Infection*, vol. 5, no. 13, pp. 1231–1240, 2003.

[301] J. Sunter and K. Gull, “Shape, form, function and *Leishmania* pathogenicity: From textbook descriptions to biological understanding,” *Open biol*, vol. 7, no. 9, p. 170 165, 2017.

[302] C. A. Araújo, A. A. Araújo, C. L. Batista, *et al.*, “Morphological alterations and growth inhibition of *Leishmania (L.) amazonensis* promastigotes exposed to zidovudine (AZT),” *Parasitol Res*, vol. 108, no. 3, pp. 547–551, 2011.

[303] J. Quero Reimão, N. Nosomi Taniwaki, and A. Gustavo Tempone, “Furazolidone is a selective *in vitro* candidate against *Leishmania (L.) chagasi*: An ultrastructural study,” *Parasitol Res*, vol. 106, no. 6, pp. 1465–1469, 2010.

[304] T. F. P. de Mello, B. M. Cardoso, H. R. Bitencourt, *et al.*, “Ultrastructural and morphological changes in *Leishmania (Viannia) braziliensis* treated with synthetic chalcones,” *Exp Parasitol*, vol. 160, pp. 23–30, 2016.

[305] R. L. M. Neto, L. M. A. Sousa, C. S. Dias, J. M. B. Filho, M. R. Oliveira, and R. C. B. Q. Figueiredo, “Morphological and physiological changes in *Leishmania* promastigotes induced by yangambin, a lignan obtained from ocotea duckei,” *Exp Parasitol*, vol. 127, no. 1, pp. 215–221, 2011.

[306] L. Podešvová, T. Leštinová, E. Horáková, J. Lukeš, P. Volf, and V. Yurchenko, *Suicidal Leishmania*, Electronic Article, 2020.

[307] S. Teixeira de Macedo Silva, G. Visbal, J. Lima Prado Godinho, J. A. Urbina, W. de Souza, and J. Cola Fernandes Rodrigues, “*In vitro* antileishmanial activity of ravuconazole, a triazole antifungal drug, as a potential treatment for leishmaniasis,” *J Antimicrob Chemother*, vol. 73, no. 9, pp. 2360–2373, 2018.

[308] P. A. Bates, “Revising *Leishmania’s* life cycle,” *Nat Microbiol*, vol. 3, no. 5, pp. 529–530, 2018.

[309] Q. Jamal, A. Shah, S. B. Rasheed, and M. Adnan, “*In vitro* assessment and characterization of the growth and life cycle of *Leishmania tropica*,” *Pak J Zool*, vol. 52, 2020.

[310] L. L. Walters, "*Leishmania* differentiation in natural and unnatural sand fly hosts," *J Eukaryot Microbiol*, vol. 40, no. 2, pp. 196–206, 1993.

[311] P. Bose, N. Baron, D. Pullaiahgari, A. Ben-Zvi, and M. Shapira, "LeishIF3d is a non-canonical cap-binding protein in *Leishmania*," *Front Mol Biosci*, vol. 10, p. 1 191 934, 2023.

[312] L. Lorenzon, J. Quilles José C., G. D. Campagnaro, *et al.*, "Functional study of *Leishmania braziliensis* protein arginine methyltransferases (PRMTs) reveals that PRMT1 and PRMT5 are required for macrophage infection," *ACS Infect Dis*, vol. 8, no. 3, pp. 516–532, 2022.

[313] V. Kumar, S. Ghosh, K. Roy, C. Pal, and S. Singh, "Deletion of glutamine synthetase gene disrupts the survivability and infectivity of *Leishmania donovani*," *Front Cell Infect Microbiol*, vol. 11, p. 622 266, 2021.

[314] A. Selvapandiyan, A. Debrabant, R. Duncan, *et al.*, "Centrin gene disruption impairs stage-specific basal body duplication and cell cycle progression in *Leishmania*," *J Biol Chem*, vol. 279, no. 24, pp. 25 703–25 710, 2004.

[315] M. A. Rodrigues, "Automation of the *in vitro* micronucleus assay using the ImageStream® imaging flow cytometer," *Cytometry A*, vol. 93, no. 7, pp. 706–726, 2018.

[316] M. A. Rodrigues, L. A. Beaton-Green, R. C. Wilkins, and M. F. Fenech, "The potential for complete automated scoring of the cytokinesis block micronucleus cytome assay using imaging flow cytometry," *Mutat Res Genet Toxicol Environ Mutagen*, vol. 836, pp. 53–64, 2018.

[317] M. A. Rodrigues, C. E. Probst, A. Zayats, *et al.*, "The *in vitro* micronucleus assay using imaging flow cytometry and deep learning," *NPJ Syst Biol Appl*, vol. 7, no. 1, p. 20, 2021.

[318] W. N. Erber, H. Y. L. Hui, T. I. Mincherton, M. Harms, S. Clarke, and K. A. Fuller, "Enhanced multi-FISH analysis of immunophenotyped plasma cells by imaging flow cytometry," *J Hum Genet*, vol. 68, no. 7, pp. 515–516, 2023.

[319] K. A. Fuller, S. Bennett, H. Hui, A. Chakera, and W. N. Erber, "Development of a robust immuno-S-FISH protocol using imaging flow cytometry," *Cytometry A*, vol. 89, no. 8, pp. 720–730, 2016.

[320] T. Tsukamoto, M. Kinoshita, K. Yamada, *et al.*, “Imaging flow cytometry-based multiplex FISH for three IGH translocations in multiple myeloma,” *J Hum Genet*, vol. 68, no. 7, pp. 507–514, 2023.

[321] V. Haridas, S. Ranjbar, I. A. Vorobjev, A. E. Goldfeld, and N. S. Barteneva, “Imaging flow cytometry analysis of intracellular pathogens,” *Methods (San Diego, Calif.)*, vol. 112, pp. 91–104, 2017.

[322] A. Smirnov, M. D. Solga, J. Lannigan, and A. K. Criss, “An improved method for differentiating cell-bound from internalized particles by imaging flow cytometry,” *J Immunol Methods*, vol. 423, pp. 60–69, 2015.

[323] K. E. McGrath, T. P. Bushnell, and J. Palis, “Multispectral imaging of hematopoietic cells: Where flow meets morphology,” *J Immunol Methods*, vol. 336, no. 2, pp. 91–97, 2008.

[324] L. Johnson, P. Lei, L. Waters, M. P. Padula, and D. C. Marks, “Identification of platelet subpopulations in cryopreserved platelet components using multi-colour imaging flow cytometry,” *Sci Rep*, vol. 13, no. 1, p. 1221, 2023.

[325] L. Samsel, P. K. Dagur, N. Raghavachari, C. Seamon, G. J. Kato, and J. P. McCoy Jr, “Imaging flow cytometry for morphologic and phenotypic characterization of rare circulating endothelial cells,” *Cytometry B*, vol. 84, no. 6, pp. 379–389, 2013.

[326] E. K. Zuba-Surma, M. Kucia, A. Abdel-Latif, *et al.*, “Morphological characterization of very small embryonic-like stem cells (VSELs) by ImageStream system analysis,” *J Cell Mol Med*, vol. 12, no. 1, pp. 292–303, 2008.

[327] E. K. Zuba-Surma, M. Kucia, W. Wu, *et al.*, “Very small embryonic-like stem cells are present in adult murine organs: ImageStream-based morphological analysis and distribution studies,” *Cytometry A*, vol. 73A, no. 12, pp. 1116–1127, 2008.

[328] E. Bulkeley, A. C. Santistevan, D. Varner, and S. Meyers, “Imaging flow cytometry to characterize the relationship between abnormal sperm morphologies and reactive oxygen species in stallion sperm,” *Reprod Domest Anim*, vol. 58, no. 1, pp. 10–19, 2023.

[329] G. H. Schneiders, J. C. Foutz, A. L. Fuller, J. Nelson, R. Rekaya, and S. E. Aggrey, “The effect of increased temperatures on viability, morphology, infectivity, and development of *Eimeria Tenella*,” *J Parasitol*, vol. 106, no. 3, pp. 428–437, 2020.

[330] P. C. Tan, K. M. McNagny, and B. Hall, *Quantitative analysis of pseudopod formation with the ImageStream cell imaging system*, Generic, 2006.

[331] V. Dashkova, D. Malashenkov, N. Poulton, I. Vorobjev, and N. S. Barteneva, "Imaging flow cytometry for phytoplankton analysis," *Methods*, vol. 112, pp. 188–200, 2017.

[332] S. Dunker, D. Boho, J. Wäldchen, and P. Mäder, "Combining high-throughput imaging flow cytometry and deep learning for efficient species and life-cycle stage identification of phytoplankton," *BMC Ecol*, vol. 18, no. 1, p. 51, 2018.

[333] M. Hildebrand, A. Davis, R. Abbriano, *et al.*, "Applications of imaging flow cytometry for microalgae," in *Imaging Flow Cytometry: Methods and Protocols*, N. S. Barteneva and I. A. Vorobjev, Eds. New York, NY: Springer New York, 2016, pp. 47–67.

[334] S. Dunker, "Imaging flow cytometry for phylogenetic and morphologicallybased functional group clustering of a natural phytoplankton community over 1 year in an urban pond," *Cytometry A*, vol. 97, no. 7, pp. 727–736, 2020.

[335] H. Baisch, H. P. Beck, I. J. Christensen, *et al.*, "A comparison of mathematical methods for the analysis of DNA histograms obtained by flow cytometry," *Cell Tissue Kinet*, vol. 15, no. 3, pp. 235–49, 1982.

[336] L. H. C. Assis, D. Andrade-Silva, M. E. Shiburah, *et al.*, "Cell cycle, telomeres, and telomerase in *Leishmania spp.*: What do we know so far?" *Cells*, vol. 10, no. 11, p. 3195, 2021.

[337] M. S. da Silva, P. A. M. Muñoz, H. A. Armelin, and M. C. Elias, "Differences in the detection of BrdU/EdU incorporation assays alter the calculation for G1, S, and G2 phases of the cell cycle in trypanosomatids," *J Eukaryot Microbiol*, vol. 64, no. 6, pp. 756–770, 2017.

[338] Q. Zhou, K. J. Lee, Y. Kurasawa, H. Hu, T. An, and Z. Li, "Faithful chromosome segregation in *Trypanosoma brucei* requires a cohort of divergent spindle-associated proteins with distinct functions," *Nucleic Acids Res*, vol. 46, no. 16, pp. 8216–8231, 2018.

[339] J. Cruz, T. Graells, M. Walldén, and K. Hjort, "Inertial focusing with sub-micron resolution for separation of bacteria," *Lab Chip*, vol. 19, no. 7, pp. 1257–1266, 2019.

[340] V. Omrani, M. Z. Targhi, F. Rahbarizadeh, and R. Nosrati, “High-throughput isolation of cancer cells in spiral microchannel by changing the direction, magnitude and location of the maximum velocity,” *Sci Rep*, vol. 13, no. 1, p. 3213, 2023.

[341] A. Russom, A. K. Gupta, S. Nagrath, D. D. Carlo, J. F. Edd, and M. Toner, “Differential inertial focusing of particles in curved low-aspect-ratio microchannels,” *New J Phys*, vol. 11, no. 7, p. 075 025, 2009.

[342] M. S. Syed, M. Rafeie, D. Vandamme, *et al.*, “Selective separation of microalgae cells using inertial microfluidics,” *Bioresour Technol*, vol. 252, pp. 91–99, 2018.

[343] E. Keinan, A. C. Abraham, A. Cohen, *et al.*, “High-reynolds microfluidic sorting of large yeast populations,” *Sci Rep*, vol. 8, no. 1, p. 13 739, 2018.

[344] M. Li, H. E. Muñoz, K. Goda, and D. Di Carlo, “Shape-based separation of microalga *Euglena gracilis* using inertial microfluidics,” *Sci Rep*, vol. 7, no. 1, p. 10 802, 2017.

[345] J. Howell, N. Hall, S. Omwenga, T. C. Hammarton, and M. Jimenez, “Impact of flagellated and elongated morphological phenotypes on the focusing behaviours of biological cells in inertial microfluidic devices,” *bioRxiv*, p. 2024.05.16.594321, 2024.

[346] G.-Y. Kim, J.-I. Han, and J.-K. Park, “Inertial microfluidics-based cell sorting,” *BioChip J*, vol. 12, no. 4, pp. 257–267, 2018.

[347] N. Xiang, H. Yi, K. Chen, *et al.*, “High-throughput inertial particle focusing in a curved microchannel: Insights into the flow-rate regulation mechanism and process model,” *Biomicrofluidics*, vol. 7, no. 4, p. 44 116, 2013.

[348] A. Abdulla, W. Liu, A. Gholamipour-Shirazi, J. Sun, and X. Ding, “High-throughput isolation of circulating tumor cells using cascaded inertial focusing microfluidic channel,” *Anal Chem*, vol. 90, no. 7, pp. 4397–4405, 2018.

[349] K. Akbarnataj, S. Maleki, M. Rezaeian, M. Haki, and A. Shamloo, “Novel size-based design of spiral microfluidic devices with elliptic configurations and trapezoidal cross-section for ultra-fast isolation of circulating tumor cells,” *Talanta*, vol. 254, p. 124 125, 2023.

[350] J. M. Burke, R. E. Zubajlo, E. Smela, and I. M. White, “High-throughput particle separation and concentration using spiral inertial filtration,” *Biomicrofluidics*, vol. 8, no. 2, p. 02 410, 2014.

[351] N. Liu, C. Petchakup, H. M. Tay, K. H. H. Li, and H. W. Hou, “Spiral inertial microfluidics for cell separation and biomedical applications,” in *Applications of Microfluidic Systems in Biology and Medicine*, M. Tokeshi, Ed. Singapore: Springer Singapore, 2019, pp. 99–150.

[352] R. Mohammadali and M. Bayareh, “Deformability-based isolation of circulating tumor cells in spiral microchannels,” *Micromachines (Basel)*, vol. 14, no. 11, p. 2111, 2023.

[353] W. Pakhira, R. Kumar, and K. M. Ibrahimi, “Distinct separation of multiple CTCs using inertial focusing phenomena utilizing single-looped spiral microfluidic lab-on-chip,” *Chem Eng Sci*, vol. 275, p. 118 724, 2023.

[354] M. E. Warkiani, G. Guan, K. B. Luan, *et al.*, “Slanted spiral microfluidics for the ultra-fast, label-free isolation of circulating tumor cells,” *Lab Chip*, vol. 14, no. 1, pp. 128–137, 2014.

[355] S. Ebrahimi and P. Bagchi, “Inertial and non-inertial focusing of a deformable capsule in a curved microchannel,” *J Fluid Mech*, vol. 929, A30, 2021.

[356] E. Guzniczak, O. Otto, G. Whyte, N. Willoughby, M. Jimenez, and H. Bridle, “Deformability-induced lift force in spiral microchannels for cell separation,” *Lab Chip*, vol. 20, no. 3, pp. 614–625, 2020.

[357] E. Guzniczak, O. Otto, G. Whyte, *et al.*, “Purifying stem cell-derived red blood cells: A high-throughput label-free downstream processing strategy based on microfluidic spiral inertial separation and membrane filtration,” *Biotechnol Bioeng*, vol. 117, no. 7, pp. 2032–2045, 2020.

[358] H. W. Hou, A. A. S. Bhagat, A. G. Lin Chong, *et al.*, “Deformability based cell margination—a simple microfluidic design for malaria-infected erythrocyte separation,” *Lab Chip*, vol. 10, no. 19, pp. 2605–2613, 2010.

[359] J. Einarsson, F. Candelier, F. Lundell, J. R. Angilella, and B. Mehlig, “Effect of weak fluid inertia upon Jeffery orbits,” *Phys Rev E Stat Nonlin Soft Matter Phys*, vol. 91, no. 4, p. 041 002, 2015.

[360] S. C. Hur, S.-E. Choi, S. Kwon, and D. D. Carlo, “Inertial focusing of non-spherical microparticles,” *Appl Phys Lett*, vol. 99, no. 4, p. 044 101, 2011.

[361] C. M. Zettner and M. Yoda, “Moderate-aspect-ratio elliptical cylinders in simple shear with inertia,” *J Fluid Mech*, vol. 442, pp. 241–266, 2001.

[362] T. Roth, L. Sprenger, S. Odenbach, and U. O. Häfeli, “Continuous form-dependent focusing of non-spherical microparticles in a highly diluted suspension with the help of microfluidic spirals,” *Phys Fluids*, vol. 30, no. 4, p. 045 102, 2018.

[363] T. Roth, L. Sprenger, S. Odenbach, and U. O. Häfeli, “Continuous form-dependent focusing of non-spherical microparticles in a highly diluted suspension with the help of microfluidic spirals,” *Phys Fluids*, vol. 30, no. 4, p. 045 102, 2018.

[364] T. Hafemann and J. Fröhlich, “Simulation of non-spherical particles in curved microfluidic channels,” *Phys Fluids*, vol. 35, no. 3, p. 033 328, 2023.

[365] S. Sofela, S. Sahloul, M. Rafeie, *et al.*, “High-throughput sorting of eggs for synchronization of *C. elegans* in a microfluidic spiral chip,” *Lab Chip*, vol. 18, no. 4, pp. 679–687, 2018.

[366] H. Feng, A. Jafek, R. Samuel, *et al.*, “High efficiency rare sperm separation from biopsy samples in an inertial focusing device,” *Analyst*, vol. 146, no. 10, pp. 3368–3377, 2021.

[367] H. Jeon, C. Cremers, D. Le, J. Abell, and J. Han, “Multi-dimensional-double-spiral (MDDS) inertial microfluidic platform for sperm isolation directly from the raw semen sample,” *Sci Rep*, vol. 12, no. 1, p. 4212, 2022.

[368] S. Nepal, H. Feng, and B. K. Gale, “Optimization of a microfluidic spiral channel used to separate sperm from blood cells,” *Biomicrofluidics*, vol. 14, no. 6, p. 064 103, 2020.

[369] J. Son, K. Murphy, R. Samuel, B. K. Gale, D. T. Carrell, and J. M. Hotaling, “Non-motile sperm cell separation using a spiral channel,” *Anal Methods*, vol. 7, no. 19, pp. 8041–8047, 2015.

[370] A. Schaap, J. Dumon, and J. d. Toonder, “Sorting algal cells by morphology in spiral microchannels using inertial microfluidics,” *Microfluid Nanofluid*, vol. 20, no. 9, p. 125, 2016.

[371] N. Xiang, Z. Shi, W. Tang, D. Huang, X. Zhang, and Z. Ni, “Improved understanding of particle migration modes in spiral inertial microfluidic devices,” *RSC Adv*, vol. 5, no. 94, pp. 77 264–77 273, 2015.

[372] N. Mori, K. Kuribayashi, and S. Takeuchi, “Artificial flagellates: Analysis of advancing motions of biflagellate micro-objects,” *Appl Phys Lett*, vol. 96, no. 8, p. 083 701, 2010.

[373] T. Beneke, F. Demay, R. J. Wheeler, and E. Gluenz, “Isolation of *Leishmania* promastigote flagella,” in *Trypanosomatids: Methods and Protocols*, P. A. M. Michels, M. L. Ginger, and D. Zilberstein, Eds. New York, NY: Springer US, 2020, pp. 485–495.

[374] D. Robinson, P. Beattie, T. Sherwin, and K. Gull, “Microtubules, tubulin, and microtubule-associated proteins of trypanosomes,” in *Methods in Enzymol*. Academic Press, 1991, vol. 196, pp. 285–299.

[375] J. Xiong, J. He, W. P. Xie, *et al.*, “Rapid affinity purification of intracellular organelles using a twin strep tag,” *J Cell Sci*, vol. 132, no. 24, jcs235390, 2019.

[376] V. Varga, F. Moreira-Leite, N. Portman, and K. Gull, “Protein diversity in discrete structures at the distal tip of the trypanosome flagellum,” *Proc Natl Acad Sci U S A*, vol. 114, no. 32, E6546–E6555, 2017.

[377] J. Cruz and K. Hjort, “High-resolution particle separation by inertial focusing in high aspect ratio curved microfluidics,” *Sci Rep*, vol. 11, no. 1, p. 13 959, 2021.

[378] A. Zick, I. Onn, R. Bezalel, H. Margalit, and J. Shlomai, “Assigning functions to genes: Identification of s-phase expressed genes in *Leishmania major* based on post-transcriptional control elements,” *Nucleic Acids Res*, vol. 33, no. 13, pp. 4235–4242, 2005.

[379] N. Nivedita, P. Ligrani, and I. Papautsky, “Dean flow dynamics in low-aspect ratio spiral microchannels,” *Sci Rep*, vol. 7, no. 1, p. 44 072, 2017.

[380] M. E. Warkiani, A. K. P. Tay, G. Guan, and J. Han, “Membrane-less microfiltration using inertial microfluidics,” *Sci Rep*, vol. 5, no. 1, p. 11 018, 2015.

[381] H. Feng, A. R. Jafek, B. Wang, H. Brady, J. J. Magda, and B. K. Gale, *Viscoelastic particle focusing and separation in a spiral channel*, Electronic Article, 2022.

[382] T. Kumar, H. Ramachandraiah, S. N. Iyengar, I. Banerjee, G. Mårtensson, and A. Russom, “High throughput viscoelastic particle focusing and separation in spiral microchannels,” *Sci Rep*, vol. 11, no. 1, p. 8467, 2021.

[383] R. J. Wheeler, “Use of chiral cell shape to ensure highly directional swimming in trypanosomes,” *PLoS Comput Biol*, vol. 13, no. 1, e1005353, 2017.

[384] M. E. Warkiani, L. Chen, C.-P. Lou, H.-B. Liu, R. Zhang, and H.-Q. Gong, “Capturing and recovering of cryptosporidium parvum oocysts with polymeric micro-fabricated filter,” *J Membrane Sci*, vol. 369, no. 1, pp. 560–568, 2011.

[385] J. Howell, T. C. Hammarton, Y. Altmann, and M. Jimenez, “High-speed particle detection and tracking in microfluidic devices using event-based sensing,” *Lab Chip*, vol. 20, no. 16, pp. 3024–3035, 2020.

[386] M. Ling and F. Baowei, “Comprehensive review of surgical microscopes: Technology development and medical applications,” *J Biomed Opt*, vol. 26, no. 1, p. 010 901, 2021.

[387] M. V. D’Ambrosio, M. Bakalar, S. Bennuru, *et al.*, “Point-of-care quantification of blood-borne filarial parasites with a mobile phone microscope,” *Sci Transl Med*, vol. 7, no. 286, 286re4–286re4, 2015.

[388] Q. Chen, H. Xie, and L. Xi, “Wearable optical resolution photoacoustic microscopy,” *J Biophotonics*, vol. 12, no. 8, e201900066, 2019.

[389] D. Jin, D. Wong, J. Li, *et al.*, “Compact wireless microscope for *in-situ* time course study of large scale cell dynamics within an incubator,” *Sci Rep*, vol. 5, no. 1, p. 18 483, 2015.

[390] K. Yang, J. Wu, S. Santos, Y. Liu, L. Zhu, and F. Lin, “Recent development of portable imaging platforms for cell-based assays,” *Biosens Bioelectron*, vol. 124-125, pp. 150–160, 2019.

[391] J. T. Collins, J. Knapper, J. Stirling, *et al.*, “Robotic microscopy for everyone: The OpenFlexure microscope,” *Biomed Opt Express*, vol. 11, no. 5, pp. 2447–2460, 2020.

[392] A. Maia Chagas, L. L. Prieto-Godino, A. B. Arrenberg, and T. Baden, “The €100 lab: A 3D-printable open-source platform for fluorescence microscopy, optogenetics, and accurate temperature control during behaviour of zebrafish, drosophila, and caenorhabditis elegans,” *PLOS Biol*, vol. 15, no. 7, e2002702, 2017.

[393] S. B. Tristan-Landin, A. M. Gonzalez-Suarez, R. J. Jimenez-Valdes, and J. L. Garcia-Cordero, “Facile assembly of an affordable miniature multicolor fluorescence microscope made of 3D-printed parts enables detection of single cells,” *PLOS ONE*, vol. 14, no. 10, e0215114, 2019.

[394] B. Javidi, A. Markman, S. Rawat, T. O'Connor, A. Anand, and B. Andemariam, "Sickle cell disease diagnosis based on spatio-temporal cell dynamics analysis using 3D printed shearing digital holographic microscopy," *Optics Express*, vol. 26, no. 10, pp. 13 614–13 627, 2018.

[395] A. Caetano, C. Santana, and R. A. de Lima, "Diagnostic support of parasitic infections with an ai-powered microscope," *Res Biomed Eng*, vol. 39, no. 3, pp. 561–572, 2023.

[396] M. Salguedo, G. Zarate, J. Coronel, *et al.*, "Low-cost 3D-printed inverted microscope to detect mycobacterium tuberculosis in a MODS culture," *Tuberculosis*, vol. 132, p. 102 158, 2022.

[397] J. W. P. Brown, A. Bauer, M. E. Polinkovsky, *et al.*, "Single-molecule detection on a portable 3D-printed microscope," *Nat Communs*, vol. 10, no. 1, p. 5662, 2019.

[398] T. T. Diep, S. H. Needs, S. Bizley, and A. D. Edwards, "Rapid bacterial motility monitoring using inexpensive 3d-printed openflexure microscopy allows microfluidic antibiotic susceptibility testing," *Micromachines (Basel)*, vol. 13, no. 11, p. 1974, 2022.

[399] S. D. Grant, G. S. Cairns, J. Wistuba, and B. R. Patton, "Adapting the 3D-printed openflexure microscope enables computational super-resolution imaging," *F1000Res*, vol. 8, p. 2003, 2019.

[400] A. C. Zehrer, A. Martin-Villalba, B. Diederich, and H. Ewers, "An open-source, high-resolution, automated fluorescence microscope," *eLife*, vol. 12, RP89826, 2024.

[401] J. Christopher, L. M. Rooney, M. Donnachie, D. Uttamchandani, G. McConnell, and R. Bauer, "Low-cost 3D printed lenses for brightfield and fluorescence microscopy," *Biomed Opt Express*, vol. 15, no. 4, pp. 2224–2237, 2024.

[402] X. Li and W. Yu, "Deep tissue microscopic imaging of the kidney with a gradient-index lens system," *Opt Commun*, vol. 281, no. 7, pp. 1833–1840, 2008.

[403] K. K. Ghosh, L. D. Burns, E. D. Cocker, *et al.*, "Miniaturized integration of a fluorescence microscope," *Nat Methods*, vol. 8, no. 10, pp. 871–878, 2011.

[404] J. Knittel, L. Schnieder, G. Buess, B. Messerschmidt, and T. Possner, "Endoscope-compatible confocal microscope using a gradient index-lens system," *Opt Commun*, vol. 188, no. 5, pp. 267–273, 2001.

[405] A. C. Sobieranski, F. Inci, H. C. Tekin, *et al.*, “Portable lensless wide-field microscopy imaging platform based on digital inline holography and multi-frame pixel super-resolution,” *Light*, vol. 4, no. 10, e346–e346, 2015.

[406] M. Vicente and Z. Zeev, “Superresolved digital in-line holographic microscopy for high-resolution lensless biological imaging,” *J Biomed Opt*, vol. 15, no. 4, p. 046 027, 2010.

[407] O. Mudanyali, D. Tseng, C. Oh, *et al.*, “Compact, light-weight and cost-effective microscope based on lensless incoherent holography for telemedicine applications,” *Lab Chip*, vol. 10, no. 11, pp. 1417–1428, 2010.

[408] I. Pushkarsky, Y. Liu, W. Weaver, *et al.*, “Automated single-cell motility analysis on a chip using lensfree microscopy,” *Sci Rep*, vol. 4, no. 1, p. 4717, 2014.

[409] S. Seo, T.-W. Su, D. K. Tseng, A. Erlinger, and A. Ozcan, “Lensfree holographic imaging for on-chip cytometry and diagnostics,” *Lab Chip*, vol. 9, no. 6, pp. 777–787, 2009.

[410] E. Serabyn, K. Liewer, C. Lindensmith, K. Wallace, and J. Nadeau, “Compact, lensless digital holographic microscope for remote microbiology,” *Opt Express*, vol. 24, no. 25, pp. 28 540–28 548, 2016.

[411] Y. Bian, T. Xing, K. Jiao, *et al.*, “Computational portable microscopes for point-of-care-test and tele-diagnosis,” *Cells*, vol. 11, no. 22, p. 3670, 2022.

[412] H. C. Koydemir, Z. Gorocs, D. Tseng, *et al.*, “Rapid imaging, detection and quantification of *Giardia lamblia* cysts using mobile-phone based fluorescent microscopy and machine learning,” *Lab Chip*, vol. 15, no. 5, pp. 1284–1293, 2015.

[413] I. Navruz, A. F. Coskun, J. Wong, *et al.*, “Smart-phone based computational microscopy using multi-frame contact imaging on a fiber-optic array,” *Lab Chip*, vol. 13, no. 20, pp. 4015–4023, 2013.

[414] J. García-Villena, J. E. Torres, C. Aguilar, *et al.*, “3D-printed portable robotic mobile microscope for remote diagnosis of global health diseases,” *Electronics*, vol. 10, no. 19, p. 2408, 2021.

[415] T. Go, G. Y. Yoon, and S. J. Lee, “Learning-based automatic sensing and size classification of microparticles using smartphone holographic microscopy,” *Analyst*, vol. 144, no. 5, pp. 1751–1760, 2019.

[416] S. A. Lee and C. Yang, “A smartphone-based chip-scale microscope using ambient illumination,” *Lab Chip*, vol. 14, no. 16, pp. 3056–3063, 2014.

[417] D. Rabha, A. Sarmah, and P. Nath, “Design of a 3D printed smartphone microscopic system with enhanced imaging ability for biomedical applications,” *J Microscopy*, vol. 276, no. 1, pp. 13–20, 2019.

[418] H. Tobon-Maya, S. Zapata-Valencia, E. Zora-Guzmán, C. Buitrago-Duque, and J. Garcia-Sucerquia, “Open-source, cost-effective, portable, 3D-printed digital lensless holographic microscope,” *Appl Opt*, vol. 60, no. 4, A205–A214, 2021.

[419] P. Purwar, S. Han, Y. Lee, B. Saha, T. Sandhan, and J. Lee, “High-resolution cost-effective compact portable inverted light microscope,” *J Microscopy*, vol. 273, no. 3, pp. 199–209, 2019.

[420] M. A. Mahowald and C. Mead, “The silicon retina,” *Sci American*, vol. 264, no. 5, pp. 76–83, 1991.

[421] G. Gallego, T. Delbrück, G. Orchard, *et al.*, “Event-based vision: A survey,” *IEEE PAMI*, vol. 44, no. 1, pp. 154–180, 2022.

[422] N. M.-C. Peter, K. Lucas, J. M. Brian, *et al.*, “Event-based camera refractory period characterization and initial clock drift evaluation,” in *Proc.SPIE*, vol. 12693, p. 126930V.

[423] Prophesee, *Event-based concepts*, `https://docs.prophesee.ai/stable/concepts.html#event-based-concepts`, Web Page, [Online; accessed 24-Mar-2024], 2024.

[424] A. Ayyad, M. Halwani, D. Swart, R. Muthusamy, F. Almaskari, and Y. Zweiri, “Neuromorphic vision based control for the precise positioning of robotic drilling systems,” *Robot Com-Int Manuf*, vol. 79, p. 102 419, 2023.

[425] T. Delbruck and M. Lang, “Robotic goalie with 3 ms reaction time at 4% cpu load using event-based dynamic vision sensor,” *Front Neurosci*, vol. 7, no. 223, p. 223, 2013.

[426] X. Huang, M. Halwani, R. Muthusamy, *et al.*, “Real-time grasping strategies using event camera,” *J Intell Manuf*, vol. 33, no. 2, pp. 593–615, 2022.

[427] B. Li, H. Cao, Z. Qu, Y. Hu, Z. Wang, and Z. Liang, “Event-based robotic grasping detection with neuromorphic vision sensor and event-grasping dataset,” *Front Neurorobotics*, vol. 14, 2020.

[428] H. Patel, C. Iaboni, D. Lobo, J.-w. Choi, and P. Abichandani, *Event camera based real-time detection and tracking of indoor ground robots*, Electronic Article, 2021.

[429] Z. Lai, I. Alzugaray, M. Chli, and E. Chatzi, “Full-field structural monitoring using event cameras and physics-informed sparse identification,” *Mech Syst Signal Process*, vol. 145, p. 106 905, 2020.

[430] X. Li, S. Yu, Y. Lei, N. Li, and B. Yang, “Intelligent machinery fault diagnosis with event-based camera,” *IEEE Trans Industr Inform*, vol. 20, no. 1, pp. 380–389, 2024.

[431] W.-j. Na, K. H. Sun, B. C. Jeon, J. Lee, and Y.-h. Shin, “Event-based micro vibration measurement using phase correlation template matching with event filter optimization,” *Measurement*, vol. 215, p. 112 867, 2023.

[432] T. Fleck, S. Pavlitska, S. Nitzsche, *et al.*, “Low-power traffic surveillance using multiple rgb and event cameras: A survey,” in *2023 IEEE International Smart Cities Conference (ISC2)*, pp. 1–7.

[433] A. Karbalaie, F. Abtahi, and M. Sjöström, “Event detection in surveillance videos: A review,” *Multimed Tools Appl*, vol. 81, no. 24, pp. 35 463–35 501, 2022.

[434] I. C. Yeh, S. Chung, Y. P. Hsu, and C. I. Huang, “Event-based surveillance video retrieval through trajectory analysis using fisheye camera,” in *2020 IEEE International Conference on Consumer Electronics - Taiwan (ICCE-Taiwan)*, pp. 1–2.

[435] G. Chen, H. Cao, J. Conradt, H. Tang, F. Rohrbein, and A. Knoll, “Event-based neuromorphic vision for autonomous driving: A paradigm shift for bio-inspired visual sensing and perception,” *IEEE Signal Process Mag*, vol. 37, no. 4, pp. 34–49, 2020.

[436] A. I. Maqueda, A. Loquercio, G. Gallego, N. Garcia, and D. Scaramuzza, “Event-based vision meets deep learning on steering prediction for self-driving cars,” *IEEE Comput Soc Conf Comput Vis Pattern Recognit*, 2018.

[437] S. Afshar, A. P. Nicholson, A. v. Schaik, and G. Cohen, “Event-based object detection and tracking for space situational awareness,” *IEEE Sensors Journal*, vol. 20, no. 24, pp. 15 117–15 132, 2020.

[438] L. J. Azzalini, E. Blazquez, A. Hadjiivanov, G. Meoni, and D. Izzo, *On the generation of a synthetic event-based vision dataset for navigation and landing*, Electronic Article, 2023.

[439] G. Cohen, S. Afshar, A. van Schaik, *et al.*, “Event-based sensing for space situational awareness,” p. 25.

[440] F. Mahlknecht, D. Gehrig, J. Nash, *et al.*, *Exploring event camera-based odometry for planetary robots*, Electronic Article, 2022.

[441] O. A. AlSattam, M. P. Mongin, A. Killian, S. Gunasekaran, and K. Hirakawa, “Toward event-based noise-robust high density particle velocimetry,” in *AIAA SCITECH 2024 Forum* (AIAA SciTech Forum), AIAA SciTech Forum. American Institute of Aeronautics and Astronautics, 2024.

[442] D. Borer, T. Delbruck, and T. Rösgen, “Three-dimensional particle tracking velocimetry using dynamic vision sensors,” *Exp Fluid*, vol. 58, no. 12, p. 165, 2017.

[443] D. Drazen, P. Lichtsteiner, P. Häfliger, T. Delbrück, and A. Jensen, “Toward real-time particle tracking using an event-based dynamic vision sensor,” *Exp Fluids*, vol. 51, no. 5, pp. 1465–1469, 2011.

[444] Z. Ni, C. Pacoret, R. Benosman, S. Ieng, and S. RÉGnier*, “Asynchronous event-based high speed vision for microparticle tracking,” *J Microscopy*, vol. 245, no. 3, pp. 236–244, 2012.

[445] Y. Wang, R. Idoughi, and W. Heidrich, “Stereo event-based particle tracking velocimetry for 3d fluid flow reconstruction,” in *Computer Vision – ECCV 2020*, A. Vedaldi, H. Bischof, T. Brox, and J.-M. Frahm, Eds., Springer International Publishing, pp. 36–53.

[446] C. E. Willert and J. Klinner, “Event-based imaging velocimetry: An assessment of event-based cameras for the measurement of fluid flows,” *Exp Fluids*, vol. 63, no. 6, p. 101, 2022.

[447] C. E. Willert, “Event-based imaging velocimetry using pulsed illumination,” *Exp Fluids*, vol. 64, no. 5, p. 98, 2023.

[448] C. Cabriel, T. Monfort, C. G. Specht, and I. Izeddin, “Event-based vision sensor for fast and dense single-molecule localization microscopy,” *Nat Photonics*, vol. 17, no. 12, pp. 1105–1113, 2023.

[449] Y. Auad, M. Walls, J.-D. Blazit, *et al.*, “Event-based hyperspectral EELS: Towards nanosecond temporal resolution,” *Ultramicroscopy*, vol. 239, p. 113 539, 2022.

[450] B. D. A. Levin, “Direct detectors and their applications in electron microscopy for materials science,” *J Phys*, vol. 4, no. 4, p. 042 005, 2021.

[451] Z. Zhang, M. S. Ma, J. K. Eshraghian, D. Vigolo, K. T. Yong, and O. Kavehei, “Work in progress: Neuromorphic cytometry, high-throughput event-based flow flow-imaging,” in *2022 8th International Conference on Event-Based Control, Communication, and Signal Processing (EBCCSP)*, pp. 1–5.

[452] X. Berthelon, G. Chenegros, T. Finateu, S. H. Ieng, and R. Benosman, “Effects of cooling on the snr and contrast detection of a low-light event-based camera,” *IEEE Transactions on Biomedical Circuits and Systems*, vol. 12, no. 6, pp. 1467–1474, 2018.

[453] Z. Ge, H. Wei, F. Xu, *et al.*, “Millisecond autofocusing microscopy using neuromorphic event sensing,” *Opt Lasers Eng*, vol. 160, p. 107 247, 2023.

[454] X. Berthelon, “Neuromorphic analysis of hemodynamics using event-based cameras analyse neuromorphique de l’hémodynamique avec des caméras évènementielles,” Thesis, 2018.

[455] CytoskeletonInc, *MemGlow™ 640: Fluorogenic membrane probe (a member of the MEMBRIGHT™ family)*, `https://www.cytoskeleton.com/live-cell-reagents/mg04-memglow-640-membright`, Web Page, [Online; accessed 23-Jan-2024].

[456] A. G. Mukhopadhyay and C. S. Dey, “Reactivation of flagellar motility in demembranated *Leishmania* reveals role of cAMP in flagellar wave reversal to ciliary waveform,” *Sci Rep*, vol. 6, no. 1, p. 37 308, 2016.

[457] G. Saggiorato, L. Alvarez, J. F. Jikeli, U. B. Kaupp, G. Gompper, and J. Elgeti, “Human sperm steer with second harmonics of the flagellar beat,” *Nat Communs*, vol. 8, no. 1, p. 1415, 2017.

[458] P. J. Tadrous, “PUMA – an open-source 3D-printed direct vision microscope with augmented reality and spatial light modulator functions,” *J Microscopy*, vol. 283, no. 3, pp. 259–280, 2021.

[459] S. C. Hur, S.-E. Choi, S. Kwon, and D. D. Carlo, “Inertial focusing of non-spherical microparticles,” *Appl Phys Lett*, vol. 99, no. 4, p. 044 101, 2011.

[460] S. M. Anthony and Y. Yu, “Tracking single particle rotation: Probing dynamics in four dimensions,” *Anal Methods*, vol. 7, no. 17, pp. 7020–7028, 2015.

[461] Y. Liu, Z. Chen, and J. Xu, “Recent advances in the microfluidic generation of shape-controllable hydrogel microparticles and their applications,” *Green Chem Eng*, vol. 5, no. 1, pp. 16–30, 2024.

[462] N. Abbasi, M. Navi, J. K. Nunes, and S. S. H. Tsai, “Controlled generation of spiky microparticles by ionic cross-linking within an aqueous two-phase system,” *Soft Matt*, vol. 15, no. 16, pp. 3301–3306, 2019.

[463] L. Wang and D. S. Dandy, “A microfluidic concentrator for cyanobacteria harvesting,” *Algal Res*, vol. 26, pp. 481–489, 2017.